UNIVERSITY OF BIRMINGHAM

A STUDY OF FINE PARTICLE GRINDING IN VERTICALLY STIRRED MEDIA MILLS VIA POSITRON EMISSION PARTICLE TRACKING TECHNOLOGY AND THE DISCRETE ELEMENT METHOD

by

YANG YANG

A thesis submitted to the University of Birmingham for the degree of

DOCTOR OF PHILOSOPHY

School of Chemical Engineering

College of Engineering & Physical Sciences

The University of Birmingham

April 2018

ABSTRACT

This study provides a comprehensive understanding of the fine particle grinding process in stirred media mills. Calcium carbonate was chosen as the feed material. The experiments were firstly conducted in a laboratory scale vertically stirred media mill under various grinding conditions. The operating variables including specific energy, rotational speed, solids concentration, grinding media type, chemical additives (dispersant) were investigated. Then, the process was scaled up to a pilot scale mill. The performance of the pilot scale mill was compared to the laboratory scale mill regarding the product size (e.g. d_{80}) and instantaneous power draw.

Positron Emission Particle Tracking technology (PEPT) was used as a tool to study the motion of the grinding media in the laboratory scale stirred media mill. Some new stirrers were proposed and analysed. The PEPT results obtained under different operating conditions were demonstrated and analysed. The Discrete Element Method (DEM) based on the Hertz-Mindlin contact model was implemented to simulate the motion of the grinding media in both laboratory scale and pilot scale mills.

A new type of stirrer is accepted by Imerys and used to produce the calcium carbonate in the industrial scale of grinding process. The energy saving is obtained up to 3 % compared to the standard stirrer currently used.

ACKNOWLEDGEMENTS

First, I would like to express my great appreciation to my supervisor Professor Neil Rowson for his patient guidance and encouragement. It is a great honour to be his student and it has been a great pleasure to work with him. I have been given a lot of freedom for choosing the research topic for the experiments during the study. I also learned a lot from him, especially his precise and positive attitudes toward the academic research.

I also must express my gratitude to Dr. Richard Tamblyn from Imerys, without his advice and help this project could not have been completed. In addition, I would also like to thank the help and technical advice from Dr. Tafadzwa Motsi and all others when I undertook the training at Imerys.

I genuinely appreciated the help from all the staff in the School of Chemical Engineering, especially Dr. Andy Ingram, Mrs Lynn Draper, Dr. Isabel Dobrinovitch who responded my questions and queries promptly. I would like to thank Dr. Paul Stanley for his help and time on the SEM training.

I also want to express my gratitude to the support from Thomas Skuse and Robert Sommerville.

Thanks to my friends Xingjie Liu, Shuai Tian, Xiaotong Zhang, Mingmig Du and all friends in the office G2 for their friendship and support.

Last but not least, I would like to thank my parents for their endless support and encourage.

Table of Contents

ABSTRACT 1
ACKNOWLEDGEMENTS 2
List of Figures 6
List of Tables 12
Nomenclature 13
Chapter 1 Introduction 16
1.1. Background 16
1.2. Objectives 18
1.3. Layout of thesis 19
Chapter 2 Literature Review 21
2.1. Introduction 21
2.2. Type of grinding mills 28
2.2.1. Introduction 28
2.2.2. Tumbling mill 30
2.2.3. Vibrating mill 31
2.2.4. Stirred media mill 32
2.3. Theory of fine grinding 36
2.3.1. Energy-size reduction relationships 37
2.3.2. Stress model 39
2.3.3. Population balance model 42
2.4. Visualised analytical methods 44
2.5. Discrete Element Method 46
2.5.1. Introduction 46
2.5.2. Governing equations 48
2.5.3. Contact models 51
2.5.4. Hertz-Mindlin model 54
2.5.5. Adhesive contact model 55
2.5.6. Liquid bridge model 56
2.6. Conclusions 58
Chapter 3 Experimental set-up and techniques 59
3.1. Introduction 59
3.2. Experimental materials 59
3.2.1. Feed mineral 59
3.2.2. Solids content of slurry 61

3.2.3. Morphology of calcite 66
3.3. Experimental apparatus 68
3.3.1. Laboratory scale mill 69
3.3.2. Pilot scale mill 71
3.3.3. Grinding media 74
Chapter 4 Grinding calcite suspensions in a vertically stirred media mill 75
4.1. Introduction 75
4.2. Experimental set-up 75
4.3. Analysis of operating variables 76
4.3.1. Specific energy input 76
4.3.2. Influence of rotational speed 81
4.3.3. Solids concentration 85
4.3.4. Grinding media size 89
4.3.5. Influence of dispersant 91
4.3.6. Application on wollastonite and perlite 96
4.4. Analysis of stirrer configurations 100
4.4.1. Introduction of stirrer configurations 100
4.4.2. Effect of number of stirrer arms 102
4.4.3. Effect of gap distance 107
4.4.4. Effect of stirrer orientation 110
4.4.5. A combination of pin and flat blade stirrers 113
4.4.6. Impact of mill lid thickness 115
4.5. Pilot scale mill 118
4.5.1. Comparison of pilot scale mill and laboratory scale mill 118
4.5.2. Application of different stirrer types 125
4.6. Conclusions 130
Chapter 5 Positron Emission Particle Tracking (PEPT) technology 131
5.1. Introduction 131
5.2. Experimental set-up 132
5.2.1. Radioactive tracer 132
5.2.2. Analysis of PEPT data 134
5.2.3. Azimuthally averaged velocity 141
5.3. Analysis of experimental data 144
5.3.1. Tip speed 145
5.3.2. Grinding media density 154
5.3.3. Grinding media size 159

5.3.4. Influence of stirrer configuration 164
5.4. Conclusions 182
Chapter 6 Discrete Element Method (DEM) simulation 184
6.1. Introduction 184
6.2. Simulation set-up 185
6.2.1. Simulation system 186
6.2.2. Simulation parameters 188
6.3. Results and discussion 190
6.3.1. Laboratory scale mill 190
6.3.2. Pilot scale mill 198
6.4. Conclusions 204
Chapter 7 Conclusions and further work recommendations 205
7.1. Conclusions 205
7.2. Further work recommendations 207
References 209
Appendix I List of published paper and attended meetings 216
Appendix II The code developed in Matlab to analyse PEPT data. 217
Script 1 for loading PEPT original data 217
Script 2 for routine used to generate azimuthally averaged 3D-velocity map 218
Script 3 for sub-function used for calculation of the tracer velocity 219
Script 4 for sub-function used to calculate azimuthally averaged variables 220
Appendix III The code developed in LIGGGHTS for DEM 222
The script A used in LIGGGHTS for laboratory scale mill. 222
The script B used in LIGGGHTS for pilot scale mill. 225
Appendix IV The published paper in peer-reviewed journal Separation Science and Technology . 228

List of Figures

Fig. 1-1. A general description of the operating units applied in milling of calcium carbonate based on the mineral size……17

Fig. 2-1. The relationship between valuable minerals (black) and gangue (white): (a) regular (b) vain (c) frame and (d) occlusion ……21

Fig. 2-2. Steps in mineral processing flowsheet……22

Fig. 2-3. A typical horizontal layout of grinding mill (feed material enters from left and leaves at top)……24

Fig. 2-4. A typical vertical layout of grinding mill……24

Fig. 2-5. The specific energy input (kWh/t) required for a size range……26

Fig. 2-6. The typical movement of the charge within tumbling mill stirred mill and vibrating mill……28

Fig. 2-7. Demonstration of the stress types occurred in all types of the mills……29

Fig. 2-8. Parabolic motion path for grinding media in tumbling mill (a) and centrifugal force and the gravitational force on a ball……31

Fig. 2-9. A diagrammatic view of the eccentric vibration mill.……32

Fig. 2-10. A typical Stirred media mill by Metso (Stirred Media Detritors)……33

Fig. 2-11. How grinding media beads approach mineral particles……35

Fig. 2-12. An active volume for two grinding media particles……41

Fig. 2-13. The illustration of forces and torques involved in DEM simulation for particle i……49

Fig. 2-14. Some typical geometries used to represent particles outline (a) sphere, (b) ellipse (c) polygon and (d) compound form……52

Fig. 2-15. (a) Contact for sphere-sphere and (b) contact for ellipse-ellipse……53

Fig. 2-16. A schematic of a particle under adhesion force and the load……56

Fig. 2-17. A schematic of liquid bridge model between two equal spheres with a non-zero contact angle……57

Fig. 3-1. Cumulative PSD of feed sample and product sample at energy input 100 kWh/t……61

Fig. 3-2. Shear stress versus shear rate for time-independent non-Newtonian fluids……62

Fig. 3-3. Shear stress (Pa) against shear rate (s^{-1}) at 50 % (w/w), 65 % (w/w) and 75 % (w/w)……63

Fig. 3-4. Viscosity (Pa·s) against shear rate (s^{-1}) at 65 % (w/w) and 75 % (w/w)……64

Fig. 3-5. SEM photographs for feed calcite at length scale 100 µm (left) and 50 µm (right)……66

Fig. 3-6. SEM photographs for calcite ground at energy 100 kWh/t (length scale at 20 µm)……67

Fig. 3-7. SEM photograph for calcite ground at energy 200 kWh/t (length scale at 10 µm)……67

Fig. 3-8. SEM photograph for calcite ground at energy 300 kWh/t (length scale at 10 μm)……68

Fig. 3-9. The experimental set-up for the laboratory scale mill……69

Fig. 3-10. Standard pin stirrer (Type a) used in the laboratory scale mill……70

Fig. 3-11. The configuration for the pilot scale mill with key components……71

Fig. 3-12. Standard pin stirrer (Type b) used in the pilot scale mill……72

Fig. 3-13. Photographs of grinding media (a) Carbolite and (b) ZirPro (ZirPro is smoother)……74

Fig. 4-1. Particle size distribution (PSD) obtained using Carbolite grinding media (size +0.8-1.2 mm) at V_t=9.81 m/s with the specific energy input 100-300 kWh/t……78

Fig. 4-2. Size reduction ratio (f_{80}/d_{80}, f_{50}/d_{50}, f_{20}/d_{20}) at specific energy input 100-300 kWh/t.....80

Fig. 4-3. SF and PSD width values d_{90}/d_{10}, (d_{90}-d_{10})/ d_{50} at specific energy input 100-300 kWh/t...81

Fig. 4-4. The values of product d_{80} are compared at V_t=5.23 m/s, 6.54 m/s, 7.85 m/s and 9.81 m/s using Carbolite size +0.8-1.2 mm (75 % (w/w) solids concentration)……82

Fig. 4-5. The relationship between the instantaneous power draw and the tip speed using Carbolite +0.8-1.2 mm (75 % solids concentration)……85

Fig. 4-6. The product d_{80} obtained at solids concentration 50 %, 65 % and 75 % (w/w) against the specific energy input……86

Fig. 4-7. A single particle captured by grinding media and a layer of particle captured by grinding media ……87

Fig. 4-8. Zirpro grinding media size range +0.7-1.4 mm, +1.6-2.0 mm and +2.0-2.4 mm……89

Fig. 4-9. The product d_{80} obtained at ZirPro grinding media size ranges +0.7-1.4 mm, +1.6-2.0 mm and +2.0-2.4 mm……90

Fig. 4-10. The relationship between electrical repulsion and van der Waals attraction (Ravina and Moramarco, 1993)……92

Fig. 4-11. The product d_{80} obtained at dispersant 0.8 %, 2.5 %, 5 % and 10 % (w/w)……95

Fig. 4-12. SEM photographs for feed perlite at length scale 50 µm……96

Fig. 4-13. SEM photographs for feed wollastonite at length scale 50 µm……97

Fig. 4-14. Size reduction ratio f_{80}/d_{80} as a function of the specific energy (kWh/t) for mineral perlite and wollastonite……99

Fig. 4-15. A typical flow path observed using stirrer Type a ……102

Fig. 4-16. The product d_{80} obtained using stirrer Type a and Type a-1 at V_t=7.85 m/s……103

Fig. 4-17. Instantaneous power draw plotted against grinding time using stirrer Type a and Type a-1 at V_t=7.85 m/s……105

Fig. 4-18. Comparison of product d_{80} obtained using stirrer Type a-2 and Type a-3 at V_t=7.85 m/s……108

Fig. 4-19. The instantaneous power draw plotted against the grinding time using stirrer Type a-2 and Type a-3 at V_t=7.85 m/s ……109

Fig. 4-20. The product d_{80} obtained using stirrer Type a-1 and Type a-4 at V_t=5.23 m/s, 65 % (w/w) solids concentrations……111

Fig. 4-21. The instantaneous power plotted against the grinding time for stirrer Type a-1 and Type a-4 at V_t=5.23 m/s……112

Fig. 4-22. The product d_{80} obtained using stirrer Type a and stirrer Type a-5 at V_t=7.85 m/s……114

Fig. 4-23. The instantaneous power measured using stirrer Type a and Type a-5 at V_t=7.85 m/s….115

Fig. 4-24. The product d_{80} using thick lid and normal lid configurations against the energy input at V_t=5.23 m/s……116

Fig. 4-25. Instantaneous power draw and grinding time measured with thick lid and normal lid…..117

Fig. 4-26. Particle size distribution obtained in the pilot scale mill at 65 % solids concentration and V_t=7.85 m/s (576 RPM) using Carbolite grinding media +0.8-1.2 mm……119

Fig. 4-27. Comparison of the product d_{80} obtained in the laboratory mill and pilot mill at V_t=7.85 m/s……121

Fig. 4-28. The comparison of the instantaneous power draw and grinding time over the laboratory mill and the pilot mill at V_t=7.85 m/s and 65 % solids concentration……123

Fig. 4-29. The photograph of stirrer Type b-1 used in the pilot scale mill……125

Fig. 4-30. 3D images for the standard stirrer (Type b) and the new stirrer (Type b-1) used in the pilot scale mill……125

Fig. 4-31. Comparison of the product d_{80} obtained using Type b and Type b-1 in the pilot scale mill……127

Fig. 4-32. The instantaneous power draw against the grinding time using stirrer Type b and Type b-1 at V_t=7.85 m/s……128

Fig. 5-1. The laboratory scale mill is placed in the space between the 2 PEPT cameras……132

Fig. 5-2. The reconstruction of the radioactive tracer location detected by a bunch of γ-rays……133

Fig. 5-3. The radionuclide decays by emitting a positron which annihilates with an electron producing a pair of back to back gamma rays ……134

Fig. 5-4. A sample of a series of original PEPT data……135

Fig. 5-5. The data extracted from PEPT shown in x, y, z, direction in the original coordinate……136

Fig. 5-6. A new 3D-coordinate is built with the reference of the stirred media mill……137

Fig. 5-7. A series of x, y and z values based in the new coordinate……138

Fig. 5-8. Sample of the rebuilt trajectory of the tracer in the grinding chamber……139

Fig. 5-9. The linear interpolation method to determine the 3D-velocity v_n at time t_n……140

Fig. 5-10. The process for calculation of the azimuthally averaged velocity……142

Fig. 5-11. The chamber is divided into the upper band, stirrer band and lower band based on the relative position of the stirrer……143

Fig. 5-12. The standard stirrer (Type a) used in PEPT experiment……144

Fig. 5-13. Details of the grinding chamber geometry with the standard stirrer Type a (units in cm).145

Fig. 5-14. The velocity in radial direction obtained from PEPT using Carbolite grinding media at V_t=5.23 m/s (800 RPM), 6.54 m/s (1000 RPM), 7.85 m/s (1200 RPM), 9.81 m/s (1500 RPM). The colour bar units in m/s……146

Fig. 5-15. The velocity in tangential direction obtained using Carbolite grinding media at 4 tip speeds: V_t=5.23 m/s (800 RPM), 6.54 m/s (1000 RPM), 7.85 m/s (1200 RPM) and 9.81 m/s (1500 RPM). The colour bar units in m/s……147

Fig. 5-16. The velocity in vertical direction from PEPT obtained using Carbolite grinding media at 4 tip speeds: V_t=5.23 m/s (800 RPM), 6.54 m/s (1000 RPM), 7.85 m/s (1200 RPM) and 9.81 m/s (1500 RPM). The colour bar units in m/s……149

Fig. 5-17. The velocity vector obtained at 4 tip speeds: V_t=5.23 m/s (800 RPM), 6.54 m/s (1000 RPM), 7.85 m/s (1200 RPM) and 9.81 m/s (1500 RPM)……150

Fig. 5-18. The normalised occupancy rate obtained using Carbolite grinding media at 4 tip speeds: 5.23 m/s (800 RPM), 6.54 m/s (1000 RPM), 7.85 m/s (1200 RPM) and 9.81 m/s (1500 RPM). The colour bar has no units……151

Fig. 5-19. The 3D-velocity profile in the radial position r/R=0.5, 0.6, 0.65 and 0.75 using Carbolite grinding media at 4 tip speeds: V_t=5.23 m/s (800 RPM), 6.54 m/s (1000 RPM), 7.85 m/s (1200 RPM) and 9.81 m/s (1500 RPM)……152

Fig. 5-20. The 3D-velocity profile in the radial position r/R=0.8, 0.86, 0.89 and 0.92 using Carbolite grinding media at 4 tip speeds: V_t=5.23 m/s (800 RPM), 6.54 m/s (1000 RPM), 7.85 m/s (1200 RPM) and 9.81 m/s (1500 RPM)……152

Fig. 5-21. The 3D-velocity profile obtained using ZirPro and Carbolite at V_t=9.81 m/s. The radial position is r/R=0.8, 0.86, 0.89 and 0.92 ……154

Fig. 5-22. The 3D-velocity profile obtained using ZirPro and Carbolite at V_t=5.23 m/s. The radial position is r/R=0.8, 0.86, 0.89 and 0.92……155

Fig. 5-23. The 3D-velocity map obtained using ZirPro and Carbolite at V_t=6.54 m/s. The colour bar unit is m/s……155

Fig. 5-24. The 3D-velocity profile obtained using ZirPro and Carbolite at V_t=6.54 m/s. The radial position is r/R=0.8, 0.86, 0.89 and 0.9……156

Fig. 5-25. The 3D-velocity map obtained using ZirPro and Carbolite at V_t=7.85 m/s. The colour bar unit is m/s ……156

Fig. 5-26. The 3D-velocity profile obtained using ZirPro and Carbolite at V_t=7.85 m/s. The radial position is r/R=0.8, 0.86, 0.89 and 0.92……157

Fig. 5-27. The 3D-velocity map obtained using ZirPro and Carbolite at V_t=9.81 m/s. The colour bar unit is m/s……157

Fig. 5-28. The 3D-velocity profile obtained using ZirPro and Carbolite at V_t=9.81 m/s. The radial position is r/R=0.8, 0.86, 0.89 and 0.92……..158

Fig. 5-29. The 3D-velocity map obtained using ZirPro grinding media size +0.7-1.4 mm, +1.6-2.0 mm and +2.0 -2.4 mm at tip speed 6.54 m/s. The colour bar unit is m/s……160

Fig. 5-30. The 3D-velocity profile obtained using ZirPro grinding media size +0.7-1.4 mm, +1.6-2.0 mm and +2.0 -2.4 mm at V_t=6.54 m/s (1000 RPM)……161

Fig. 5-31. The velocity vector obtained using ZirPro grinding media size +0.7-1.4 mm, +1.6-2.0 mm and +2.0-2.4 mm at V_t=6.54 m/s (1000 RPM)……162

Fig. 5-32. The occupancy rate obtained using ZirPro grinding media size +0.7-1.4 mm, +1.6-2.0 mm and +2.0-2.4 mm at V_t=6.54 m/s (1000 RPM)……163

Fig. 5-33. Geometry for the grinding chamber with the 3 layers of the pin stirrer (Type a-1) (units in cm)……164

Fig. 5-34. The 3D-velocity map (left, units in m/s), vector (middle) and normalised occupancy rate(right) obtained using 3 layers of the pin stirrer (Type a-1) at V_t=4.58 m/s (700 RPM). The colour bar units in m/s……165

Fig. 5-35. Detailed geometry for the grinding chamber with the 3 layers of pin stirrer (Type a-1) and a thickness enhanced top cover (units in cm)……167

Fig. 5-36. The 3D-velocity map (left, units in m/s), velocity vector (middle) and normalised occupancy rate (right) obtained using 3 layers of the pin stirrer and the thick lid at V_t=4.58 m/s (700 RPM)….167

Fig. 5-37. The 3D-velocity profile obtained using stirrer Type a-1 with and without thick lid at V_t=4.58 m/s (700 RPM). The radial position r/R=0.4, 0.5, 0.6 and 0.7……..169

Fig. 5-38. Detailed geometry for stirrer Type a-2 (2 pairs of the pitched blades) and its relative position in the grinding chamber (units in cm)……170

Fig. 5-39. The 3D-velocity map (left), velocity vector (middle) and normalised occupancy rate (right) obtained using stirrer Type a-2 at 5.23 m/s (800 RPM)……171

Fig. 5-40. The 3D-velocity map (left), velocity vector (middle) and normalised occupancy rate (right) using stirrer Type a-2 at V_t=7.85 m/s (1200 RPM)……171

Fig. 5-41. The 3D-velocity profile obtained using ZirPro and stirrer Type a-2 at V_t=5.23 m/s (800 RPM) and 7.85 m/s (1200 RPM) at radial position r/R=0.4, 0.5, 0.6 and 0.7……173

Fig. 5-42. Detailed geometry for stirrer Type a-3 consisted by 2 layers of pitched blades and a pair of pin stirrers (units in cm)……174

Fig. 5-43. The 3D-velocity map (left), velocity vector (middle) and normalised occupancy rate (right) using stirrer Type a-3 at V_t=5.23 m/s (800 RPM)……175

Fig. 5-44. The 3D-velocity map (left), velocity vector (middle) and normalised occupancy rate (right) using stirrer Type a-3 at V_t=7.85 m/s (1200 RPM)……175

Fig. 5-45. The 3D-velocity profile obtained using ZirPro grinding media and stirrer Type a-3. V_t=5.23 m/s (800 RPM) and 7.85 m/s (1200 RPM) at radial position r/R=0.4, 0.5, 0.6 and 0.7……177

Fig. 5-46. Detailed geometry for stirrer Type a-4 consisted of 3 pairs of flat stirrers (units in cm)….178

Fig. 5-47. The 3D-velocity map (left), velocity vector (middle) and normalised occupancy rate (right) obtained using stirrer Type a-4 at V_t=5.23 m/s (800 RPM)..... 179

Fig. 5-48. The 3D-velocity map (left), velocity vector (middle) and normalised occupancy rate using stirrer Type a-4 at V_t=7.85 m/s (1200 RPM).....180

Fig. 5-49. The 3D-velocity profiles obtained using ZirPro grinding media with stirrer Type a-4 at V_t=5.23 m/s (800 RPM) and 7.85 m/s (1200 RPM). The radial position r/R=0.4, 0.5, 0.6 and 0.7.....181

Fig. 6-1. 3D CAD pictures of the laboratory mill with Type a (a) and Type a-5 (b). The chamber wall is transparent to show the stirrer configuration.....187

Fig. 6-2. 3D CAD pictures of the pilot scale mill with Type b (left) and Type b-1 (right). The chamber wall is transparent in order to show the stirrer configuration.....187

Fig. 6-3. Initially packed particle bed in the laboratory mill with the standard stirrer (t=0 s).....190

Fig. 6-4. The distribution of instantaneous velocity in a cliped section in the laboratory mill using the standard stirrer (Type a) at V_t=5.23 m/s. (a) instantaneous velocity distribution and (b) velocity vector at time 1.5 s.....191

Fig. 6-5. Comparison of the azimuthally averaged velocity map obtained by DEM (left) and PEPT (right) at V_t= 5.23 m/s (standard stirrer).....192

Fig. 6-6. Comparison of the azimuthally averaged 3D-velocity distribution obtained using DEM and PEPT at radial position r/R=0.5, 0.6, 0.7, 0.8 and 0.9.....194

Fig. 6-7. The distribution of instantaneous velocity obtained using Type a-5 at V_t=5.23 m/s (800 RPM). (a) Velocity distribution and (b) velocity vector 195

Fig. 6-8. The azimuthally averaged 3D-velocity map obtained using Type a-5 196

Fig. 6-9. Comparison of the azimuthally averaged 3D-velocity distribution obtained using the stirrer Type a and stirrer Type a-5 at the radial position r/R=0.5, 0.6, 0.7, 0.8 and 0.9.....197

Fig. 6-10. The distribution of instantaneous velocity obtained in the pilot scale mill using standard stirrer (Type b) at V_t=5.23 m/s. (a) velocity distribution and (b) velocity vector.....199

Fig. 6-11. The distribution of instantaneous velocity in the pilot scale mill using stirrer Type b-1 at V_t=5.23 m/s. (a) velocity distribution and (b) velocity vector.....200

Fig. 6-12. Comparison of the azimuthally averaged 3D-velocity maps obtained in the pilot scale mill using Type b (a) and Type b-1 (b) at V_t=5.23 m/s (376 RPM).....201

Fig. 6-13. Comparison of the azimuthally averaged 3D-velocity profiles obtained in the pilot scale mill using Type b (the standard stirrer) and stirrer Type b-1 at radial position r/R=0.5, 0.6, 0.7, 0.8 and 0.9.....202

List of Tables

Table 2-1. Stages of crushing or grinding according to the size of particles ……23

Table 2-2. Types of industrial stirred media mills……36

Table 2-3. Bond Index for some selected materials……39

Table 2-4. The parameters for the Hertz-Mindlin contact model……53

Table 3-1. The feed size of calcite……60

Table 3-2. Technical specifications for both laboratory and pilot mills based on the standard stirrer configurations……72

Table 4-1. Details of PSD for energy input 0-300 kWh/t obtained using Carbolite grinding media size +0.8-1.2 mm (75 % solids concentration, V_t=9.81 m/s)……79

Table 4-2. The details of product d_{80} obtained at V_t=5.23 m/s 6 .54 m/s 7.85 m/s and 9.81 m/s using Carbolite grinding media size +0.8-1.2 mm (75 % (w/w) solids concentration)……82

Table 4-3. The grinding time consumed at V_t=5.23 m/s, 6.54 m/s 7.85 m/s and 9.81 m/s to obtain the same specific energy input using Carbolite +0.8-1.2 mm (75 % (w/w) solids concentration)……84

Table 4-4. Details of d_{80} at 50 %, 65 % and 75 % (w/w) solids concentration……86

Table 4-5. The product d_{80} obtained using ZirPro grinding media size +0.7-1.4 mm, +1.6-2.0 mm and +2.0-2.4 mm……90

Table 4-6. Details of the product d_{80} obtained at the dispersant concentrations 0.8 %, 2.5 %, 5 %, 10 % (w/w)……94

Table 4-7. Details of the product d_{80} size for perlite and wollastonite……98

Table 4-8. The Moh's hardness and density of calcite, perlite and wollastonite……99

Table 4-9. Details of the stirrer types and the top lids tested on the laboratory scale mill……100

Table 4-10. Comparison of the product d_{80} using stirrer Type a and Type a-1 at V_t=7.85 m/s (1200 RPM)……103

Table 4-11. Product d_{80} obtained using stirrer Type a-2 and Type a-3 at V_t=7.85 m/s (1200 RPM)……107

Table 4-12. Product d_{80} obtained using Type a-1 and Type a-4 at V_t=5.23 m/s……110

Table 4-13. Product d_{80} obtained using stirrer Type a-5 at V_t=7.85 m/s……113

Table 4-14. Product d_{80} obtained using the thick lid and normal lid at V_t=5.23 m/s……116

Table 4-15. Product d_{80} obtained at V_t=7.85 m/s in the pilot scale mill……119

Table 4-16. Product d_{80} obtained at V_t=7.85 m/s in the laboratory scale mill……120

Table 4-17. Product d_{80} obtained using stirrer Type b and Type b-1 in the pilot scale mill……126

Table 6-1. Detailed DEM simulation parameters for both laboratory and pilot scale mills……189

Nomenclature

a	Contact radius in adhesive contact model (m)
$\vec{a}$	Acceleration of particle (ms^{-2})
$b(x,y)$	Breakage function refers to the fragment size distribution of a particle of size x resulted from an initial particle of size y ($y > x$).
C_v	Solids volume fraction (%)
d	Grinding media radius (m)
d_{10}	Particle diameter that 10 % of sample mass is less than this value (μm)
d_{12}	Distance between particles (m)
d_{20}	Particle diameter that 20 % of sample mass is less than this value (μm)
d_{50}	Particle diameter that 50 % of sample mass is less than this value (μm)
d_{80}	Particle diameter that 80 % of sample mass is less than this value (μm)
d_{90}	Particle diameter that 90 % of sample mass is less than this value (μm)
d_b	Diameter of ball media in ball mill (m)
d_o	Overlap distance between particles (m)
d_{GM}	Diameter of grinding media (m)
d_s	Stirrer diameter (mm)
D	Diameter of mineral particle (m)
D_c	Chamber diameter (mm)
D_s	Shell diameter of ball mill (m)
D_f	Particle size of final product (m)
D_i	Particle size of initial product (m)
e_r	Coefficient of restitution
E	Total energy (kWh)
$E(t)$	Cumulative power from the start of the grinding till the time point t (kWh)
$E_m(t)$	Specific energy input after grinding time t ((kWh/t))
f_{20}	20 % of feed material mass is less than this particle diameter (μm)
f_{50}	50 % of feed material mass is less than this particle diameter (μm)
f_{80}	80 % of feed material mass is less than this particle diameter (μm)
f_{ij}^n	Contact force between particle i and j in normal direction (N)
f_{ij}^t	Contact force between particle i and j in tangential direction (N)
$\vec{F}$	Total force acting on particle (N)
F_{ij}^c	Contact force between particle i and j (N)
F_i^f	Fluid force acting on particle i (N)
F_i^g	Gravity received by particle i (N)
F_{ik}^{nc}	Non-contact force between particle i and k (N)
g	Gap distance between tip of stirrer and wall (mm)
G	Shear modulus (Pa)
G_{ij}^*	Equivalent shear modulus for particle i and j (Pa)
H	Chamber height (mm)
I_i	Inertia moment of particle i ($kg \cdot m^2$)
$k_{n,ij}$	Normal stiffness coefficient between particle i and j
$k_{t,ij}$	Tangential stiffness coefficient between particle i and j
K_b	Constant for equation 2.6
K_k	Constant for equation 2.4

K_r	Constant for equation 2.3
m	Mass of particle (kg)
$m(x,t)$	Weight fraction of the particle size within range x + ∂x at time t (%)
m_{ij}^*	Equivalent mass for particle i and j (kg)
m_i	Mass for particle i (kg)
m_j	Mass for particle j (kg)
$m_{mineral}$	Mass of dry mineral
m_p	Total mass of particle (kg)
m_{water}	Mass of water
$M_{r,ij}$	Rolling friction torque between particle i and j (N · m)
$M_{t,ij}$	Tangential torque between particle i and j (N · m)
n	Rotational speed in stress model (RPM)
N_c	Number of grinding media contacted by mineral particle
$N_{critical}$	Critical speed of ball mill (RPM)
N_p	Total number of particles
N_r	Rotational speed of stirrer mill (RPM)
$P(t)$	Instantaneous power at time t (W)
P_s	Probability that a particle is caught and sufficiently stressed at one contact with grinding media bead (%)
r	Horizontal distance from the chamber centre (m)
r_1	Radius of particle (m)
r_2	Radius of particle (m)
R	Radius of the chamber bottom (m)
R_i	Vector (from the centre of particle i to the contact point P) with magnitude equal to radius of particle i
R_{ij}^*	Equivalent radius for particle i and j (m)
S	Bottom area of grinding mill chamber (cm^2)
S_n	Constant for the Hertz-Mindlin model
S_t	Constant for the Hertz-Mindlin model
$S(x)$	Selection function for particle size of x
SE	Stress energy in a stirred media mill (N · m)
SE_{GM}	Stress energy of a grinding media (N · m)
SN	Stress number
SD (σ)	Standard deviation
t	Grinding time (s)
u_s	Velocity in definition of shear viscosity (ms^{-1})
v	Poisson ratio
$\vec{v}$	Velocity of particle (ms^{-1})
$v_{n,ij}$	Relative velocity in normal direction between particle i and j (ms^{-1})
$v_{t,ij}$	Relative velocity in tangential direction between particle i and j (ms^{-1})
V_c	Volume of grinding chamber (L)
V_i	Tangential velocity for particle i (ms^{-1})
V_t	Tip speed of stirrer (ms^{-1})
W_i	Bond Work Index (kWh/t)
x	Particle size (m)
y	Particle size (m)
y_s	Distance perpendicular to fluid velocity in definition of shear viscosity (m)

Y_{ij}^{*}	Equivalent Young's modulus for particle i and j (Pa)

Greek symbols

β	Constant for the Hertz-Mindlin model
$\gamma_{n,ij}$	Normal damping coefficient between particle i and j
$\gamma_{t,ij}$	Tangential damping coefficient between particle i and j
$\delta_{n,ij}$	Overlap distance in normal direction between particle i and j (m)
$\delta_{t,ij}$	Overlap distance in tangential direction between particle i and j (m)
ε	Void packing density (%)
θ	Contact angle in liquid bridge model (rad)
μ	Shear viscosity (Pa · s)
μ_r	Coefficient of rolling friction
ρ_{GM}	Density of grinding media (kg/m^3)
τ	Shear stress (Pa)
σ	Liquid surface tension (NS^{-1})
φ	Volume fraction of grinding media (%)
φ_{solid}	Solids concentration for mineral slurry (%)
ω_i	Self-rotational velocity of particle I (rds/s)
$\Delta\gamma$	Variation in adhesion energy (J)
ΔP	Pressure difference across the air-liquid interface (Pa)
$\emptyset$	Half-filing angle in liquid bridge model (rad)

Abbreviations

DEM	Discrete Element Method
DVLO	Deryaguin, Landau, Verwey and Overbeek theory
PSD	Particle size distribution
PBE	Population balance equations
RPM	Revolutions per minute
SEM	Scanning Electron Microscopy
SMD	Stirred Media Detritor

Chapter 1 Introduction

1.1. Background

As a world leader in mineral-based specialities for industry, Imerys is based in over 50 countries and has 250 industrial sites (Imerys, 2017). In 2016, the total revenues of the company were €4165M (Imerys, 2017). Imerys provides functional solutions and mineral-based materials for a great number of sectors from processing industries to consumer goods and building products. The company has a leading position in markets across 4 main business groups: energy solutions and specialities, filtration and performance additives, ceramic materials and high resistance minerals (Imerys, 2017).

In the business group of energy solutions and specialities, one key product is ground calcium carbonate (GCC) used as a paper filler or an additive for polymer film. The production of calcium carbonate is up to 7.5 Mt per annum (Tamblyn, 2009). Around 200 stirred media mills have been deployed in calcium carbonate processing plants globally (Jankovic et al., 2003). The energy consumed for the mineral size reduction accounts for approximately 30 % of total energy demand for the whole mining operation (Tromans, 2008).

However, the actual energy used in the particle breakage process is very low as milling is an energy inefficient process. Only 3-5 % of the total input energy is utilised by the grinding mill for particle breakage. This inefficiency increases dramatically when the particle size decreases (Moore, 2012). Hence, there is considerable potential for energy saving and process optimisation. The improvement in energy efficiency does not only mean great savings in operational cost, but also a great reduction in carbon emissions.

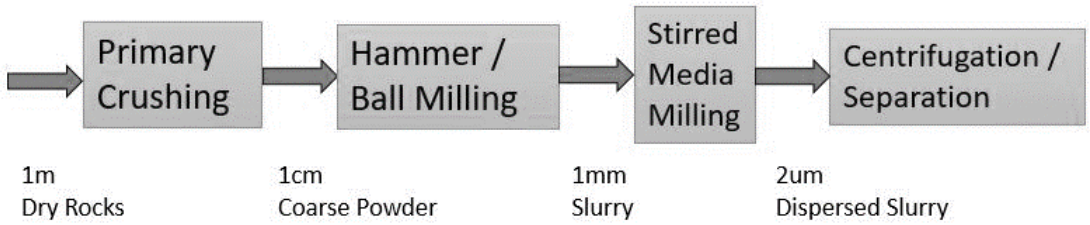

Fig. 1-1. A general description of the operating units applied in milling of calcium carbonate based on the mineral size (Tamblyn, 2009).

Based on the particle size of mineral, a summary of the operating units applied in the comminution process is shown in Fig. 1-1. When the ore is mined, the size of rock is up to 1 meter. A primary crusher (e.g. jaw crusher) is used to reduce the rock size to a manageable level (below 1 cm). The product from the jaw crusher is crushed by a hammer or ball mill in a dry condition. When the size is reduced below 1 mm, the mineral powder is dispersed into water to form a slurry. The slurry is ground with grinding media in a vertically stirred media mill. After the grinding process, a centrifugation or separation process is applied to recover the fine mineral particles of the correct size range.

The throughput and quality (e.g. size range) of the mineral product greatly depends on the performance of the stirred media mill. In 1969 Imerys first applied stirred media mill at a production scale in a kaolin plant, the optimal operation of stirred media mill is established based on this experience. There are still no standard parameters for the grinding process so far because the different operational controls have an influence on each other. The understanding of the grinding mechanism in stirred media mill is still very limited. This has greatly prevented further development of the grinding process.

As a large supplier of calcium carbonate for the paper industry, a finer product is required by the customer. Rising energy costs continually increase the pressure on Imerys to

maintain a competitive position in the market. Possible solution is to make modifications on the process route via optimising the operating parameters and adjustments to the mill.

1.2. Objectives

This study aims to provide a comprehensive understanding of the grinding mechanism in stirred media mills and identify a potential solution for improving the grinding efficiency. Specifically, the study examines the effect of several operating conditions with respect to the size reduction of the mineral, and energy consumption in the mill to achieve optimal grinding conditions. The investigated parameters include specific energy input, rotational speed, solids concentration, grinding media (type and size) and dosage of dispersant. Some modifications are made to the stirrer configuration to study the influence caused by stirrer design. Some innovative designs are proposed and expected to improve the grinding efficiency.

The mill configuration has been designed and investigated as a black box for a long time. To develop more rational configurations, Positron Emission Particle Tracking (PEPT) technology is used to study the flow of grinding media within the grinding chamber under different operating conditions. This technology provides an insight into the grinding chamber to understand the flow behaviour of the grinding media. It aims to obtain better understanding regarding to the movement of the grinding media caused by the new stirrer configurations. The experimental results of a pilot scale mill aim to provide guidelines in scaling the new developments from the laboratory scale mill to the full-scale production line.

With developments in computing technology, numerical simulation is widely utilised to solve engineering problems. In terms of the research cost and efficiency, simulation methods show advantages over traditional experiments. This application is still at an early

stage for vertically stirred media mills. To simulate the grinding media movement in the mill, a numerical model based on the Discrete Element Method (DEM) is proposed. The study aims to achieve viable simulation results compared to the PEPT results. Detailed descriptions of the particle collisions are presented to understand the contacting mechanism.

The optimum operating conditions for the grinding process are established through trial and error tests. Hence, all the data demonstrated in this study attempts to offer a comprehensive outline for the further improvement of the process.

1.3. Layout of thesis

Chapter 1 briefly introduces the background and object of the study.

Chapter 2 reviews current technology and the types of grinding mills used in the industrial process. This chapter also demonstrates some advantages of vertically stirred media mill over other traditional methods. The existing literature on grinding theory is reviewed. The visualised analytical method (PEPT) is reviewed with other optical methods. The theory of DEM is presented and reviewed.

Chapter 3 introduces the experimental procedure, apparatus and equipment used in the study. The morphology and rheology of the feed mineral (calcite) is analysed in detail.

Chapter 4 presents experimental results regarding to operating conditions and stirrer configuration. The study of the operating conditions looks at the product quality and the energy consumption under various conditions. The study of the stirrer configurations looks at the mill performance using several different configurations of stirrer.

Chapter 5 introduces the experimental set-up for PEPT. The experimental results obtained with PEPT in a laboratory scale mill are analysed and discussed. The flow behaviour is demonstrated to identify the potential improvement by modification of the stirrer.

Chapter 6 introduces the simulation system of DEM. The flow movement of the grinding media observed by PEPT is reproduced on DEM. The simulation of DEM is conducted at both laboratory scale mill and pilot scale mill. The detailed simulation results are analysed and discussed.

Chapter 7 concludes the research work and proposes some potential fields for future study.

Chapter 2 Literature Review

2.1. Introduction

Comminution, one of the oldest terms in mineral processing, refers to the process in which the size of a solid material is progressively reduced by impact, compression, attrition or abrasion (Kanda and Kotake, 2007). The purpose is to expose and liberate valuable mineral from the gangue, as these valuable minerals are intimately surrounded by the other non-valuable materials as shown in Fig. 2-1. Adequate liberation of valuable minerals is important for downstream processing such as physical separation (magnetic separation, froth flotation etc.) or chemical/biochemical leaching. If the size of the ore is too large for the downstream process, it reduces recovery and grade of the valuable component regenerated.

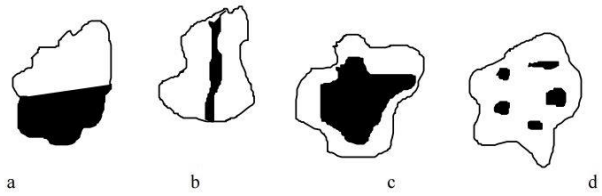

Fig. 2-1. The relationship between valuable minerals (black) and gangue (white): (a) regular (b) vain (c) frame and (d) occlusion (Drzymala, 2007; Kelly and Spottiswood, 1989).

According to Gupta (2003), a complete mineral comminution process flowsheet from the ore to the final product is grouped into front-end operations (crushing) and back-end operations (milling) as shown in Fig. 2-2. The primary crushing is the first operation applied to freshly mined ore. It is mainly accomplished by impact or compression in a dry process to break the ore size to a level that can be transported out the mining zone for ease of handling. The crusher performance is assessed by the size reduction ratio defined as the ratio of feeding material size over product size (Wills, 1997). Typically, the size reduction

ratio based on d_{80} is 6:1 for a jaw crusher and 5:1 for a cone crusher. The crushing is a simple process that the size reduction ratio is inadequate to provide good quality of mineral to meet the standard required by the industrial process. Hence, extra operations such as secondary crushing or grinding are essential to further improve fineness of the product.

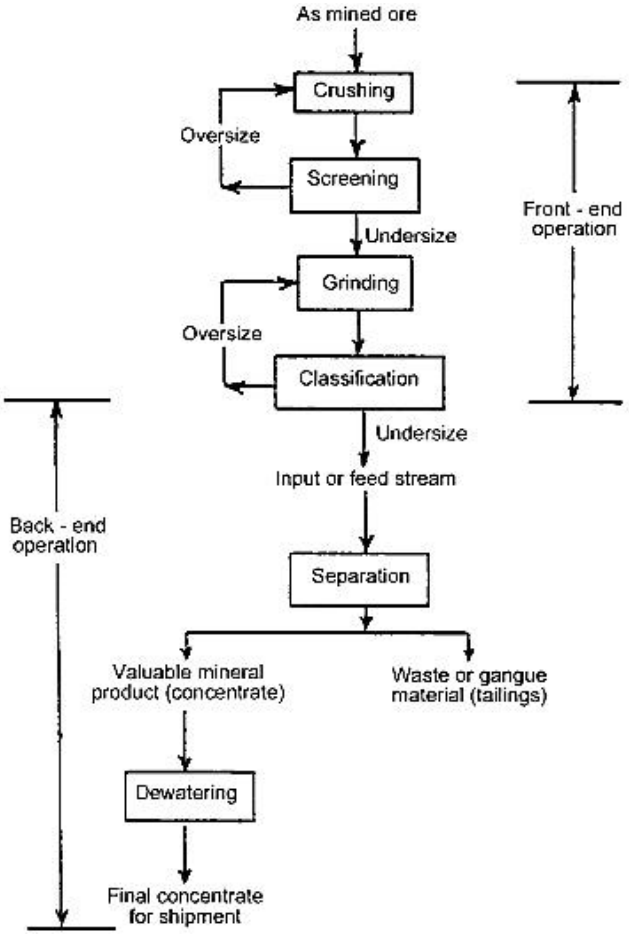

Fig. 2-2. Steps in a typical mineral processing flowsheet (Gupta, 2003).

Table 2-1. Stages of crushing or grinding according to the size of particles (Drzymala, 2007).

Comminution type	Maximum particle size (mm)	
	feed	product
Primary crushing	1500	500
Secondary crushing	500	150
Tertiary crushing	150	50
Coarse (primary) grinding	50	5
Secondary grinding	5	0.5
Fine grinding	0.5	0.05
Ultrafine (colloidal) grinding	0.05	<0.005

Table 2-1 illustrates a category for determination of the crushing or grinding processes based on the feed/product size. To obtain a particle size in the micron range, it shows that grinding methods are more suitable with respect to the efficiency and effectiveness. The tumbling ball mill is the most popular machine for the grinding process. It is mainly accomplished by cascading metallic balls or steel rods in a mill chamber where the mineral is mixed with these balls. The mixture of the mineral and the balls or rods is charged into a cylindrical chamber driven by a motor at slow speed. Gravity is the main source providing impact force for the balls or rods to break the mineral.

However, the energy cost of the tumbling ball mill is found to be 20~50 % greater than the vertically stirred media mill when the product size requirement is d_{80} < 75 μm (Shi et al., 2009). The demand for the finer product at lower energy cost motivates the study of the vertically stirred media mill.

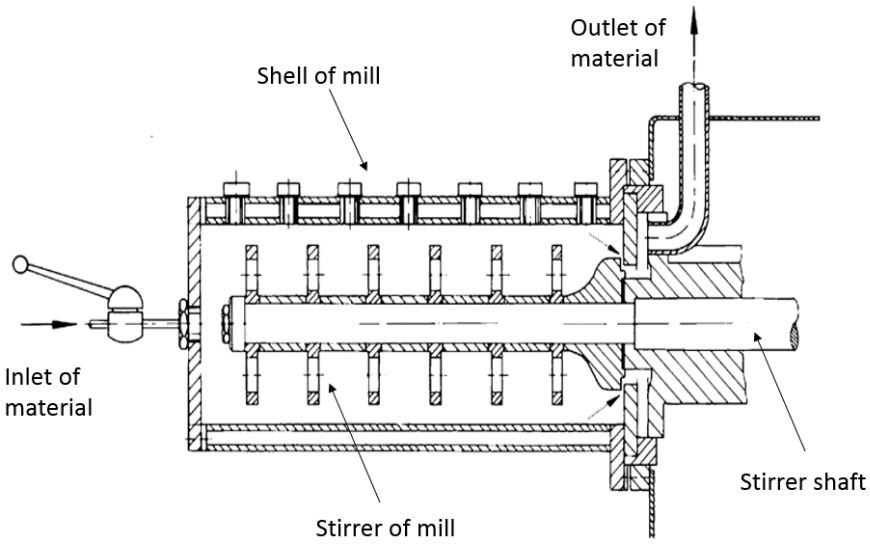

Fig. 2-3. A typical horizontal layout of the grinding mill (feed material enters from left and leaves at top) (Kwade and Schwedes, 2007).

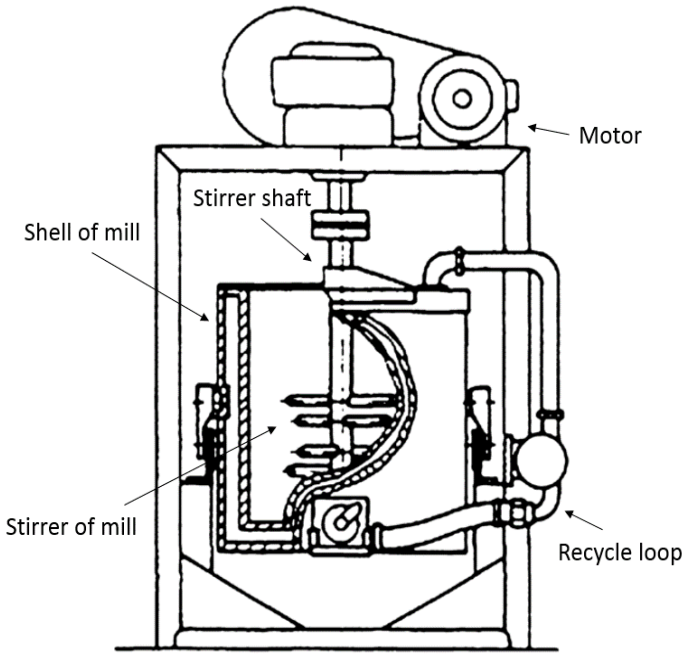

Fig. 2-4. A typical vertical layout of the grinding mill (Kwade and Schwedes, 2007).

Recently, stirred media mills have been widely used in the mineral industry to replace the ball mill, particularly for ultra-fine grinding where the product size is d_{80}<10 μm (Altun et al., 2013). To meet the requirement in the industrial process, both horizontal (see Fig. 2-3)

and vertical (see Fig. 2-4) layouts are available currently. The stirred media mill principally works in a wet mode. Some water is added and mixed with the dry mineral at 30∼70 % solids concentration (w/w). The water functions as a lubricant. This greatly enhances energy efficiency and reduces the air pollution via dust generation compared to the dry mode.

Unlike the ball mill, the driving force of a stirred mill is supplied by an agitator which revolves at a high speed. The suspension or slurry (the mixture of water and mineral) is charged into a cylindrical steel chamber normally lined with a polyurethane liner to reduce the wear. The mill chamber is stationarily mounted either vertically or horizontally. The motion of the charge is imparted via a stirrer driven by a motor. The grinding media (sometimes referred to as grinding beads) are added to mix with the slurry. The grinding media can be ceramic beads or zircon beads, depending on the specific physical property of the feed material. The grinding media is treated as an operating variable (Kwade et al., 1996).

It has been reported that the stirred media mill demonstrates better performance when grinding minerals with a particle size in the micron scale compared to the ball mill (Wang and Forssberg, 2007; Xiao et al., 2012). The improvement is seen because the kinetic energy provided by the stirrer is supplied by a different mechanism. The forces used to break particles in a ball mill are the impact and abrasive stress generated from the collision between large rigid balls and the mineral. While the cylindrical mill rotates, the charged ball is raised up and falls freely to impact with the mineral. The maximum force applied on the mineral approximately equals the weight of the ball. The rotational part is the mill body. Thus, the rotational speed is limited by a critical circumferential speed. The critical value is the centrifugation speed that is fast enough to just raise the ball and fall freely. If the speed

is beyond the critical speed, the centrifuge force can push the ball against the mill wall. The ball will never fall. Hence, the rotational speed is just 2/3 or 3/4 of the critical speed (normally <4 m/s) in a plant operation (Kwade and Schwedes, 2007).

However, the circumferential speed applied in a stirred media breaks this limitation. The agitator speed in a stirred media mill can reach 20 m/s under some specific circumstance (Kwade and Schwedes, 2007). At this high tip speed, the grinding media and mineral interact with each other at high kinetic energy. Consequently, the collision intensity between the grinding media and mineral in the stirred media mill is more intensive than the ball mill. Due to the high-stress intensity, the stirred media mill is more suitable for the fine or ultra-fine particle grinding process. The stirred media mill has attracted great attention from the mineral industry.

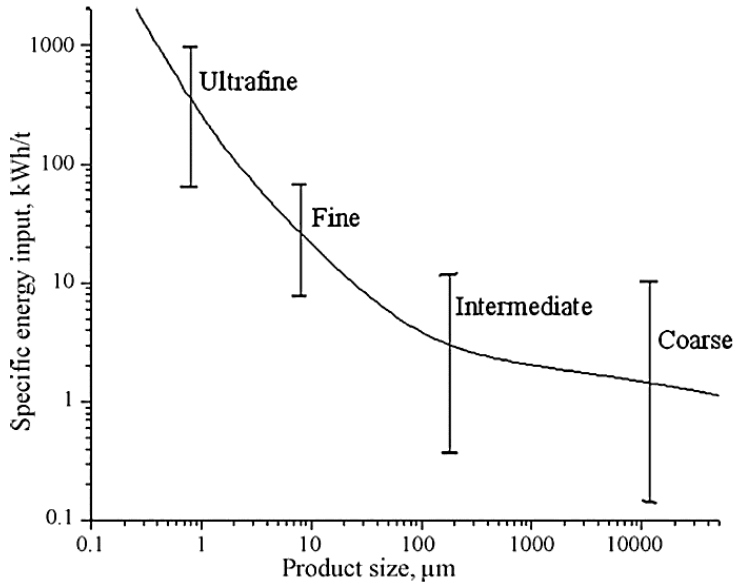

Fig. 2-5. The Specific energy input (kWh/t) required for a particular size range (Wang and Forssberg, 2007).

Milling inherently is a high-energy consumption process. The stirred media mill demonstrates a great improvement in the energy efficiency over the traditional device (e.g. ball mill), but the energy consumption is still large. Most of the kinetic energy is dissipated purely as heat and noise resulting in low energy utilisation. As the product size decreases, the size reduction process becomes even more inefficient alongside an increase in specific energy (kWh/t) consumption (see Fig. 2-5).

The goal of the optimisation in the grinding process is to improve the energy utilisation over the unit mass of the mineral. When the initial size of feed material is coarse, a large amount of the fracture energy is required, but the fracture energy per unit mass is low at this stage. When the particle size declines, the total amount of the fracture energy also decreases. However, the fracture energy over unit mass increases rapidly (Gupta, 2003).

Some research has focused on the optimisation of the grinding process in stirred media mills (Altun et al., 2013; Breitung-Faes and Kwade, 2013; Engstrom et al., 2013). In the past decade, many possible operating parameters (e.g. impeller speed, solids density, mill design, and media density/shape) that may influence the grinding performance have been identified and investigated.

These operating variables are divided into 4 groups. The first group studies the operating parameters of the mill namely grinding time, grinding media, tip speed etc. Then, a group is classified based on the operation mode of the mill which includes batch grinding, continuous grinding or circuit. The third group is mainly a study of the chemistry or physical properties of the suspension (for example solids concentration or suspension viscosity). The last group is about the mill geometry such as type and size (Kwade, 2004).

2.2. Type of grinding mills

2.2.1. Introduction

Due to a wide range of the mineral materials, different types of grinding mills have been developed to meet various requirements by the mineral industry for a broad size range of product. By consuming energy (mainly electricity), the grinding mill breaks a solid particle into smaller sizes. In general, grinding mills are categorised into 3 types: 1) tumbling mills, 2) stirred media mills, 3) vibrating mill as shown in Fig. 2-6.

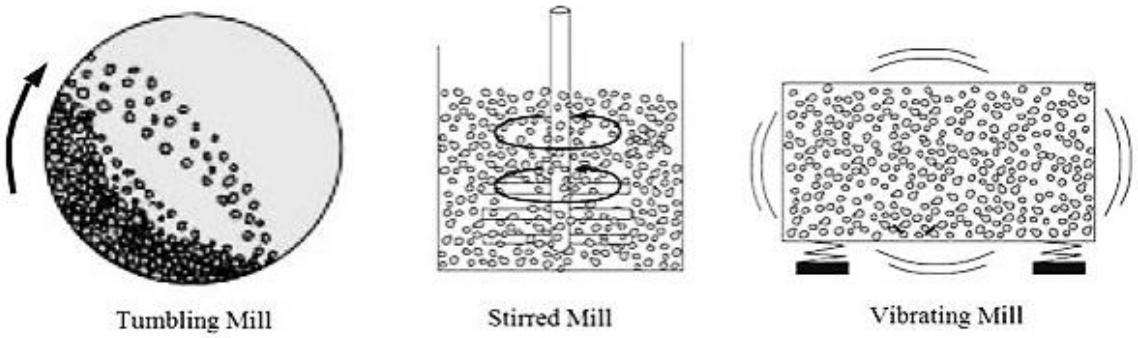

Fig. 2-6. The typical movement of the charge within tumbling mill stirred mill and vibrating mill (Kumar, 2015).

Recently, a new type of mill known as high pressure grinding rolls (HPGRs) has been developed and widely acknowledged (Moore, 2012). The purpose of the HPGRs is still the reduction of product size through minimum energy demand. However, there are many issues still unsolved for the HPGR before it could be more widely applied in the minerals industry. The roll wear is the main concern when it is consistently contacted by moist particles under high pressure. Although some leading mineral equipment companies (e.g. FLSmidth and Xstrata Technology) have been developing and testing the HPGRs, the circuit design of HPGRs is still a challenge in the context of the operability and eco-efficiency.

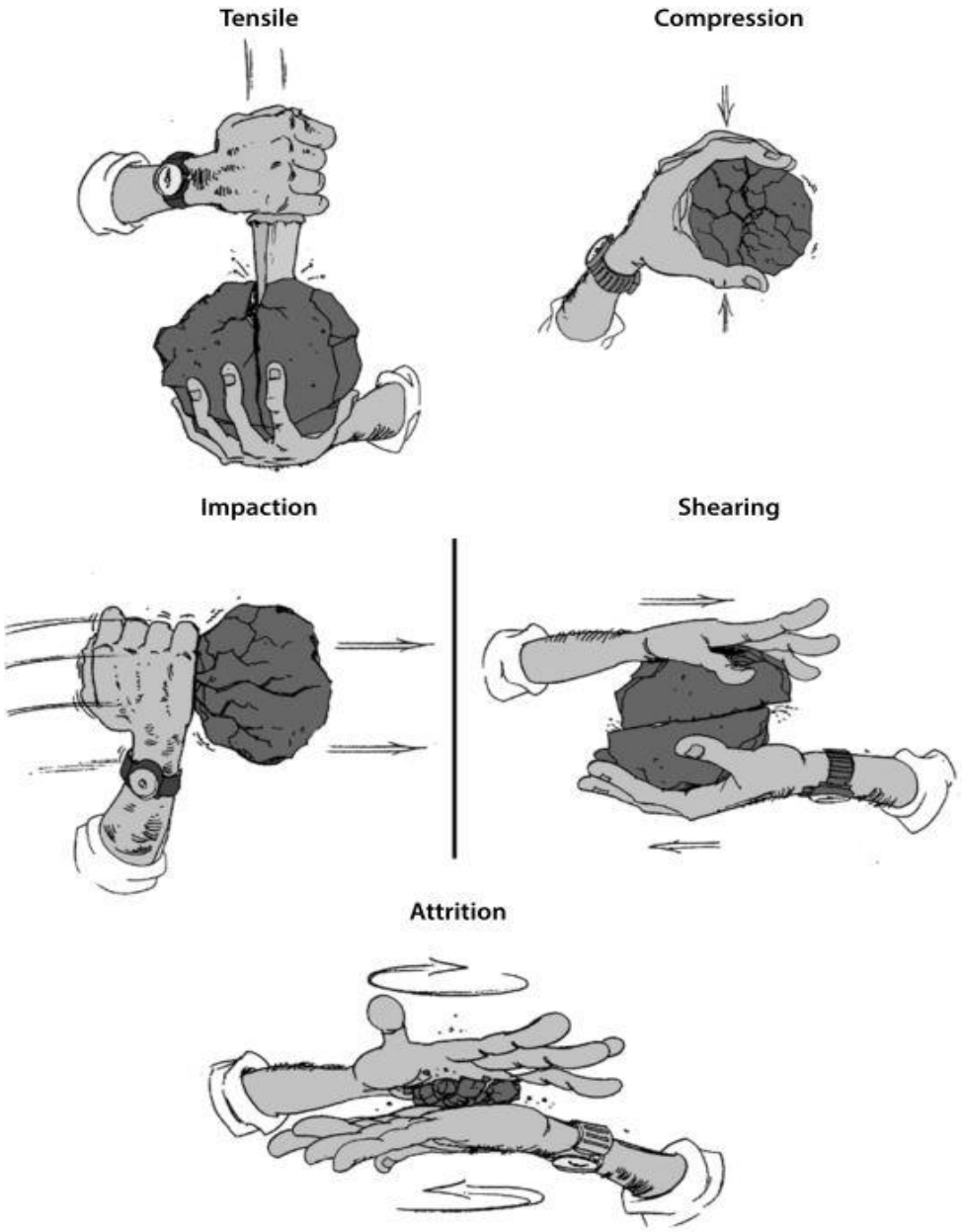

Fig. 2-7. Demonstration of the stress types occurred in all types of the mills (Basics in Minerals Processing, 2017).

In all types of the grinding mills, the form of mechanical activation in each type mill is no more than the 5 stress types as shown in Fig. 2-7. The tensile force is obtained by applying a pressure on a point of the material resulting in stretch. It normally cuts the material into several smaller parts. It is mostly seen in jaw crushers for relative larger particles. The compression force presses normal force from two opposite directions resulting in a wide

particle size distribution of the product. It occurs when the force reaches the break or rupture point of the material inner force as most materials are able to withstand some tiny deformation (Tamblyn, 2009). Impact force is a sudden shock force acting on the material. A combination of compression and impact forces are very common in the tumbling ball mill. Shearing force also known as abrasion, breaks the particle by the shear forces through the grinding media. The attrition removes some very fine parts from a larger particle by a collision between particles themselves. All these stress types can happen simultaneously in one specific grinding mill.

2.2.2. Tumbling mill

A tumbling mill normally consists of a slightly inclined or horizontal rotating cylindrical shell partially filled by the grinding media occupying less than half the volume of the mill. Based on the type of grinding media, the tumbling mill has a variety of configurations such as ball mill (e.g. steel/ceramic ball used as grinding media), rod mill (e.g. steel rod used as grinding media) and AG/SAG (autogenous or semi-autogenous) mill. The AG mill uses the feed material itself as grinding media and the SAG is partially charged with grinding media. Also, all these mills can operate at both wet and dry conditions.

While the shell is rotating anti-clockwise as shown in Fig. 2-8a, the charge is lifted from the bottom of the shell by the friction force from the liner or lifters. When it reaches a specific height point P as shown in Fig. 2-8b, the balance between gravity and centrifugal force is disrupted (see Fig. 2-8b). The charge falls freely down to the bottom of the shell. The path line shown in Fig. 2-8a indicates a typical parabolic loop of grinding media movement.

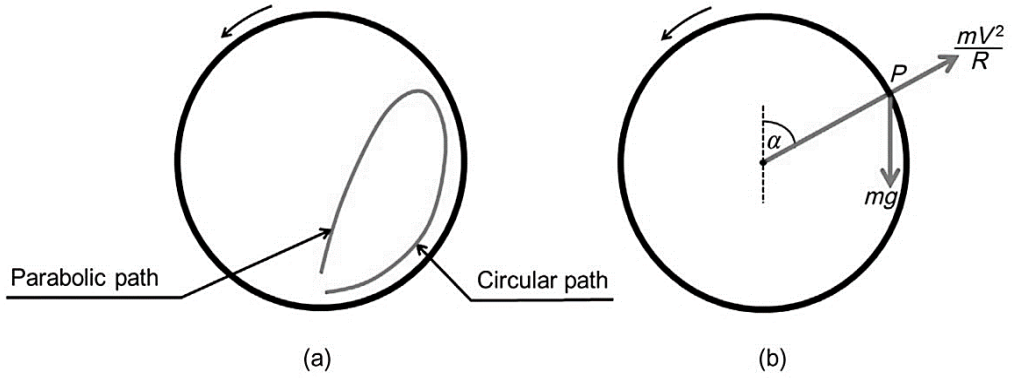

Fig. 2-8. Parabolic motion path for grinding media in tumbling mill (a) and centrifugal force and the gravitational force on a ball (Wills and Finch, 2016).

An obvious limitation of the tumbling ball mill is centrifugal speed. As centrifugal speed increases, the charge will eventually be unable to fall off and move at the same speed with the shell. The maximum centrifugal speed is defined as the critical speed $N_{critical}$ (RPM). When the rotational speed exceeds the critical speed, the grinding media are forced to walls of mill. The motion routine shown in Fig. 2-8 will be no longer validate. The critical speed $N_{critical}$ (RPM) is calculated as Eq. [2.1] :

$$N_{critical} = \frac{42.3}{\sqrt{D_s - d_b}} \qquad [2.1]$$

where D_s is the diameter of the mill shell and d_b is the diameter of the ball.

If the revolving shell exceeds the critical value, the ball mill is unable to work properly. The restriction over the rotational speed undoubtedly limits the power input which is an important parameter to improve grinding efficiency.

2.2.3. Vibrating mill

A vibrating mill consists of a mill chamber/pipe containing the mineral material and grinding media up to 80 % of the total volume. The mill chamber is driven by an out of balance weight on a circular or elliptic trajectory (Balaz, 2008). It is possible to be operated in either

wet or dry mode. The vibrating frequency and horizontal/vertical amplitudes are 2 main parameters affecting the performance of a vibrating mill. For an industrial operation, the normal frequencies are set in 16-19 rev/s and amplitudes below 6 mm (Gock and Kurrer, 1999). The possible acceleration speed is up to 10 g (Balaz, 2008). A typical structure of eccentric vibrating mill is shown in Fig. 2-9.

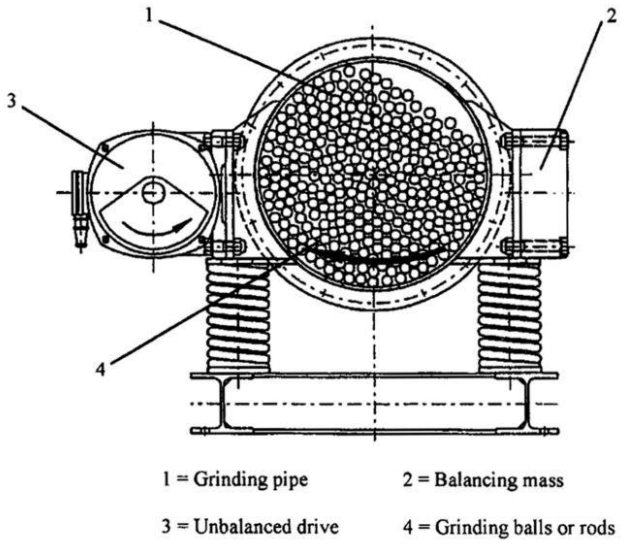

Fig. 2-9. A diagrammatic view of the eccentric vibration mill (Gock and Kurrer, 1999).

The vibrating mill is commonly used for the preparation of very fine product in pharmaceutical industry. Some researchers obtained Nano-sized product in the vibrating mill (Baláž et al., 2004). The performance of the mill is limited by the low throughput and batch operation. The long grinding times are necessary for fine product generation. Additionally, due to the high filling ratio, the temperature unavoidably increases and causes a large amount of the energy wasted as heat.

2.2.4. Stirred media mill

When the required fineness of the product is below 100 μm, the grinding process is qualified as the fine grinding (Launder and Spalding, 1974). It was reported that the stirred media mill could save energy up to 35 % compared to tumbling mills to achieve the same

level in the fine grinding process (Xiao et al., 2012). The energy efficiency of the tumbling mill declines dramatically while the product size continues to decrease to d_{80} (80 % passing size) below 75 μm. The particle upper size limitation of product is approximately 40-45 μm using a tumbling mill (Shi et al., 2009). However, this product quality is not fine enough to meet the current requirement by most industrial applications.

To liberate the ultra-fine valuable material (d_{80} < 10 μm) from the gangue, a stronger energy intensity is required. The stirred media mill has been utilised for this fine or ultra-fine grinding processes since it was introduced by Klein and Szegvary in 1928 (Kwade and Schwedes, 2007) due to its advantages such as larger capacity, higher efficiency and more reliability. In the last few decades, a large amount of research had been published regarding the study of the stirred media mill (Ohenoja et al., 2013; Ouattara and Frances, 2014; Radziszewski, 2013; Tamblyn, 2009; Theuerkauf; and Schwedes, 1999; Wang and Forssberg, 2000; Yang et al., 2017; Zheng et al., 1997). Many types of the stirred media mill have been developed and applied for the industrial process. A typical plant-scale vertically stirred media mill is shown in Fig. 2-10.

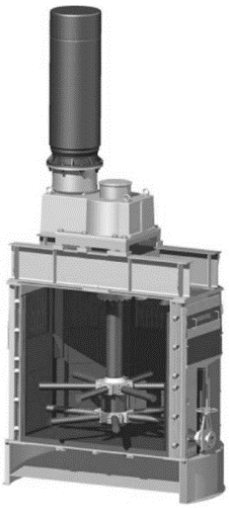

Fig. 2-10. A typical Stirred media mill used by Metso (Stirred Media Detritors).

With regard to the tip speed (defined as tangential speed of the stirrer tip), the stirred media mill is classified into 2 groups: low-speed mills (operating at about 3 m/s) and high-speed mills (higher than 15 m/s) (Jankovic et al., 2003). The Metso Vertimill and the Eirich Tower Mill are two typical low speed stirred mills. Gravity is still an important factor in these low-speed mills. The product size d_{80} can be obtained as fine as 15 μm. The high-speed mill fluidises the charge. It has ability to generate a product size d_{80} down to 5 μm or even finer (Wills and Finch, 2016). Representative high- speed mills are Mesto Stirred Media Detritor (SMD) and Xstrata Isamill. These mills are mainly used for regrinding processes where high energy intensity is required.

The grinding media in the stirred mill is also a very important factor affecting mill efficiency and performance. The size of the grinding media normally ranges from 2~10 mm. To reduce the wear, the grinding media is made of compounds based on the zirconia, aluminium oxide or ceramic materials.

The volume of the grinding media used to fill the mill chamber is usually 50~80 % of total the volume. When the stirrer/impeller rotates at an optimal speed (beyond the just suspended speed), the grinding media is fluidised by the stirrer. Depending on the geometry of the stirrer, the motion of the grinding media can be very different. The mechanism of the breakage in a stirred media mill mainly depends on the shearing force caused by the interaction between the mineral materials and the grinding media.

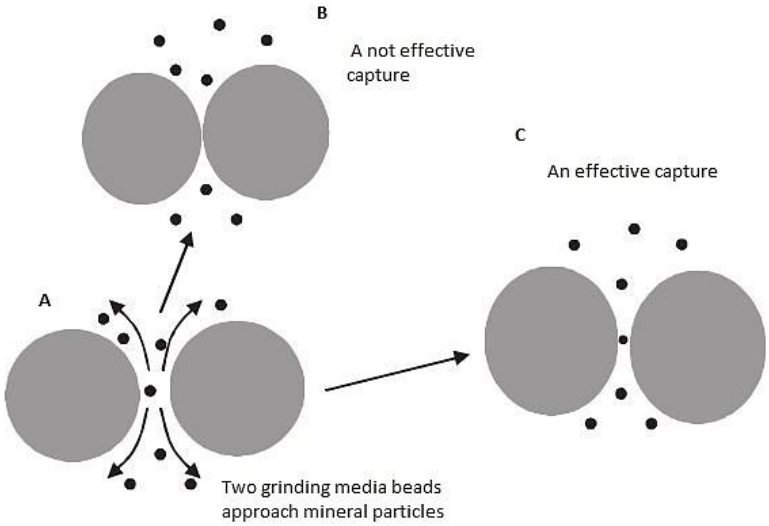

Fig. 2-11. How grinding media beads approach mineral particles (Kwade and Schwedes, 2007).

Fig. 2-11A illustrates an ideal collision for only two grinding media beads. These two grinding media beads are moving against each other and some mineral particle is likely to be trapped. When they approach the mineral particle, some mineral particles are stressed. Sometimes no mineral particle is broken as indicated in Fig. 2-11B. In this case, the collision consumes a lot of energy and the energy dissipates as heat or sound. In Fig. 2-11C, some mineral particles are broken by the collision of two grinding beads. In fact, most of the kinetic energy is not efficiently transferred to the grinding process as the effective collision is at a low probability. The capture of the mineral particles is normally by a layer of the grinding media. The probability of capture of the mineral particle depends on many factors such as the ratio of the diameter of the grinding media over the mineral particle. The grinding process in the stirred media mill is still not fully understood. Over 40 parameters have been identified as directly or indirectly affecting the grinding process. These parameters normally affect the process simultaneously. This undoubtedly raises the complexity of the understanding of the process.

So far, no universal standard has been defined for the evaluation of the mill performance. Each type of the mineral has its unique physical property. This makes it difficult to develop one general standard for the operation of the stirred media mill to cover all the materials. Hence, different stirred media mills have been developed for a specific application. Table 2-2 illustrates some features of the current major types of the stirred media mills.

Table 2-2. Types of industrial stirred media mills (Wills and Finch, 2016).

Mill Name	IsaMill	Vertmill/Tower Mill	Stirred Media Detritor	VXP Mill	HIGMill
Manufacture	Glencore	Metso/Eirich	Mesto	FLSmidth	Outotec
Orientation	Horizontal	Vertical	Vertical	Vertical	Vertical
Stirrer shape	Disc	Screw	Pin	Disc	Disc
Stirrer tip speed (m/s)	19-23	<3	3-8	10-12	8-12
Density of solids (v/v)	10-30 %	30-50 %	10-30 %	10-30 %	10-30 %
Power intensity (kW/m^3)	300-1000	20-40	50-100	240-756	100-300
Grinding media size (mm)	1-3	12-28	1-8	1.5-3	1-6

2.3. Theory of fine grinding

It is estimated that the grinding process accounts for approximately 1∼10 % of all the energy consumed globally (Holdich, 2002). This is due to the low energy efficiency in the grinding mill where the electric energy is dissipated mostly as heat or used for the deformation of particle and equipment or other mechanical losses (sound, vibration, friction). The study found that as little as 3∼5 % of the actual input energy is theoretically required (Holdich, 2002). Therefore, it is of great benefit to identify the relationship between the energy consumption and the performance of the grinding mill in order to optimise the grinding process.

2.3.1. Energy-size reduction relationships

Depending on the mill type and the operation method, the quantity of the energy input is measured in different ways. The specific energy input is a common and precise measurement for the energy consumed by the mill. It has been identified as a major parameter affecting the product size. It is defined as the total energy input over the mass of dry material in the mill. The power drawn by the mill is defined as the total energy input. This is different from the energy consumed by the mill motor. For a batch operation, the specific energy input after grinding time t is calculated as Eq. [2.2]:

$$E_m(t) = \frac{E(t)}{m_p} = \int_0^t \frac{P(t)dt}{m_p} \quad [2.2]$$

$P(t)$ is the instantaneous power at time *t* and m_p is the total mass of the dry mineral particle. $E(t)$ is the cumulative power from the start of the grinding till the time point t. This is a direct method to measure the consumption of the total energy used for the grinding process.

Additionally, some energy models have been developed to predict the relationship between the energy consumption and the product size. Von Rittinger (1867) postulated that the energy consumption per unit mass is proportional to the new surface produced via the grinding process. The specific surface area is inversely proportional to the particle diameter. Rittinger's law is demonstrated in Eq. [2.3]:

$$E = K_r(\frac{1}{D_f} - \frac{1}{D_i}) \quad [2.3]$$

where E is the total energy; D_f and D_i are the final and initial product size respectively and K_r is a constant. An obvious downside of the theory is that the energy absorbed by elastic

deformation of the mineral particle (greater than that required for created new surface) is ignored.

Based on the theory of stress analysis or plastic deformation, Kirpicev (1874) and Kick (1885) stated another theory. They assumed that the energy consumption per unit mass is proportional to the reduction ratio of the particle volume. Thus, the energy is proportional to the size reduction ratio. The Kick-Kirpicev's law is demonstrated as Eq. [2.4]:

$$E = K_k(ln\frac{D_f}{D_i}) \quad [2.4]$$

where K_k is a constant.

The problem for this theory is that the energy required to reduce particle size from 2 cm to 1 cm is the same as from 1~0.5 cm. This simplification is reasonable for the course grinding process, but it may cause a large estimation error over the fine or ultra-fine grinding processes.

Bond (1952) assumed that the energy required to break a particle size D is proportional to $D^{5/2}$. Thus, the energy per unit mass is based on the relationship shown as Eq. [2.5]:

$$E \propto [\frac{D_f^{5/2}}{D_f^3} - \frac{D_i^{5/2}}{D_i^3}] \quad [2.5]$$

giving $E = K_b(\frac{10}{\sqrt{D_f}} - \frac{10}{\sqrt{D_i}})$ [2.6]

where K_b is also defined as Bond Work Index (W_i), a comminution parameter indicating the resistance of the material to grinding.

The Bond index numerically means energy (kWh) required to reduce one specific material size to d_{80}=100 μm (80 % passing size) from infinite size. Table 2-3 shows the Bond index of some common materials.

Table 2-3. Bond Index for some selected materials (Drzymala, 2007).

Material	Wi (kWh/t)	Material	Wi (kWh/t)
Barite	4.73	Limestone	12.74
Bauxite	8.78	Coal	13
Fluorite	8.91	Quartz	13.57
Quartzite	9.58	Granite	15.13
Ferrosilicon	10.01	Graphite	43.56
Dolomite	11.27	Emery	56.7

2.3.2. Stress model

Kwade et al. (1996) proposed a so-called stress model to describe the physical process in a stirred media mill. It quantifies characterisation of the stirred mill by concepts such as stress frequency and stress energy. The stress frequency indicates the number of stress events (stress number, SN) applied by the mill per unit time. The energy transferred to the mineral particle for each single stress event is defined as the stress energy. The stress model numerically reflects the stress intensity offered by a specific mill and it is not affected by the product size.

The stress number is defined as Eq. [2.7]:

$$SN = \frac{N_c \cdot P_s}{N_p} \qquad [2.7]$$

where N_c is the number of grinding media contacted by mineral particle, P_s is the probability that a particle is caught and sufficiently stressed at one contact with grinding media bead, N_p is the total number of particles. It is impossible to obtain SN directly by Eq. [2.7] because the total number of particles is normally impossible to obtain.

Hence, a correlation equation is derived as Eq. [2.8]:

$$SN \propto \frac{\varphi(1-\varepsilon)}{1-\varphi(1-\varepsilon))C_v} \cdot \frac{nt}{d_{GM}^2} \quad [2.8]$$

where φ is the volume fraction of the grinding media, $(1-\varepsilon)$ is the packing density, C_v is the solids volume fraction, n is the rotational speed, t is the operating time and d_{GM} is the diameter of the grinding media.

The stress energy (SE) in a stirred media mill is proportional to the stress energy of the grinding media (SE_{GM}), also defined as a simplified stress energy. The relationship is demonstrated as Eq. [2.9]:

$$SE \propto SE_{GM} = d_{GM}^3 v_t^2 \rho_{GM} \quad [2.9]$$

where d_{GM} is the diameter of grinding media, v_t is the tip speed of stirrer and ρ_{GM} is the density of grinding media. SE_{GM} is the maximum stress energy during the grinding process because no grinding media could be accelerated to match the tip speed of the stirrer.

When the geometry of the mill and grinding media are determined, the distribution of the grinding media stress can be predicated. By varying the size or density of the grinding media and tip speed, it is possible to optimise the stress distribution. An optimal stress energy is when the mill produces the finest product with the least specific energy input. The stress model depends greatly on the extensive experimental data and empirical relationships. According to the stress energy model, the rotational speed is required to be set as fast as possible to achieve a greater stress number. The size of the grinding media is required to be set as small as possible to obtain the optimal contact between the grinding media and the mineral particle.

The grinding mechanism in a stirred media mill is very complicated, particularly when the filling material is not homogeneous. For example, a typical wet grinding process involves water, grinding media and mineral powder where three different materials are mixed. To simplify the process, several hypotheses are essential to apply to the stress model. The stress model is derived from the stress event involved with a single particle. In fact, this is not likely when the stirred media beads, mineral particle, and water are mixed together in a mill. They are driven by a stirrer which transfers energy to the load. The grinding media is much larger than the mineral particle as shown in Fig. 2-12 where the grinding media radius is d and the diameter of mineral particle is D. The hatched area is the active volume for grinding.

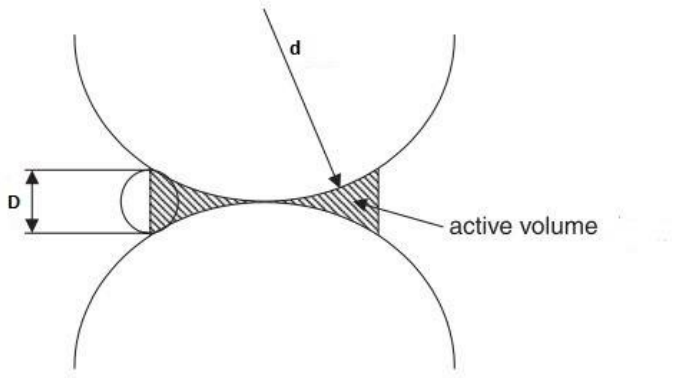

Fig. 2-12. An active volume for two grinding media particles.

Whilst few particles could fill the active volume, only the largest particle is assumed to be broken by the compression of the media for the stress model. For higher solids concentrations, it is very likely that a bed of particles is filled into the active volume. In this case, the energy may not be sufficient to break all the particles. The lack of definition of the multi-particle breakage event undoubtedly may cause some errors in the estimation of the stress number and stress energy. In fact, to enhance the throughput, a wet grinding process

is usually carried out at a high solids concentration (Guida et al., 2010). Here the elastic deformation of the mineral particle is also likely to happen in the active grinding volume at high solid loading. The amount of the energy just consumed by the particle deformation is much larger than the actual energy consumed to break the mineral particle in the actual grinding process.

2.3.3. Population balance model

A population balance model normally consists of some ordinary differential equations. The model is also referred to as the population balance equation (PBE). It is basically derived from the concept of conservation of mass. The model can apply in both batch and continuous grinding processes at either steady or unsteady state. For a fully mixed batch grinding process, a general expression is shown as Eq. [2.10] (Austin, 1971a; Gaudin and Meloy, 1962):

$$\frac{\partial m(x,t)}{dt} = -S(x)m(x,t) + \int_x^{\infty} b(x,y)S(y)\,m(y,t)dy \qquad [2.10]$$

$m(x,t)$ is the weight fraction of the particle size within range $x + \partial x$ at time t. $S(x)$ is the selection function for the particle size of x. The breakage function $b(x,y)$ refers to the fragment size distribution of a particle of size x resulted from an initial particle of size y ($y > x$).

The first term on the right-hand side of Eq. [2.10] refers to the death rate of particle size x at time t. It means that a particle with original size x is broken into several smaller particles. The second term on the right-hand side refers to the birth rate of the particle of size x generated from the particles with size ranging from y to the maximum boundary size of particles. Hence, the weight fraction for a specific size group maintains a dynamic balance as both inlet and outlet terms affects simultaneously.

The PBEs describe a dynamic evolution of all the particles with size against time by tracking the weight fraction of different groups of particle size (Austin, 1981). According to the fragmentation mechanism proposed by Varinot et al. (1997), the coarse particle will be broken down into finer fragments through abrasion, cleavage, and fracture. Then, the weight fraction of the large particle reduces. Also, the weight fraction of the fine particles increases. The total mass of all particles is conserved for a batch grinding process. Consequently, the total number of the particle increases against time while the overall size distribution moves to a narrower range.

The PBEs have been widely used to evaluate and predict the performance of grinding processes with reasonable accuracy. The selection function and breakage rate are the two main sub-functions required to be determined via experimental data, as these functions are not universal and vary against material and grinding process. The selection function $S(x)$ indicates the probability that a particle of size x will be captured and ground by the grinding media. The breakage function $b(x, y)$ describes the size distribution of the fragment from a larger particle. The accuracy of the PBEs is based on the selection of the breakage function and this has attracted a lot of attention for determination of a proper breakage function (Austin, 1971a, 1981; Bilgili and Scarlett, 2005; Varinot et al., 1997).

To solve the PBEs, a discrete method is usually adopted as it tracks the size evolution by classifying the product size into each discrete size category and corresponding weight fraction (Austin, 1971b). However, It is not suitable for a fine wet grinding process, because the initial particle size is not strictly a mono size sample and the insufficient resolution of discrete elements is another factor that limits the application of the model as the particle size range is much finer than the product obtained decades ago (Varinot et al., 1999; Varinot

et al., 1997). Also, most breakage rate functions are based on 1st order kinetics neglecting the multi-particle interactions which are the main source for error. Some researchers have been trying to develop non-linear breakage kinetics and this shows potential and predictive capability for modelling the grinding process (Orumwense, 1992; Yekeler et al., 2001).

2.4. Visualised analytical methods

Some visualised analytical methods have been used to study single or multi-phase mixing processes for a long time. The common methods such as Particle Image Velocimetry (PIV), Planar Laser Induced Fluorescence (PLIF) and Laser Doppler Anemometry (LDA) are based on optical technology. These methods have demonstrated a reliable accuracy and contributed a lot for the study of dilute suspensions (Bakalis and Karwe, 2002; Barigou, 2004; Giuseppina Montante, 2014; Montante et al., 2012; Ramsay et al., 2016). A common limitation of these methods is that they all require optical access to the target system (Bakalis et al., 2006). Hence, these methods are not ideal for the grinding process where a slurry with high solids concentration is involved. The light (e.g. laser) could be absorbed by the slurry causing an error for the measurement. In most cases, the grinding vessel is made of metal and filled with ceramic grinding media. The system is almost opaque. This experimental condition greatly limits the application of these optical methods.

Positron Emission Particle Tracking (PEPT) technology is a relatively new method developed at the University of Birmingham, UK (Parker et al., 1993). It is becoming more popular due to its unique advantage of being able to be applied on an opaque system. It broadens the options for studing of the grinding process. PEPT is based on the theory of Positron Emission Tomography (PET) extensively used for medical purposes. It was modified and transferred as

PEPT to observe flow dynamics in a vessel (Barigou, 2004; Barley et al., 2004; Guida et al., 2010, 2011; Liu and Barigou, 2013). The technology has been proved to be an effective method to measure the velocity profile and corresponding occupancy distribution within an opaque grinding chamber (Bakalis et al., 2006).

Compared with PIV, PLIF or LDA, PEPT overcomes the requirement that the grinding chamber must be a transparent vessel so that the light beam can pass through and then be scattered by a tracer particle (Barigou, 2004). Instead of the light beam, PEPT detects γ-rays emitted from a tracer particle to track the trajectory of the tracer. The tracer is a positron-emitting radioactive grinding media bead labelled by radioisotopes ^{18}F irradiated in a cyclotron so the tracer shows no difference in physical properties from the other grinding media. It assumes that the radioactive grinding media faithfully follows the flow dynamic inside the mill chamber. It continually emits pairs of back-to-back γ-rays generated from electron-positron annihilation (Barigou, 2004). The γ-rays are detected by 2 separate stationary detectors (PEPT cameras). By collecting bunches of the γ -rays, a 3-dimensional space is virtually built and the trajectory of the tracer is reconstructed within the space via an algorithm developed by the School of Physics, University of Birmingham (Conway-Baker et al., 2002).

Basically, a 3-D Cartesian coordinate is set up based on the space between 2 detectors. At each time point, the position of the tracer is tracked by recording the corresponding positions on x, y and z coordinates. Generally, one pair of γ-rays secures one position. Other grinding media may cause distraction of the detected γ-rays leading to an error on the located position. To avoid the error, normally 200-500 pairs of γ-rays are captured to locate one position. This greatly improves accuracy. The PEPT camera can collect 10^5 events s^{-1}

(one event means one pair of γ-rays) to reconstruct the tracer position within an error below 0.5 mm at particle speeds up to 2 m/s. Sometimes reliable reconstruction positions can be obtained at particle speeds up to 10 m/s (Parker et al., 1993).

2.5. Discrete Element Method

2.5.1. *Introduction*

In recent decades, the Discrete Element Method (DEM) has been widely used to model the motion of particles via identifying the interaction forces for either particle-particle or particle-fluid (coupled with CFD) systems (Blais and Bertrand, 2017; Cleary et al., 2006a; Kimura et al., 2007; Sinnott et al., 2006; Yang et al., 2006). The method offers a reliable solution for many problems which are impossible or extremely difficult to resolve by traditional experimental methods. By tracking collisions for every single particle, DEM can provide accurate dynamic information such as velocity, trajectory and force for each particle in the target system.

Currently, DEM is based on two major concepts for modelling particle deformation: hard or soft particle model (Di Renzo and Di Maio, 2004; Padros, 2014; Zhu et al., 2007). The hard particle model assumes the particle to be an impenetrable body and no overlap is allowed for the collision between two particles. This model has been commonly applied for modelling collisions between atoms or molecules which have strong repulsion at very close distance. The interaction between the particles is still based on a single collision mechanism which restricts the model to apply in a system where multiple collisions are involved (Di Renzo and Di Maio, 2004). However, the model is suitable for molecular dynamics simulation or the study of certain colloidal model systems (Zhu et al., 2007).

Cundall and Strack (1979) first proposed a soft particle model where the deformation of the particle was considered. They also described a detailed force-displacement for a deformed particle. In contrast to the hard particle model, the overlap between particles is considered. The model can precisely simulate the elastic, plastic and frictional forces that the particle received during the collision. Once these forces are identified, the particles translational and rotational motion are derived by Newton's 2nd Law. Then, precise simulation data such as particle velocity and location at either micro or macro scale can be obtained for any specific system. This enables DEM to be extensively applied in the modelling of particle packing/mixing processes or free particle flow.

With current computational ability, DEM is capable of simulating millions of particles. This allows DEM to be used in the simulation of the grinding process in a mill where a large amount of grinding media is involved (Cleary et al., 2006a, b; Morrison et al., 2009; Sinnott et al., 2006; Yang et al., 2006). To achieve an efficient grinding condition, it normally requires extensive experiments to collect data. This inevitably incurs at a lot of cost and effort. There are also some limitations, it is still impossible to track the trajectories of all grinding media in any laboratory devices. The impact force produced during the particle collision cannot be measured directly by any experimental methods. However, DEM provides a possibility to generate reliable and accurate data for analysing the grinding performance.

The vertical stirred media mill has been widely used due to its simple structure and ease of operation. However, the optimisation of the mill greatly depends on trial and error tests due to inadequate understanding of the bulk behaviour of the grinding media in the mill. The flow pattern in the mill is a very important factor affecting the mill efficiency and product

quality. Instead of extensive experiments, a numerical model is applied to obtain macro-dynamic information (forces velocity distribution) at very low cost. DEM has been proved as an effective method for study of the particle packing and flow. Its application in vertical stirred media mill is still very rare. Based on the soft particle model, DEM was applied in the study to simulate the flow of grinding media in the vertical stirred media mill. A simplified soft contact model was developed to predict the flow pattern of the grinding media under various operating conditions.

2.5.2. Governing equations

Newton's 2nd Law is the most basic principle to describe the force applied on a particle and the influence on its movement (see Eq. [2.11]).

$$\vec{F} = m\vec{a} = m\frac{d\vec{v}}{dt} \qquad [2.11]$$

m is the mass of the particle and $\vec{a}$ is the acceleration caused by the total force $\vec{F}$ acting on the particle. $\vec{v}$ is the velocity of the particle.

Newton's 2nd Law can be applied to describe the motion of a granular material in either translational or self-rotational movement. To describe the forces received by the particle, some sophisticated equations are derived to accurately reflect the interaction between the particles. When many particles are mixed in a confined system, the motion of a single particle is directly affected by its surrounding particles. The particle may receive contact forces or non-contact forces. This depends on its shape, size and location. For a specific particle i shown in Fig. 2-13, some typical forces and torques that the particle i may receive from the particle j and k during the collision are shown in Fig. 2-13.

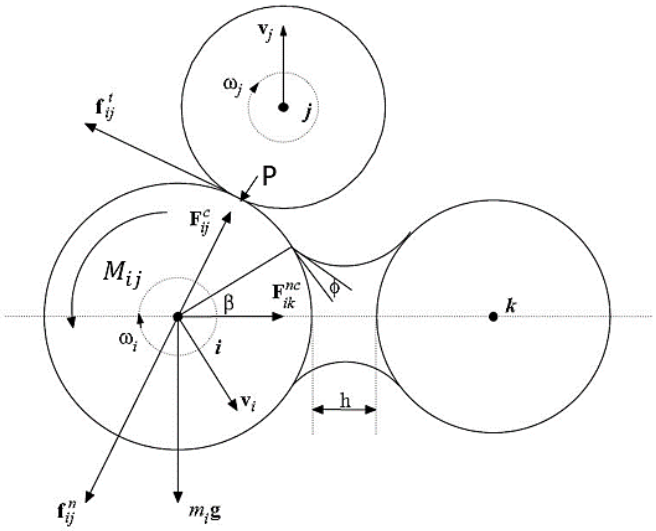

Fig. 2-13. The illustration of forces and torques involved in DEM simulation for particle i (Zhu et al., 2007).

As seen from Fig. 2-13, particle i clearly touches with particle j. The contact force is denoted as F_{ij}^c. The contact point indicated as point P between 2 particles i and j is a very small and flat area due to the deformation of the particles. A unique feature for the soft particle model is that the overlap is allowed for the particle collision. If a virtual contact plane is constructed based on the finite contact area, the contact force F_{ij}^{c} can be split into 2 perpendicular components (normal force f_{ij}^n and tangential force f_{ij}^t).

For the particles i and k, there is a clear distance (h) indicating the particles are not in touch. In some circumstances, particle i may be affected by the non-contact forces F_{ik}^{nc} from particle k. The common non-contact forces are van der Waals, electrostatic forces or liquid bridge. The magnitude of the non-contact forces normally is very small ($10^{-4}\sim10^{-8}$ N). These forces affect particle flow behaviour when the size is equivalent to the scale of an atom or molecule. If a fluid is involved in the modelling system, the particle-fluid interaction force F_i^f also needs to be considered (mainly drag force). The body force F_i^g (normally gravity) for particle i is referred to as $m_i g$.

By substituting all these forces into Eq. [2.11], a general governing equation to describe the movement of particle i for the translational velocity V_i is written as:

$$m_i \frac{dV_i}{dt} = \sum_j F_{ij}^c + \sum_k F_{ik}^{nc} + F_i^f + F_i^g \quad [2.12]$$

Additionally, the particle's self-motion caused by the torque from the contacting particle is also considered in the soft particle model. The moment of inertia (I_i) of particle i is described as Eq. [2.13] (Blais and Bertrand, 2017),

$$I_i \frac{d\omega_i}{dt} = \sum_j (M_{t,ij} - M_{r,ij}) \quad [2.13]$$

where ω_i refers to the self-rotational velocity of particle i.

$M_{t,ij}$ is the tangential torque caused by the contact force in the tangential direction (f_{ij}^t). It is calculated as Eq. [2.14] (Blais and Bertrand, 2017; Yang et al., 2006):

$$M_{t,ij} = R_i \times f_{ij}^t \quad [2.14]$$

where R_i is a vector (from the centre of particle i to the contact point P) with the magnitude equal to the radius of the particle i.

$M_{r,ij}$ is an additional torque slowing down the relative rotation between the particles and is referred to as the rolling friction torque (Goniva et al., 2012; Zhu and Yu, 2003; Zhu et al., 2007). The equation used to determine the rolling friction torque is shown as:

$$M_{r,ij} = \mu_r R_i \left| f_{ij}^t \right| \widehat{\omega_i} \quad [2.15]$$

where μ_r is the coefficient of rolling friction and f_{ij}^t is the contact force in a normal direction.

In fact, it requires extremely large computation capacity to calculate the sum of the forces or torques applied on each particle directly. A particle is not only affected immediately by its surrounding particles or fluid, but also can be disturbed from some particles at a relatively long distance. Theoretically, it requires to identify all the potential particles that may interact with the target particle before the exact forces are possible to be calculated, but this is out of the bounds of possibility with current computing technology.

To simplify the calculation of the forces, DEM simulation applies a cut off range to limit the number of the potential particles associated with the target particle. Thus, the total forces applied on the target can be calculated. The prediction of the future location is acquired based on the forces by applying a very minor increment over the time (millionths of a second) referred to as time-step. When the target particle is at a new position after a time-step, the list of surrounding particles is updated based on the cut-off range with the new location of the particle centre. The procedure is repeated for every particle at each time-step to obtain the dynamic information of the particle motion.

2.5.3. Contact models

Several reviews (Cleary et al., 2006a; Di Renzo and Di Maio, 2004; Zhu and Yu, 2003; Zhu et al., 2007) indicated that great effort had been devoted into the theoretical development of DEM over the past two decades. This rapid development is closely related to the great improvement in computing technology. This makes it possible to solve more complicated interaction laws or contact models which define the overlap distance and the contact forces.

The first step to apply contact model is to determine the contact forces and torques occurring during the particle impact before the general Eq. [2.12] and Eq. [2.13] can be solved numerically. Then, particle trajectories and velocities are calculated accordingly. The

contact forces depend on the particle shape and physical properties (e.g. Young's modulus, hardness, friction coefficient). There is still no available approach to accurately acquire the stress force distribution over the contact area for particles with an irregular shape.

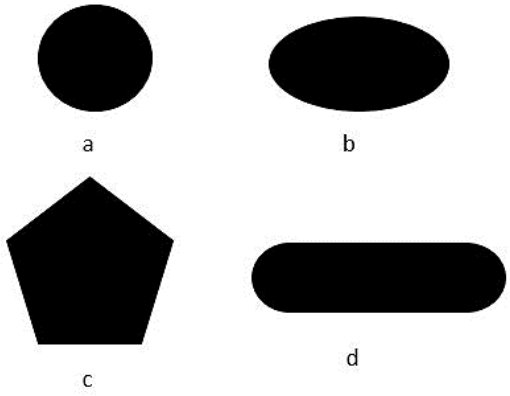

Fig. 2-14. Some typical geometries used to represent particles outline (a) sphere, (b) ellipse (c) polygon and (d) compound form (Padros, 2014).

Hence, some basic geometric shapes (see Fig. 2-14) are used to represent the modelling object. Nevertheless, the sphere is the most common shape used in DEM. In fact, few granular materials outside the laboratory are perfect spheres. Using an equivalent circle to represent the actual granular shape significantly simplifies the contact model and it also saves great computational effort. Many researchers (Di Renzo and Di Maio, 2004; Morrison et al., 2009; Sinnott et al., 2006; Yang et al., 2006) demonstrated reliable results can be achieved by using spherical particles in DEM.

Some non-spherical geometrical shapes such as a polygon or polyhedron are also used to represent complex particle shapes. More accurate results can be achieved compared to the spherical particles, but it increases computational cost which is from the underlying mathematical equations of determining whether a particle is in contact with neighbouring particles and contact force direction.

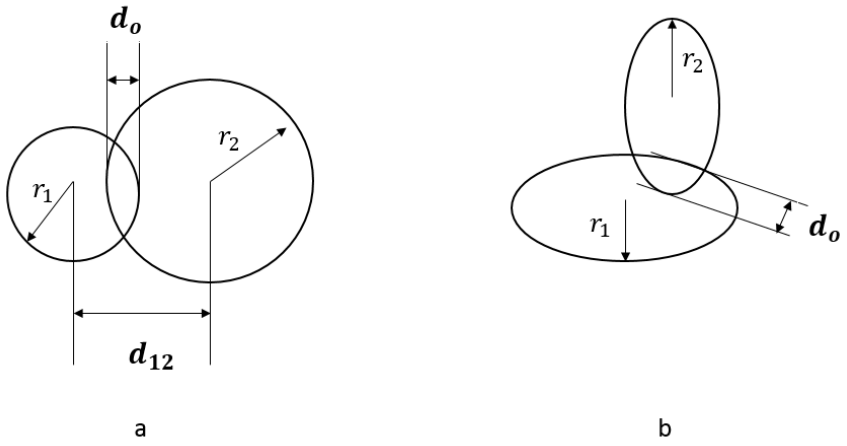

Fig. 2-15. (a) Contact for sphere-sphere. (b) Contact for ellipse-ellipse.

Once the particle shape is determined, a contact law based on the geometry is used to confirm the overlap distance d_o (displacement) between the particles. Fig. 2-15 clearly demonstrates 2-particle contact for sphere-sphere and ellipse-ellipse contact. For the sphere-sphere contact, two particles distance d_{12} is smaller than the sum of two particles radius ($r_1 + r_2$). The details of the overlap such as contact width and area can also be calculated accordingly. If a non-spherical geometry (ellipse-ellipse) is applied, the underlying mathematics may be complicated to determine the contact.

Mostly, the contact models are based on the soft particle system. The overlap for the particle-particle contact is considered. The reported models are classified into linear and non-linear models in terms of the approach for calculating the contact distance and forces. A typical linear spring-dashpot model is proposed by Cundall and Strack (1979). In their theory, a linear relationship is developed to describe the forces and the particle displacement. In contrast, a non-linear model applies a more complicated relationship.

2.5.4. Hertz-Mindlin model

A well-developed non-linear elastic model is the Hertz-Mindlin model. Hertz (1882) proposed a non-linear relationship to describe the contact force and particle displacement in a normal direction. In a tangential direction, the force-displacement relationship is reported by Mindlin and Deresiewicz (1953). They demonstrated that the forces and particle displacement in the tangential direction should be calculated based on the loading history and change rate of normal and tangential force or displacement. A general equation for Hertz-Mindlin model is shown as:

$$F_{c,ij} = \underbrace{(k_{n,ij}\ \underbrace{\delta_{n,ij}}_{\substack{normal\\ overlap}} - \gamma_{n,ij}\ \underbrace{v_{n,ij}}_{\substack{normal\\ relative\ velocity}})}_{normal\ force} + \underbrace{(k_{t,ij}\ \underbrace{\delta_{t,ij}}_{\substack{tangential\\ overlap}} - \gamma_{t,ij}\ \underbrace{v_{t,ij}}_{\substack{tangential\\ relative\ velocity}})}_{tangential\ force} \quad [2.16]$$

where $k_{n,ij}$ and $k_{t,ij}$ are the normal and tangential stiffness coefficients. $\gamma_{n,ij}$ and $\gamma_{t,ij}$ are the normal and tangential damping coefficients. $\delta_{n,ij}$ and $\delta_{t,ij}$ are the particle overlap distances in normal and tangential direction. $v_{n,ij}$ and $v_{t,ij}$ are the relative velocities in normal and tangential direction. The determination of the parameters is demonstrated in Table 2-4. These parameters are linked to the material properties (Y=Young's modulus, v=Poisson ratio, e_r=coefficient of restitution and G=shear modulus).

Table 2-4. The parameters for the Hertz-Mindlin contact model.

Normal stiffness	$k_{n,ij} = \frac{4}{3} Y_{ij}^* \sqrt{R_{ij}^* \delta_{n,ij}}$	Constant	$\beta = \frac{\ln(e_r)}{\sqrt{ln^2(e_r) + \pi^2}}$
Tangential stiffness	$k_{t,ij} = 8 G_{ij}^* \sqrt{R_{ij}^* \delta_{n,ij}}$	Equivalent Young's modulus	$\frac{1}{Y_{ij}^*} = \frac{(1 - v_i^2)}{Y_i} + \frac{(1 - v_j^2)}{Y_j}$
Normal damping	$\gamma_{n,ij} = -2\sqrt{\frac{5}{6}} \beta \sqrt{S_n m_{ij}^*} \geq 0$	Equivalent radius	$\frac{1}{R_{ij}^*} = \frac{1}{R_i} + \frac{1}{R_j}$
Tangential damping	$\gamma_{t,ij} = -2\sqrt{\frac{5}{6}} \beta \sqrt{S_t m_{ij}^*} \geq 0$	Equivalent mass	$\frac{1}{m_{ij}^*} = \frac{1}{m_i} + \frac{1}{m_j}$

Constant	$S_n = 2Y_{ij}^* \sqrt{R_{ij}^* \delta_{n,ij}}$	Equivalent shear modulus	$\frac{1}{G_{ij}^*} = \frac{2(2+v_i)(1-v_i)}{Y_i} + \frac{2(2+v_j)(1-v_j)}{Y_j}$
Constant	$S_n = 2Y_{ij}^* \sqrt{R_{ij}^* \delta_{n,ij}}$		

The Hertz-Mindlin contact model states a relation between the overlap and the force when two particles collide against each other. The model shows a close dependency on four physical properties of the material which are Young's modulus (Y), Poisson ratio (v), shear modulus (G) and coefficient of restitution (e_r). Besides, the multi-particle collisions can also be dealt with by the model. The influence of the particle properties can be directly reflected via the forces and velocities of the particles. However, the limit of the Hertz-Mindlin model is that no long-range inter-particle forces (e.g. Van der Waals and capillary force) are provided.

2.5.5. Adhesive contact model

To incorporate the adhesion force into the Hertz Model for contact force in a normal direction, Johnson-Kendall-Roberts (1971) developed an adhesive contact model (JKR) based on the balance between the stored elastic energy and the loss in the surface energy (Johnson et al., 1971). Both impact pressure and adhesive force are related to the contact radius. The modified normal force is shown as Eq. [2.17]:

$$F_{ij}^c = \frac{4Y_{ij}^* a^3}{3R_{ij}^*} - 2\sqrt{2\pi Y_{ij}^* a^3 \Delta\gamma} \qquad [2.17]$$

where a is the contact radius (see Fig. 2-16) and $\Delta\gamma$ is the variation in adhesion energy.

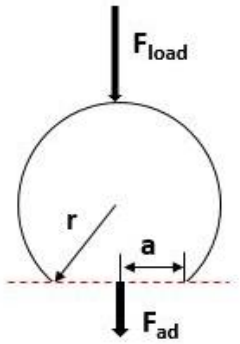

Fig. 2-16. A schematic of a particle under adhesion force and the load (Pardos, 2014).

Similar to the JKR model, Derjaguin et al. (1975) derived their version of an adhesion contact model (DMT model) shown as Eq. [2.18]:

$$F_{ij}^{c} = \frac{4Y_{ij}^{*}a^{3}}{3R_{ij}^{*}} - 2\pi\Delta\gamma R_{ij}^{*} \qquad [2.18]$$

Compared to the JKR model, the DMT model deals with the forces caused by particle deformation and adhesion effect separately. Hence, DMT model is straightforward to apply in DEM.

2.5.6. Liquid bridge model

A liquid bridge with capillary force appears when two wet particles are within a close distance. A schematic of the liquid bridge model with a non-zero contact angle is shown in Fig. 2-17. The capillary force is caused by the surface tension (gas/liquid/solid interfaces) and difference of hydrostatic pressure within the liquid bridge. Fisher (1926) used a toroidal approximation to model the shape of the liquid bridge. The capillary force is decided by the following Eq. [2.19] (Lian et al., 1993; Zhu et al., 2007):

$$F_{i}^{f} = 2\pi\sigma R sin\emptyset \sin(\emptyset + \theta) + \pi R^{2}\Delta P sin^{2}\emptyset \qquad [2.19]$$

σ is the liquid surface tension. $\emptyset$ is the half-filing angle and θ is the contact angle. The pressure difference across the air-liquid interface ΔP is determined by the Laplace-Young equation.

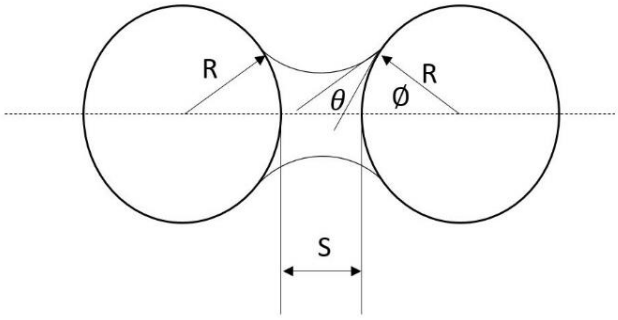

Fig. 2-17. A schematic of the liquid bridge model between two equal spheres with a non-zero contact angle (Lian et al., 1993).

The drawback of the liquid bridge model is that the exact solution of the capillary force is hard to implement with DEM. Hence, some approximation procedures are proposed to link the capillary force with the liquid bridge volume and distance between the particles (Willett et al., 2000). Normally, when the gap between the particles is smaller than the rupture distance, a liquid bridge is assumed to appear and the liquid is homogeneous within the liquid bridge.

2.6. Conclusions

Recently, application of fine particle grinding using vertically stirred media mill has been increased dramatically as the finer product is required from the mineral industry. The stirrer media mill shows a great improvement over energy efficiency than ball mill. Due to the limit on the capacity, the vibrating mill is difficulty to be applied in a large scale.

Several models have been reported to predict the relationship between the energy consumption and the product size. They all demonstrated good accuracy under some specific assumption and conditions which are hardly to meet in the industrial process.

Due to its reliability and accuracy, PEPT is considered as a reliable tool to study the motion of the grinding media inside a stirred media mill. PEPT is investigated in combination with DEM which shows ability to accurately simulate the forces that a particle may encounter in free flow. The most important factor affecting particle flow is recognised as the contact force due to the collision (Di Renzo and Di Maio, 2004). Hertz-Mindlin contact model is reviewed and it is a suitable model for simulating the collisions between the grinding media in the vertically stirred media mill.

Chapter 3 Experimental set-up and techniques

3.1. Introduction

The study is trying to investigate the performance of the vertically stirred media mills through measuring particle size reduction, power consumption and grinding time under various operating parameters e.g. solids loading, specific energy utilizations, tip speed, grinding media and configuration of the stirrers. These parameters are reported to be the most important factors affecting the grinding efficiency. Calcite is chosen as the feed mineral and its particle size distribution (PSD) is examined at different levels of energy input to show the grinding efficiency under various operating conditions. The wet grinding process is performed on two different scales of the vertically stirred media mills (laboratory scale and pilot scale mills).

3.2. Experimental materials

3.2.1. Feed mineral

Calcium carbonate (calcite, $CaCO_3$) supplied by Imerys is used as feed material in all experiments. The density of calcite is 2710 kg/m^3. It has a hardness of 3.0 on the Moh's scale (Tamblyn, 2009). The substantial reserves and widely distribution over the world make calcite cheap and easy to access. Due to these characteristics, calcite is commonly used as a paper filler. The paper properties such as strength, smoothness and non-transparency are directly influenced by the filler size. To improve these properties, a finer filler is always required. Similarly, in the pharmaceutical industry or pigment grinding, fine grain size is also desired by the manufacturers. The interests in fine grinding technology have been continually growing over the last 20 years for achieving finer particle size at lower energy cost (Radziszewski, 2013).

Table 3-1. The feed size of calcite.

	d_{90} *(μm)*	d_{80} *(μm)*	d_{50} *(μm)*	d_{20} *(μm)*	d_{10} *(μm)*
Test 1	33.9	26.8	15.6	7.9	5.0
Test 2	34.0	27.0	15.7	8.2	5.3
Test 3	33.9	26.9	15.8	8.3	5.5
Ave	33.9	26.9	15.7	8.1	5.2
SD (σ)	0.03	0.05	0.11	0.18	0.23

In this study, the grinding efficiency is evaluated by the product size obtained under various operating conditions. Particle size distribution (PSD) is determined by a laser diffraction particle size analyser (Malvern Mastersizer 2000) in the School of Chemical Engineering. The size parameters of the feed calcite (e.g. d_{80}=26.9 μm) are exhibited in Table 3-1.

The size parameter d_{80} indicates the maximum size that 80 % of the total particles can pass through. It is the most commonly used parameter in the mineral industry to evaluate the product size. Similarly, the parameters d_{90}, d_{50}, d_{20} and d_{10} indicate the size that 90 %, 50 %, 20 % and 10 % of the particles are smaller than the corresponding values respectively. In Table 3-1, the terms Ave and *SD (σ)* denote the average value and the standard deviation respectively. The *SD (σ)* is calculated by Eq. [3.1] shown below:

$$SD(\sigma) = \sqrt{\frac{1}{N-1}\sum(x_i - \bar{x})^2} \qquad [3.1]$$

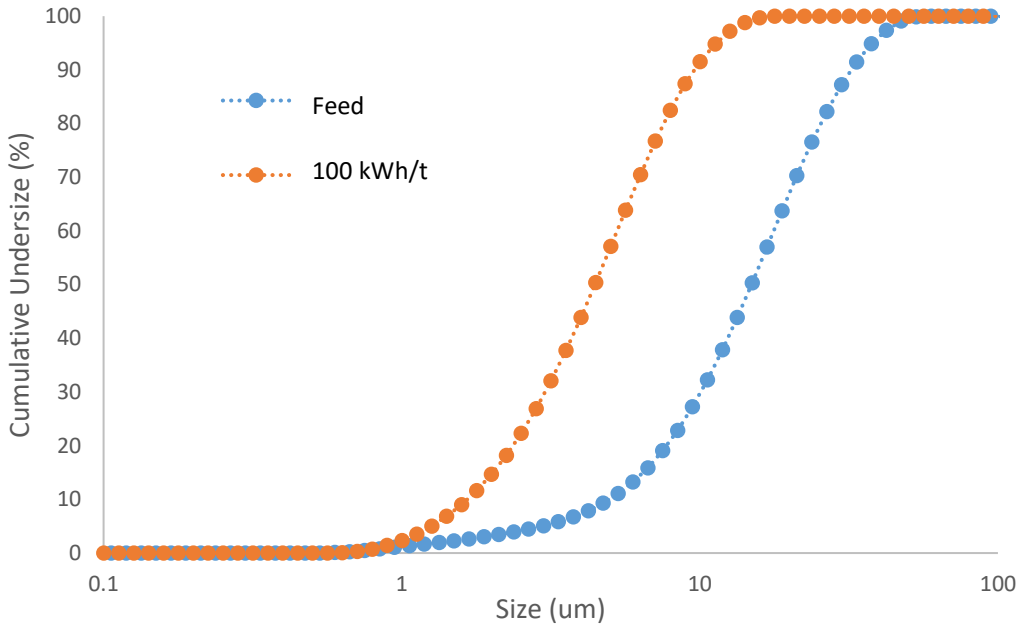

Fig. 3-1. Cumulative PSD of feed sample and product sample at energy input 100 kWh/t (Measured by Malvern Mastersizer 2000).

Fig. 3-1 compares cumulative PSD of the feed sample with the cumulative PSD of the product (d_{80}=7.4 μm) obtained at the specific energy input 100 kWh/t. The curve for the particle size distribution clearly moves from the right to the left indicating that the particle fineness is improved.

3.2.2. Solids content of slurry

In a wet grinding process, dry mineral powder is mixed with the water to form a homogeneous slurry. The ratio between the water and the mineral directly determines the physical properties of the slurry. The fraction of dry mineral over whole weight of the slurry is defined as solids concentration also called solids loading (w/w). Eq. [3.2] is used for the determination of the solids concentration.

$$\varphi_{solid} = \frac{m_{mineral}}{m_{mineral} + m_{water}} \quad [3.2]$$

The solids concentration is an important variable affecting the grinding efficiency. The influence of solids concentration becomes more evident on the grinding process when the particle size is reduced to several microns. Thus, the understanding of slurry rheology at different levels of solids concentration plays an important in the optimisation of the grinding process. Fig. 3-2 illustrates some characteristics for non-Newtonian fluids.

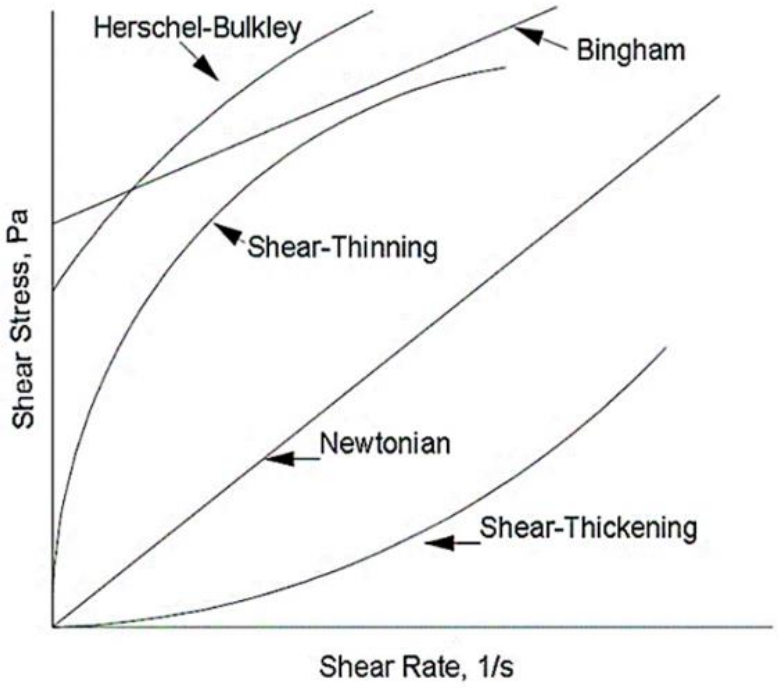

Fig. 3-2. Shear stress versus shear rate for time-independent non-Newtonian fluids (Steffe, 1996).

The shear viscosity expresses the resistance ability of the fluid to shearing flow. The viscous force (shear stress τ) is described by Eq. [3.3] below:

$$\tau = \mu \frac{\partial u_s}{\partial y_s} \qquad [3.3]$$

where $\frac{\partial u_s}{\partial y_s}$ is the local shear velocity and coefficient μ is the shear viscosity.

Rearranging Eq. [3.3], the shear viscosity is obtained as:

$$\mu = \frac{shear\ stress}{shear\ rate} \qquad [3.4]$$

When the viscosity μ is a constant, the shear stress is linearly proportional to the local shear rate. The fluid with this characterisation is defined as a Newtonian fluid. If μ is a variable, the fluid is defined as a non-Newtonian fluid.

To identify the rheology of the slurry, the shear stress was measured at solids concentrations of 50 %, 65 % and 75 % (w/w). The slurry was obtained after mixing for 10 minutes to ensure particles uniformly dispersed in the water. The measurements were performed on an AR-2000 rheometer (TA instruments, USA) with a 40 mm 4° diameter cone geometry with a gap of 1000 μm at temperature 25 ℃

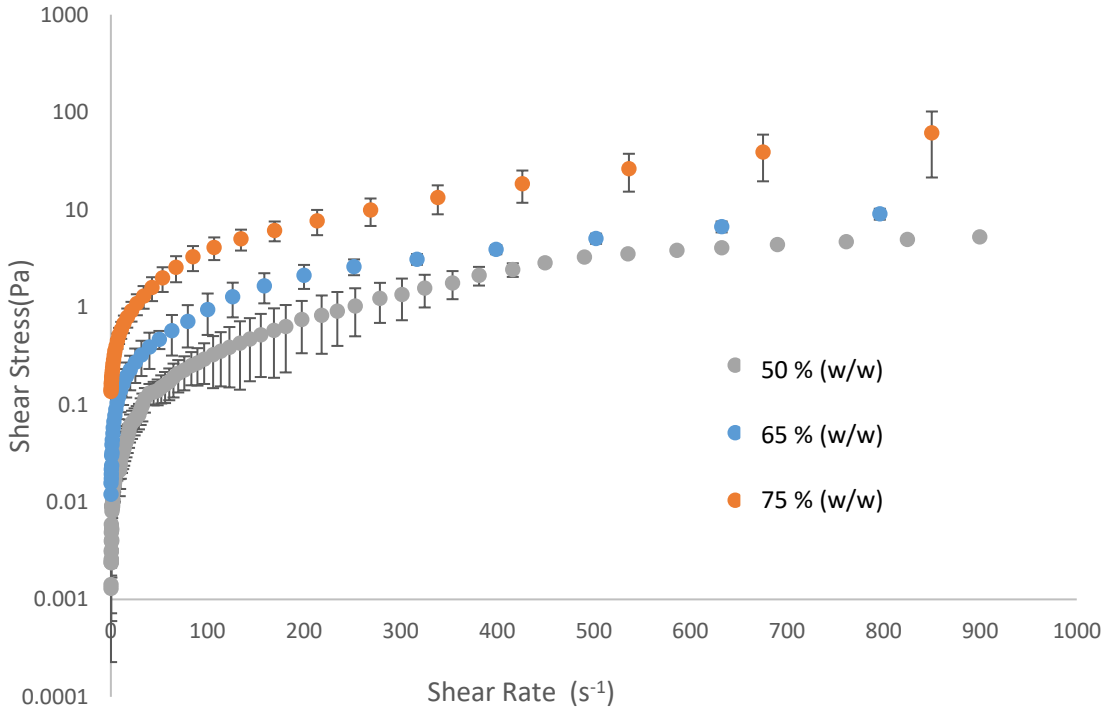

Fig. 3-3. Shear stress (Pa) against shear rate (s^{-1}) at 50 %, 65 % and 75 % (w/w) solids concentrations.

The curves of shear stress versus shear rate are exhibited in Fig. 3-3. The error bar indicates the standard deviation of the measurements. The curve gradient represents the local viscosity. The viscosity reflects the resistance ability of the mineral slurry. The trend shown in the figure implies that the slurry with a lower solids concentration has less resistance.

As seen in Fig. 3-3, the calcite slurry exhibits a typical non-Newtonian character (shear thinning). The shear stress rises sharply before the shear rate reaches 200 s^{-1}. The corresponding gradient of the curve (viscosity) decreases rapidly. Then, the shear stress slowly increases against the shear rate up to 900 s^{-1}. The slurry at 75 % (w/w) solids concentration clearly shows a higher shear stress at the same shear rate indicating that higher solids concentration causes greater resistance. The lowest shear stress is observed at 50 % (w/w) solids concentration. The gradient of the curve in Fig. 3-3 is the instantaneous viscosity. A relationship between viscosity and shear rate is derived as shown in Fig. 3-4.

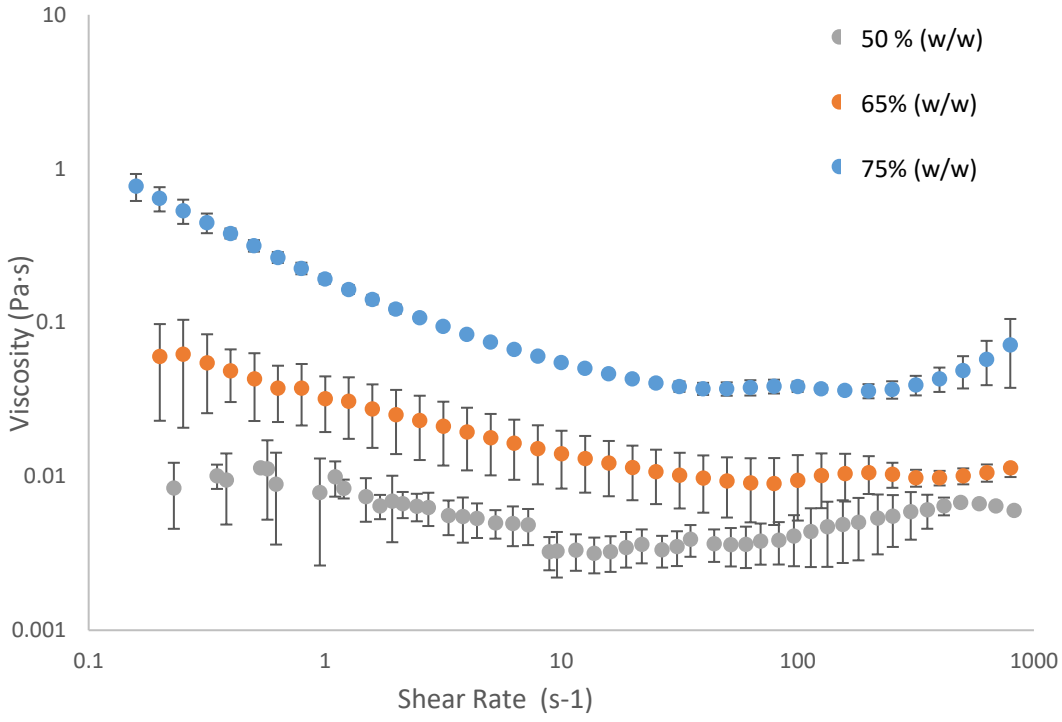

Fig. 3-4. Viscosity ($Pa \cdot s$) against shear rate (s^{-1}) at 50 %, 65 % and 75 % (w/w)

Fig. 3-4 exhibits the evolution of the viscosity against shear rate at solids concentration 50 %, 65 % and 75 % (w/w). It clearly shows that the viscosity decreases against the shear rate at all levels of solids concentrations. This proves that the slurry is a typical shear-thinning non-Newtonian fluid. Decreasing the solids concentration, the shear thinning characterisation is less obvious. Bernhardt et al. (1999) observed similar phenomenon on limestone slurry at 60 % (w/w) and 55 % (w/w) solids concentration. As the solids concentration increases, the mineral slurry rheology shows stronger non-Newtonian characterisation. Decreasing the solids concentration, the viscosity also decreases and the flow-ability is greatly increased.

As seen from Fig. 3-4, when the solids concentration decreases, the slurry progressively shows less non-Newtonian behaviour. Over all the ranges of the shear rate, the slurry at 75 % (w/w) solids concentration shows greater viscosity than 65 % (w/w) followed by the 50 % (w/w) solids concentration. When the shear rate range is beyond 100 s^{-1} close to 1,000 s^{-1}, the viscosity tends to slightly increase for solids concentration at 75 % (w/w) and 50 % (w/w). Greenwood et al. (2002) explained that this phenomenon is mainly caused by the sedimentation of the particle in the rheometer. At a lower shear rate, gravity and drag force may prevent the motion of the particles and the resistance forces caused by the particles are not evident. When the higher shear force is applied, the motion of the particles is more intense. Thus, the impact is more obvious leading to enhancement of the resistance.

3.2.3. Morphology of calcite

Scanning Electron Microscopy (SEM) is used to observe the morphology of the calcite. Fig. 3-5 illustrates SEM photographs of the feed calcite sample. As seen from the images, the feed sample is very coarse and irregular in shape. The size distribution is also not uniform. The diameter of the largest particle can be up to 100 μm and the smallest particle is approximately 5 μm. The surface is relatively rough as these particles are crushed from some larger particles in the upstream process.

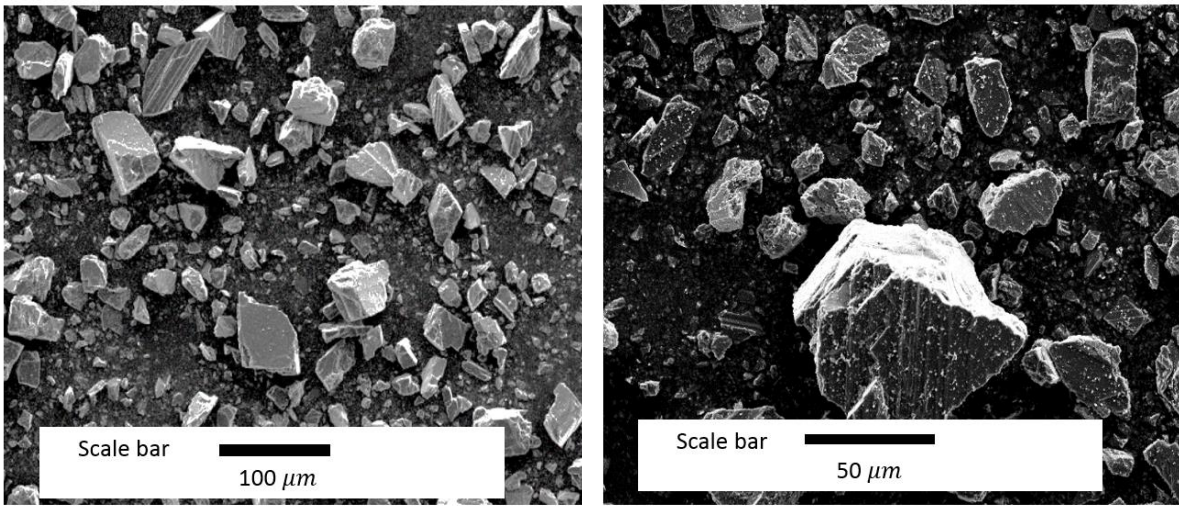

Fig. 3-5. SEM photographs for feed calcite at length scale 100 μm (left) and 50 μm (right).

The shape of the most particles is blocky and non-spherical adopting the characteristic rhombohedral shape of mineral calcite. This undoubtedly increases the complexity of the study. Thus, an equivalent spherical diameter is used. The simplification greatly improves the analysis efficiency. This also shows no obvious influence on evaluation of the product fineness.

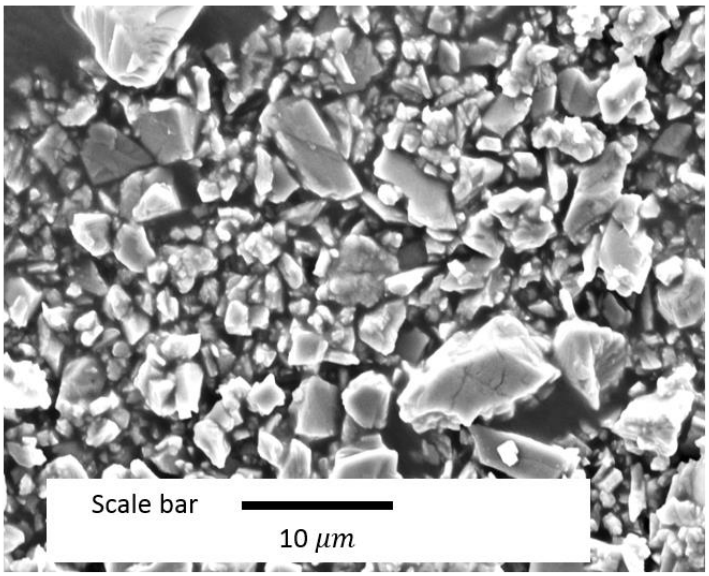

Fig. 3-6. SEM photographs for calcite ground at energy 100 kWh/t (scale at 10 μm).

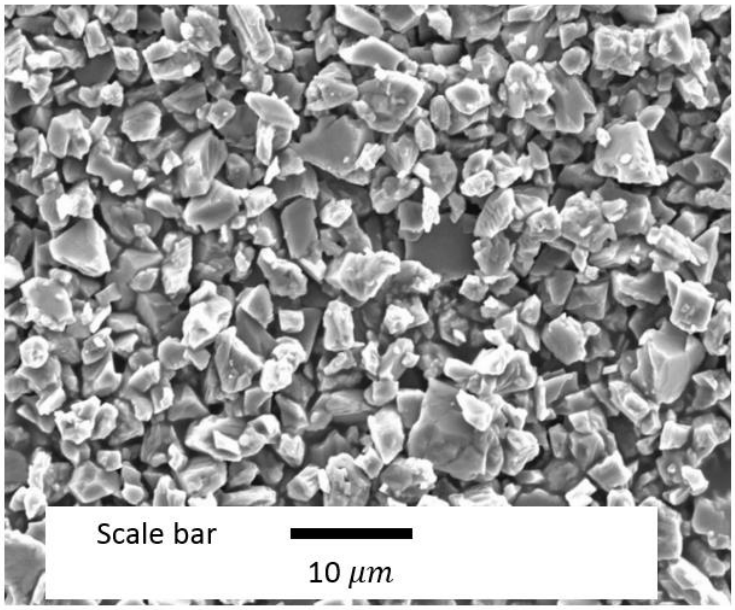

Fig. 3-7. SEM photograph for calcite samples ground at energy 200 kWh/t (scale at 10 μm).

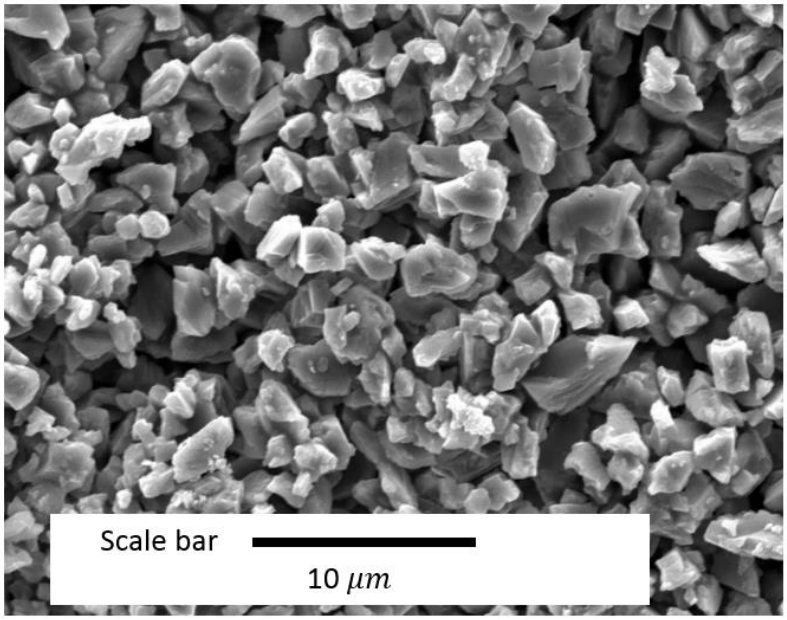

Fig. 3-8. SEM photograph for calcite samples ground at energy 300 kWh/t (scale at 10 μm).

To provide an insight into the morphology of the calcite particle obtained at different specific energy inputs, Fig. 3-6, Fig. 3-7 and Fig. 3-8 illustrate calcite particles ground at the specific energy inputs 100, 200 and 300 kWh/t respectively. As expected, the particle size is greatly reduced. At the specific energy input 100 kWh/t, the largest particle size is about 10 μm far smaller than the feed particle size shown in Fig. 3-5. Increasing the specific energy input to 200 kWh/t and 300 kWh/t, the particle fineness is further improved as shown in Fig. 3-7 and Fig. 3-8 respectively. Overall, the particle size and shape captured by the SEM clearly illustrates the evolution of the particle size reduction at different levels of the specific energy input.

3.3. Experimental apparatus

There are two vertically stirred media mills utilised in the study, a laboratory scale mill and a pilot scale mill. Both mills are designed by G.T.Jones & Co. (Cornwall, UK) and used by

Imerys. The layout and configuration of these two vertically stirred media mills are similar to the Stirred Media Detritors (SMD) manufactured by Metso. Currently, these two mills are only available for batch processing, thus the influence of inlet and outlet flow is not considered.

3.3.1. Laboratory scale mill

Fig. 3-9 exhibits some key components of the laboratory scale mill. The standard stirrer configuration is illustrated in Fig. 3-10. The laboratory scale mill consists of a grinding chamber (V_c=2.9 L), a digital controller for altering rotational speed and a vertically mounted stirrer driven by an electrical motor. The standard stirrer consists two pairs of pin stirrers with 90° offset angle. The inner surface of the mill chamber is coated with polyethylene to reduce the wear. The power drawn by the stirrer is measured via a torque sensor located under the mill chamber bottom.

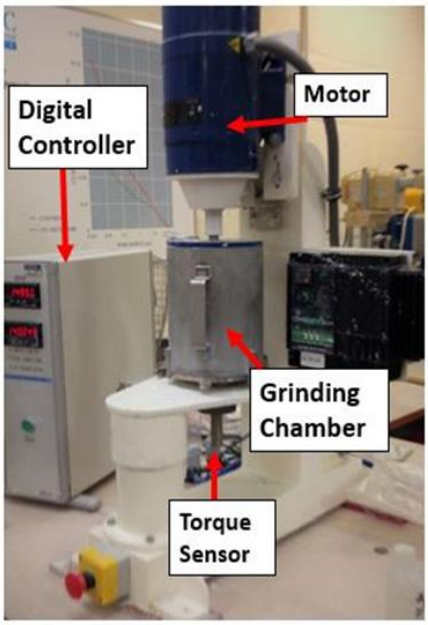

Fig. 3-9. The experimental set-up for the laboratory scale mill.

Fig. 3-10. The standard pin stirrer (Type a) used in the laboratory scale mill.

Feed materials are prepared by the following steps. Firstly, some dry powdered calcite is added into the grinding chamber directly. Then, the stirrer begins to rotate at a relative slow speed while the grinding media is added and mixed with the dry calcite. Finally, the water is added to the grinding chamber. The stirrer rotates at a low speed (approximately 200 RPM) until a homogeneous slurry is formed. Note the slurry refers to the mixture of the mineral powder and water. Then, the rotational speed is set to the required value. The operating parameters and information such as instantaneous power consumption, circumferential speed and total energy are recorded by the digital controller. To prevent spilling of the slurry and the grinding media, the grinding chamber is covered by a lid.

3.3.2. Pilot scale mill

The layout of the pilot scale mill is shown in Fig. 3-11. The basic components are similar with the laboratory scale mill. Nevertheless, the grinding chamber volume (V_c) is increased from 2.9 L to 22.8 L by 7.86 times. Additionally, the cross-sectional shape of the mill chamber is changed from circle to octagon to replicate plant-scale mills. The effective grinding area is increased which produces higher flow-ability for the charge. This also increases the probability to form a vortex around the shaft and a stagnant zone around the wall and the bottom of the grinding pot. The cross-sectional plan of the grinding chamber is designed as an octagon shape for the pilot scale mill to avoid these phenomena. This design increases the friction from the chamber wall and prevents the slurry flowing as an entire block and avoids the vortex caused by the centrifugal force around the stirrer as much as possible.

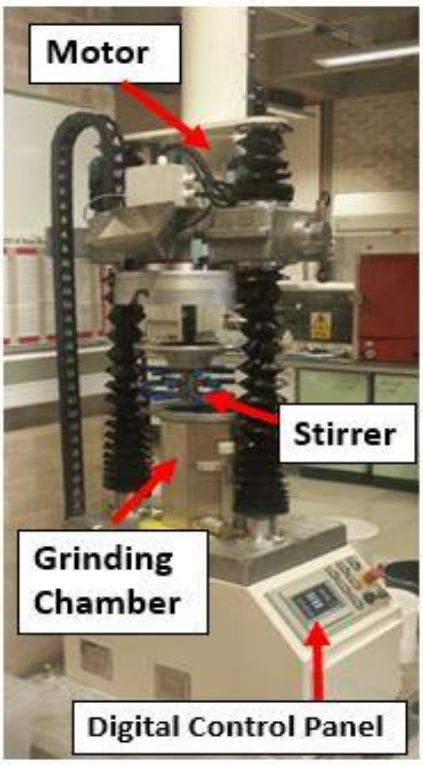

Fig. 3-11. The configuration for the pilot scale mill with key components.

Fig. 3-12. The standard pin stirrer (Type b) used in the pilot scale mill.

The standard configuration of the stirrer used in the pilot scale mill is exhibited in Fig. 3-12. The stirrer consists of 18 pin arms. The angle contained by the adjacent stirrer arms is 60°. The stirrer is used as the standard configuration (*Type b*) in the pilot scale mill unless otherwise stated. The technical specifications for two mills are compared in Table 3-2.

Table 3-2. Technical specifications for both laboratory and pilot mills based on the standard stirrer configurations.

	Laboratory scale (circle)	Pilot scale (octagon)
Chamber diameter, $D_c(mm)$	140	272
Chamber Height, $H(mm)$	190	370
Stirrer diameter,$d_s(mm)$	125	260
Stirrer shaft diameter (mm)	40	20
Gap between tip and wall, g (mm)	7.5	6
Bottom area, S (cm^2)	154	617
Chamber volume, V_c (L)	2.9	22.8
Rotational speed, N_r (RPM)	300-1,500	150-700

As seen from Table 3-2, the gap distances (g) between the stirrer tip and the wall of the grinding chamber are 7.5 mm and 6 mm for the laboratory scale mill and the pilot scale mill

respectively. This gap dimension is very close. This produces nearly the same collision intensity between the charge materials or the charge and the chamber wall when the same tip speed velocity is applied. The diameters for grinding chamber (D_c) and stirrer (d_s) are increased by approximately 2 times. The tip speed of the stirrer is the maximum speed obtained in the mill. The velocity of the grinding media should not exceed this value. Hence, it is essential to keep identical tip speed on both mills for scale-up. To achieve the same tip speed (V_t), different rotational speed (N_r) is applied. The relationship is described by Eq. [3.5] shown as:

$$V_t = \frac{2\pi N_r}{60} d_s \qquad [3.5]$$

The instantaneous power is recorded automatically by the digital control panel on the pilot scale mill. The mechanism for measuring the power absorbed by the mill is the same as the laboratory scale mill. It firstly measures the torque force. Then, the torque is transferred into the power draw. The operating parameters such as power consumption, rotational speed and torque are downloaded when the grinding process is completed. The material filling procedure follows the same routine applied on laboratory scale mill.

3.3.3. Grinding media

Two different types of the grinding media used in the experiments are shown in Fig. 3-13. One type is Carbolite (see Fig. 3-13a) supplied by CARBO. The main composition is aluminium silicate ($Al_2O_3 \cdot SiO_2$). The bead size range is +0.8 to -1.2 mm with an apparent specific gravity 2.7 ± 0.1. The other one is ZirPro (see Fig. 3-13b), a zirconium-based grinding media supplied by Saint-Gobain. The size range is +0.7 to -1.4 mm, with an apparent specific gravity 3.2 ± 0.1. The surface of Zirpro is slightly smoother than Carbolite due to the respective manufacturing process.

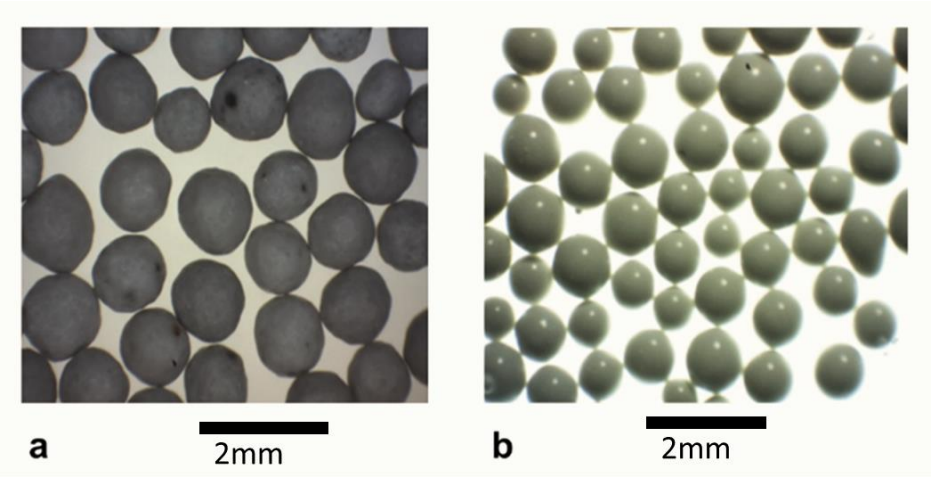

Fig. 3-13. Photographs of grinding media (a) Carbolite and (b) ZirPro (ZirPro is smoother).

For all the experiments conducted in the study, the media filling ratio (φ) is constant at 52 % (v/v) in line with the technical requirement of Imerys. There is no significant difference between grinding media observed when the filling ratio (φ) is lower than 40 % (Ohenoja et al., 2013). It has been reported that the higher media filling ratio improves the grinding efficiency (Altun et al., 2013). However, the energy consumption will also be increased accordingly. Also, high filling ratios increase the amount of the energy transferred into heat caused by the attrition between grinding media.

Chapter 4 Grinding calcite suspensions in a vertically stirred media mill

4.1. Introduction

The grinding experiments with calcite were initially conducted in the laboratory scale mill under various operating conditions. The operating variables including specific energy input, rotational speed, solids concentration, type of grinding media, chemical additives (dispersant) have been investigated. These variables have been regarded as the major factors affecting the efficiency of the fine particle grinding process (Jeong et al., 2015; Ohenoja et al., 2013; Ouattara and Frances, 2014; Zheng et al., 1997). Their influences on the mill performance were investigated through the product size distribution, instantaneous power draw and grinding time. The influence of different stirrer configurations was also studied in the laboratory scale mill. So far, the literature about the influence of stirrer configuration on vertically stirred media mill is very limited (Altun et al., 2014). To fill this gap, some new stirrer configurations are proposed and applied. Their performance is demonstrated and analysed by comparison with the current standard stirrer. The comparative grinding experiments were also carried out in a pilot scale mill using the pilot-380 vertically stirred mill.

4.2. Experimental set-up

The laboratory scale mill was used to investigate the influences of different operating conditions. During the grinding process, the samples of product were measured at 5 levels of the specific energy input 100, 150, 200, 250 and 300 kWh/t. The corresponding particle size (e.g. d_{80}) of the sample was measured and the corresponding grinding time was recorded. The effect of rotational speed was studied by setting V_t to 5.23 m/s (equivalent

to 800 RPM), 6.54 m/s (equivalent to 1000 RPM), 7.85 m/s (equivalent to 1200 RPM) and 9.81 m/s (equivalent to 1500 RPM). Note that the standard value of tip speed used on site at Imerys is 6.54 m/s for grinding calcite. The experimental results obtained at solids concentrations 50 %, 65 % and 75 % (w/w) were compared at V_t=6.54 m/s to study the influence of solids concentration. To study the effect of grinding media size, 3 types of ZirPro grinding media with size range: +0.7-1.4 mm, +1.6-2.0 mm and +2.0-2.4 mm were used. The influence of dispersant was studied at the dispersant concentrations 0.8%, 2.5%, 5 % and 10 % (w/w). The application of the grinding mill on the other minerals such as wollastonite and perlite was also demonstrated.

Additionally, 5 different configurations of the stirrer were presented and studied in the laboratory scale mill. The experiments were conducted at 65 % solids concentration and the V_t was set at 7.85 m/s (1200 RPM) unless otherwise stated. ZirPro grinding media with size +0.7-1.4 mm was used for the experiments about the stirrer configuration. The grinding process in the pilot scale mill was studied at V_t= 7.85 m/s (576 RPM). The total charge of slurry was scaled up to 10 kg. A standard pin stirrer (*Type b*) and a new stirrer type (*Type b-1*) scaled up from the laboratory scale mill were tested in the pilot scale mill.

4.3. Analysis of operating variables

4.3.1. Specific energy input

Over 40 operating variables have been identified as influencing the grinding efficiency in a vertically stirred media mill. Depending on the mineral type and the structure of mill, the influence is significantly different for each variable. A vertical stirred media mill has its own unique optimal conditions for one specific mineral. This undoubtedly increases the

complexity of investigation of the grinding process. So far, there has been no general "trend" derived to describe the process given so many unpredictable factors.

This study focuses on the relationship between the product quality and the energy consumption. The goal is to achieve the finest particle size whilst consuming the least energy. The specific energy input (energy consumption over the unit weight of the mineral) is commonly accepted as the most important variable which determines the efficiency of grinding process. It is defined as the total energy consumed by the mill over the unit weight of feed mineral in dry condition (Kwade and Schwedes, 2007).

Apart from the size parameters (e.g. d_{80} or d_{50}), there are some other values also used to evaluate the product size. The Steepness Factor (SF) defined as d_{50}/d_{20} describes the trend of the PSD curve "broad" or "narrow". If the SF factor is less than 2, the PSD curve is relatively narrow indicating the distribution of the particle size is within a relatively small range. Additionally, the ratio d_{80}/d_{20} is used as a supplementary factor as it is related to the size parameter d_{80}. The PSD width defined by the ratio $(d_{90} - d_{10})/d_{50}$ evaluates the span of the PSD curve. Also, it can be represented by the ratio $(d_{80} - d_{20})/d_{50}$ relating the ratio of d_{80} and d_{20}. As the particle size reduces, both parameters SF and PSD width decrease. Note that the trend in variation may not be applicable for bimodal distributions. In this study, the size parameter d_{80} is mainly used to indicate the product size, in line with Imerys reporting techniques.

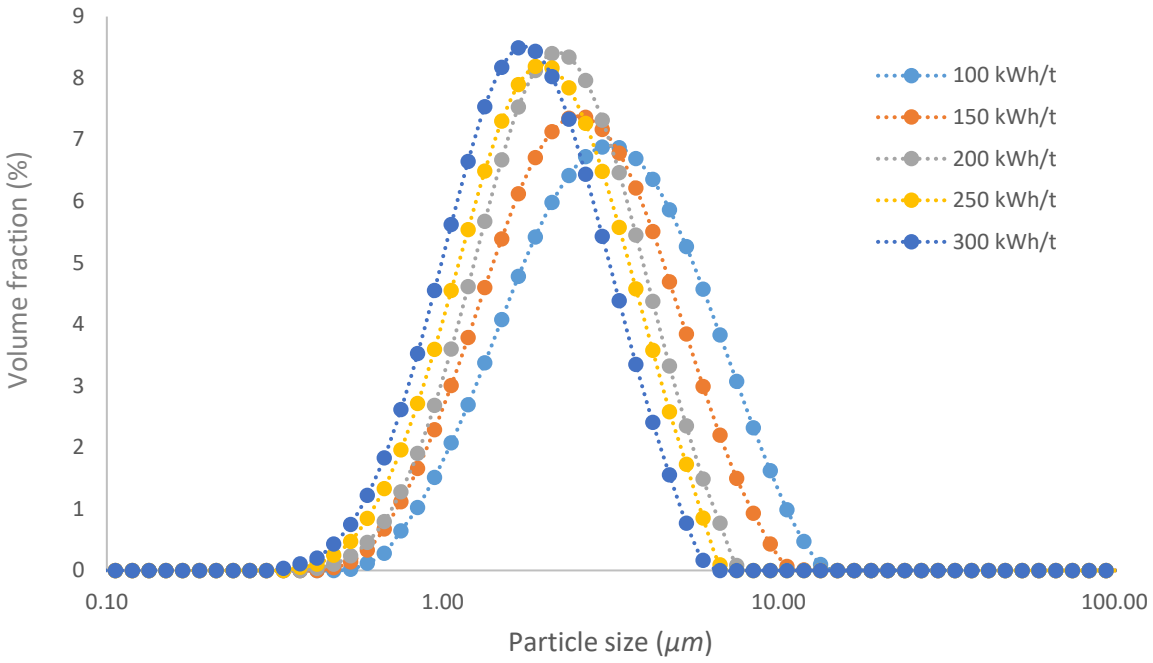

Fig. 4-1. Particle size distribution (PSD) obtained using Carbolite grinding media (size +0.8-1.2 mm) at V_t=9.81 m/s with the specific energy input 100~300 kWh/t (Measured by Malvern Mastersizer 2000).

The experiments were conducted using Carbolite grinding media (size +0.8-1.2 mm). The slurry was mixed at 75 % (w/w) solids concentration and the tip speed (V_t) was 9.81 m/s. The product samples were measured at the specific energy input 100, 150, 200, 250 and 300 kWh/t. Fig. 4-1 shows the PSD of the product samples obtained at the specific energy input 100~300 kWh/t. The PSD curves are clearly shifted from the right to the left with increasing the specific energy input. The maximum particle size is beyond 10 μm at the specific energy input 100 kWh/t. When the energy is increased to 300 kWh/t, the overall particle size distribution is below 10 μm. A narrower width of the size distribution is also observed with increasing the specific energy input (see Fig. 4-1).

Table 4-1. PSD obtained at specific energy input 0~300 kWh/t obtained using Carbolite grinding media size +0.8-1.2 mm (75 % solids concentration, V_t=9.81 m/s).

Energy Input (kWh/t)	d_{10} (μm)	*SD* (σ)	d_{20} (μm)	*SD* (σ)	d_{50} (μm)	*SD* (σ)	d_{80} (μm)	*SD* (σ)	d_{90} (μm)	*SD* (σ)
feed	5.2	0.23	8.1	0.18	15.7	0.11	26.9	0.05	33.9	0.03
100	1.3	0.12	1.7	0.14	3.1	0.19	5.2	0.21	6.7	0.18
150	1.1	0.12	1.4	0.12	2.5	0.13	4.1	0.14	5.3	0.14
200	1.1	0.13	1.3	0.10	2.1	0.11	3.4	0.05	4.2	0.03
250	0.9	0.10	1.2	0.10	1.9	0.10	3.1	0.11	3.8	0.12
300	0.8	0.06	1.1	0.06	1.7	0.06	2.7	0.07	3.4	0.08

The particle size parameters (e.g. d_{10}, d_{20}, d_{50}, d_{80} and d_{90}) are shown in Table 4-1. At the specific energy input 100 kWh/t, the d_{10} is 1.3 μm. It is slightly reduced to 0.8 μm at 300 kWh/t. This implies that it is extremely hard to reduce particle size further when the size is already very fine. However, the d_{80} reflects more information about the size variation. By increasing every 50 kWh/t, the d_{80} decreases 0.63 μm on average. The d_{80} is finally reduced to 2.7 μm at the specific energy input 300 kWh/t which is 10 times smaller than the feed d_{80}=26.9 μm.

Fig. 4-2 shows size reduction ratios against the specific energy input. The values of f_{20}, f_{50}, f_{80} are 20%, 50% and 80% passing particle size for feed material respectively. When increasing the specific energy input, all reduction ratio increases constantly. This indicates that the overall size of calcite is decreasing. The reduction ratio f_{80}/d_{80} is increased from 5.1 to 9.9. The curves of f_{50}/d_{50} and f_{20}/d_{20} demonstrate similar trend shown in Fig. 4-2.

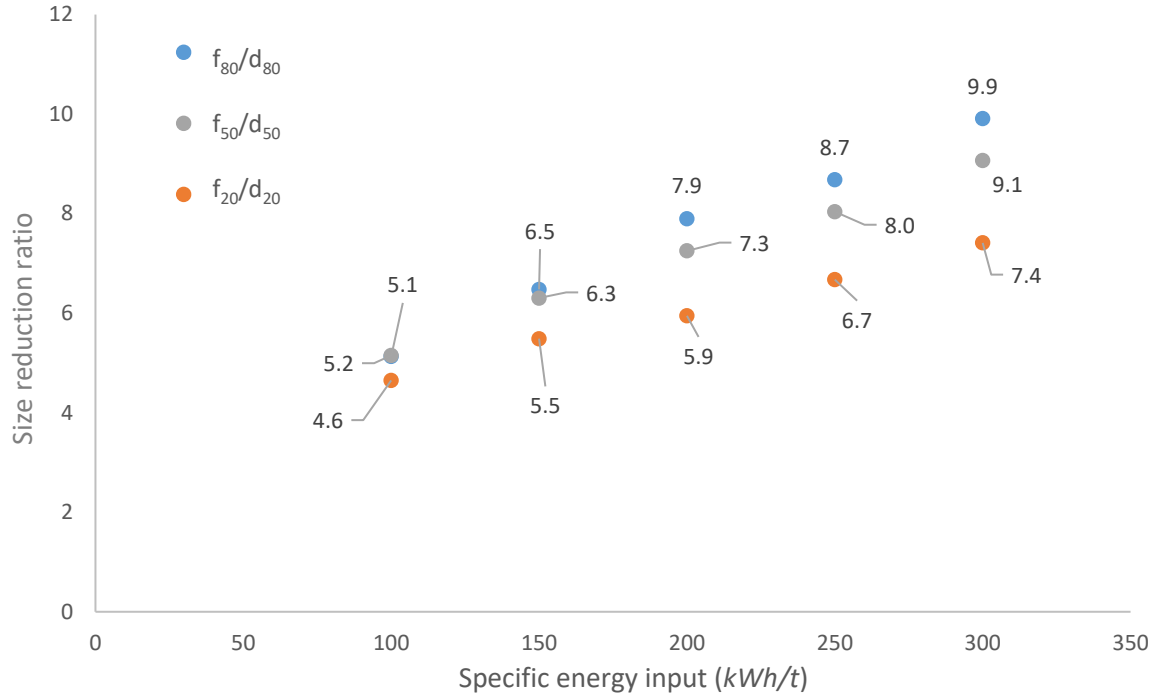

Fig. 4-2. Size reduction ratio (f_{80}/d_{80}, f_{50}/d_{50}, f_{20}/d_{20}) at specific energy input 100~300 kWh/t.

When the Steepness Factor d_{50}/d_{20}) is less than 2, the size distribution is described as "narrow" indicating a highly uniform size distribution of the product which is useful for many applications. The details of the SF and PSD width are illustrated in Fig. 4-3. The value of d_{50}/d_{20} decreases slightly from 1.7 at the specific energy input 100 kWh/t to 1.6 at 300 kWh/t. The difference is not obvious but it remains stable under 2 indicating a highly narrow size distribution of the product. The PSD width (d_{90}/d_{10}) clearly declines and this implies the particle size becomes more uniform with increasing the specific energy input.

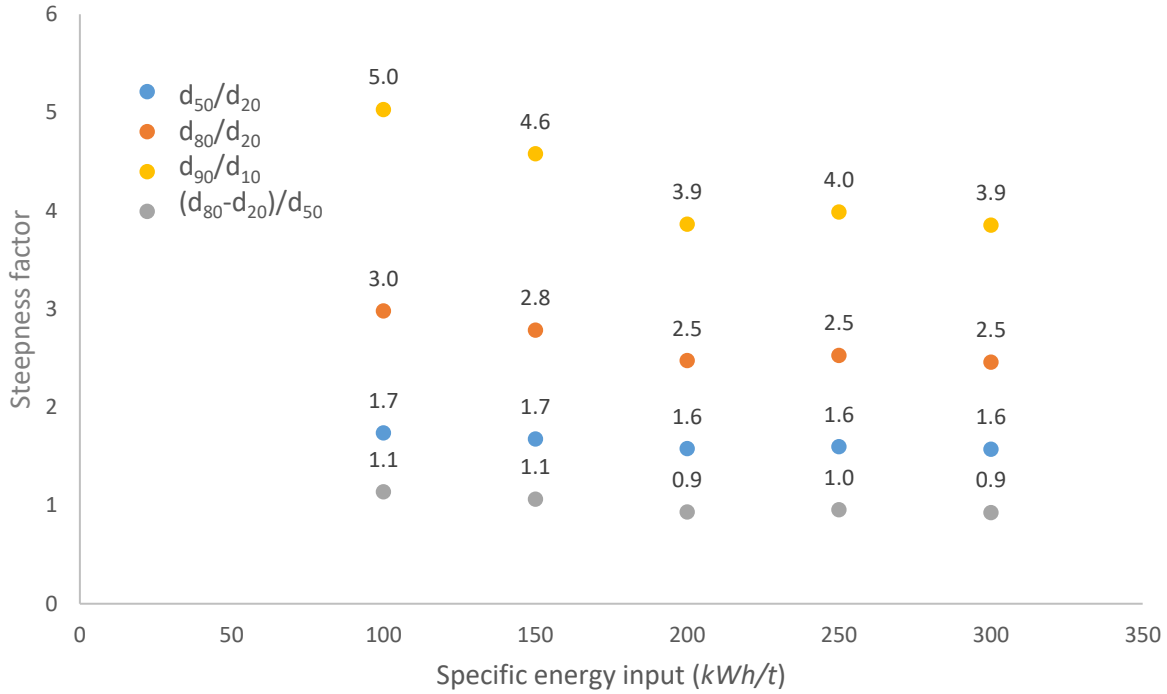

Fig. 4-3. SF and PSD width values d_{90}/d_{10}, $(d_{90}\text{-}d_{10})/d_{50}$ at the specific energy input 100~300 kWh/t.

The specific energy input is a quantity indicating the energy consumed over the unit mineral weight. This is more meaningful and direct than the total grinding time at revealing the relationship between the product size and the energy consumption. In this study, the results are normally analysed at the same specific energy input unless otherwise stated.

4.3.2. Influence of rotational speed

The rotational speed of the stirrer is an important variable affecting both power draw and product size. So far, there has been no generic conclusion to describe the influence of the rotational speed on the mill efficiency. A higher tip speed may not result in finer product and vice versa. Unlike the ball mill, the rotational speed of a vertical mill is no longer limited by the mill critical speed and gravity. The vertical stirred mill has more flexibility in the

variation of the speed range. The experiments with a wide range of the rotational speed are essential to achieve the optimal operating conditions.

Table 4-2. The details of product d_{80} obtained at V_t=5.23, 6.54, 7.85 and 9.81 m/s using Carbolite grinding media size +0.8-1.2 mm (75 % (w/w) solids concentration).

Tip speed (m/s)	5.23		6.54		7.85		9.81	
Specific Energy (kWh/t)	d_{80} (μm)	*SD* (σ)	d_{80} (μm)	*SD* (σ)	d_{80} (μm)	*SD* (σ)	d_{80} (μm)	*SD* (σ)
100	6.7	0.21	6.3	0.14	5.9	0.89	5.2	0.21
150	4.6	0.15	4.1	0.13	4.3	0.08	4.1	0.14
200	3.2	0.05	3.3	0.06	3.6	0.03	3.4	0.05
250	2.8	0.03	2.9	0.05	3.1	0.11	3.0	0.11
300	2.5	0.09	2.6	0.11	2.8	0.06	2.7	0.07

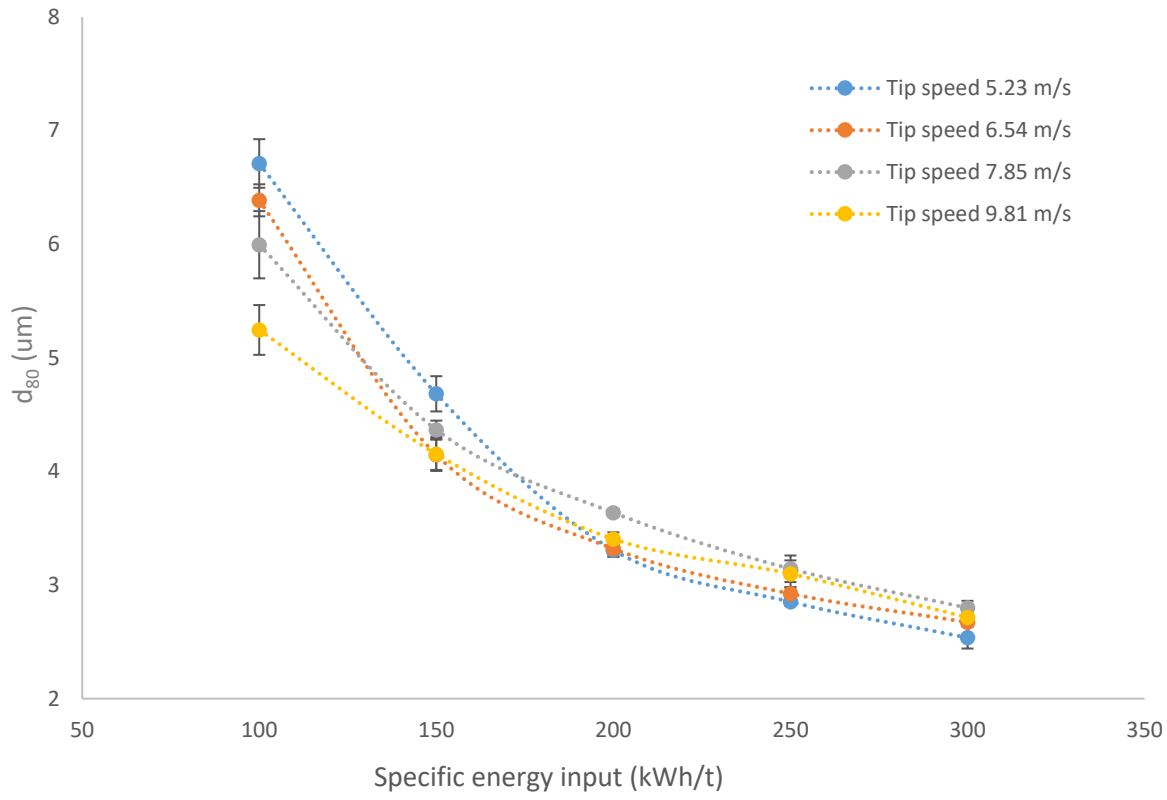

Fig. 4-4. The values of product d_{80} are compared at V_t=5.23 m/s, 6.54 m/s, 7.85 m/s and 9.81 m/s using Carbolite size +0.8-1.2 mm (75 % (w/w) solids concentration*).*

The experiments were conducted using Carbolite grinding media (size +0.8-1.2 mm). The slurry was mixed at 75 % (w/w) solids concentration. The rotational speed range was tested from 800~1500 RPM corresponding to V_t= 5.23~9.81 m/s. The samples of the product were measured at the specific energy input 100, 150, 200, 250 and 300 kWh/t separately to avoid influence of the energy input. The detailed d_{80} of the product is listed in Table 4-2. The evolution of d_{80} at different tip speed is plotted in Fig. 4-4.

At the specific energy input 100 kWh/t, the finest product is obtained at the highest tip speed V_t=9.81 m/s with d_{80}=5.2 μm. The coarsest product is d_{80}=6.7 μm obtained at the lowest tip speed V_t=5.23 m/s as shown in Table 4-2. This implies that the finer product size is obtained using a higher tip speed due to the stronger collision intensity when specific energy input is not very large (below 150 kWh/t). For the low energy input, the grinding time is short, fast rotational speed is more helpful in reducing the product size.

The d_{80} of the product obtained at V_t= 5.23 m/s drops significantly in the specific energy input range 150~250 kWh/t. In the range 200-300 kWh/t, the finest product is obtained at the lowest tip speed V_t=5.23 m/s. At 300 kWh/t the product obtained at V_t= 5.23 m/s shows the finest product with d_{80}=2.5 μm. The values of d_{80} obtained at V_t= 6.54 m/s, 7.85 m/s and 9.81 m/s are 2.6 μm, 2.8 μm and 2.7 μm respectively. This is interesting to note that when the specific energy put is increased (larger than 200 kWh/t) a lower tip speed is more efficient in reducing the product size.

The tip speed directly affects the grinding time. The faster tip speed means the less time to reach the same specific energy input. The details of grinding time measured at different tip speed are listed in Table 4-3. To reach the specific energy input 300 kWh/t, it takes 44.1 minutes at V_t=9.81 m/s. This grinding time is 6, 20 and 50 minutes quicker than the grinding

time measured at V_t=7.85 m/s, 6.54 m/s and 5.23 m/s respectively. Although the finest product is obtained at the lowest tip speed V_t=5.23 m/s, but the difference over the product size of d_{80} is within 0.2 μm.

Table 4-3. The grinding time consumed at V_t=5.23 m/s, 6.54 m/s 7.85 m/s and 9.81 m/s to obtain the same specific energy input using Carbolite +0.8-1.2 mm (75 % (w/w) solids concentration).

Specific Energy (kWh/t)	100	150	200	250	300
V_t (m/s)	Time (min)	Time (min)	Time (min)	Time (min)	Time (min)
5.23	30.8	46.3	61.5	77.2	94.5
6.54	23.1	34.4	46.0	58.2	70.7
7.85	17.1	25.7	34.3	42.5	50.9
9.81	16.0	23.8	29.4	38.2	44.1

A higher tip speed means a larger instantaneous power draw. Hence, it takes a shorter time to achieve the same specific energy input at a higher tip speed (see Table 4-3). Ouattara and Frances (2014) also studied the effect of tip speed and pointed out that a higher tip speed would reduce grinding time but with no significant improvement on the product fineness. At a lower tip speed, if the same specific energy is supplied, it could also generate similar PSD than a higher tip speed.

In fact, when the specific energy input is not very high (< 150 kWh/t), the improvement over the product size by using a higher tip speed is evident as shown in Fig. 4-4. When the energy input is greater than 150 kWh/t, there is no clear difference over the product size when using a higher tip speed. A lower tip speed can also produce the same fineness of the product as a higher speed. However, it takes a much longer time with a lower tip speed to reach the same amount of energy input. This it undoubtedly will greatly reduce the throughput of the product.

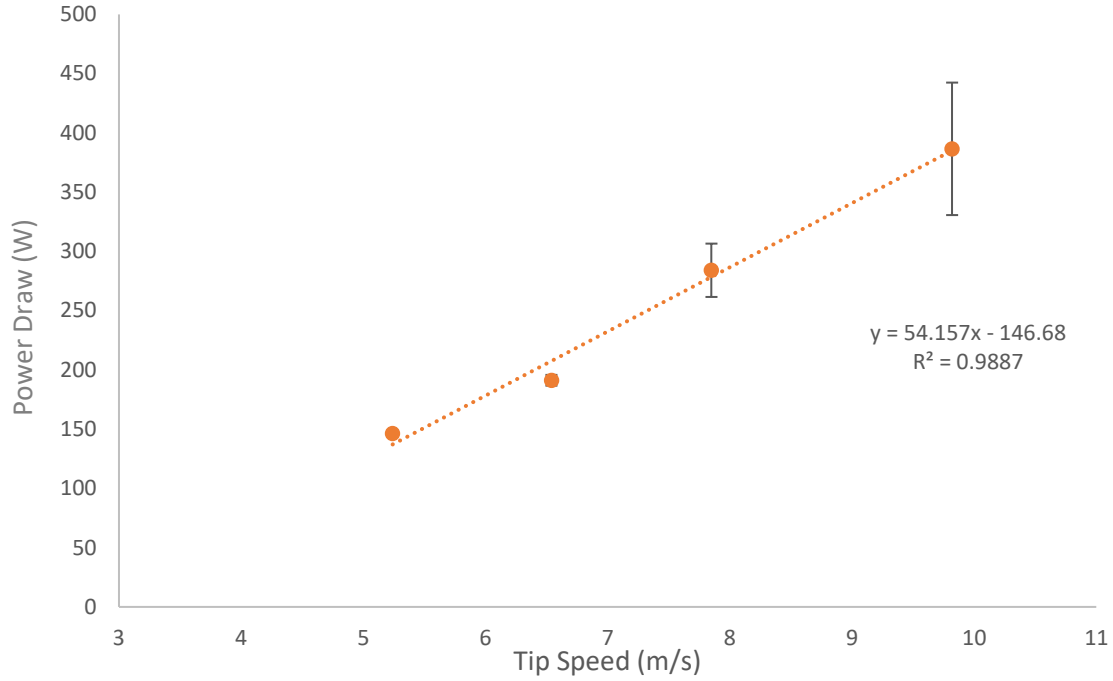

Fig. 4-5. The relationship between the instantaneous power draw and the tip speed using Carbolite grinding media size +0.8-1.2 mm (75 % solids concentration).

Fig. 4-5 shows a linear relationship between the instantaneous power draw and the tip speed. The power draw is 146 W at V_t=5.23 m/s. By increasing the tip speed, the power draw is rapidly increased to 386 W at V_t=9.81 m/s. The instantaneous power draw is increased more than twice by simply increasing the tip speed from 5.23 m/s to 9.81 m/s. At a unit time, more energy is drawn from the stirrer to the mill when a higher tip speed is applied. When the specific energy is identical, a higher tip speed is apparently more efficient.

4.3.3. Solids concentration

Solids concentration is another important variable affecting the grinding process. Moys (2015) stated that a highly viscous slurry is more likely to reduce the relative velocity (slip velocity) of the grinding media compared to a less viscous slurry. When two grinding media particles approach each other, the viscous slurry will fill into the area between two media particles diminishing the relative speed. It has been expected to minimise this barrier effect

as much as possible, because the particles in a stirred mill are mainly broken via this contact. During the contact, shear stress occurs and a small bit of the particle is taken off. Repeatedly, a finer particle is obtained. This mechanism is unlike a tumbling ball where the impact force (due to cascading of balls) is the main force to break the particles (He et al., 2004).

Table 4-4. Details of d_{80} at 50 %, 65 % and 75 % (w/w) solids concentration.

Energy Input (kWh/t)	100		150		200		250		300	
Solid loading	d_{80} (μm)	*SD* (σ)	d_{80} (μm)	*SD* (σ)	d_{80} (μm)	*SD* (σ)	d_{80} (μm)	*SD* (σ)	d_{80} (μm)	*SD* (σ)
50 %	5.3	0.05	3.6	0.04	2.8	0.06	2.4	0.05	2.1	0.01
65 %	6.8	0.08	4.9	0.47	4.0	0.49	3.5	0.85	2.7	0.10
75 %	7.7	0.27	5.7	0.15	4.3	0.06	3.6	0.07	3.2	0.04

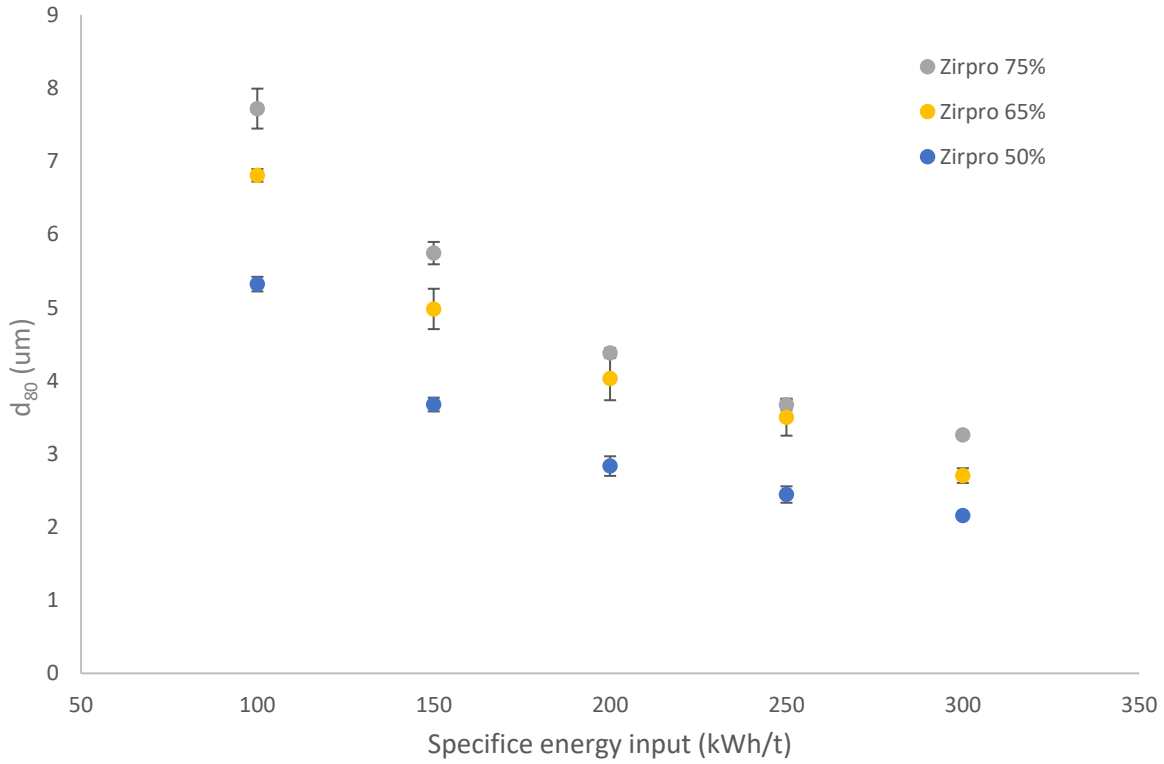

Fig. 4-6. The product d_{80} obtained at solids concentration 50 %, 65 % and 75 % (w/w) against the specific energy input (Measured by ZirPro size +0.7-1.4 mm at tip speed 6.54 m/s).

The effect is evaluated by comparing the product d_{80} at different levels of the solids concentration. The experiment was conducted with ZirPro grinding media size +0.7-1.4 mm at a constant V_t=6.54 m/s. The sample was tested at the specific energy inputs of 100, 150, 200, 250 and 300 kWh/t. The details of d_{80} are illustrated in Table 4-4. The corresponding variation of d_{80} is plotted in Fig. 4-6.

At the specific energy input 100 kWh/t, the finest product size d_{80}=5.3 μm is obtained at 50 % (w/w) solids concentration. This product size is much finer than the product size d_{80}=6.8 μm and d_{80}=7.7 μm obtained at 65 % and 75 % (w/w) solids concentration respectively. When the specific energy reaches 300 kWh/t, the d_{80} obtained at 50 % (w/w) solids concentration lowers significantly to 2.1 μm. The finest product is obtained at the lowest solids concentration compared to d_{80}=2.7 μm and d_{80}=3.2 μm obtained at 65 % and 75 % (w/w) solids concentration respectively.

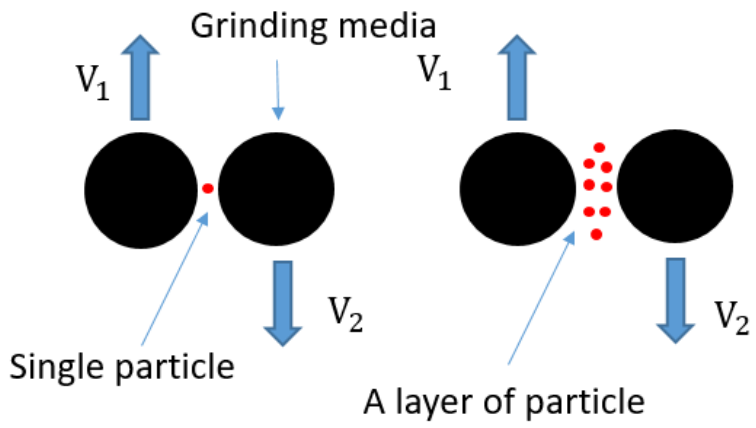

Fig. 4-7. A single particle captured by grinding media and a layer of particle captured by grinding media.

The results indicate that a slurry with a higher solids concentration produces coarser product when the specific energy input is identical. When the solids concentration is very

high, it enhances the probability for the mineral particles to be nipped by the grinding media, but it may not necessarily result in improvement of the effective breakage of single particle. Many particles are likely to stick together and form a packed layer between the gap of the two grinding media beads (see Fig. 4-7). At the same stress force, it is more difficult to break a layer of the particles instead of a single or fewer particles for a single stress event.

Ouattara and Frances (2014) found a different trend and reported that a higher solids concentration is helpful for a finer particle size. In their study, the samples were milled at a much lower range of solids concentration (0.3- 0.05 % w/w). At such low solids concentration, the probability that a particle captured by grinding beads may play a dominant role is increased. Increasing solids concentration undoubtedly enhances the opportunity for mineral particle to be trapped by the grinding media. Thus, a higher solids concentration may yield a finer product under these specific conditions. In this study, the solids concentration of the slurry is much higher and an opposite phenomenon is observed.

4.3.4. Grinding media size

Ohenoja et al. (2013) pointed out that the target particle size is approximately 1/1000 of the grinding media size. For example, given an average product size 2 μm, the grinding media size is approximately 2 mm. This experimental theory is a useful guidance in the preliminary estimation of grinding media size.

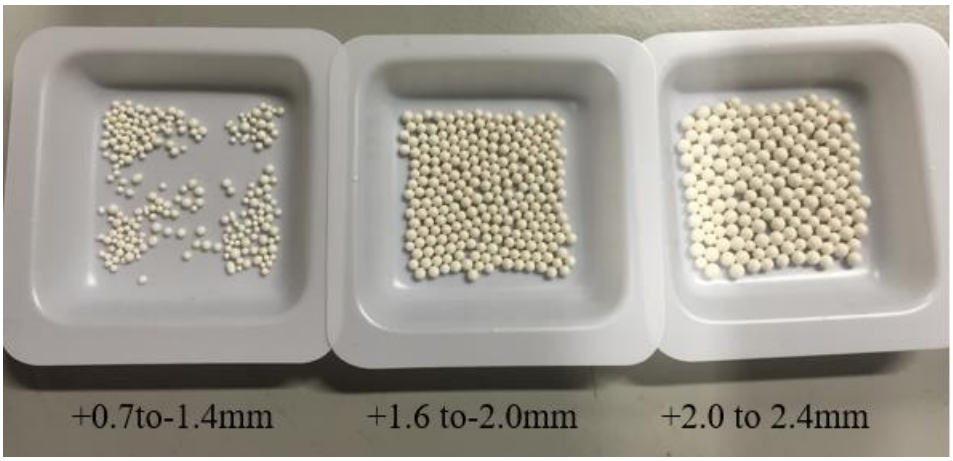

Fig. 4-8. ZirPro grinding media size range +0.7-1.4 mm, +1.6-2.0 mm and +2.0-2.4 mm.

The control experiments were conducted via 3 different ZirPro grinding media size ranges: +0.7-1.4 mm, +1.6-2.0 mm and +2.0-2.4 mm (see Fig. 4-8). The samples were ground at V_t= 6.54 m/s and 65 % (w/w) solids concentration. The product d_{80} obtained with different size of ZirPro grinding media is listed in Table 4-5. Overall, a finer grinding product is obtained with a smaller bead diameter. The comparable trends are plotted in Fig. 4-9.

As seen from Table 4-5, d_{80} of the finest product is 2.0 μm at the specific energy input 300 kWh/t using ZirPro grinding media size +0.7-1.4 mm. The coarser product, of which d_{80}=2.4 μm and d_{80}=2.8 μm are obtained using ZirPro size +1.6-2.0 mm and ZirPro size +2.0-2.4 mm respectively. The smaller grinding media size proves to be more efficient when the other operating conditions are identical. This implies that less specific energy is utilised to obtain the specific product fineness if the grinding media size is smaller.

Table 4-5. The product d_{80} obtained using ZirPro grinding media size +0.7-1.4 mm, +1.6-2.0 mm and +2.0-2.4 mm at tip speed 6.54 m/s and 65 % solids concentrations.

Energy Input (kWh/t)	100		150		200		250		300	
Size (mm)	d_{80} (μm)	*SD* (σ)	d_{80} (μm)	*SD* (σ)	d_{80} (μm)	*SD* (σ)	d_{80} (μm)	*SD* (σ)	d_{80} (μm)	*SD* (σ)
+0.7-1.4	4.1	0.07	3.1	0.022	2.6	0.020	2.4	0.07	2.0	0.07
+1.6-2.0	5.3	0.23	3.9	0.149	3.0	0.102	2.7	0.07	2.4	0.03
+2.0-2.4	6.6	0.33	4.7	0.071	4.2	0.182	3.5	0.05	2.8	0.11

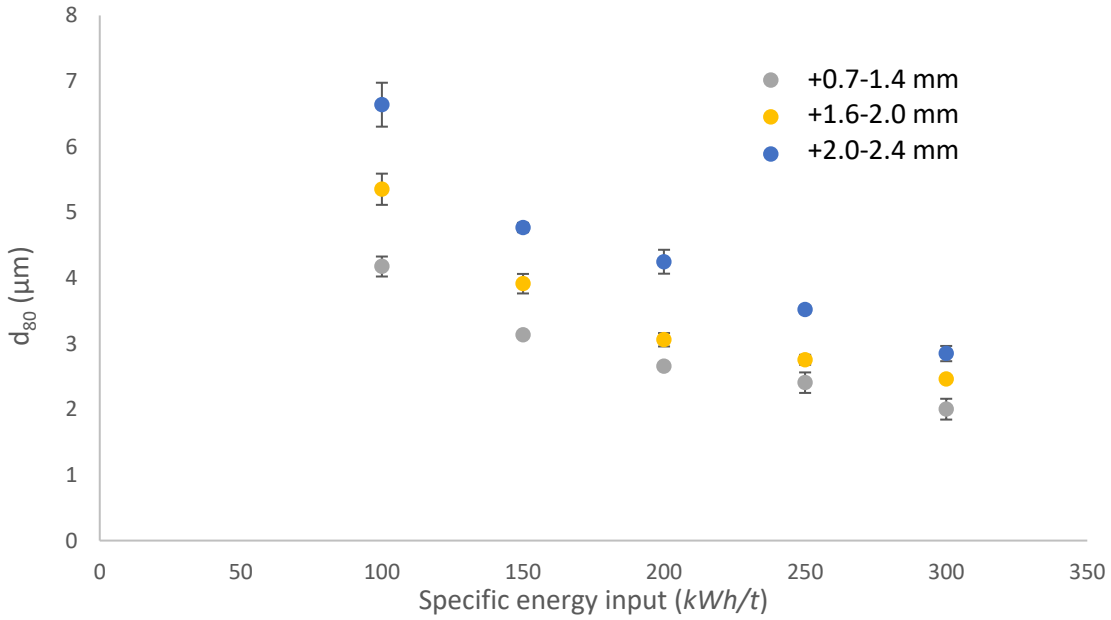

Fig. 4-9. The product d_{80} obtained at ZirPro grinding media size ranges +0.7-1.4 mm, +1.6-2.0 mm and +2.0-2.4 mm.

Comminution is a high energy and costly process. Any small improvement would save a large amount of the energy at industrial scale. For example, if the product d_{80} is required to be 3 μm, the grinding media size +0.7-1.4 mm clearly saves the specific energy input up to 50 kWh/t and 150 kWh/t compared to the grinding media size +1.6-2.0 mm and +2.0-2.4 mm respectively as seen from Fig. 4-9.

Altun et al. (2013), Jankovic et al. (2003), Wang and Forssberg (2000) and Kwade et al. (1996) investigated the impact of grinding media size using either vertical or horizontal stirred media mill. They also found that the finer grinding media size is more efficient.

The finer grinding media size would also improve the flow-ability of the charge. Less kinetic energy will be wasted purely as heat caused by the attrition between the grinding media. However, if the grinding media is too small, an effective collision is more difficult to happen. Thus, it is important to determine a correct size for the specific grinding process. In the study, the grinding media size is much greater than the particle size (approximately 1000 times). In this case, flow-ability plays a more important role. A smaller size of the grinding media demonstrates a higher efficiency as a finer product is obtained at the same specific energy input.

4.3.5. Influence of dispersant

The DLVO theory (Deryaguin and Landau, 1941; Verwey and Overbeek, 1948) described how particles interact under the effect of two opposing forces: electrostatic repulsion and van der Waals attraction. The theory assumes that the effect of two forces are additive and the relationship is shown in Fig. 4-10.

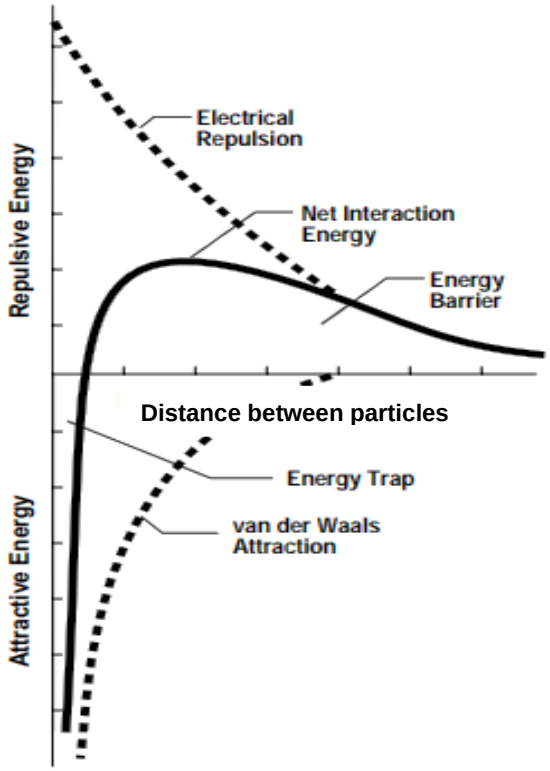

Fig. 4-10. The relationship between electrical repulsion and van der Waals attraction (Ravina and Moramarco, 1993).

When the distance between particles is reduced, the absolute values of both electrostatic repulsion and van der Waals attraction are increased significantly. The increasing rates of these two forces are not the same and greatly depend on the distance. When the distance is far, the effect of electrostatic repulsion is greater than van der Waals attraction. The particles will not agglomerate at this distance. Energy is required to overcome this repulsion and the level of energy required increases as the particles are driven closer and closer. With decreasing of the distance, the effect of van der Waal gradually becomes greater than electrostatic repulsion and particles are attractive to each other. Before this occurs, sufficient kinetic energy is required to overcome the energy barrier. The effect of

electrostatic repulsion can be efficacity modified by adding a small amount of the chemical dispersants (Ravina and Moramarco, 1993).

To improve the grinding efficiency, there are many available chemical dispersants being applied into the grinding process. An appropriate dosage of the dispersant could efficiently prevent flocculation by altering the electrostatic on the particle surface via covering Polyelectrolyte-based dispersants (Greenwood et al., 2002). Particularly, when the high solids concentration is applied, adding appropriate dosage of the dispersant can greatly reduce the slurry viscosity. However, excess dispersant will increase the viscosity of underlying medium (water) and significantly drop the energy barrier eventually causing flocculation.

For the vertically stirred media mill, the study of dispersant dosage is rare for calcium carbonate and its effect on grinding mechanism is complicate. Attrition force between the grinding media and mineral particle is essential for breakage in a stirred media mill. The breakage mainly depends on but is not limited to the shear force. The presence of optimal dosage of dispersant may improve the fluidity of the particle by reducing the viscosity of the slurry. In this case, the shear stress may decline and fail to generate sufficient force for the breakage.

To study the influence of the dispersant in a stirred media mill, the product size obtained at the dispersant concentrations 0.8 %, 2.5 %, 5 % and 10 % (w/w) were investigated. The minimum level of the dispersant was set at 0.8 % in line with Imerys standard operating conditions. The dispersant concentration is based on the total dry weight of the mineral. The dispersant type is Sokalan CP 6340 (main composition: acrylic acid) supplied by BASF.

The experiments were conducted at V_t=7.85 m/s. The solids concentration was fixed at 65%. ZirPro grinding media size +0.7-1.4 mm was applied.

Table 4-6. d_{80} values obtained at different levels of the dispersant.

Specific Energy Input (kWh/t)	100		150		200		250		300	
Concentration (%)	d_{80} (μm)	*SD* (σ)	d_{80} (μm)	*SD* (σ)	d_{80} (μm)	*SD* (σ)	d_{80} (μm)	*SD* (σ)	d_{80} (μm)	*SD* (σ)
0.8	5.6	0.15	3.7	0.28	2.9	0.06	2.5	0.03	2.2	0.03
2.5	5.7	0.20	3.8	0.08	3.3	0.01	2.8	0.02	2.5	0.02
5.0	6.1	0.24	4.5	0.08	3.6	0.04	3.2	0.02	2.8	0.06
10.0	9.0	0.09	6.2	0.11	5.4	0.14	4.3	0.05	3.6	0.05

The details of the product d_{80} are listed in Table 4-6. It is interesting to note that the coarser product is obtained at a higher dispersant concentration. It appears that the increase in dispersant dosage decreases the product fineness. The finest product is obtained at the dispersant concentration 0.8 % (w/w). At 100 kWh/t, the product with dispersant concentration 10 % (w/w) is d_{80}=9.0 μm while the product ground at 0.8 % (w/w) is d_{80}=5.6 μm. At 300 kWh/t, the product obtained at 0.8 % (w/w) dispersant is d_{80}=2.2 μm which is still smaller than the results obtained at dispersant concentration 2.5 %, 5 % and 10 % (w/w).

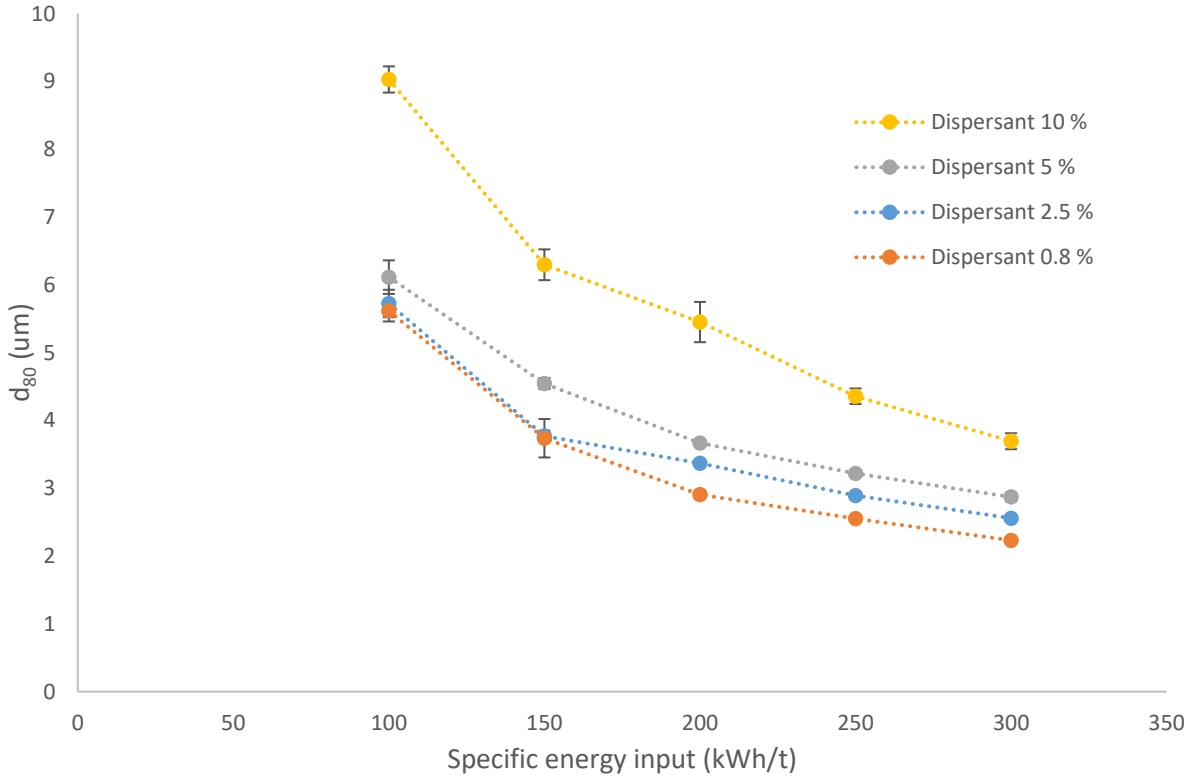

Fig. 4-11. The product d_{80} obtained at dispersant concentrations 0.8 %, 2.5 %, 5 % and 10 % (w/w) at V_t=7.85 m/s (ZirPro grinding media size +0.7-1.4 mm).

Fig. 4-11 illustrates the variation of product d_{80} as a function of the specific energy input at the dispersant dosages of 0.8 %, 2.5 %, 5 % and 10 % (w/w). It can be seen from this graph that increasing the dosage of dispersant resulted in a coarser particle size. The phenomenon has also been reported in the work by Öksüzoğlu and Uçurum (2016) and Zheng et al. (1997). This behaviour is probably caused by the following reasons. The dispersant diminishes the strength of attrition. Compared to water, dispersant (an organic polymer) could greatly enhance the flow-ability by reducing the interaction force such as Van der Waals attractive force between the particles. Less attractive force implies the shear stress between the particles is also decreased. The size reduction of particle in a stirred media mill greatly depends on the shear stress. The attrition with insufficient shear stress is not helpful in improving the grinding efficiency.

4.3.6. Application on wollastonite and perlite

For each type of mineral, a unique comminution result might be expected as the physical properties (e.g. density, hardness or crystal morphology) are not identical. A vertically stirred media mill is capable of coping with the differences in various mineral properties. As well as calcite, perlite and wollastonite were selected to be tested in the laboratory scale mill. These two minerals are often used as construction materials or a raw material in the pigment industry.

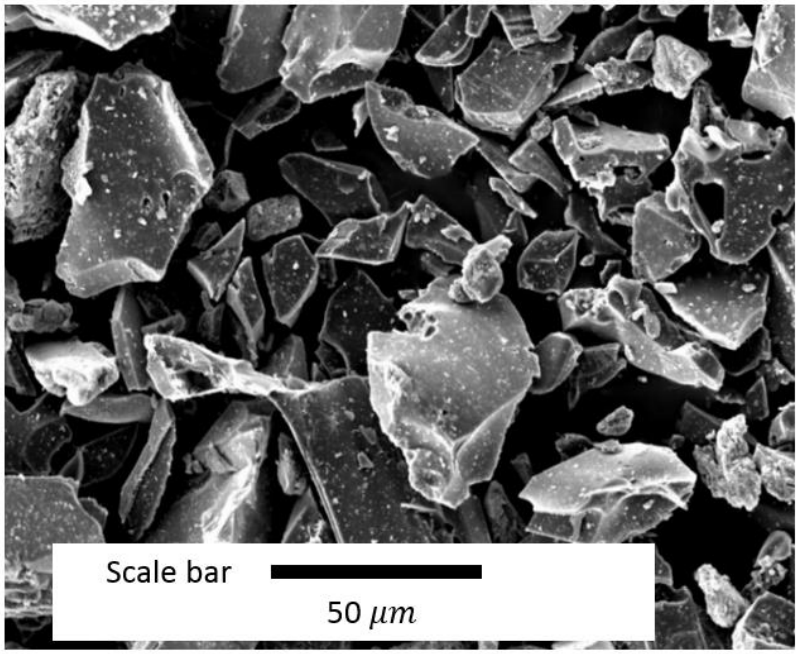

Fig. 4-12. SEM photograph for feed perlite at length scale 50 µm.

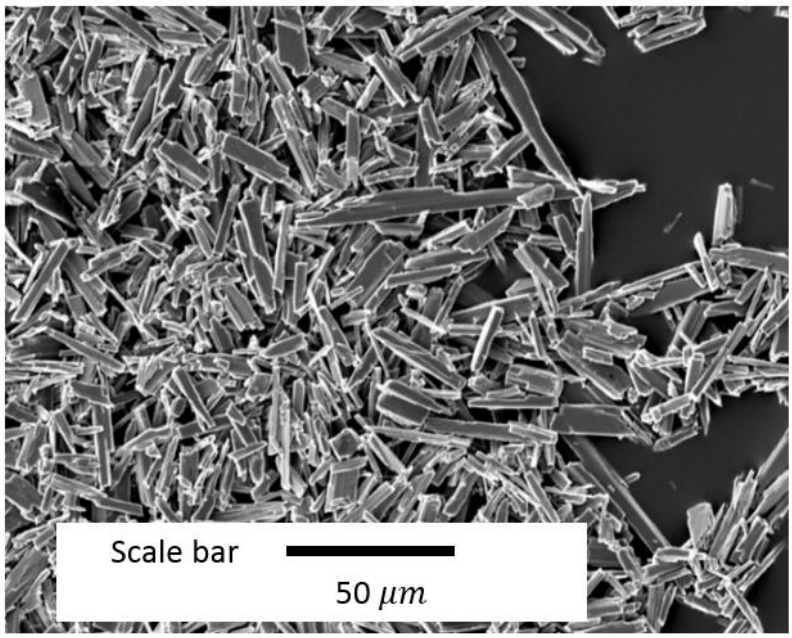

Fig. 4-13. SEM photograph for feed wollastonite at length scale 50 µm.

Fig. 4-12 and Fig. 4-13 exhibit SEM photographs of the feed samples of perlite and wollastonite respectively. Perlite is an amorphous, hydrated glassy volcanic rock of rhyolitic composition. Mohs hardness is 5.5 with a specific gravity 2.2-2.4. The main components are silicon oxide (SiO_2), aluminium oxide (Al_2O_3) and sodium oxide (Na_2O) accounting more than 90 wt %. Its solubility in water is negligible. Perlite is often used as a construction material for ceiling tiles, gypsum boards, lightweight concrete or plasters. The sample of perlite in the study is supplied by Imerys.

Wollastonite is a calcium silicate mineral that contains a small amount of iron, magnesium and manganese substituting for calcium. Mohs hardness is 4.5 to 5.0 with specific gravity 2.86 to 3.09. It is insoluble in water and wollastonite occurs as bladed crystal masses, single crystals can show an acicular particle shape and it exhibits a white colour. Due to its high brightness and whiteness, it is used primarily in ceramics, paint filler and plastics. In

metallurgical applications, wollastonite also serves as a flux for welding, a slag conditioner and to protect the surface of molten metal during the continuous casting of steel.

The experiments were conducted at V_t=7.85 m/s. The solids concentration was at 65% (w/w) and ZirPro grinding media (size +0.7-1.4 mm) was used. The details of product d_{80} as a function of the specific energy are listed in Table 4-7.

Table 4-7. Detailed product d_{80} for perlite and wollastonite.

Specific energy input (kWh/t)	*0*		*100*		*150*	
Size (μm)	f_{80}	*SD (σ)*	d_{80}	*SD (σ)*	d_{80}	*SD (σ)*
Perlite	43.2	0.31	12.6	0.08	10.4	0.01
Wollastonite	76.7	0.21	11.0	0.14	9.7	0.05
Specific energy input (kWh/t)	*200*		*250*		*300*	
Size (μm)	d_{80}	*SD (σ)*	d_{80}	*SD (σ)*	d_{80}	*SD (σ)*
Perlite	9.3	0.01	7.4	0.01	4.9	0.01
Wollastonite	9.1	0.02	8.2	0.18	7.7	0.03

The finest product size of perlite (d_{80}=4.9 μm) and wollastonite (d_{80}=7.7 μm) are obtained at 300 kWh/t. The product size of perlite is finer than wollastonite. It is probably due to the larger feed size for wollastonite compared to perlite.

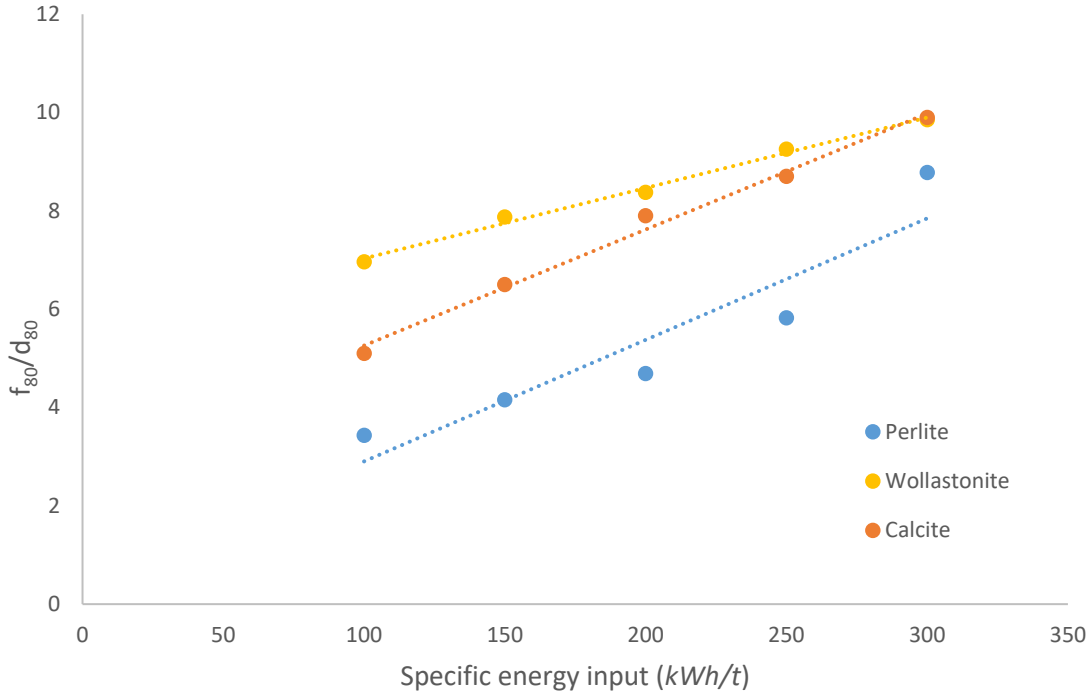

Fig. 4-14. Size reduction ratio f_{80}/d_{80} as a function of the specific energy input (kWh/t) for perlite, wollastonite and calcite.

As seen from Fig. 4-14, the reduction ratio f_{80}/d_{80} of wollastonite is much higher than perlite. It implies for the same amount of energy consumption the mill illustrates better energy efficiency in grinding of wollastonite. The particle size of wollastonite is reduced dramatically from f_{80}=76.7 μm (feed size) to d_{80}=11.0 μm at specific energy 100 kWh/t where the d_{80} is almost the same with perlite. This appears to be mainly caused by the difference in the particle shape as these two minerals have similar density and hardness. A summary of Moh's hardness and density of the mineral calcite, perlite and wollastonite is listed in Table 4-8.

Table 4-8. The Moh's hardness and density of calcite, perlite and wollastonite.

	Moh's hardness	Density (kg/m^3)
Calcite	3.0	2,710
Perlite	5.5	2,200
Wollastonite	4.5	2,870

4.4. Analysis of stirrer configurations

4.4.1. Introduction of stirrer configurations

In this section, the experimental results obtained in the laboratory scale mill with different types of the stirrer are analysed. The performance of these stirrers is analysed through the product size, grinding time and instantaneous power consumption. The photographs of these stirrers are shown in Table 4-9.

Table 4-9. Details of the stirrer types and the top lids tested in the laboratory scale mill.

	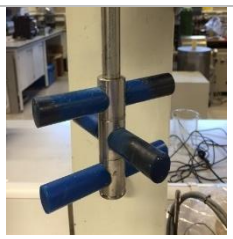		
Stirrer *Type a*	Stirrer *Type a-1*	Stirrer *Type a-2*	Stirrer *Type a-3*
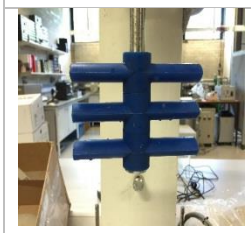	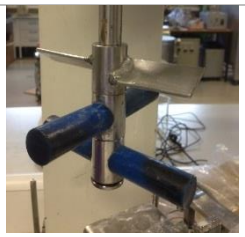		
Stirrer *Type a-4*	Stirrer *Type a-5*	Thick lid (left) and normal lid (right)	

In section 4.4.2, the effect caused by different number of stirrer arms is analysed. The stirrer *Type a*, a typical pin stirrer with 90° offset angle, is the standard design used in the laboratory scale mill. Its performance is compared with the stirrer *Type a-1,* which is based on the configuration of the stirrer *Type a,* but an extra pair of pin arms is added.

In section 4.4.3, the effect of gap distance between the stirrer arms is studied by using the stirrer *Type a-2* and *Type a-3*. *Type a-2* consists of 2 pairs of blade arms with 45° pitched

angle. The distance between the upper and lower arms is 6 cm. *Type a-3* is designed based on *Type a-2*, but the gap distance is reduced to 1.3 cm.

In section 4.4.4, the effect of stirrer orientation is studied by comparing the stirrer *Type a-1* and *Type a-4*. *Type a-4* has the same number of stirrer arms as the type a-1, but it consists of 3 pairs of parallel stirrer arms and the offset angle is 0°.

In section 4.4.5, the performance of the stirrer *Type a-5* which is designed based on *Type a*, but a pair of blade stirrer with 45° pitched angle is added above the pin stirrers. The top blades provide force to pump slurry downwards.

Additionally, a thickness enhanced lid is applied instead of the normal lid to reduce the grinding chamber volume. The results are analysed in section 4.4.6. The thick lid applies top pressure to the suspension and this alters the flow pattern of the slurry by passively compressing the slurry down. This modification aims improving the grinding efficiency through increasing the inner pressure within the grinding chamber.

Barley et al. (2004) reported the flow pattern obtained using the standard stirrer (*Type a*) in a vertically stirred media mill (see Fig. 4-15). It shows that the flow path has an upper circuit and a lower circuit. A vortex shaped free surface is observed around the stirrer shaft. The area where the stirrer locates is defined as impeller band which is assumed to be the field that the particle is intensively ground via abrasion, compression and fracture.

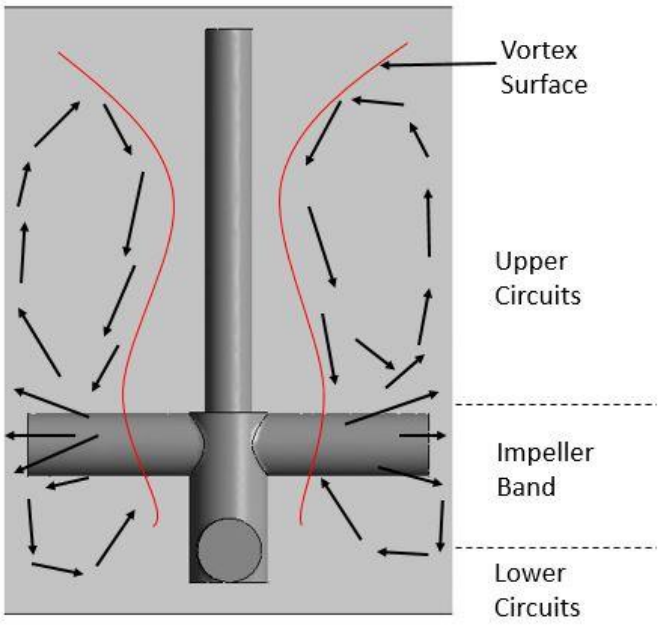

Fig. 4-15. A typical flow path observed using the stirrer Type a (Barley et al., 2004).

Optimisation of the variables (tip speed, solids concentration and grinding media) does little to alter the particle flow behaviour. The wet grinding process in a vertically stirred media mill has many common phenomena with the hydrodynamic mixing process. To explore how the geometry of the stirrer affects the flow behaviour, it is of great importance to explore the impact from the stirrer configuration.

4.4.2. Effect of number of stirrer arms

Based on *Type a*, an extra pair of stirrer arms are added to *Type a-1.* The comparison for *Type a* and *Type a-1* were conducted at rotational speed 1200 RPM (V_t=7.85 m/s). The details of d_{80} obtained using these 2 types of the stirrers are compared in Table 4-10. The d_{80} is measured at 5 levels of the specific energy input 100, 150, 200, 250 and 300 kWh/t. The evolution of d_{80} against the specific energy input is plotted in Fig. 4-16.

Table 4-10. Comparison of d_{80} using the stirrer Type a and Type a-1 at V_t=7.85 m/s (1200 RPM).

Energy Input (kWh/t)	d_{80} *at* V_t= 7.85 m/s			
	Type a (μm)	*SD* (σ)	*Type a-1*(μm)	*SD* (σ)
100	6.7	0.10	4.9	0.09
150	4.9	0.15	4.1	0.24
200	3.8	0.07	3.5	0.09
250	3.3	0.14	2.7	0.01
300	2.8	0.12	2.3	0.09

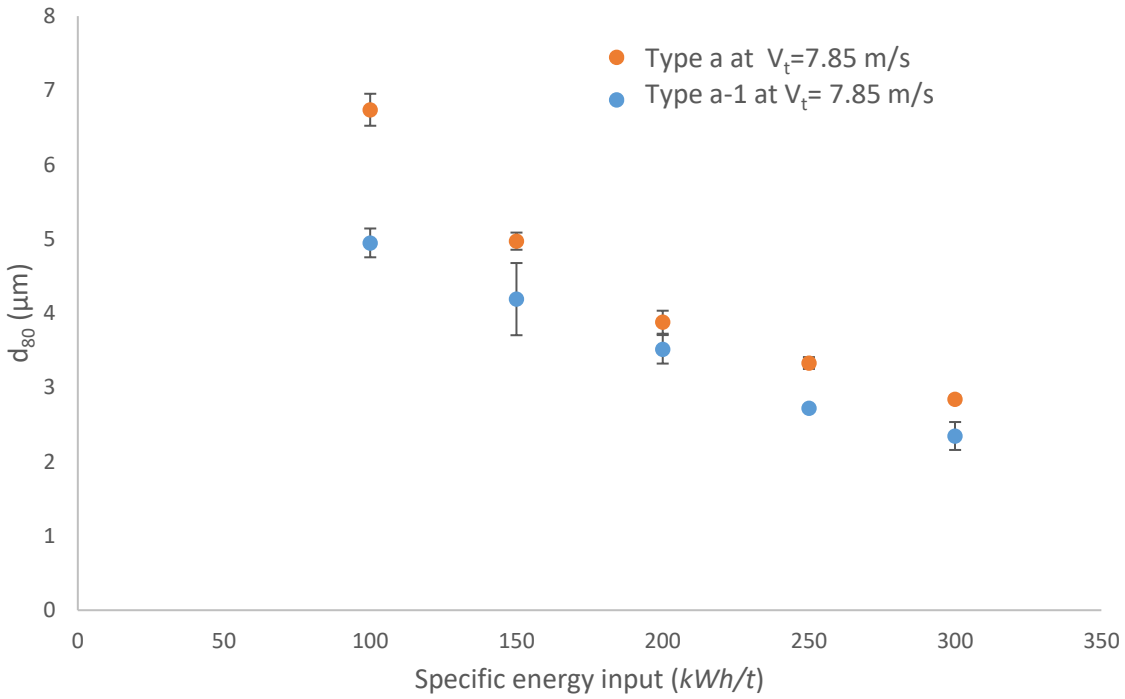

Fig. 4-16. The product d_{80} obtained using the stirrer Type a and Type a-1 at V_t=7.85 m/s (ZirPro grinding media size +0.7-1.4 mm and 65 % solids concentration).

An evident difference in the configuration for *Type a* and *Type a-1* is the number of stirrer arms. The operating conditions are identical for the experiments with both types of the stirrer. At all levels of the specific energy input, the finer product was obtained using the stirrer *Type a-1*.

In a stirred media mill, the predominant mechanism of particle breakage is through two media particles sliding past one another, nipping the particles within the overlap area. This also applies to 2 layers of the grinding media particles sliding past one another (Radziszewski, 2013). This sliding mechanism occurs in the field where a significant velocity difference over the grinding media is observed. In other words, this implies the field where the velocity gradient exists between different particles or layers of particles is an important physical factor directly related to the efficiency of the breakage. The impeller band is the area where the large velocity gradient exists. The velocity gradient is the source for the shear force which is recognised as the most important force for breakage mechanism in a stirred media mill. By increasing the number of the stirrer arms, *Type α-1* significantly increases the effective shear field.

Additionally, the contact surface between the particle and the stirrer surface is another area where this gradient velocity exists. The particles alongside the surface of the stirrer undoubtedly moves faster than the particles further away from the surface. A larger number of the stirrer arms means more contact surface. Thus, the field where the velocity gradient exists can be greatly improved by using the stirrer *Type α-1* compared to the stirrer *Type α*.

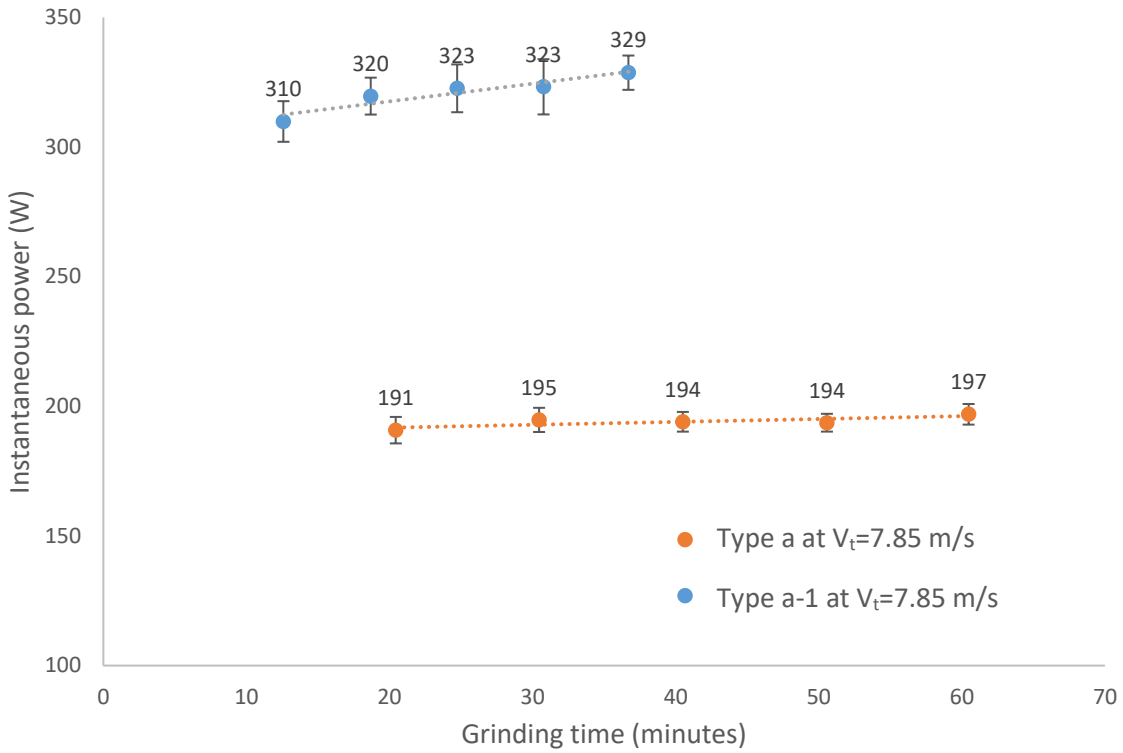

Fig. 4-17. Instantaneous power draw plotted against grinding time using the stirrer Type a and Type a-1 at V_t=7.85 m/s (ZirPro grinding media size +0.7-1.4 mm and 65 % solids concentration).

Although the product size is improved by using the stirrer *Type a-1*, the instantaneous power draw is correspondingly increased. Fig. 4-17 shows the instantaneous power consumption (W) against grinding time (minute) at V_t=7.85 m/s. The instantaneous power is measured directly by a torque sensor. The measured time points are the actual grinding time used to obtain the specific energy input 100, 150, 200, 250 and 300 kWh/t. The data is collected from the time point that the specific energy 100 kWh/t has reached. This is to ensure the system has achieved a dynamic equilibrium state. The recorded power is as accurate as the power used to grind mineral instead of mixing the grinding media and the mineral slurry. At the beginning of each experiment, the mineral slurry was firstly charged into the grinding chamber then followed by the grinding media. Hence, it takes approximately 10~15 minutes to uniformly mix all the materials. During this period, the

recorded power is slightly larger than the real power required to grind the mineral, so it is not necessary to record the data.

As seen from Fig. 4-17, the instantaneous power consumption for the stirrer *Type a-1* reaches 321 W on average comparing to 194 W obtained using the stirrer *Type a*. The additional pair of the stirrer arms has increased the instantaneous power draw by 64 % at V_t=7.85 m/s. This great improvement reduces the overall grinding time from 60 minutes (*Type a)* to 36 minutes (*Type a-1)*.

Although the stirrer *Type a-1* causes higher instantaneous power draw than *Type a*, the specific energy input is identical. In other words, the total energy consumption is identical, thus no extra energy is consumed by using *Type a-1*. Hence, the stirrer *Type a-1* shows better grinding efficiency than the stirrer *Type a* given the finer product size and shorter grinding time.

In ideal circumstances, each trend line should be a horizontal line because the instantaneous power draw should be a stable value when the operating conditions are kept constant during the grinding process. In fact, the water in the slurry will be evaporated when the temperature inside the mill chamber is increased due to the heat generated by the mechanical forces such as friction. Loss of the water essentially increases the solids concentration of the slurry. Correspondingly, the slurry viscosity is slowly increased resulting in greater resistance to the stirrer from the charge. Hence, the instantaneous power gradually increases over the grinding process.

Clearly, the gradient of the trend line using *Type a-1* is steeper than *Type a*. Also, the discrepancy for instantaneous power is larger for *Type a-1* compared to *Type a*. This implies more water is evaporated using *Type a-1* during the grinding process. In the laboratory scale

mill, the variation in instantaneous power draw is within the acceptable range (<6 %). When this modification is applied on the industrial process, it may require supplementary addition of water to maintain a stable instantaneous power draw.

4.4.3. Effect of gap distance

To explore the influence of the gap distance between the stirrer arms, the performance of stirrer *Type a-2* and *Type a-3* are analysed. The gap distance between the stirrer arms for *Type a-2* is 6 cm which is much greater than the gap distance 1.3 cm for *Type a-3.*

Both types include 2 pairs of flat blade stirrers with a pitched angle at 45°. An advantage of the blade type stirrer is to alter the movement direction of slurry and grinding media. When the slurry is stirred by a pin type stirrer, the movement direction of the slurry is arbitrary. The pitched angle for the blade stirrer arm is designed to pump the bottom slurry upwards and the top slurry downwards to strengthen the slurry convention and improve the filling area within the impeller band. The product size obtained using the stirrer *Type a-2* and *Type a-3* are compared in Table 4-11. The evolutions of product d_{80} against the specific energy input for the 2 types are shown in Fig. 4-18.

Table 4-11. Product d_{80} obtained using the stirrer Type a-2 and Type a-3 at V_t=7.85 m/s (1200 RPM).

Energy Input (kWh/t)	d_{80} at V_t=7.85 m/s			
	Type a -2 (μm)	*SD (σ)*	*Type a-3* (μm)	*SD (σ)*
100	4.5	0.22	5.3	0.15
150	4.1	0.08	4.6	0.12
200	2.8	0.03	3.4	0.08
250	2.5	0.04	2.9	0.08
300	2.1	0.06	2.4	0.02

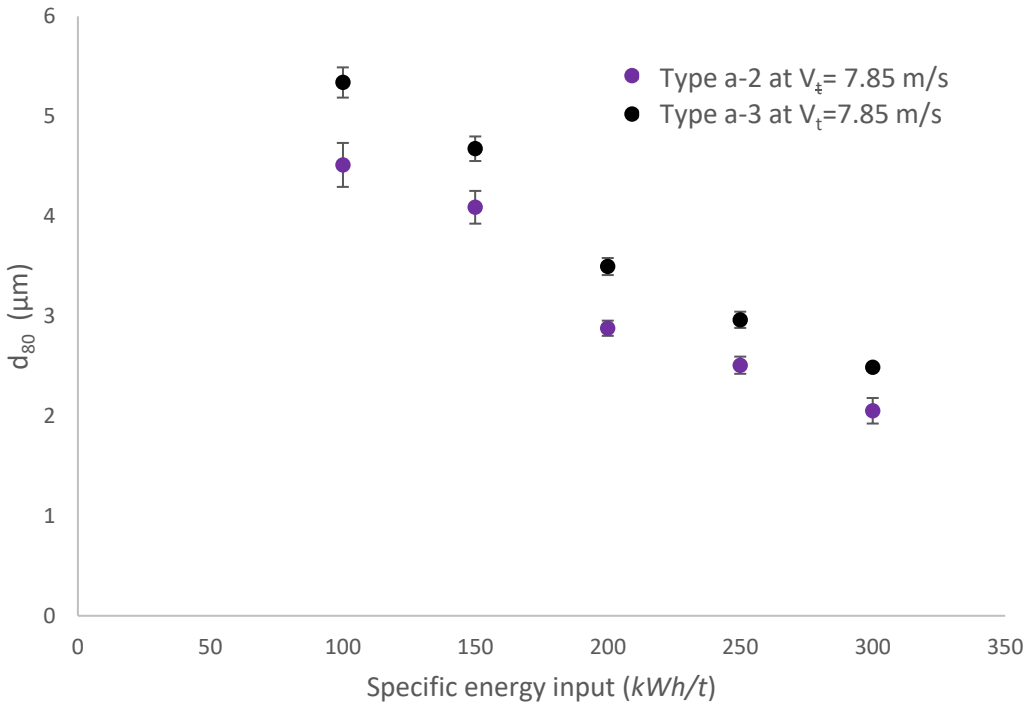

Fig. 4-18. Comparison of product d_{80} obtained using the stirrer Type a-2 and Type a-3 at V_t=7.85 m/s (ZirPro grinding media size +0.7-1.4 mm and 65 % solids concentration).

The design purpose of the stirrer *Type a-2* is to provide sufficient room for the slurry to be retained in the impeller band where the stirrer rotates rapidly. The opposite direction of the upper and the lower flat blade stirrer arms is designed to produce the counter flow of the charge in the impeller band and to cause more intensive collisions. The performance of the stirrer *Type a-2* is compared with *Type a-3* which also has the inline (parallel) layout of the flat blade stirrer arms but the gap distance is significantly reduced.

The product d_{80} obtained using *Type a-2* indicates a finer particle size than the product obtained using *Type a-3* in the range of specific energy input 100~300 kWh/t. When the gap distance is large enough in the impeller band, the slurry is pumped to the chamber bottom by the upper flat blade and it encounters the slurry pushed up from the lower flat blade. The collision of the slurry with two opposite directions of forces undoubtedly is much

more aggressive. *Type a-3* has the same layout as *Type a-2*, but the impact seems less intense as the gap is reduced.

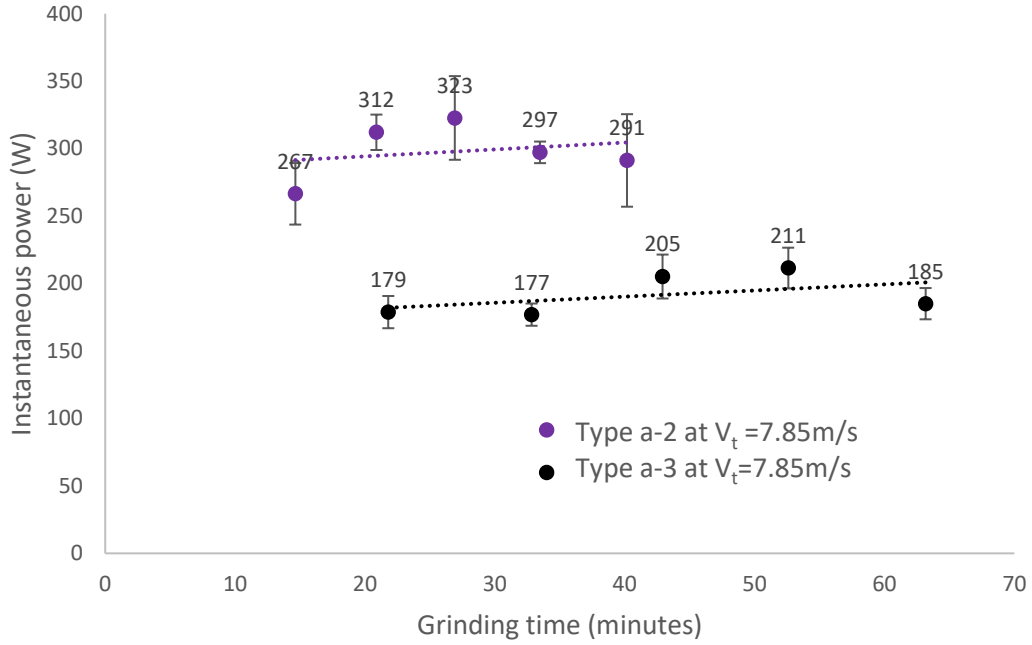

Fig. 4-19. The instantaneous power draw plotted against the grinding time using the stirrer Type a-2 and Type a-3 at V_t=7.85 m/s (ZirPro grinding media size +0.7-1.4 mm and 65 % solids concentration).

The power drawn by the stirrer *Type a-2* and *Type a-3* are shown in Fig. 4-19. The instantaneous power draw using the stirrer *Type a-2* is much greater than the power draw using *Type* a-3. This implies more resistance from the grinding media is encountered by the stirrer *Type a-2*. When the gap distance is increased, the filling of the charge is increased in the impeller band. Thus, more power is consumed to maintain the same tip speed. However, the grinding time to reach 300 kWh/t is greatly reduced from 63 minutes using *Type a-3* to 40 minutes using *Type a-2*. Overall, the variation over the product size and the power using *Type a-2* and *Type a-3* indicates that the grinding performance is closely linked to the flow pattern inside the grinding chamber (Heath et al., 2017).

4.4.4. Effect of stirrer orientation

To study the effect of stirrer orientation (parallel or offset), the product obtained using the stirrer *Type a-4* are compared with the product obtained using *Type a-1* at constant V_t=5.23 m/s (800 RPM). The lower tip speed (V_t=5.23 m/s) is used to avoid the spillage of the slurry because the height of the slurry level will be greatly increased by using the parallel layout with 3 pairs of stirrer arms (*Type a-4*). *Type a-4* is designed based on *Type a-1,* but the stirrer arms of *Type a-4* are set up inline (parallel). The shape of the cross-section is changed from a circle (*Type a-1*) to an elliptic (*Type a-4*) to ensure the charge can flow through the gap between the stirrer arms. Table 4-12 shows the detailed product d_{80} obtained using the stirrer *Type a-1* and *Type a-4* at V_t= 5.23 m/s (800 RPM). The comparison of the d_{80} evolution is shown in Fig. 4-20.

Table 4-12. The details of d_{80} obtained using Type a-1 and Type a-4 at V_t=5.23 m/s.

Energy Input (kWh/t)	d_{80} at V_t=5.23 m/s			
	Type a-1 (μm)	*SD* (σ)	*Type a-4* (μm)	*SD* (σ)
100	5.7	0.09	5.3	0.13
150	4.0	0.24	3.7	0.04
200	3.1	0.09	3.0	0.10
250	2.9	0.01	2.6	0.06
300	2.3	0.09	2.1	0.02

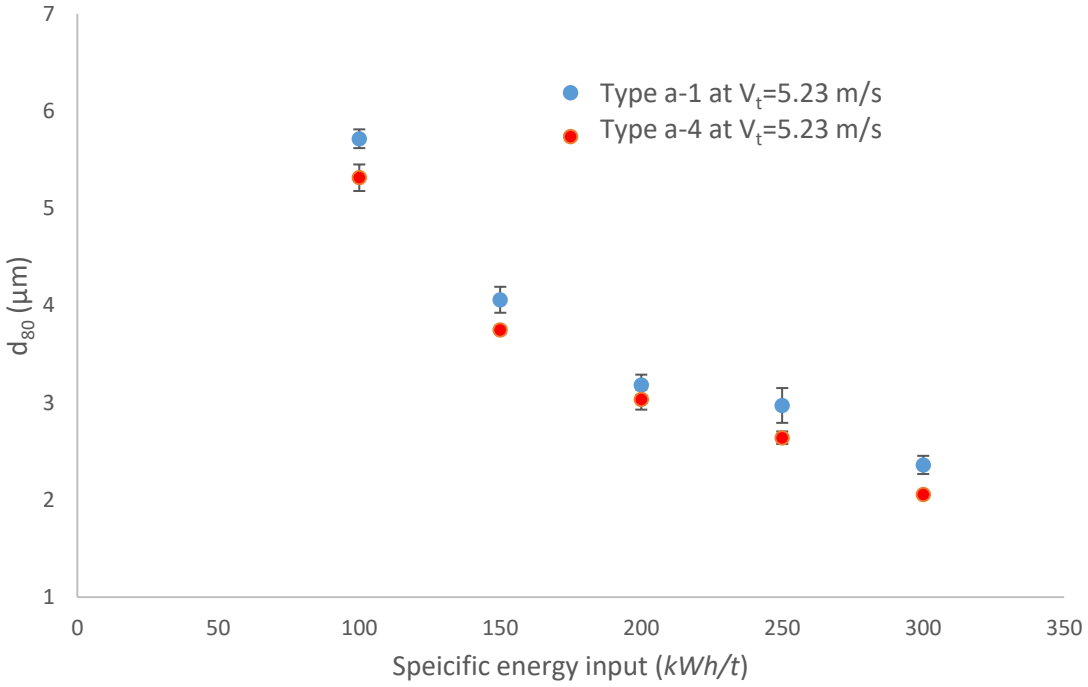

Fig. 4-20. The product d_{80} obtained using the stirrer Type a-1 and Type a-4 at V_t=5.23 m/s (ZirPro grinding media size +0.7-1.4 mm and 65 % solids concentration).

As seen from Fig. 4-20, the product size is slightly improved by using *Type a-4* compared to the results obtained using *Type a-1* in the range of the specific energy input 100~300 kWh/t. When the stirrer *Type a-4* is used, the charge is pushed as a solid block. Abrasion occurs at the surface of the mill chamber. This is believed to be the main source for the shear force. The parallel stirrer layout causes compression when the slurry flows through the narrow gap between the stirrer arms. This probably is the reason that *Type a-4* shows slightly better performance than *Type a-1*.

The measured instantaneous power draw and grinding time are illustrated in Fig. 4-21. The alteration on the stirrer orientation shows very little change on the instantaneous power draw and grinding time. The averaged instantaneous power for using *Type a-4* is 167 W slightly higher than 156 W for using *Type a-1*. The grinding time for achieving the specific

energy input 300 kWh/t is very close, 76 minutes and 73 minutes for *Type a-4* and *Type a-1* respectively.

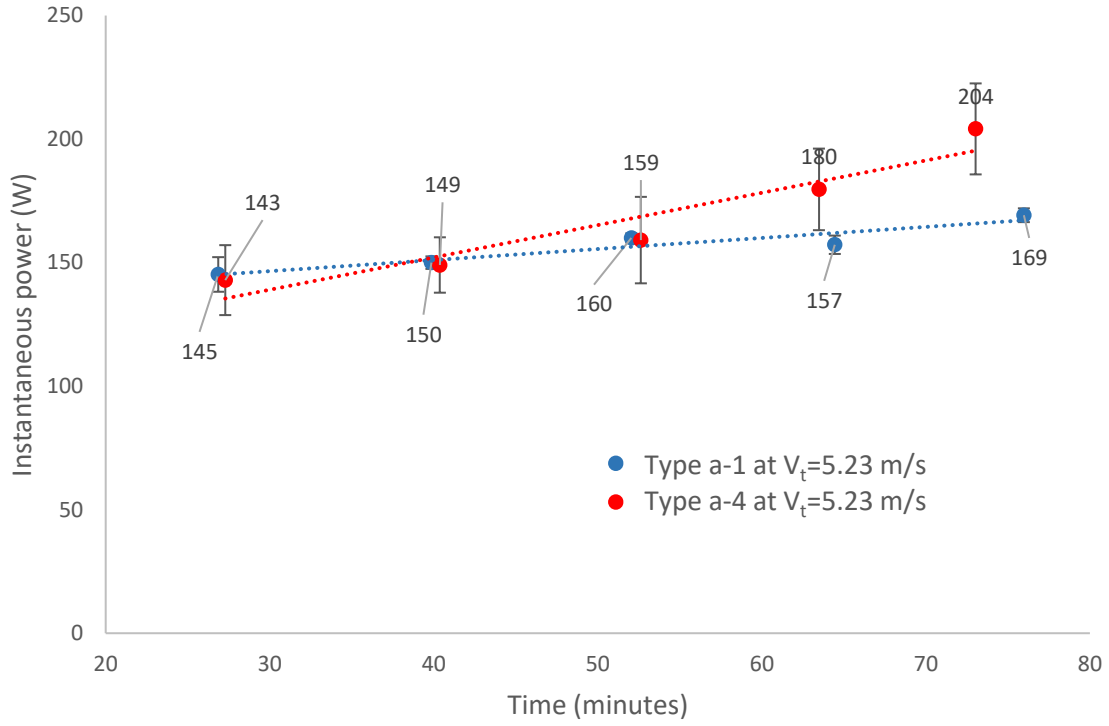

Fig. 4-21. The instantaneous power plotted against the grinding time for stirrer Type a-1 and Type a-4 at V_t=5.23 m/s (ZirPro grinding media size +0.7-1.4 mm and 65 % solids concentration).

The higher discrepancy for *Type a-4* indicates the flow behaviour is not stable in the mill chamber compared to the performance of *Type a-1.* The power trend for *Type a-4* moderately increases with the grinding time. This indicates unstable power draw for stirrer *Type a-4*. *Type a-4* consists 3 stirrer arms as *Type a-1.* Only by changing the stirrer orientation, the grinding efficiency is not significantly improved.

4.4.5. A combination of pin and flat blade stirrers

The design of *Type a-5* is a combination of pin and flat blade stirrers. The upper blade stirrer is expected to generate force to compress the slurry flow down to the bottom of grinding chamber. Under the same operating conditions, *Type a-5* should accelerate the slurry upper circulation compared to the standard stirrer *Type a*. The grinding media is expected to absorb more kinetic energy from the upper blade stirrer arms as the contact surface is significantly increased. The experiments were conducted at V_t=7.85 m/s (1200 RPM) and solids concentration was kept at 65 %. The detailed product d_{80} obtained using *Type a-5* are shown in Table 4-13. The detailed results of product d_{80} obtained using *Type a* are shown in Table 4-10. The trend of product d_{80} using *Type a-5* is compared with product d_{80} obtained using the standard stirrer *Type a* in Fig. 4-22.

Table 4-13. Details of d_{80} using stirrer Type a-5 at V_t=7.85 m/s.

Specific Energy Input (kWh/t)	*Type a-5* at V_t=7.85 m/s	
	d_{80} (μm)	*SD (σ)*
100	5.9	0.04
150	4.2	0.13
200	3.6	0.17
250	3.2	0.05
300	2.6	0.01

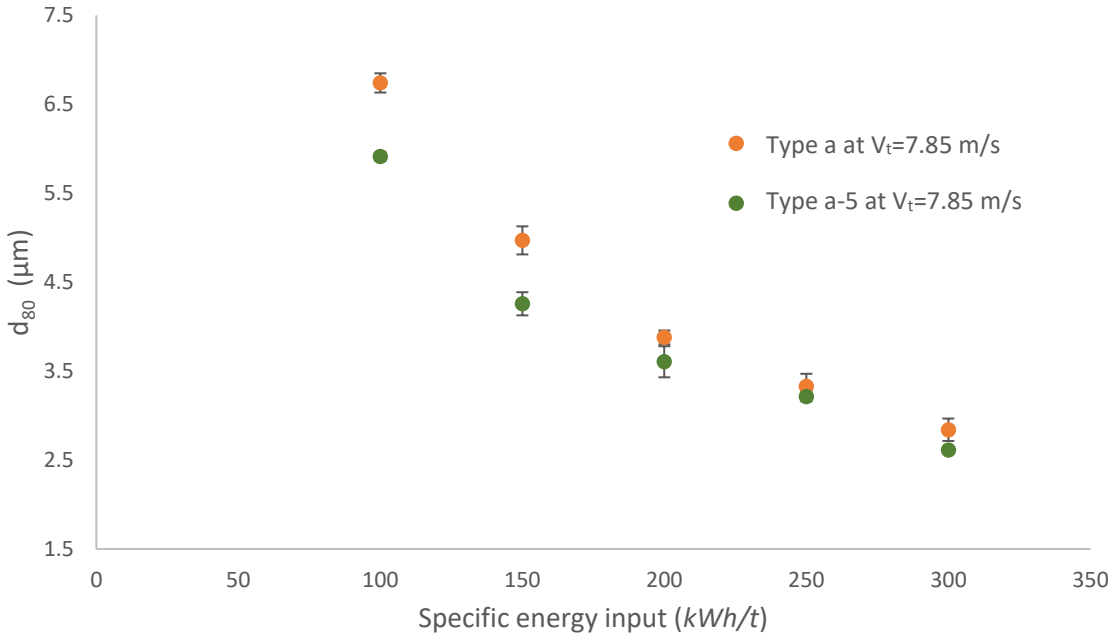

Fig. 4-22. The product d_{80} obtained using stirrer Type a and stirrer Type a-5 at V_t=7.85 m/s (ZirPro grinding media size +0.7-1.4 mm and 65% solids concentration).

As seen from Fig. 4-22, stirrer *Type a-5* achieves a finer particle size than the product obtained using stirrer *Type a*. Due to the extra force generated by the blade stirrer. The fluidisation of the suspension is improved compared to the flow pattern observed by the standard stirrer (*Type a*). This causes stronger interaction between the grinding media. The extra pressure is imparted on the suspension toward the chamber bottom. This incurs strong slip velocity between the grinding media moving upwards and downwards which can generate large shear stress. Thus, the overall grinding efficiency is improved.

The instantaneous power draw and the grinding time measured using stirrer *Type a* and *Type a-5* are compared in Fig. 4-23. The instantaneous power draw for stirrer *Type a-5* is clearly greater than the power draw for stirrer *Type a* by 100 W. The grinding time to reach the specific energy input 300 kWh/t is reduced from 60 minutes (*Type a*) to 40 minutes (*Type a-5*). As the blade stirrer has a larger contact surface with the suspension, the

resistance received by the stirrer is increased. To maintain the same tip speed, the power draw using stirrer *Type a-5* undoubtedly is larger than the power draw using stirrer *Type a*.

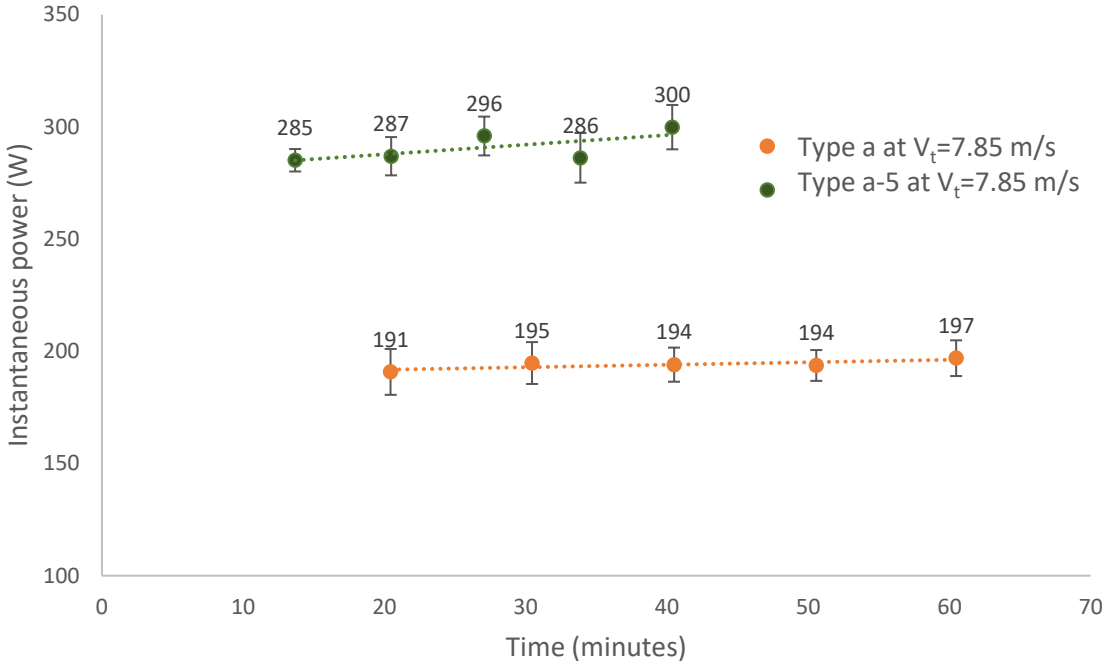

Fig. 4-23. The instantaneous power measured using stirrer Type a and Type a-5 at V_t=7.85 m/s (ZirPro grinding media size +0.7-1.4 mm and 65 % solids concentration).

4.4.6. Impact of mill lid thickness

Increasing the lid thickness will effectively reduce the void area in the upper band of the grinding chamber. Two lids with different thicknesses were tested at V_t=5.23 m/s. The thick lid's height is 5.3 cm whereas the normal lid is 1.8 cm. The thick lid decreases the grinding volume by 31 %. When the slurry level is lifted by the stirrer, the thick lid works as a barrier to prevent the slurry level increasing. It presses the slurry to flow back into the stirrer band and the inner pressure is accordingly increased. In this case, the vortex free surface will be modified. The mass of the slurry stressed by the stirrer will be increased. This is expected to greatly enhance the grinding efficiency.

Table 4-14. The details of product d_{80} obtained using the thick lid and normal lid at V_t=5.23 m/s.

Specific Energy Input (kWh/t)	d_{80} (μm) at V_t=5.23 m/s			
	Thick lid	*SD (σ)*	*Normal lid*	*SD (σ)*
100	4.2	0.10	5.7	0.06
150	3.4	0.20	4.0	0.14
200	2.6	0.05	3.1	0.02
250	1.4	0.06	2.9	0.31
300	1.1	0.13	2.3	0.22

Table 4-14 compares the product d_{80} achieved by the thick lid and normal lid in the range of the specific energy input 100~300 kWh/t. The finest product (d_{80}=1.1 μm) is achieved at 300 kWh/t when the thick lid is applied with stirrer *Type a-1*. As seen from Fig. 4-24, the thick lid demonstrated better grinding efficiency over the normal lid with stirrer *Type a-1*.

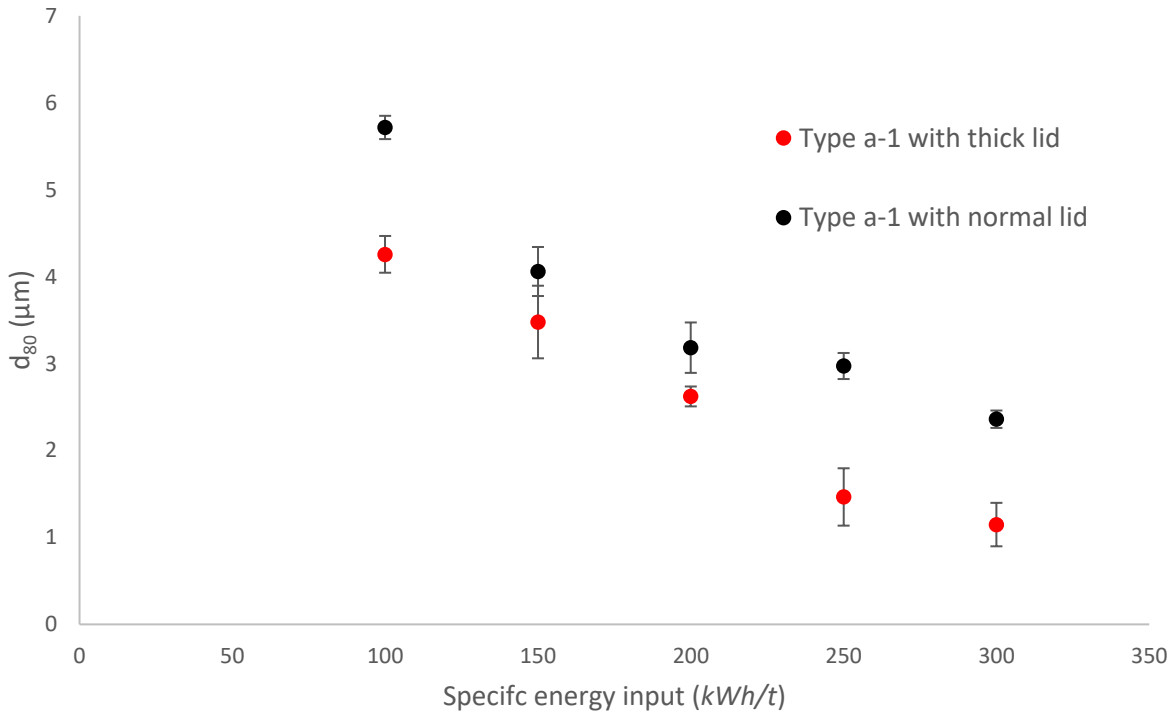

Fig. 4-24. The product d_{80} using thick lid and normal lid configurations against the energy input at V_t=5.23 m/s (ZirPro grinding media size +0.7-1.4 mm and 65 % solids concentration).

The grinding volume is greatly reduced using the thick lid. This means the packing density around the stirrer band is considerably increased. The stirrer undoubtedly received more resistance. Hence, the power draw with the thick lid is much higher than the power draw using the normal lid as illustrated in Fig. 4-25. This implies the slurry is sufficiently mixed by increasing the thickness of the lid. The power usage moderately goes up against grinding time. As the volume of the grinding chamber is greatly reduced, it is difficult for the heat to dissipate. The accumulated heat generated under these conditions boils the water inside the mill. It is estimated that the temperature inside the grinding chamber can be raised to 70~90 ℃.

This causes a loss of a greater amount of water as it evaporates into the air. As the function of the water is much like a lubricant. Without enough water, the friction force between the particles or grinding media will drop the flow-ability of the slurry leading to more resistance to the stirrer.

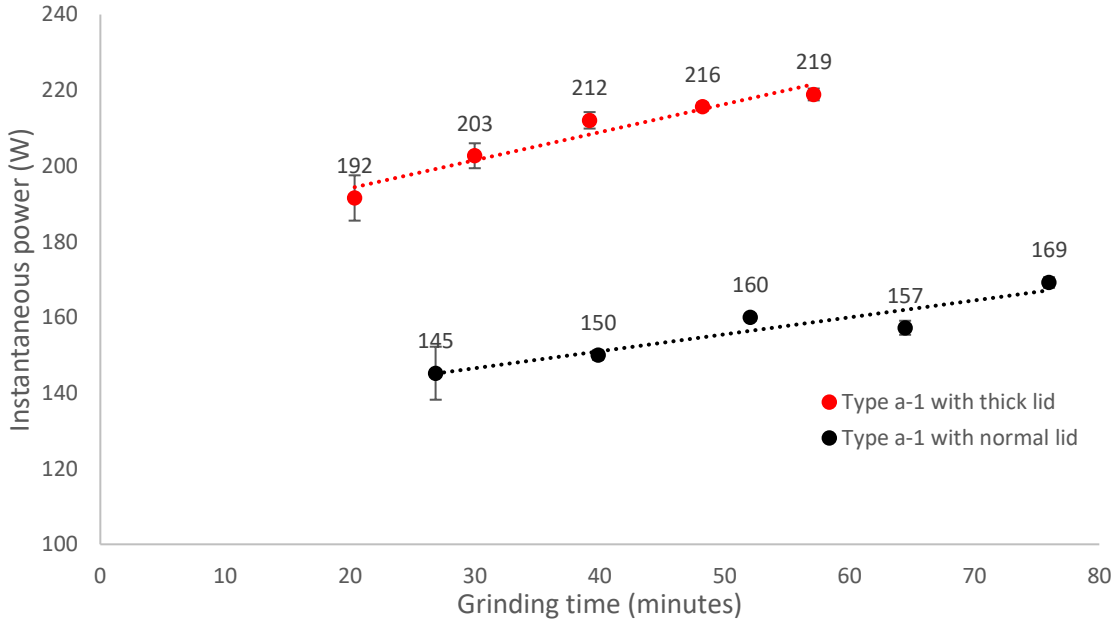

Fig. 4-25. Instantaneous power draw and grinidng time measured using thick lid and normal lid at V_t =5.23 m/s (ZirPro grinding media size +0.7-1.4 mm and 65 % solids concentration).

4.5. Pilot scale mill

The grinding process in the laboratory scale mill was scaled up to a pilot scale mill. The performance of the pilot scale mill was compared to the laboratory scale mill regarding the product d_{80} and the instantaneous power draw. The product samples obtained in the pilot scale mill were also measured at the specific energy input of 100, 150, 200, 250 and 300 kWh/t. This ensures that the product samples were obtained at the equal energy based on the unit mass of the dry calcite. This also avoids the variation over the energy input caused by the difference of the volume capacity of different scale of the mills.

4.5.1. Comparison of pilot scale mill and laboratory scale mill

The amount of the calcite and grinding media charged into the mill chamber were greatly increased for the experiment in the pilot scale mill. The total mass of the slurry was scaled from 1 kg (laboratory scale mill) up to 10 kg (pilot scale mill) of which the dry calcite was 6.5 kg and the water was 3.5 kg. Hence, the solids concentration was kept at 65 % (w/w). The grinding media filling ratio was maintained at 52 % (v/v) to be consistent with the conditions in the laboratory scale mill. The experiments were conducted at the rotational speed of 576 RPM corresponding to V_t=7.85 m/s (1200 RPM for the laboratory scale mill). Carbolite grinding media (size +0.8-1.2 mm) was used in both mills. The stirrer type used in the pilot scale mill was the standard pin stirrer (*Type b*) (see Fig. 3-12).

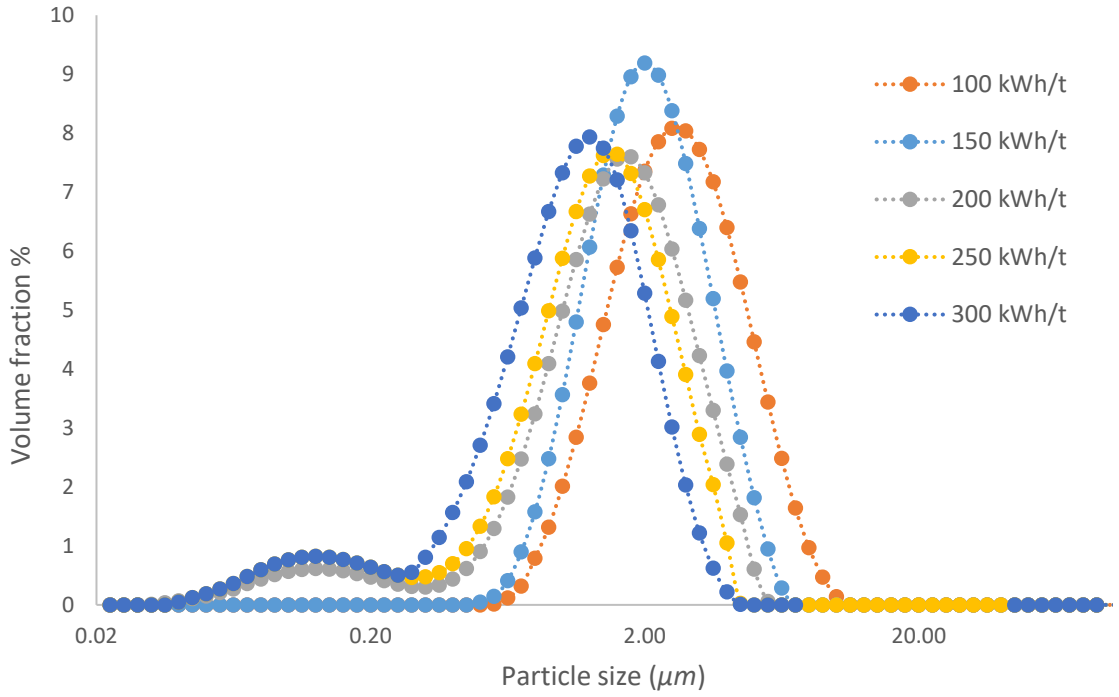

Fig. 4-26. Particle size distribution obtained in the pilot scale mill at 65 % solids concentration and V_t=7.85 m/s (576 RPM) (Carbolite grinding media size +0.8-1.2 mm).

Fig. 4-26 demonstrates the overall product size distribution (PSD) obtained in the pilot scale mill at the specific energy inputs 100~300 kWh/t. The corresponding size parameters (e.g. d_{80}, d_{50} and d_{20}) are illustrated in Table 4-15. The product d_{80} obtained in the laboratory scale mill under the same operating conditions is listed in Table 4-16.

Table 4-15. Detailed product d_{80} obtained at V_t=7.85 m/s in the pilot scale mill (Carbolite grinding media size +0.8-1.2 mm, 65 % solids concentration).

Specific Energy Input (kWh/t)	Pilot mill at V_t=at 7.85 m/s					
	d_{80} (μm)	*SD* (σ)	d_{50} (μm)	*SD* (σ)	d_{20} (μm)	*SD* (σ)
100	4.1	0.15	2.4	0.10	1.5	0.09
150	2.9	0.08	1.9	0.04	1.2	0.06
200	2.4	0.02	1.4	0.01	0.8	0.04
250	2.0	0.01	1.3	0.08	0.8	0.10
300	1.9	0.11	1.1	0.02	0.6	0.01

Table 4-16. Detailed product d_{80} obtained at V_t=7.85 m/s in the laboratory scale mill (Carbolite grinding media size +0.8-1.2 mm, 65 % solids concentration).

Specific Energy Input (kWh/t)	Laboratory mill at V_t=7.85 m/s	
	d_{80} (μm)	*SD* (σ)
100	5.2	0.15
150	4.3	0.16
200	3.1	0.13
250	2.6	0.11
300	1.9	0.09

As seen from Fig. 4-26, the overall size distribution shows a similar trend as the PSD curves observed in the laboratory scale mill (see Fig. 4-1). However, the curves for the specific energy input at 200, 250 and 300 kWh/t exhibit another peak. It is interesting to note that the size range of the lower peak is between 0.02-0.2 μm indicating the presence of some extremely fine particles. This can be explained by the overgrinding due to the inhomogeneous system in the pilot scale mill. When the volume of the grinding chamber is increased from 2.9 L (laboratory scale) to 22.8 L (pilot scale) by 7.8 times, the product uniformity is not as good as the product obtained in the laboratory scale mill.

As the volume of the charged slurry and the grinding media were also increased, it is difficult to mix the slurry and grinding media uniformly instantly in the pilot scale mill. The flow-ability may also be affected. In the pilot scale mill, it needs more time for the circulation in the grinding chamber to bring the particles outside of the impeller band into the central area where the collisions occur more frequently. This will cause the different fineness in particle as the intensity of grinding for each particle is not the same.

Additionally, the mass concentration of the slurry may not be the same at any point in the mill chamber as the particles tend to settle down at the chamber bottom due to the gravity.

A stagnant area may be formed at the corner of the chamber bottom. This is a common problem when the grinding chamber is scaled up by 7.8 times in volume. If the system is not highly homogeneous, during the grinding process, the collision rate and shear stress received by each particle are not identical. Some particles might be excessively ground to extremely fine size because these particles collide with one another more frequently. This trend on the product size distribution is not observed in a laboratory scale mill because the inhomogeneous distribution of the material is lower in a smaller grinding chamber.

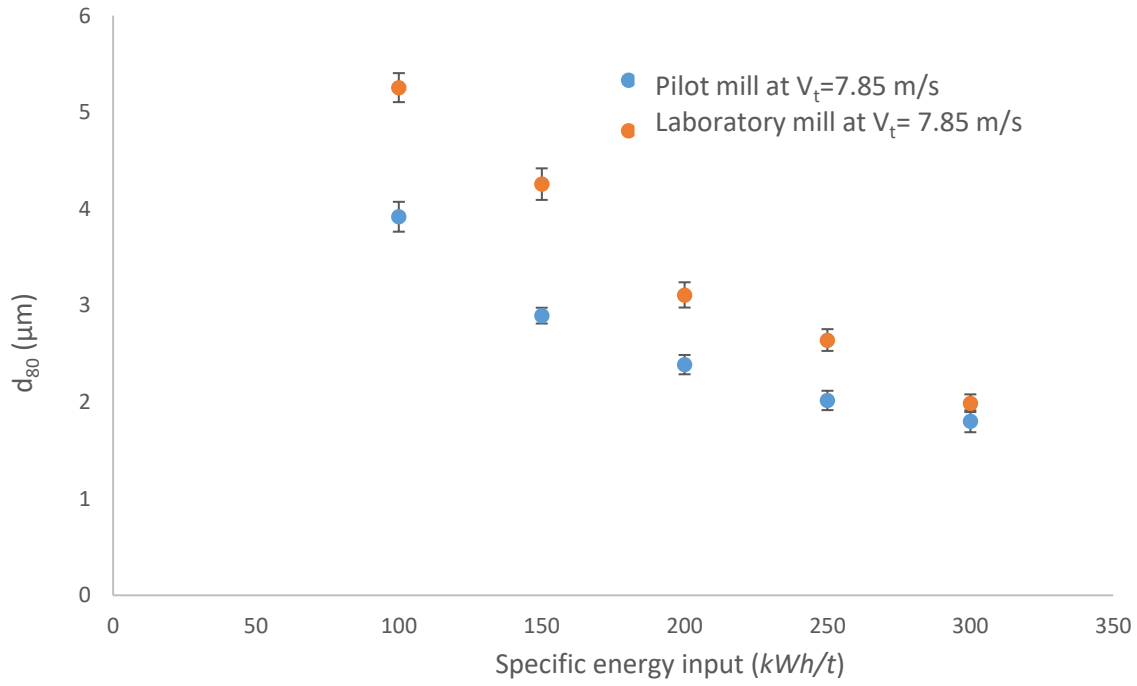

Fig. 4-27. Comparison of the product d_{80} obtained in laboratory mill and pilot mill at V_t=7.85 m/s (Carbolite grinding media size +0.8-1.2 mm, 65 % solids concentration).

Fig. 4-27 compares the product d_{80} obtained from both mills at V_t=7.85 m/s. Although the mill scale is greatly increased, the finer product size was observed on the pilot scale mill. For the specific energy input at 100 kWh/t, the product d_{80} in the pilot scale mill is 4.1 μm which is much finer than the d_{80}=5.2 μm for the product in the laboratory scale mill. The

difference over the d_{80} was gradually reduced with increasing the specific energy input seen from Fig. 4-27.

The variation of the product d_{80} can be caused by the different configuration of the stirrers in both mills. Compared to the standard pin stirrer *Type a* used in the laboratory scale mill, the stirrer *Type b* used in the pilot scale mill has an increased number of stirrer arms (9 pairs) to match a larger grinding chamber for the pilot scale mill. The offset angle between the stirrer arms is also reduced from 90 ° (laboratory scale mill) to 30 °(pilot scale mill). This modification of the stirrer configuration ensures that the equivalent stress intensity can be provided when the grinding volume is greatly increased.

The comparison of the instantaneous power draw is demonstrated in Fig. 4-28. The power trend of the pilot scale mill slightly decreases from 1,391 W at 100 kWh/t to 1,226 W at 200 kWh/t, then it increases to 1,338 W at 300 kWh/t. Overall, the average power draw is increased from 177 W for the laboratory scale mill to 1,295 W for the pilot scale mill by 7.3 times. The grinding time for reaching 300 kWh/t is increased from 60 minutes (laboratory scale mill) to 89 minutes (pilot scale mill).

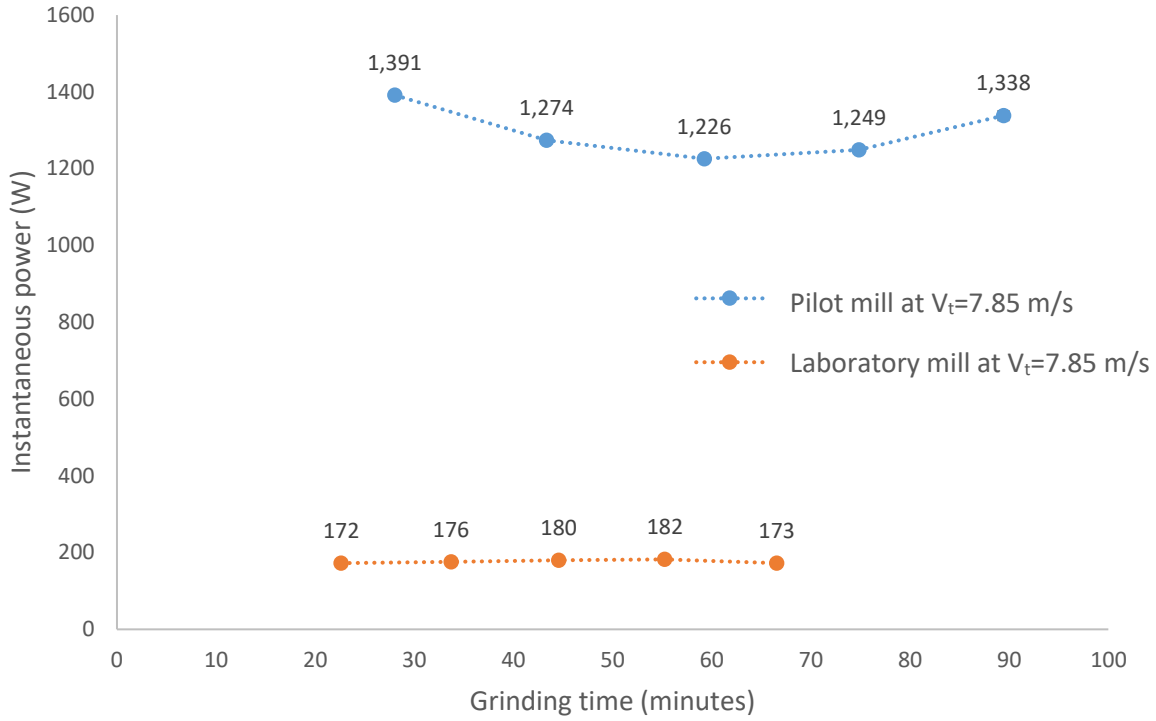

Fig. 4-28. The comparison of the instantaneous power draw and grinding time over the laboratory mill and the pilot mill at V_t=7.85 m/s (Carbolite grinding media size +0.8-1.2 mm, 65 % solids concentration).

At the beginning of the grinding process, water, dry calcite and grinding media were not mixed very well in the pilot scale mill. The resistance caused by the friction was great, so the instantaneous power draw was high. When the charged materials were mixed sufficiently, a uniform system was achieved and the power draw gradually dropped. As the grinding process continued, some water was lost due to evaporation. The number of the particle collisions in the pilot scale mill was much greater than the number in the laboratory scale mill. This means more heat is generated in the pilot scale mill and the evaporation becomes greater. Hence, the solids concentration was increased. The power draw was increased again. The discrepancy of instantaneous power draw was no more than 10 W for the laboratory scale mill. When the materials weight was increased by 7.8 times for the pilot

scale mill, the difference in the instantaneous power draw reached about 165 W. This implies either the homogeneity of the system or the evaporation of the water can significantly affect the power consumption when the scale is greatly increased.

When the grinding process is scaled up from the laboratory scale to the pilot scale. The main issue is the distribution of the stress intensity in the grinding chamber is not uniform. Some field far away from the stirrer (e.g. bottom, chamber wall) may not produce sufficient force for the collisions. The breakage of particles will be hard to happen. Also, the turbulent flow regimes will be reduced and some stagnant area may be formed at the corner of the grinding chamber. It is nearly motionless for the grinding media in these fields. The grinding media and mineral particles are highly possible to settle down which causes a decline in product quality. Normally, some baffles are recommended to add in a large-scale grinding chamber to reduce the impact.

4.5.2. Application of different stirrer types

Several different configurations of the stirrers have been tested in the laboratory scale mill. Based on the performance, the greater the number of stirrer arms and the narrower gap between the stirrer arms will improve the grinding efficiency. The ideal was applied in the pilot scale mill and a combination of the pin stirrer and flat blade (*Type b-1*) was designed for the pilot scale mill (see Fig.4-29). The configuration is based on the stirrer *Type a-5*.

Fig. 4-29. Photograph of the stirrer Type b-1 used in the pilot scale mill.

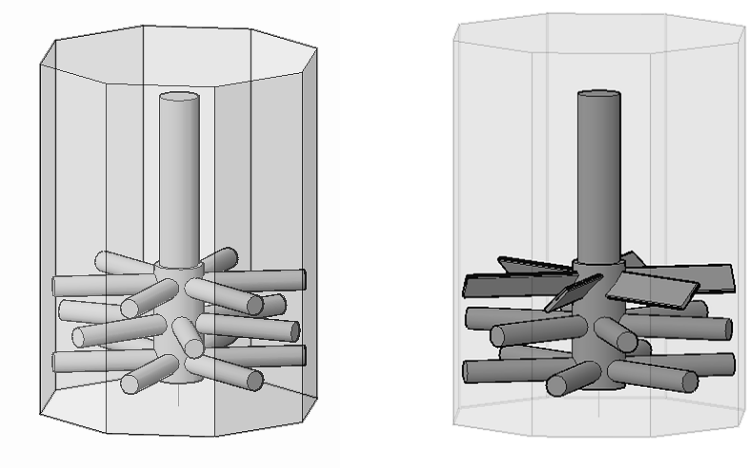

Type b *Type b-1*

Fig. 4-30. 3D images for the standard stirrer (Type b) and the new stirrer (Type b-1) used in the pilot scale mill.

As the volume of grinding chamber is increased for the pilot scale mill, a larger empty area exists above the stirrer and beneath the lid. By replacing the pin stirrer arm in the upper layer of stirrer *Type b* with flat blades, a new stirrer type *Type b-1* is designed and expected to pump the slurry down towards the chamber bottom. In the laboratory scale mill, this modification demonstrated an improvement on the collision intensity and degree of the product size reduction. Hence, the idea of the design was applied in the pilot scale mill. The 3D images for stirrer *Type b* and *Type b-1* are shown in Fig. 4-30.

Comparison experiments were conducted at 65% solids concentration. The V_t was 7.85 m/s (567 RPM). ZirPro grinding media (size +0.7-1.4 mm) was used. The detailed product size d_{80} was shown in Table 4-17. Overall, stirrer *Type b-1* produced a finer product than *Type b* over the specific energy range 100~300 kWh/t. The difference over the product d_{80} is shown in Fig. 4-31.

Table 4-17. Detailed product d_{80} using stirrer Type b and Type b-1 in the pilot scale mill at V_t=7.85 m/s (Zirpro grinding media size +0.7-1.4 mm and 65 % solids concentration).

Energy Input (kWh/t)	d_{80} at V_t=7.85 m/s			
	Type b	*SD (σ)*	*Type b-1*	*SD (σ)*
100	6.6	0.17	4.6	0.06
150	3.8	0.07	3.3	0.12
200	3.1	0.18	2.8	0.08
250	2.6	0.05	2.3	0.13
300	2.4	0.06	2.1	0.06

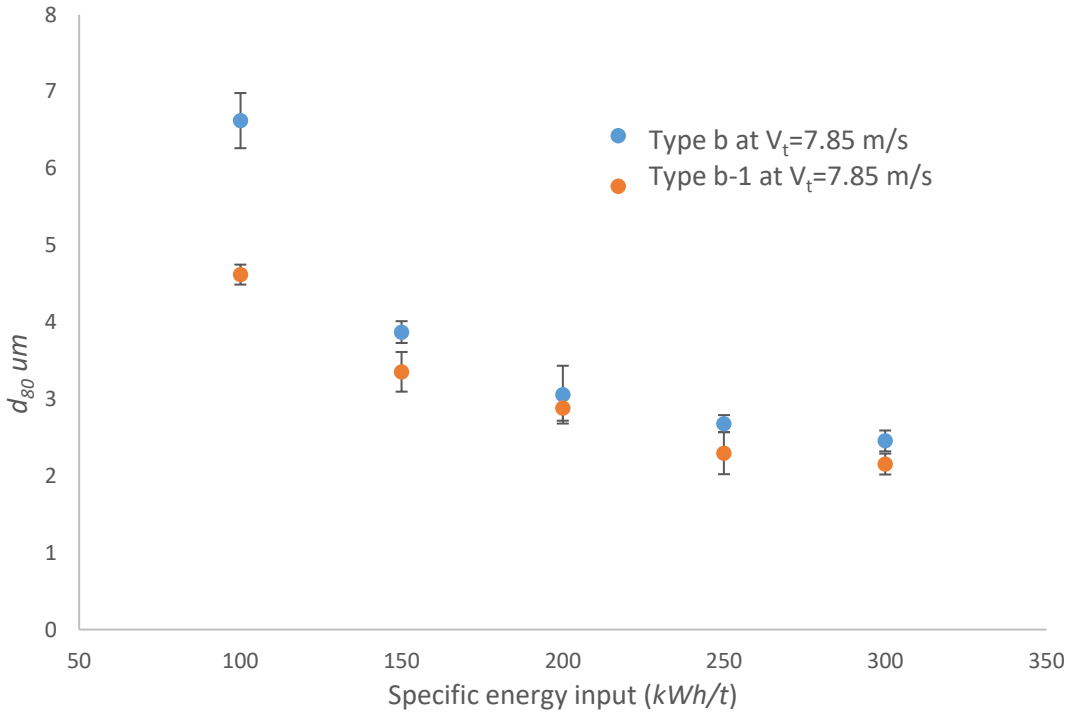

Fig. 4-31. Comparison of the product d_{80} obtained using Type b and Type b-1 in the pilot scale mill at V_t=7.85 m/s (ZirPro grinding media size +0.7-1.4 mm and 65 % solids concentration).

As seen from Fig. 4-31, when the specific energy input is increased, the product d_{80} obtained declines gradually for both stirrer types. The curve of d_{80} obtained using stirrer *Type b-1* is clearly below the curve for stirrer *Type b* indicating a finer product obtained from *Type b-1* at the same specific energy input. The improvement of d_{80} observed in the pilot scale mill is consistent with the results observed in the laboratory scale mill. *Type b-1* has shown an effective and reliable increase in the grinding efficiency without extra energy input.

The instantaneous power draw and the grinding time consumed by *Type b* and *Type b-1* are illustrated in Fig. 4-32. The instantaneous power draw by *Type b-1*(mean value 1209 W) is slightly larger than *Type b* (mean value 1136 W). Thus, it is quicker for *Type b-1* to reach the target energy input comparing to *Type b*. The grinding time is reduced from 73 minutes

(*Type b*) to 68 minutes (*Type b-1*). The change in instantaneous power draw is not large seen from the results of the pilot scale mill. When this is applied on the industrial scale, the improvement of the grinding efficiency will be significant.

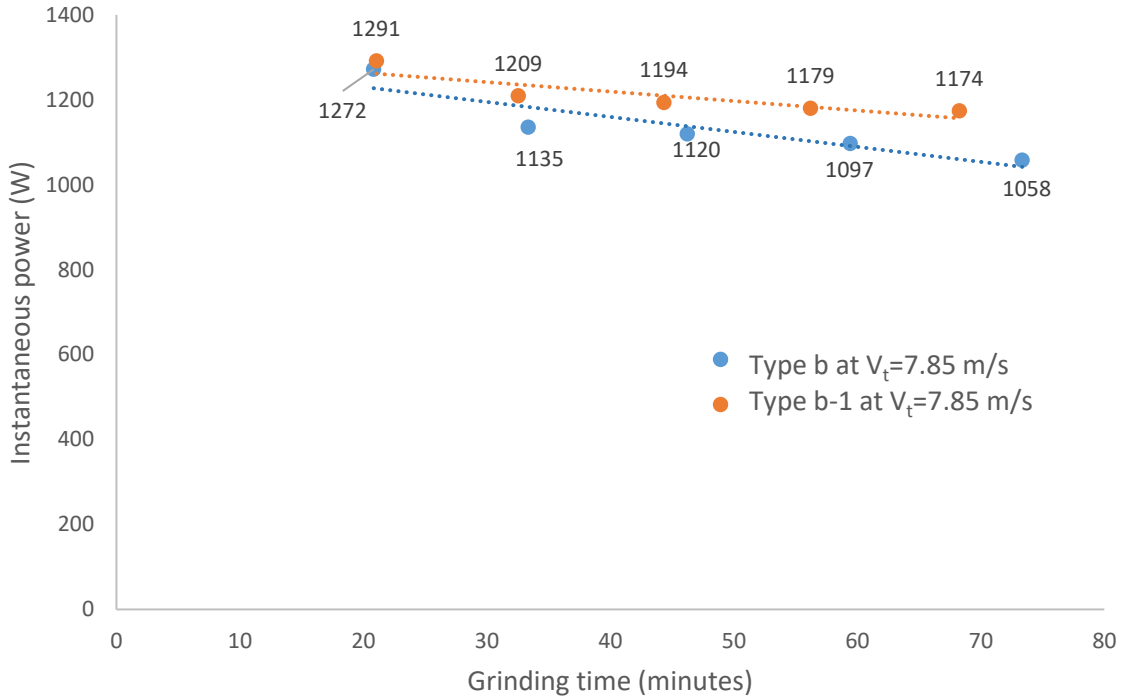

Fig. 4-32. The instantaneous power draw against the grinding time using stirrer Type b and Type b-1 at V_t=7.85 m/s (ZirPro grinding media size +0.7-1.4 mm and 65 % solids concentration).

The overall variation of the instantaneous power draw observed from both stirrer types shows a declining trend. This can be caused by the poorly mixed materials at the beginning. When a more homogeneous system is formed during the process, the power drops down. To avoid the influence of the water evaporation, the supplementary water is added during the grinding process.

For the experiments using stirrer *Type b-1*, the load is continually pumped back into the stirrer region due to the downwards force generated by the flat blade. This influence was already demonstrated by the corresponding results obtained in the laboratory scale mill.

The filling of the material in the impeller region is increased. Also, the contact surface for the flat blade is higher than the pin stirrer. Hence, it costs more power to drive the stirrer as more resistance is received. However, the magnitudes of power draw from both types are very close as the number of the stirrer arms and distance between the stirrer arms remain identical.

When the same amount of specific energy input is applied, the pitched blade stirrer demonstrates a more energy efficient design than the pin stirrer on both pilot scale and laboratory scale mills. Under the same operating conditions, the blade stirrer provides more shear surface to contact with the charge. Additionally, the angle of the blade effectively controls the flow direction of the charge. The flow behaviour in the stirred mill is very different from the traditional ball mill. The grinding process in a vertically stirred media mill has some of the elements observed in the fluid mixing process but the grinding process is more complicated as the slurry (suspension) and grinding media (solid particle) are two separated phases. The results on either pilot scale or laboratory scale indicates that the influence of the stirrer configuration on the flow pattern is of great value to further optimise the energy efficiency.

4.6. Conclusions

Based on the grinding results obtained from the laboratory scale mill, it is concluded that the vertical stirred media mill is an effective and reliable tool to obtain fine particles under specific operational conditions. The effect of the operating factors such as specific energy, rotational speed, solids concentration, grinding media size and stirrer configurations are analysed. The relationship between the particle size and the energy is demonstrated at various operating conditions.

The optimal tip speed (V_t) is proved to be 5.23 m/s (800 RPM) in the laboratory scale mill as the finest product is obtained at 300 kWh/t. A lower solids concertation is more energy efficient at the current experimental conditions, because the product obtained at 50 % solids concentration shows finer size than the product obtained at both 65 % and 75 % solids concertation. The finest grinding media size ZirPro +0.7-1.4 mm is demonstrated to be the most suitable grinding media as the finest product is obtained by using this type of grinding media. The most appropriate dispersant dosage for the grinding process is proved to 0.8 %. Excess amount of dispersant shows no improvement in energy efficiency.

The performances of some new stirrer types are studied in the laboratory scale. *Type a-5*, a combination of pin and blade stirrer, is demonstrated to be more energy efficient than the rest types. Then, the configuration is scaled up for the pilot scale mill. *Type b-1* designed based on *Type a-5* for the pilot scale mill is demonstrated to be better than the standard pin stirrer.

Chapter 5 Positron Emission Particle Tracking (PEPT) technology

5.1. Introduction

The measurement of the grinding media velocity in the grinding chamber can be difficult, because the grinding chamber is normally made of metal which is not transparent. Thus, the traditional optical method (e.g. Particle Image Velocimetry) is not suitable. To solve the problem, Positron Emission Particle Tracking (PEPT) has been used in this study. The experiments with PEPT are conducted in the laboratory scale mill and the results were analysed in this chapter.

The operating variables including stirrer tip speed, grinding media density and size, configuration of stirrer are the major factors affecting the grinding process. The influence of these variables on product size, power consumption and grinding time are analysed in Chapter 4.

However, these operating variables also have a great influence on the flow behaviour of the charge inside the grinding chamber. Some researchers investigated the influences based on the stress intensity model (Becker et al., 2001; Kwade, 2004). The limitation is that the detailed velocity distribution of the grinding media in the grinding chamber remains unknown. PEPT is a reliable and accurate tool to measure the velocity distribution of the grinding media. The data from PEPT under different operating conditions are recorded and interpreted into visualised data by a linear interpolation method. The azimuthally averaged velocity map, velocity vector map and occupancy rate map are plotted to compare the results obtained with PEPT under various conditions.

5.2. Experimental set-up

Initially, PEPT records a series of time points and the corresponding locations of a radioactive tracer in a 3D Cartesian coordinate. The 3D Cartesian coordinate is virtually built in the confined space between the 2 γ-ray detectors (PEPT cameras) as shown in Fig. 5-1. Based on a corner of the confined space, the location of the tracer is recorded in x, y, z directions in the 3D Cartesian coordinate as indicated in Fig. 5-1. When the time and locations in the 3D Cartesian coordinate are obtained, the trajectory of the trace are reconstructed. Finally, the velocity of the tracer at different locations can be calculated.

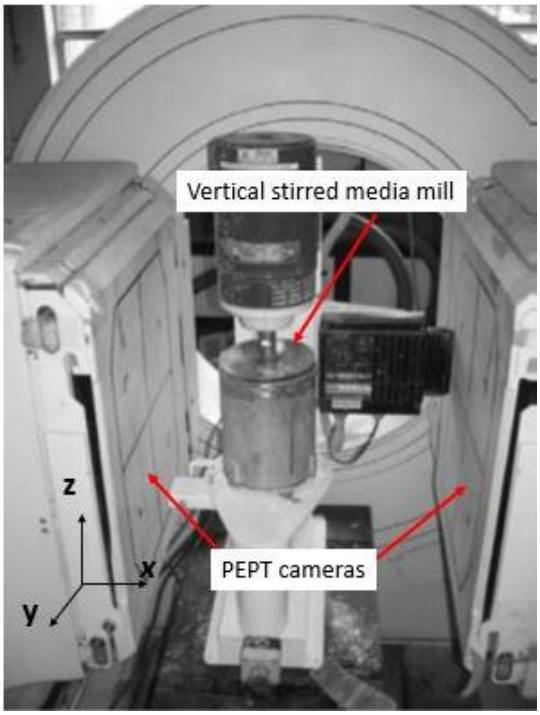

Fig. 5-1. The laboratory scale mill is placed in the space between the 2 PEPT cameras.

5.2.1. Radioactive tracer

The radioactive tracer is added into the grinding chamber at the beginning of each grinding experiment. The tracer is produced by irradiating a random grinding media bead directly in a cyclotron using a 33 MeV ^3He beam in the School of Physics. Some oxygen atoms in the grinding media bead are converted into the radioisotope ^{18}F. An advantage of this

irradiation method is that the physical properties (e.g. density and shape) of the radioactive tracer are identical to the other grinding media (Tamblyn, 2009). Thus, its flow behaviour is isokinetic with the other grinding media. The velocity of the tracer will be identical to the grinding media. The location of the tracer is reconstructed by the γ-rays emitted from the ^{18}F as shown in Fig. 5-2. Those reconstructed points are connected in a continuous time order to identify the tracer trajectory. The reconstructed path of the tracer truly reflects the motion of the grinding media. If enough time is provided, the tracer can travel to every corner within the grinding chamber. A map for the velocity distribution within the grinding chamber is obtained.

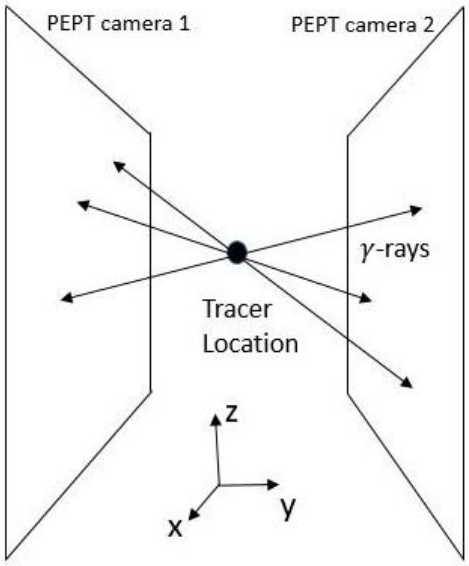

Fig. 5-2. The reconstruction of the radioactive tracer location detected by a bunch of γ-rays.

The radioisotope ^{18}F has been demonstrated to be an ideal radioisotope for PEPT (Bakalis et al., 2006; Fan et al., 2006). Compared to the other radioisotopes such as ^{66}Ga, ^{22}Na, ^{61}Cu and ^{64}Cu, its half-life is approximately 109 minutes which is neither too short to cover the experiment with PEPT nor too long to remain a persistent impact on the environment.

For ^{18}F , 2 back to back gamma rays (see Fig. 5-3) are generated at the energy scale of 511 keV which is demonstrated to give a better accuracy in tracking the location from the detectors (Fan et al., 2006; Parker et al., 1993). While the tracer is moving with the other grinding media, the radionuclide ^{18}F decays by emitting positrons which annihilate with electrons. The process is described by Eq. [5.1] and Eq. [5.2]. where e^+ denotes a positron, e^- denotes an electron and v^e denotes an electron neutrino.

$$^{18}F \rightarrow {}^{18}O + e^+ + v^e \quad [5.1]$$

$$e^+ + e^- \rightarrow 2\gamma \quad [5.2]$$

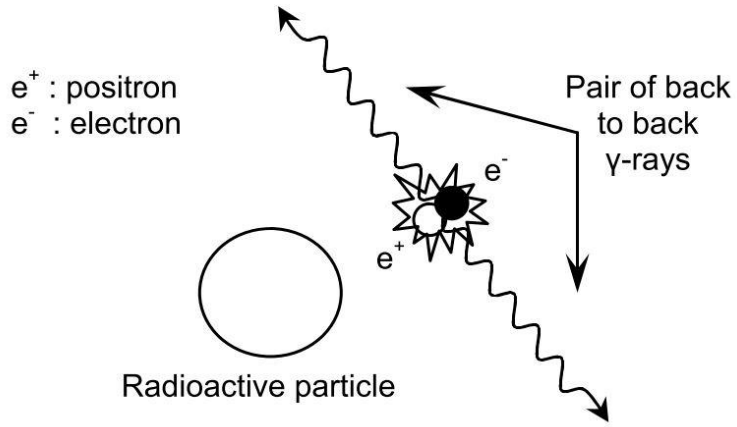

Fig. 5-3. The radionuclide decays by emitting a positron which annihilates with an electron producing a pair of back to back gamma rays (Van Lam Cheun U, 2009).

For each experiment with PEPT, the grinding time is recorded when the stirrer starts to rotate. The time used for each run is 15 minutes. This is plenty time to capture sufficient positions (approximately 1×10^5 points) of the tracer to cover almost the all area within the grinding chamber.

5.2.2. Analysis of PEPT data

A sample of the original data obtained by the tracer is illustrated in Fig. 5-4. The 'separation' value indicates the distance between the 2 PEPT cameras (470 mm). The value is constant

when the distance has been adjusted to ensure that the mill is just located in the centre of the 2 PEPT cameras. The displacement values denote the distance range on x, y, z direction for the 3D Cartesians coordinate built within the space. The f_{opt} and number of events per slice are two important parameters assigned based on the experimental configuration to filter the position data.

```
Separation=   470

f(opt) :  0.050      Displacement parameters :    300,   400,  1500

Fixed slices:    250 events/slice,    1 locations/slice

       4.8     273.0     390.4     270.9       1.2       0.0      0.00   12
      13.6     271.4     390.3     270.1       0.9       0.0      0.00   11
      21.6     271.9     389.4     265.9       0.8       0.0      0.00   11
      31.9     271.0     389.4     264.0       0.9       0.0      0.00   11
      40.8     271.5     388.8     265.4       0.6       0.0      0.00   11
      50.0     271.2     388.0     264.1       0.8       0.0      0.00   11
      60.3     272.6     389.3     259.7       1.0       0.0      0.00   11
      67.9     270.9     392.4     254.9       1.0       0.0      0.00   11
      75.3     270.1     393.7     256.3       0.7       0.0      0.00   11
      83.8     269.4     392.5     254.2       1.1       0.0      0.00   11
      93.0     268.6     392.9     252.7       1.0       0.0      0.00   11
     103.8     268.8     390.9     250.4       1.5       0.0      0.00   11
     113.3     268.9     391.7     250.9       1.0       0.0      0.00   11
     122.7     269.9     389.5     244.9       1.1       0.0      0.00   11
     131.4     269.4     387.3     246.4       1.1       0.0      0.00   11
     140.1     268.2     387.6     243.3       0.9       0.0      0.00   11
     148.8     268.8     388.5     237.9       1.0       0.0      0.00   11
     159.2     270.7     388.2     239.1       1.0       0.0      0.00   11
     166.8     268.2     389.1     233.7       1.1       0.0      0.00   11
     178.7     270.9     389.6     228.4       0.9       0.0      0.00   11
     187.9     271.7     389.4     229.5       0.8       0.0      0.00   11
```

Fig. 5-4. A sample of a series of original PEPT data.

When the γ-rays are captured, 200-500 pairs of γ-rays are grouped into a slice. One location is calculated by one slice of γ-rays. Theoretically, 2 pairs of γ-rays are enough to determine a location. For a hundred pairs of γ-rays, not all of them are validating for the reconstruction of the tracer location. The material surrounding the tracer may absorb and disturb some γ-rays resulting in error. These γ-rays are corrupted and must be filtered. For the case shown in Fig. 5-4 where the f_{opt} is 0.05 and the events/slice is 250. This means that 12 (0.05×250)

events (pairs) are used for determination of one location. The values for f_{opt} and number of events /slice are obtained by trial and error for each set of data (Chiti, 2007). The relative standard deviation of the position error is shown in the 5^{th} column for each event.

As seen in Fig. 5-4, the 1^{st} column denotes the time point with units in millisecond (ms). The 2^{nd}, 3^{rd} and 4^{th} columns refer to the position on x, z and y axis (mm) respectively. The 6^{th} and 7^{th} columns are not used. The last column shows an actual number of γ -rays used to determine the location.

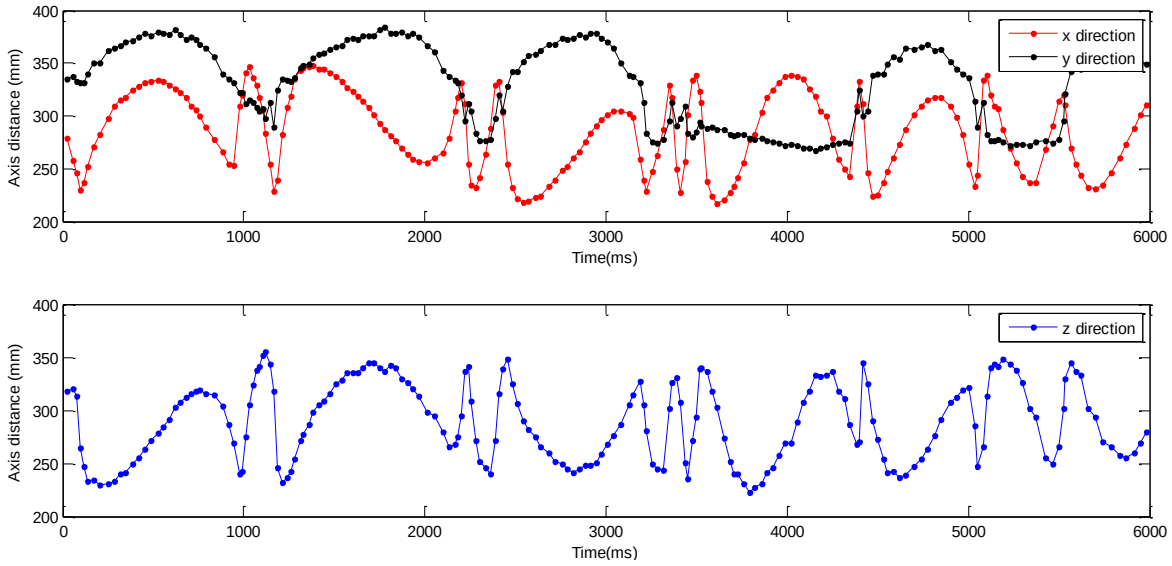

Fig. 5-5. The data extracted from PEPT shown in x, y, z, direction in the original coordinate.

Fig. 5-5 shows a sample of recorded data position in the original spatial coordinate. The original spatial coordinate sets the origin point at the corner of one PEPT camera. Thus, all the values are positive ranging from 200-400 (mm) indicated in Fig. 5-5. These values are then transferred into a new 3D-Cartesian coordinate to directly reflect the tracer position in the mill chamber. The new 3D-Cartesian sets the original point at the centre of the chamber. The x, y and z values are rescaled based on the new coordinate shown in Fig. 5-6.

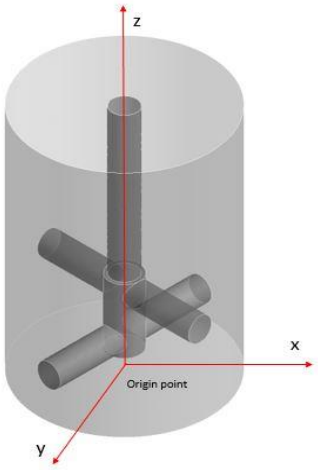

Fig. 5-6. A new 3D-coordinate is built with the reference of the stirred media mill.

To transfer the tracer position from the original coordinate to the new coordinate, Eq. [5.3], Eq. [5.4] and Eq. [5.5] are used respectively for the values in x, y and z direction:

$$x_n = x_i - \frac{x_{max}+x_{min}}{2} \quad [5.3]$$

$$y_n = y_i - \frac{y_{max}+y_{min}}{2} \quad [5.4]$$

$$z_n = z_i - z_{min} \quad [5.5]$$

where x_n, y_n and z_n are the tracer position in the new coordinate corresponding to the original position for x_i y_i and z_i . The x_{max} and y_{max} are the recorded maximum distance in the original coordinate and the x_{min} , y_{min} and z_{min} are the recorded minimum distance.

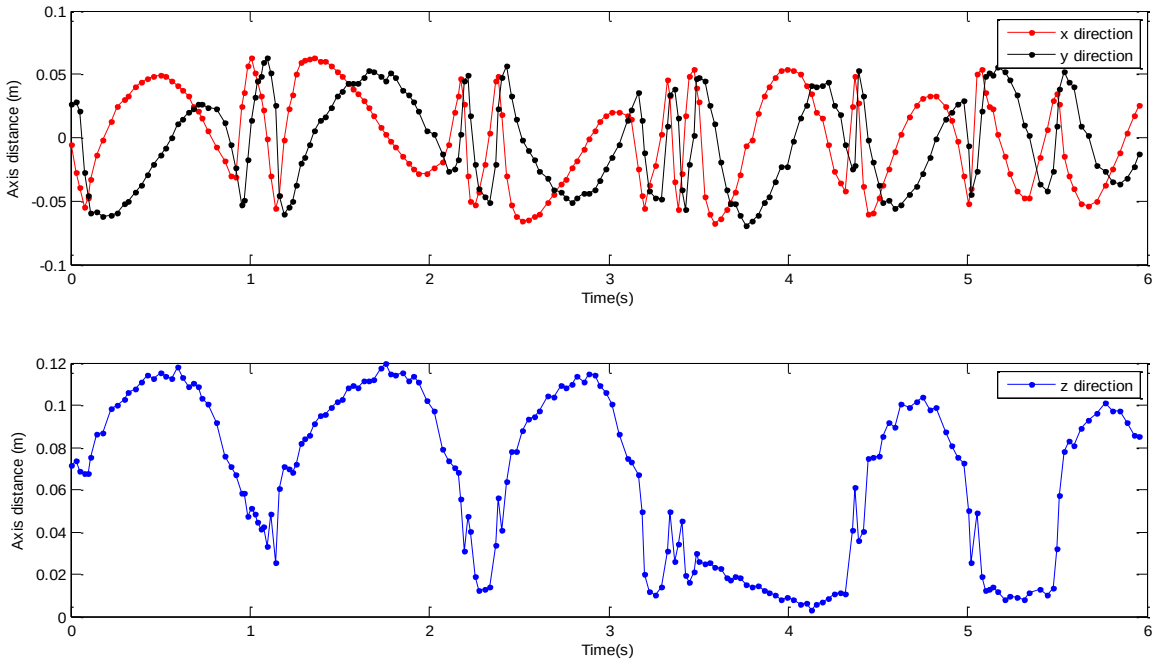

Fig. 5-7. A series of x, y and z values based in the new coordinate.

A new set of data of the time points and tracer locations are demonstrated in Fig. 5-7. In the x and y directions, the zero value indicates the centre of the grinding chamber bottom. The radius of the chamber bottom is 0.07 m. All the values in the x and y direction should be within the range from -0.07 m to 0.07 m. In the z direction, the values are within the range 0.12 m to 0 m which is reasonable as the maximum height of the chamber is 0.19 m. The level height of the slurry depends on the operating conditions, but it should not exceed 0.19 m. An example of the tracer trajectory with reference to the grinding chamber is plotted in Fig. 5-8.

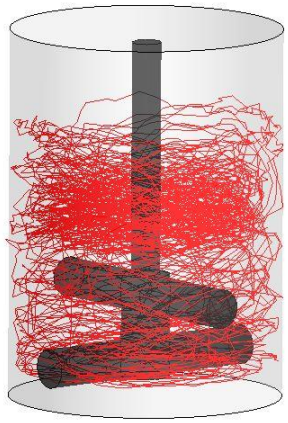

Fig. 5-8. Sample of the rebuilt trajectory of the tracer in the grinding chamber.

When the position of the new 3D Cartesian coordinate is known, it is possible to calculate the tracer velocity at the corresponding tracer location. There are 3 methods used to determine the tracer velocity (Chiti, 2007). The simple way (see Eq. [5.6]) is the 2-point method in which the velocity is obtained by the distance between 2 sequential points over time. Based on the 2-point method, a more complicated method in which the velocity is determined as an average value of 6 points (see Eq. [5.7]) has been developed.

$$v_n = \frac{\sqrt{x_n^2+y_n^2+z_n^2}-\sqrt{x_{n-1}^2+y_{n-1}^2+z_{n-1}^2}}{t_n-t_{n-1}} \quad [5.6]$$

$$v_n = 0.1\frac{\sqrt{x_{n+5}^2+y_{n+5}^2+z_{n+5}^2}-\sqrt{x_n^2+y_n^2+z_n^2}}{t_{n+5}-t_n} + 0.15\frac{\sqrt{x_{n+4}^2+y_{n+4}^2+z_{n+4}^2}-\sqrt{x_{n-1}^2+y_{n-1}^2+z_{n-1}^2}}{t_{n+4}-t_{n-1}}$$
$$0.25\frac{\sqrt{x_{n+3}^2+y_{n+3}^2+z_{n+3}^2}-\sqrt{x_{n-2}^2+y_{n-2}^2+z_{n-2}^2}}{t_{n+3}-t_{n-2}} + 0.25\frac{\sqrt{x_{n+2}^2+y_{n+2}^2+z_{n+2}^2}-\sqrt{x_{n-3}^2+y_{n-3}^2+z_{n-3}^2}}{t_{n+2}-t_{n-3}}$$
$$0.15\frac{\sqrt{x_{n+1}^2+y_{n+1}^2+z_{n+1}^2}-\sqrt{x_{n-4}^2+y_{n-4}^2+z_{n-4}^2}}{t_{n+1}-t_{n-4}} + 0.1\frac{\sqrt{x_n^2+y_n^2+z_n^2}-\sqrt{x_{n-5}^2+y_{n-5}^2+z_{n-5}^2}}{t_n-t_{n-5}} \quad [5.7]$$

Either the 2-point (differentiation method) or 6-point (weighted average method) method assumes the time interval is small enough to use the average speed to represent the

instantaneous speed. In other words, the accuracy depends on the time interval. To avoid the error caused by the time interval, a linear fitting method is proposed by Chiti (2007). This is a linear interpolation method to obtain the velocity by finding the best fit line $x_i = v_x * t_i + C$ for the 5 continues points shown in Fig. 5-9.

For 5 sequential locations of the tracer, their x positions are x_1 x_2 x_3 x_4 x_5 at time t_1 t_2 t_3 t_4 t_5 respectively. A best fitting line is easy to define as: $x_n = v_x * t_n + C$ as illustrated in Fig. 5-9. The V_x is the gradient of the line and it also represents the velocity in the x direction at the time t_n for point x_n. Similarly, the velocity in y and z directions are obtained by this method. The actual 3D-velocity (combination of the velocity in x, y and z directions) v_n is determined by Eq. [5.8]:

$$v_n = \sqrt{v_x^2 + v_y^2 + v_z^2} \qquad [5.8]$$

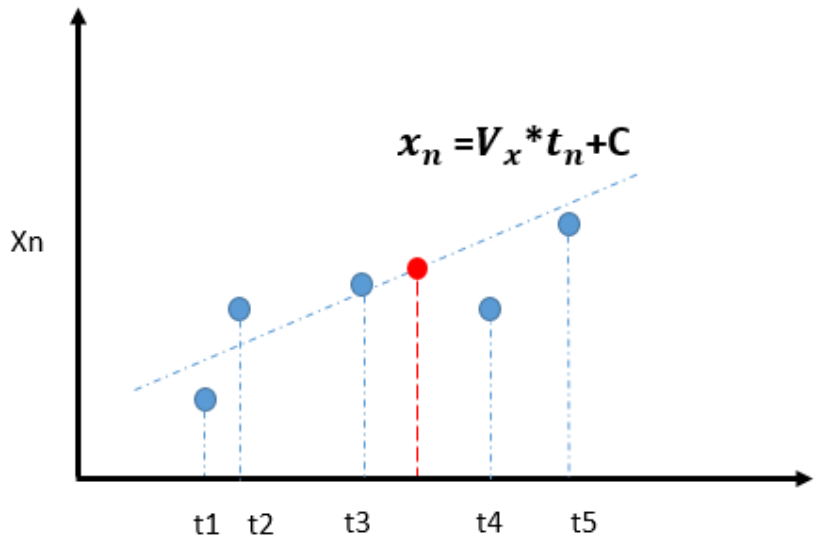

Fig. 5-9. The linear interpolation method to determine the 3D-velocity v_n at time t_n.

These 3 methods produce similar results when the time interval is < 8 ms (Chiti, 2007). The linear interpolation method is demonstrated to be more accurate and flexible than the

other two methods when the time resolution is in the range 8 ms to 20 ms (Chiti, 2007). The averaged time interval applied with PEPT is approximately 10-15 ms as indicated in Fig. 5-4. Thus, the linear interpolation method is more suitable for the current experimental conditions. The method has also been used and reported in other literature and demonstrated to be more accurate and reliable than the 2-point or 6-point method (Guida et al., 2010; Liu, 2013; Liu and Barigou, 2013; Marigo, 2012).

5.2.3. Azimuthally averaged velocity

As a typical Lagrangian method, PEPT records discrete location of the tracer against corresponding time point. The velocity of the tracer derived from the trajectory reflects the flow behaviour of the tracer. The motion of the tracer is simultaneously affected by the other grinding media. By recording sufficient location of the tracer, the velocity field of grinding media within the chamber is obtained from the velocity distribution of the tracer. A Eulerian velocity map is possible to be interpreted from the Lagrangian data obtained with the tracer. The Eulerian velocity map is a visualised tool to evaluate the flow character of the charge under different operating conditions. To convert the Lagrangian data into the Eulerian velocity map, the grinding chamber is divided into finite 3D volume cells by meshes shown in Fig. 5-10. During the grinding process, the tracer may pass the same 3D volume cell many times. The trajectory that passes the same 3D volume cell are grouped to obtain the average value for velocity in the cell. As shown in Fig. 5-10, the line 1 (or curve) and line 2 (or curve) pass the same 3D volume cell at different times. Without accounting for angular position, these 2 trajectories are grouped into the same 2D square cell. Thus, an azimuthally averaged velocity is possible to be calculated to represent the velocity in the cell.

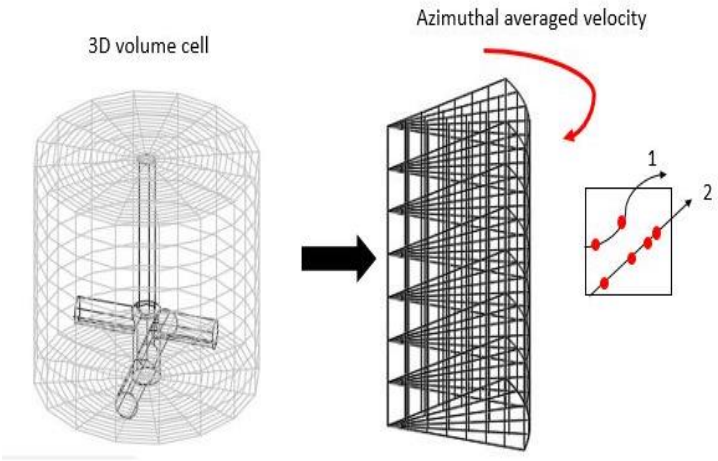

Fig. 5-10. The process of calculation of the azimuthally averaged velocity.

Initially, the grinding chamber is divided into a 3D mesh with dimensions $100 \times 20 \times 150$ (radial × angular × height). Then, it is transferred into a 2D grid by eliminating one dimension in the angular direction. The 2D grid has 2 dimensions in radial and height with dimensions 100×150 (radial × height). The recorded locations within the same radial distance and height distance are grouped into the same square cell in the 2D grid. The number of the trajectory passing through the same 2D square cell is counted. The frequency is normalised by the maximum number counted in the 2D square cells. The averaged velocity in each 2D square cell is defined as the sum of the trajectory distance divided by the total residential time in the cell. The equation is shown as:

$$\bar{v} = \frac{\sum_i v_i \Delta t_i}{\sum_i \Delta t_i} \qquad [5.9]$$

Eq. [5.9] is applied to calculate the velocity in x, y, z direction and the 3D-velocity for the corresponding azimuthally averaged value.

The grinding chamber is a symmetrical cylinder. The half section indicated by the red line is used as the area to show the distribution of the velocity and tracer residence time (see Fig 5-11). The area is divided into the upper band, stirred band and lower band by the relative position to the stirrer.

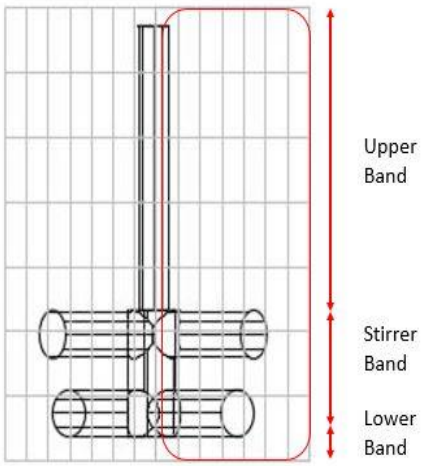

Fig. 5-11. The chamber is divided into the upper band, stirrer band and lower band based on the relative position of the stirrer.

5.3. Analysis of experimental data

The PEPT results obtained under the different operating conditions (e.g. tip speed, type of grinding media and geometry of stirrer) are analysed and compared. The velocity map, vectors of flow direction and frequency rate are demonstrated.

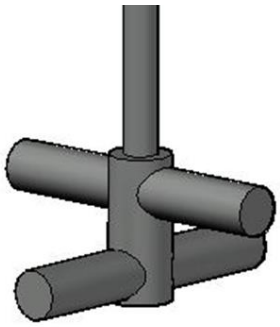

Fig. 5-12. The standard stirrer (Type a) used in PEPT experiment.

The laboratory scale mill of which the chamber volume is 2.9 L is used for experiment. The ratio of the charged slurry is 33 % (v/v) based on the chamber volume. The grinding media filling ratio is 52 % (v/v) based on the whole volume of the charge. The standard stirrer *Type a* (see Fig. 5-12) is used for the experiment unless otherwise stated. This pin-type stirrer has no specific pitched angle so no extra force is generated to pump fluid upwards or downwards. The type grinding media, tip speed and solids concentration are specified in each set of the experiment.

The geometry of the grinding chamber and the relative position of the standard stirrer *Type a* are demonstrated in Fig. 5-13. The diameter of the grinding chamber is 0.14 m (D_c) and the height is 0.19 m (H). The diameter of the standard stirrer *Type a* is 0.125 m (d_s). Thus, the ratio of the stirrer diameter over the diameter of the grinding chamber is 0.89 (d_s/D_c). This indicates the gap between the wall of the chamber and tip of the stirrer is very narrow.

The aspect ratio of the grinding chamber is 0.73 (D_c/H) and the bottom clearance distance is 0.017 m. This distance allows the slurry to move under the stirrer.

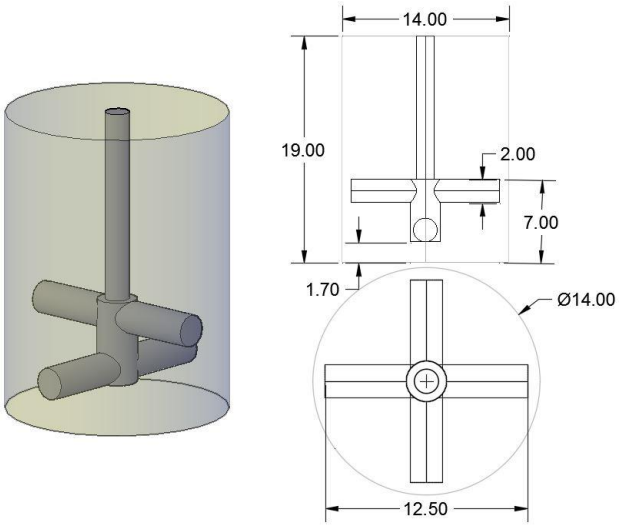

Fig. 5-13. The grinding chamber geometry with the standard stirrer Type a (units in cm).

5.3.1. Tip speed

To study the effect of tip speed on the flow pattern, the experiments with PEPT were conducted with Carbolite (grinding media size +0.8-1.2 mm; density 2.71 g/cm^3) at 4 tip speeds: V_t=5.23 m/s (800 RPM), 6.54 m/s (1000 RPM), 7.85 m/s (1200 RPM) and 9.81 m/s (1500 RPM). The solids concentration was 75 % (w/w). The results for the grinding media velocity distribution are presented into radial, tangential and vertical directions.

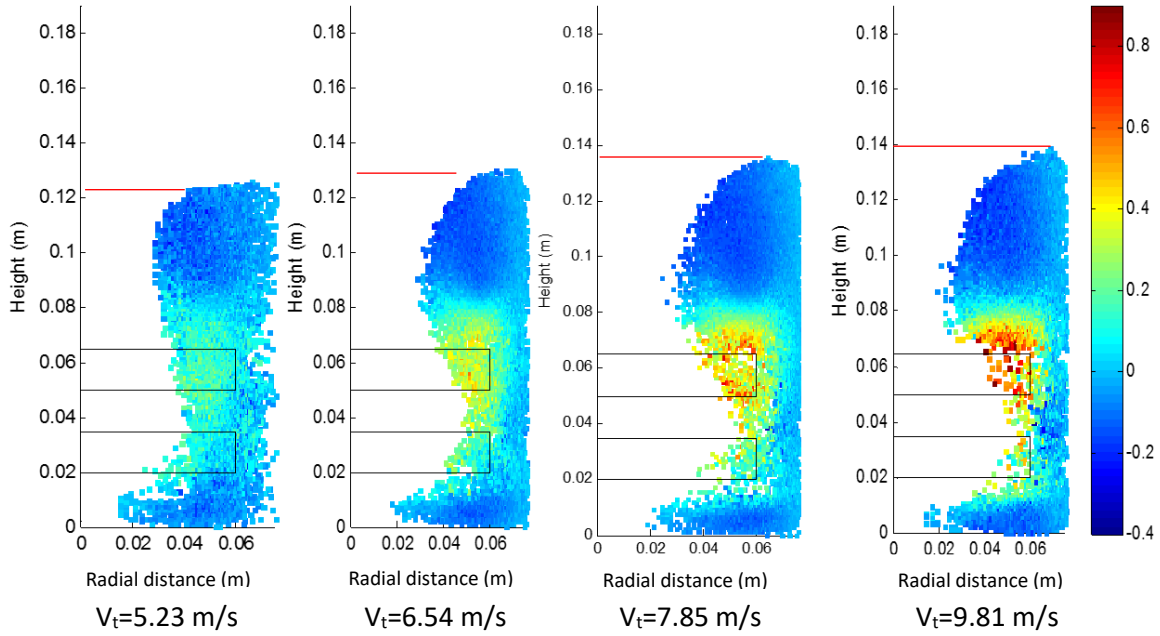

Fig. 5-14. The velocity in radial direction using Carbolite (grinding media size +0.8-1.4 mm) at V_t=5.23 m/s (800 RPM), 6.54 m/s (1000 RPM), 7.85 m/s (1200 RPM), 9.81 m/s (1500 RPM). The colour bar units in m/s.

Fig. 5-14 shows the distribution of the velocity in the radial direction (from the chamber centre points to the wall) at 4 different tip speeds. The vertical and horizontal axis of the graphs are the real distance for the chamber height and radius respectively. The velocity magnitude is indicated by the colour bar with dimensional units in m/s.

By increasing the tip speed, the velocity around the stirrer band is clearly increased. The coloured field is where the tracer is tracked. The unoccupied field (white area) around the stirrer band expands with increasing the tip speed. At the highest tip speed V_t=9.81 m/s, the maximum velocity for the grinding media in radial direction reaches 0.8 m/s in the stirrer band. The level of the slurry (indicated by the red line) is approaching 0.14 m. When the V_t drops down to 5.23 m/s, the slurry level drops to 0.12 m. The area marked by the

dark blue and green indicates the radial velocity is within 0.2 m/s. The maximum radial speed observed at lowest tip speed V_t=5.23 m/s is no more than 0.4 m/s.

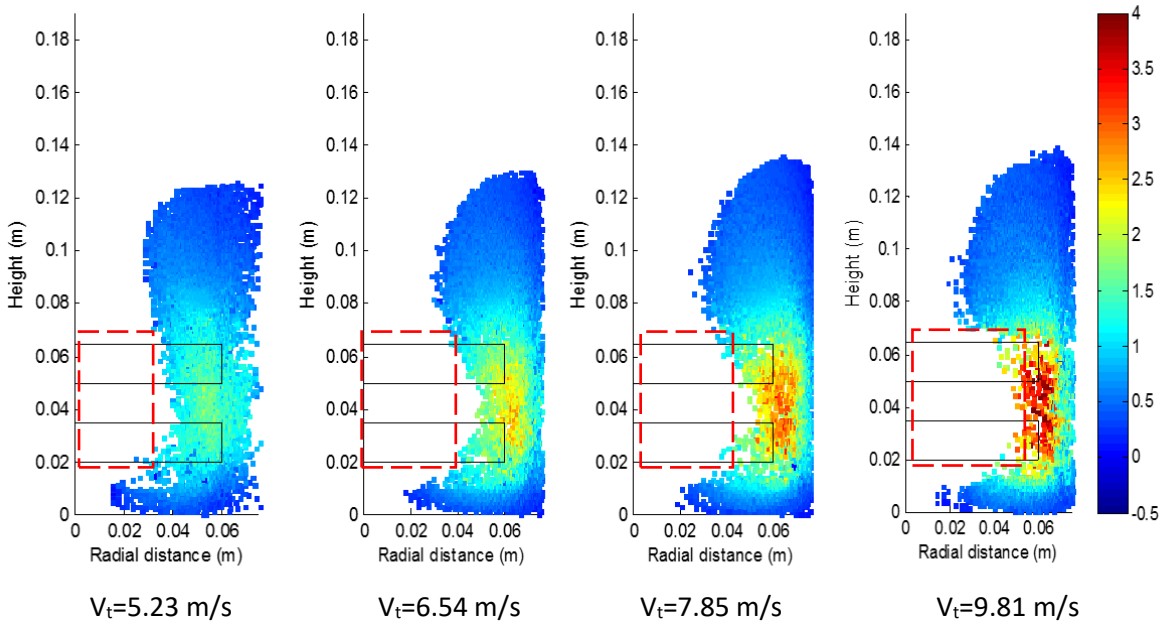

Fig. 5-15. The velocity in tangential direction using Carbolite (grinding media size +0.8-1.4 mm) at V_t=5.23 m/s (800 RPM), 6.54 m/s (1000 RPM), 7.85 m/s (1200 RPM), 9.81 m/s (1500 RPM). The colour bar units in m/s.

Fig. 5-15 displays the map of tangential velocity obtained at 4 tip speeds: V_t=5.23 m/s (800 RPM), 6.54 m/s (1000 RPM), 7.85 m/s (1200 RPM) and 9.81 m/s (1500 RPM). The tangential velocity range expands to the maximum value 3.5 m/s which is much larger than the magnitude of the velocity in the radial direction (no more than 1 m/s). This implies that when the stirrer rotates, the kinetic energy of the grinding media is gained primarily in the tangential direction. The tangential velocity is also the main source for the shear stress. The shear stress between particle/particle and particle/wall is the main force for breaking particles.

Although the largest magnitude of tangential velocity is observed at the highest tip speed V_t=9.81 m/s, it resulted in the largest unoccupied area indicated by the red box (see Fig. 5-15). The tangential velocity of the grinding media is increased with increasing the tip speed, but the filled area in the stirrer band is decreased due to the large centrifugal force. This explains why the particle size cannot be efficiently reduced by simply increasing the tip speed. It is important to balance the filling of the grinding media into the stirrer band and the tangential velocity of the grinding media.

Compared with the velocity magnitude observed in the radial direction, the overall magnitude of the velocity in the tangential direction is much higher. However, the upper band still indicates very slow movement of the grinding media. The velocity either in radial or tangential direction observed in the upper band is not improved by increasing the tip speed. As a typical non-Newtonian (shearing thinning) suspension, the viscosity of the slurry in the upper band is much larger than the rest of the chamber as the velocity is not very high.

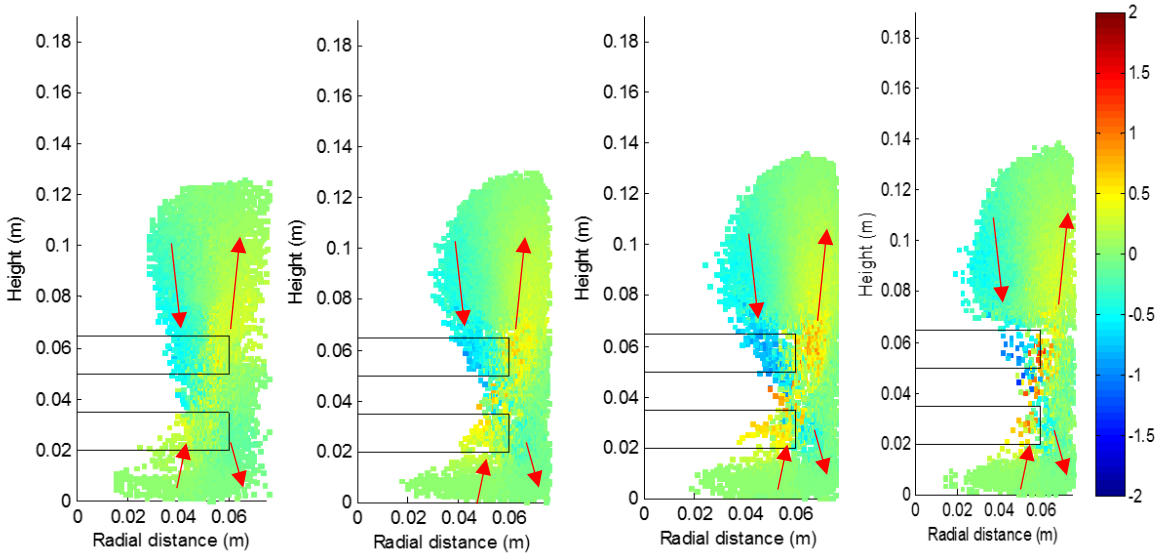

Fig. 5-16. The velocity in vertical direction using Carbolite (grinding media size +0.8-1.4 mm) at V_t=5.23 m/s (800 RPM), 6.54 m/s (1000 RPM), 7.85 m/s (1200 RPM), 9.81 m/s (1500 RPM). The colour bar units in m/s.

Fig. 5-16 displays the map of the velocity in the vertical direction. The observed velocity range is between -2 m/s to 2 m/s. The negative value indicates the velocity moving downwards (towards the grinding chamber bottom) while the positive value means moving up. The flow direction is indicated by the red arrow. A clear convection flow is observed in both upper band and lower band.

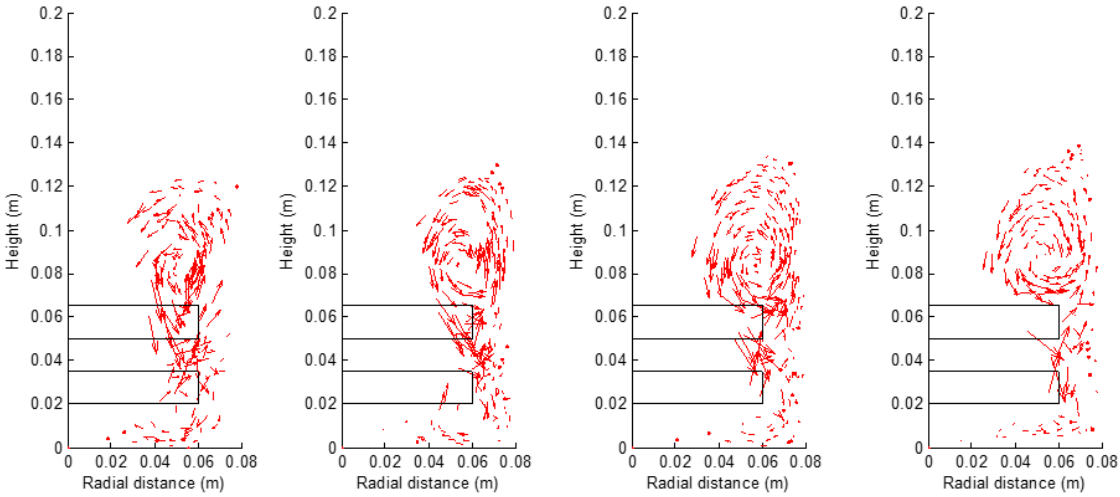

Fig. 5-17. The velocity vector using Carbolite (grinding media size +0.8-1.4 mm) at V_t=5.23 m/s (800 RPM), 6.54 m/s (1000 RPM), 7.85 m/s (1200 RPM), 9.81 m/s (1500 RPM).

Fig. 5-17 exhibits the two circulations obtained at 4 different tip speeds: V_t=5.23 m/s (800 RPM), 6.54 m/s (1000 RPM), 7.85 m/s (1200 RPM) and 9.81 m/s (1500 RPM). The loop shape in the upper band is clearly modified by increasing the tip speed. A similar flow path for the grinding media was also reported by Barley et al. (2004). In the upper band, the grinding media near the wall is moving upward denoted as the positive velocity while the grinding media near the shaft is moving down towards the impeller area. The opposite flow direction of the grinding media is observed in the lower band. Overall, a counter-clockwise circulation is formed in the upper band and a small clockwise circulation is observed in the lower band area between the stirrer band and the chamber floor.

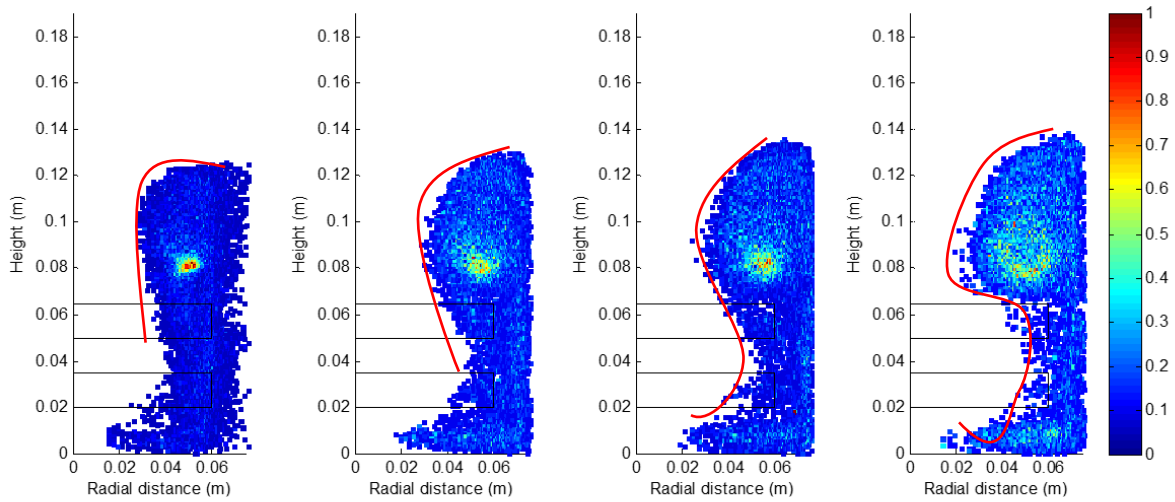

Fig. 5-18. The normalised occupancy rate obtained using Carbolite (grinding media size +0.8-1.4 mm) at V_t=5.23 m/s (800 RPM), 6.54 m/s (1000 RPM), 7.85 m/s (1200 RPM), 9.81 m/s (1500 RPM). The colour bar has no units.

Fig. 5-18 displays the occupancy rate obtained at 4 tip speeds V_t=5.23 m/s (800 RPM), 6.54 m/s (1000 RPM), 7.85 m/s (1200 RPM) and 9.81 m/s (1500 RPM). It is normalised by the maximum pass number obtained in each corresponding square cell to enhance the clarity. With increasing the tip speed, the average occupancy is increased. This implies that the tracer is moving more randomly. Hence, more uniformly distributed locations are tracked by increasing the tip speed. No tracer location is detected near the shaft or in the chamber centre. A vortex-shape free surface is formed steadily. The outline of the vortex (indicated by the red line) exhibits an obvious variation against the tip speed. With increasing the tip speed, the void area in the stirrer band is clearly increased.

If a vertical line along the chamber height is drawn at the radial position r (horizontal distance from the chamber centre), the ratio (r/R where R is the radius of the chamber bottom) indicates the relative position of the vertical line. The values of 3D-velocity on the vertical line are extracted.

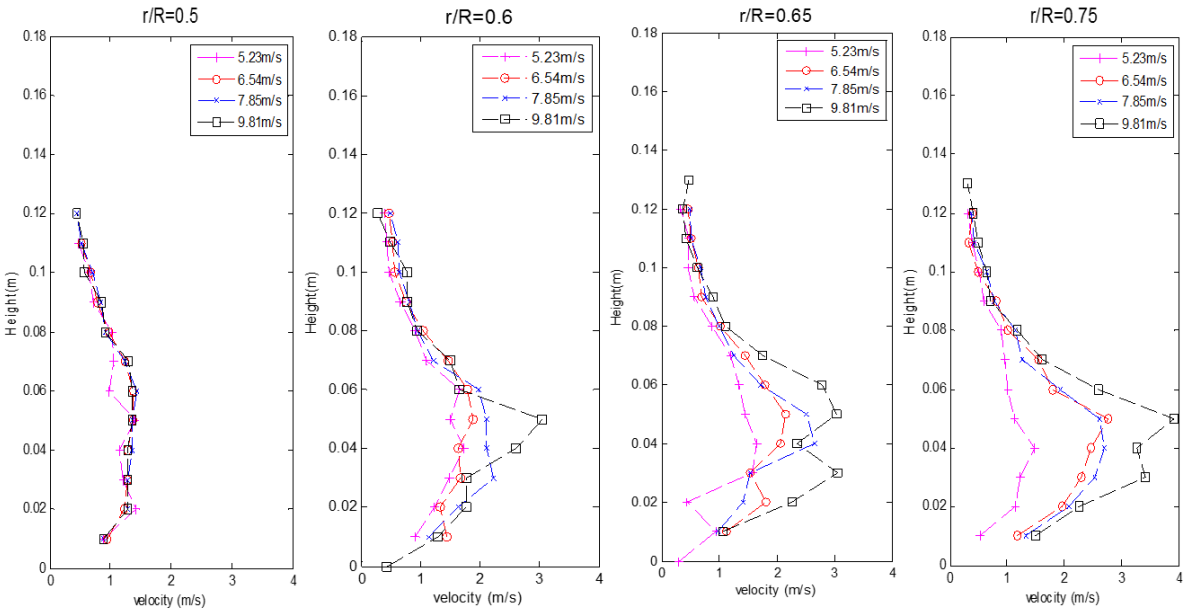

Fig. 5-19. The 3D-velocity profile in the radial position r/R=0.5, 0.6, 0.65 and 0.75 using Carbolite (grinding media size +0.8-1.4 mm) at V_t=5.23 m/s (800 RPM), 6.54 m/s (1000 RPM), 7.85 m/s (1200 RPM), 9.81 m/s (1500 RPM).

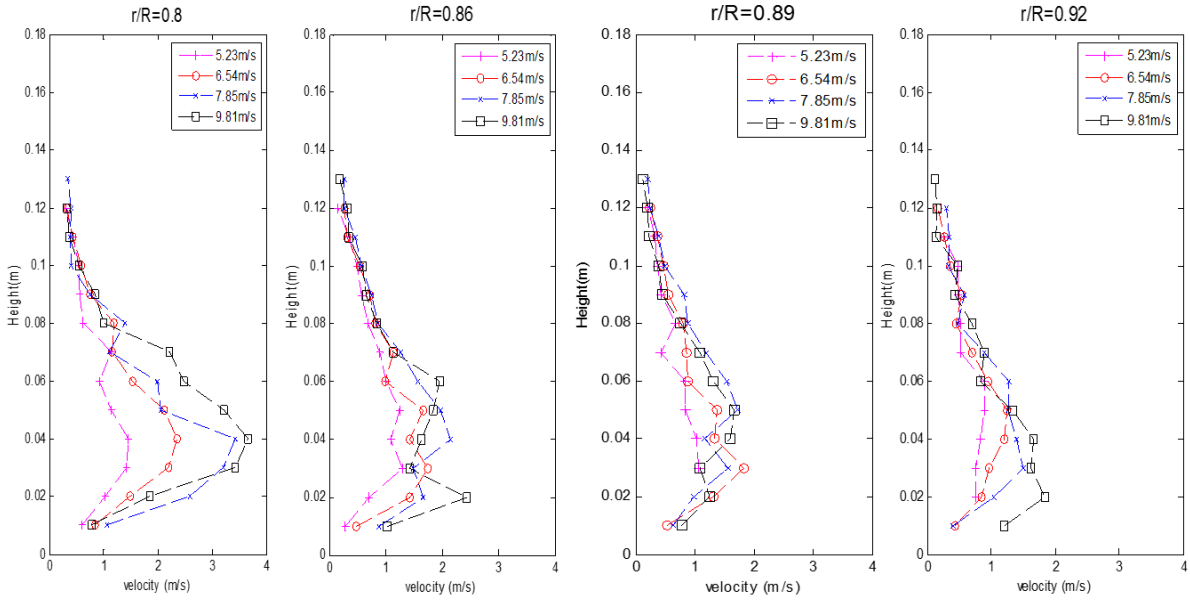

Fig. 5-20. The 3D-velocity profile in the radial position r/R=0.8, 0.86, 0.89 and 0.92 using Carbolite (grinding media size +0.8-1.4 mm) at V_t=5.23 m/s (800 RPM), 6.54 m/s (1000 RPM), 7.85 m/s (1200 RPM), 9.81 m/s (1500 RPM).

The values of 3D-velocity extracted from the vertical line at different positions are compared in Fig. 5-19 (r/R=0.5, 0.6, 0.65 and 0.75) and Fig. 5-20 (r/R=0.8, 0.86 0.89 and 0.92). The ratio r/R indicates the relative distance of the vertical line to the chamber

centre. For example, if r/R=0.89, it means the radial position (r) of the vertical line is 6.25 cm. The chamber radius is 0.7 cm. Thus, r/R= 6.25/0.7.

From r/R=0.5 to r/R=0.75, when the tip speed is constant, the 3D-velocity is increased with increasing the radial location r (see Fig. 5-19). Contrarily, from r/R= 0.89 to r/R=0.92 (see Fig. 5-20), the 3D-velocity is decreased with increasing the radial location (r). This implies from the area around the stirrer to the chamber wall, the particle velocity increases to a maximum then it drops. This trend causes a velocity gradient to exist in the gap between the tip of the stirrer and the chamber wall. This also demonstrates that the motion of grinding media slows down when the grinding media approaches the chamber wall.

At the same r/R, the 3D-velocity is higher when a higher tip speed is applied. Above the height 0.08 m where is the upper band, no significant difference in the 3D-velocity is observed when increasing the tip speed at any radial position of r/R. Between the height 0.08-0.02 m (impeller band), the 3D-velocity at the same location (r/R) is significantly increased by increasing the tip speed. This concludes that the influence of different tip speed mainly affects the velocity profile in the impeller band. No obvious influence on the velocity distribution is observed in either upper band or lower band.

5.3.2. Grinding media density

The maps of the 3D-velocity obtained using 2 different grinding media (ZirPro and Carbolite) are shown in Fig. 5-21 (V_t= 5.23 m/s), Fig. 5-23 (V_t= 6.54 m/s), Fig. 5-25 (V_t=7.85 m/s) and Fig. 5-27 (V_t= 9.81 m/s). The details of corresponding 3D-velocity profiles at r/R from 0.8 to 0.92 (this range is close to the stirrer tip) are compared in Fig. 5-22, Fig. 5-24, Fig. 5-26 and Fig. 5-28 respectively. Carbolite has a specific gravity 2.7 $\pm$ 0.1, while ZirPro has a specific gravity 3.2 $\pm$ 01. The size range for both grinding media is +0.8 -1.2 mm. The solids concentration is maintained at 75 % (w/w).

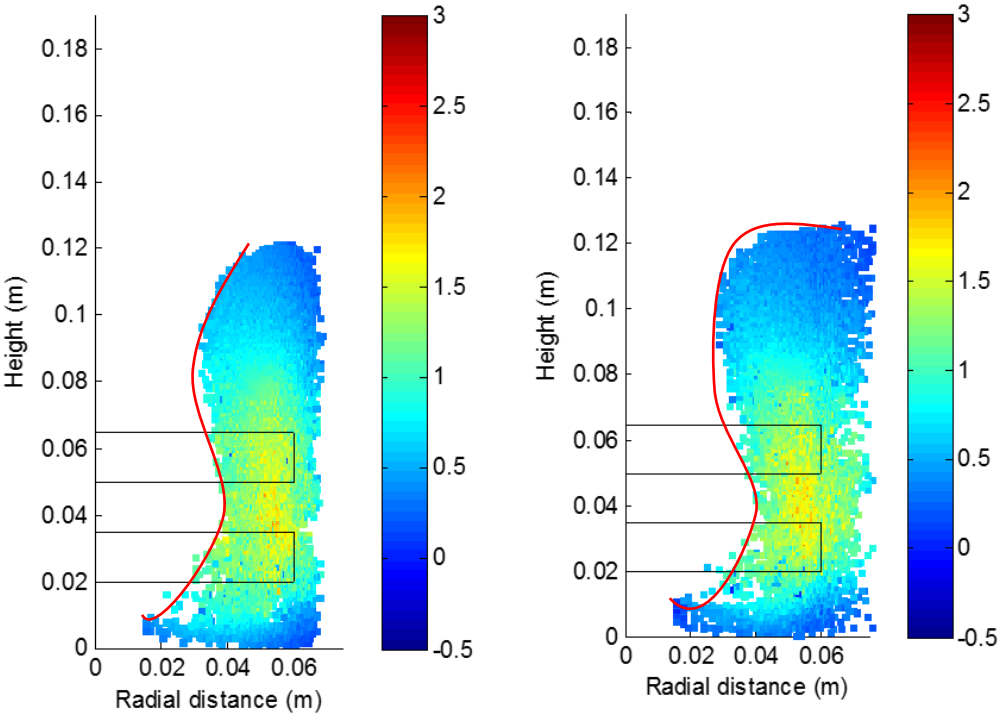

Fig. 5-21. The 3D-velocity map obtained using ZirPro and Carbolite at V_t=5.23 m/s. The colour bar units in m/s.

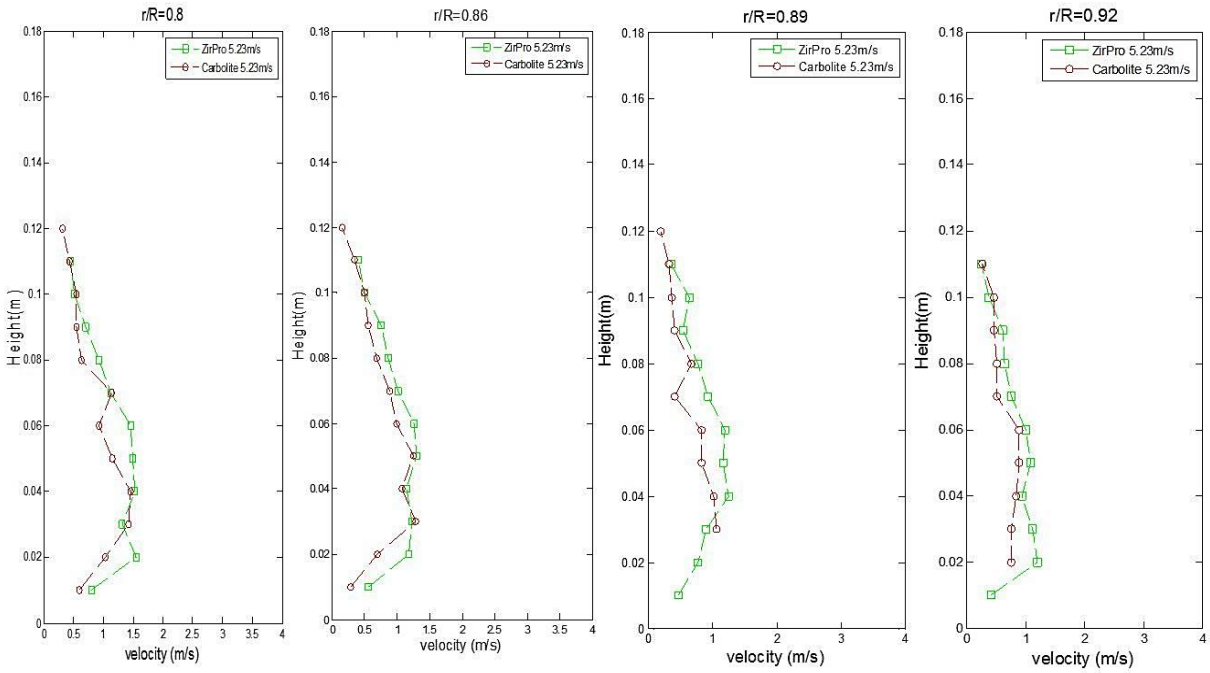

Fig. 5-22. The 3D-velocity profile obtained using ZirPro and Carbolite at V_t=5.23 m/s. The radial position is r/R=0.8, 0.86, 0.89 and 0.92.

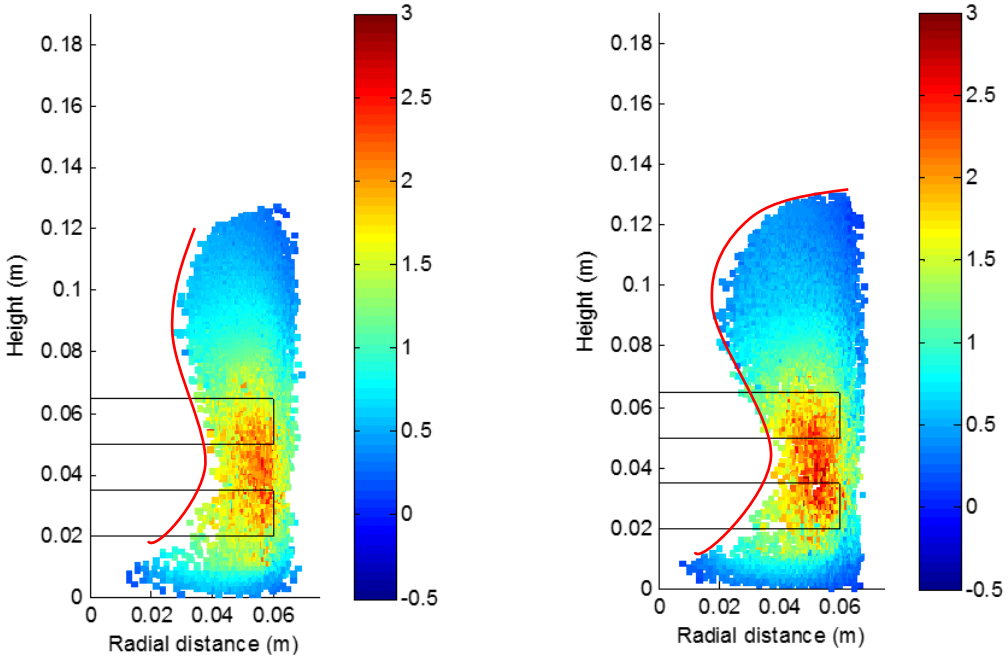

ZirPro at V_t=6.54 m/s Carbolite at V_t=6.54 m/s

Fig. 5-23. The 3D-velocity map obtained using ZirPro and Carbolite at V_t=6.54 m/s. The colour bar units in m/s.

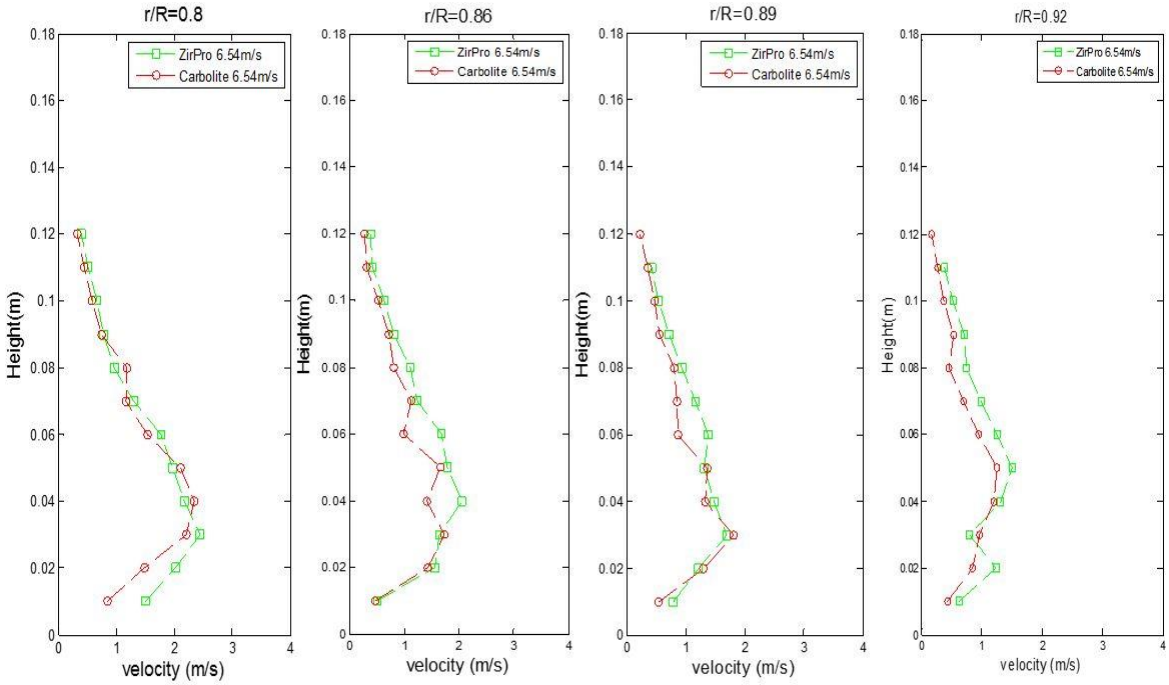

Fig. 5-24. The 3D-velocity profile obtained using ZirPro and Carbolite at V_t=6.54 m/s. The radial position is r/R=0.8, 0.86, 0.89 and 0.92.

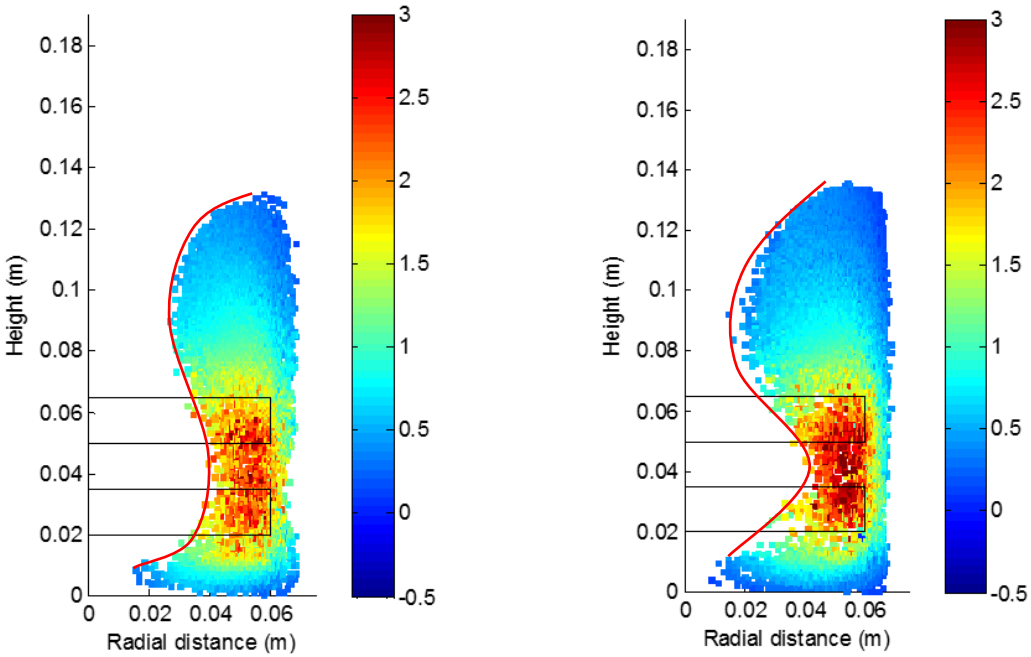

Fig. 5-25. The 3D-velocity map obtained using ZirPro and Carbolite at V_t=7.85 m/s. The colour bar units in m/s.

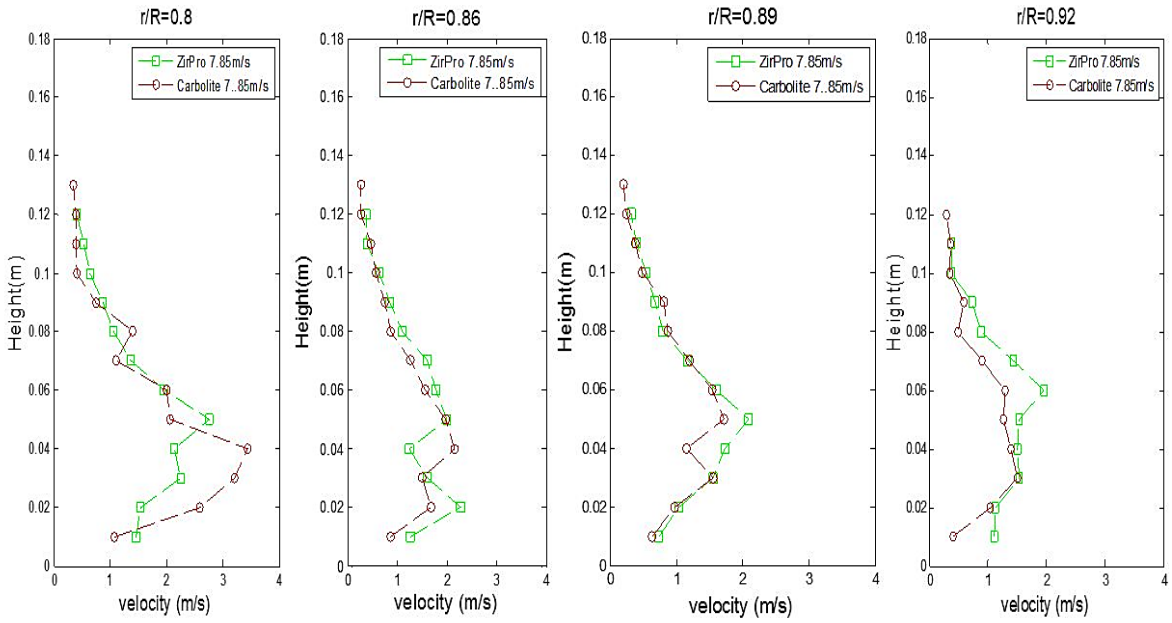

Fig. 5-26. The 3D-velocity profile obtained using ZirPro and Carbolite at V_t=7.85 m/s. The radial position is r/R=0.8, 0.86, 0.89 and 0.92.

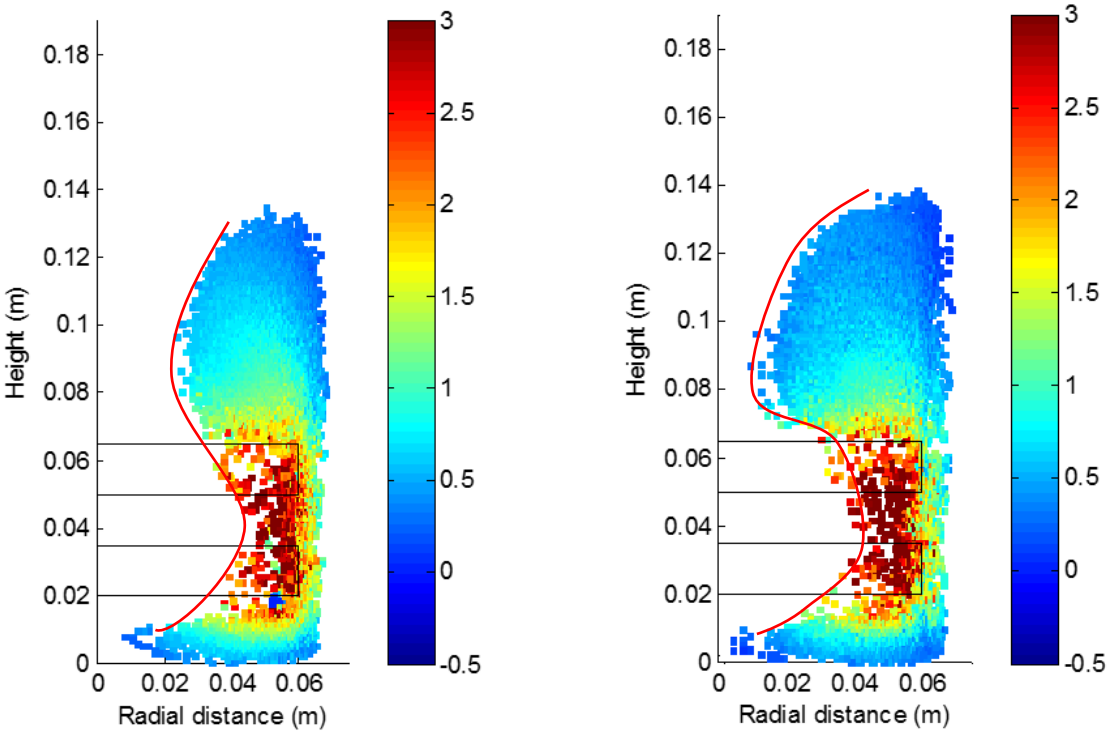

ZirPro at V_t=9.81 m/s

Carbolite at V_t=9.81 m/s

Fig. 5-27. The 3D-velocity map obtained using ZirPro and Carbolite at V_t=9.81 m/s. The colour bar units in m/s.

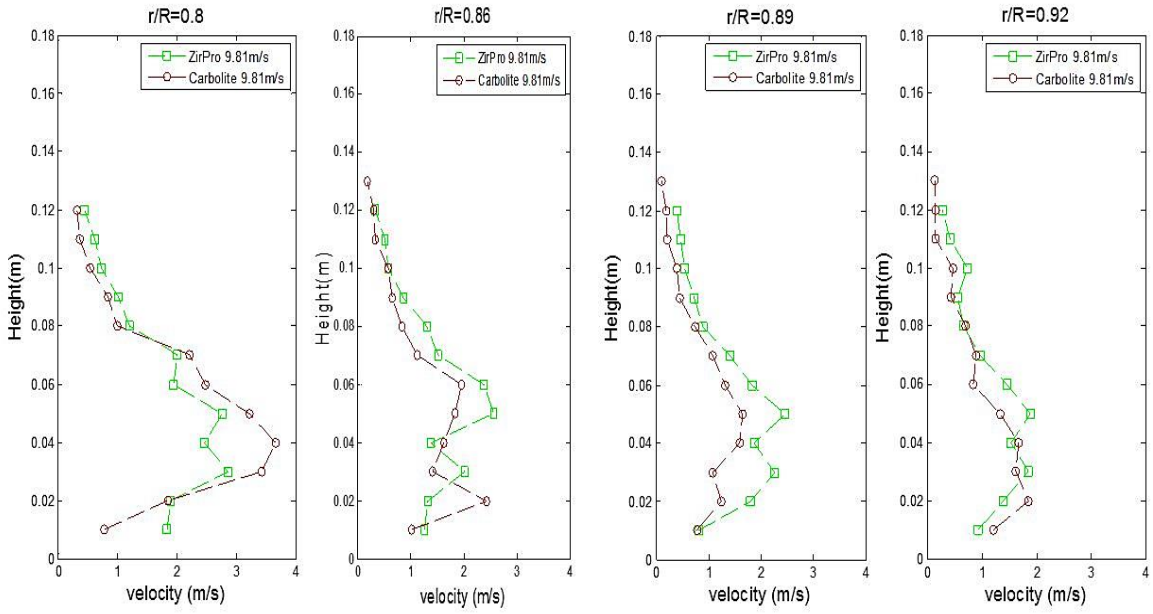

Fig. 5-28. The 3D-velocity profile obtained using ZirPro and Carbolite at V_t=9.81 m/s. The radial position is r/R=0.8, 0.86, 0.89 and 0.92.

At the lowest tip speed V_t=5.23 m/s (see Fig. 5-21), the 3D-velocity maps obtained using ZirPro and Carbolite are similar. A difference is observed in the outline shape of the vortex indicated by the red line in the graphs. At the same tip speed, more grinding media is present in the area where the height is over 0.08 m in the velocity map from Carbolite than ZirPro. In the impeller band (height < 0.08 m), more grinding media is present when using ZirPro. A smoother free surface of the vortex is observed in the velocity map using ZirPro compared to Carbolite. This phenomenon becomes more obvious when the higher tip speed is applied (for V_t=6.54 m/s see Fig. 5-23, V_t=7.85 m/s see Fig. 5-25 and V_t=9.81 m/s see Fig. 5-27).

The detailed 3D-velocity profiles using ZirPro and Carbolite are compared in Fig 5-22 (V_t=5.23 m/s), Fig 5-24 (V_t=6.54 m/s), Fig 5-26 (V_t=7.85 m/s) and Fig 5-28 (V_t=9.81 m/s). The magnitude of the 3D-velocity obtained using ZirPro is slightly larger than the 3D-velocity using Carbolite at the radial position r/R=0.86, 0.89 and 0.92. Especially at radial position

r/R=0.89 and 0.92 where the gap between the stirrer tip and chamber wall occurs, it is clear to see that the 3D-velocity profile obtained using ZirPro displays a higher magnitude than the results obtained using Carbolite. At r/R=0.8 close to the shaft, the velocity of Carbolite grinding media shows slightly higher magnitude than the velocity of ZirPro as the denser grinding media is more likely to settle down.

This is of great importance to improve the grinding efficiency because any improvements in the laboratory scale mill can be scaled up when the volume of grinding mill is increased. The small alteration in the mill chamber would result in a great improvement in the efficiency of the energy utilisation.

5.3.3. Grinding media size

The different size of ZirPro grinding media is used to study the influence of the grinding media size. The size range used for the experiments are: +0.7-1.4 mm, +1.6-2.0 mm and +2.0-2.4 mm. The V_t is constant at 6.54 m/s (1000 RPM) and solids concentration is 75 % (w/w). The 3D-velocity map obtained with PEPT is shown in Fig. 5-29. The corresponding 3D-velocity profile along the chamber height is plotted in Fig. 5-30.

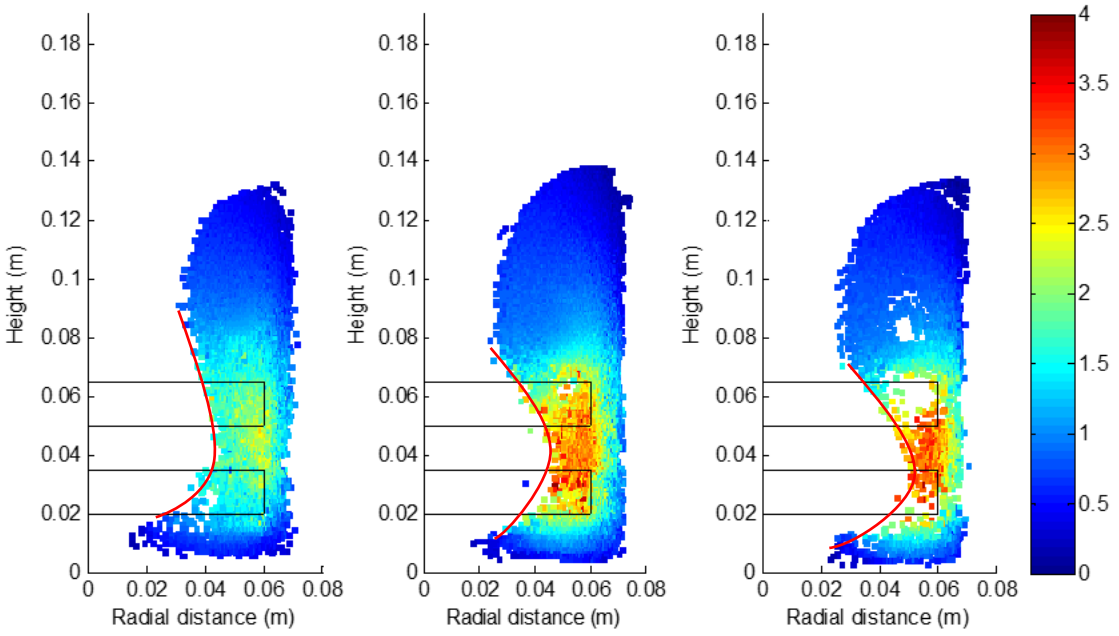

Fig. 5-29. The 3D-velocity map obtained using ZirPro grinding media size +0.7-1.4 mm, +1.6 -2.0 mm and +2.0 -2.4 mm at V_t=6.54 m/s. The colour bar units in m/s.

When the size of the grinding media is increased, it is observed that the overall magnitude of the velocity in the stirrer band (height 0.02~0.08 m) is increased significantly shown in Fig. 5-29 (indicated by colour 'yellow' turning to 'red'). Also, the void field indicated by the red curve is deeper when using a larger size of ZirPro grinding media. The slurry level slightly increases. An evident difference in the velocity is only observed in the impeller band. The slurry motion in the upper band is still slow (<1.5 m/s). This implies the transfer of the movement from the stirrer to the upper band is still not effective when the grinding media size is increased.

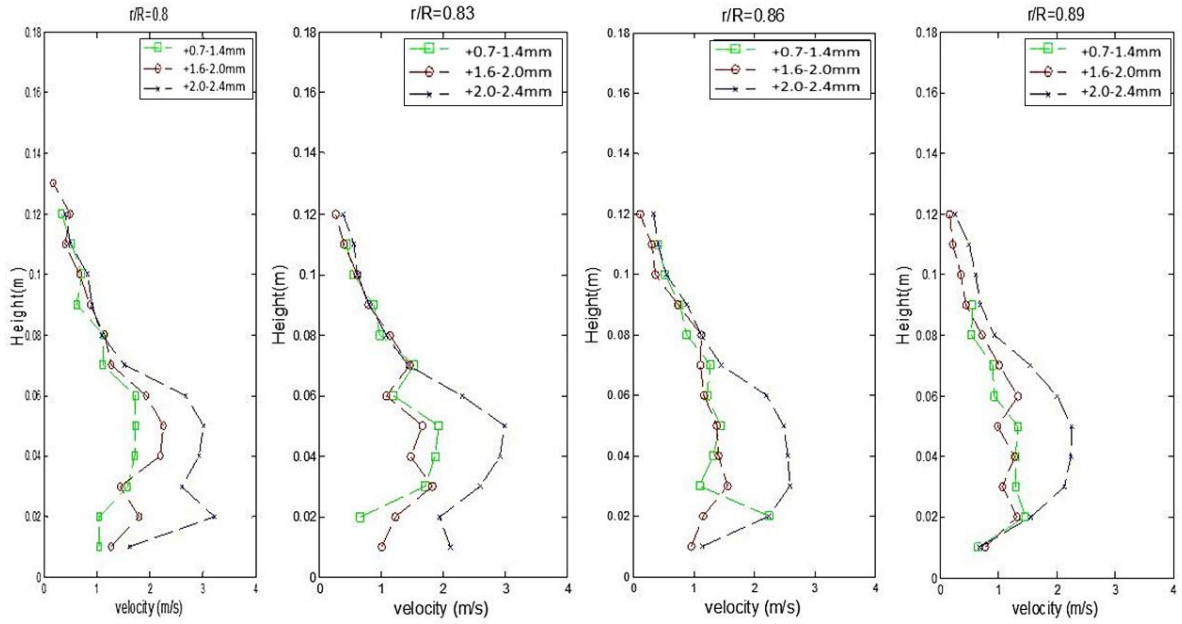

Fig. 5-30. The 3D-velocity profile obtained using ZirPro grinding media size +0.7-1.4 mm, +1.6-2.0 mm and +2.0 -2.4 mm at V_t=6.54 m/s (1000 RPM).

The detailed velocity profile is shown in Fig. 5-30. At the radial position r/R=0.8, 0.86, 0.89 and 0.92, the improvement in the velocity of the grinding media when using a larger grinding media size is clearly demonstrated in the chamber height 0.02 to 0.08 m. The largest velocity is obtained when the largest grinding media size (+2.0-2.4 mm) is used. However, in the upper band, there is no obvious variation in the velocity when the grinding media is changed to a larger size. The size of the grinding media still has limited influence to improve the motion in the upper band.

The 3D-velocity map (see Fig. 5-29) clearly proves that a larger size of the grinding media gives a higher magnitude of velocity in the impeller band. Although it takes more energy to centrifuge a larger grinding media to achieve the same speed, the larger grinding media size (greater weight) will apply stronger stress force on the mineral particle. The limitation is that the improvement is exclusive to the impeller band.

The impeller band is the major field where the mineral particle is broken through the interaction with the grinding media. The 3D-velocity map already shows that a larger size of the grinding media is more helpful in improving the velocity. However, a lower filling of the grinding media in the impeller band is observed when a larger size of the grinding media is used. The phenomenon is indicated by the red curve in Fig. 5-29. Decreasing the amount of the grinding media filled in the impeller band reduces the total number of the effective stress events. The high speed may result in strong stress intensity, but lack of the sufficient stress number may also decrease the grinding efficiency.

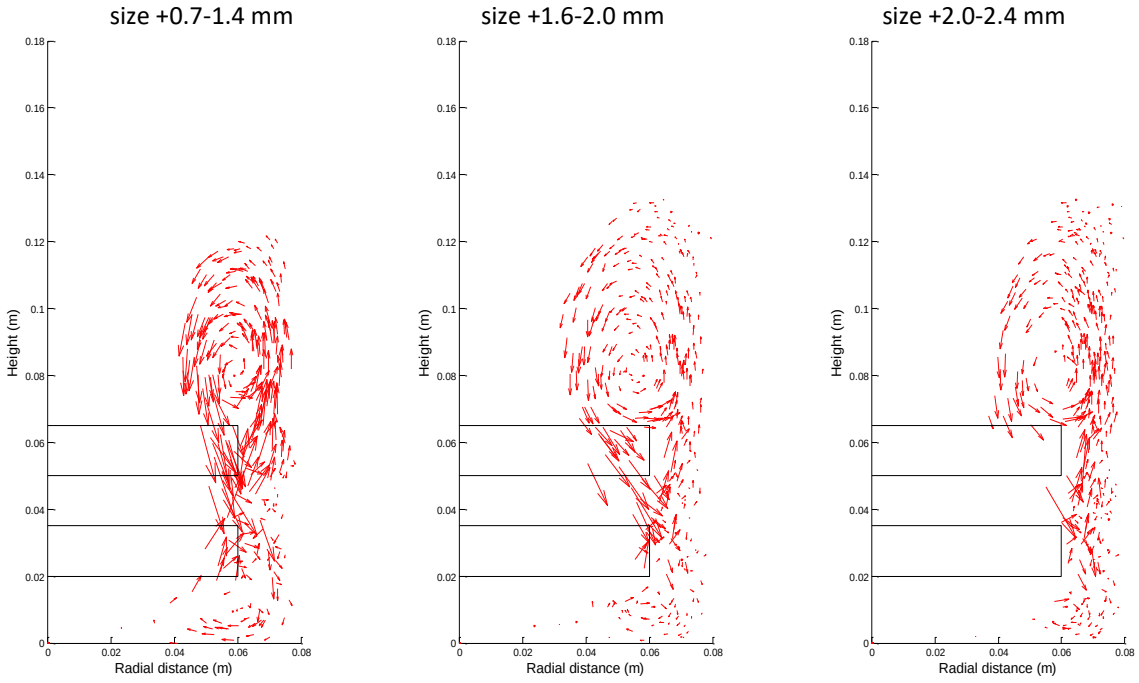

Fig. 5-31. The velocity vector obtained using ZirPro grinding media size +0.7-1.4 mm, +1.6-2.0 mm and +2.0-2.4 mm at V_t=6.54 m/s (1000 RPM).

The velocity vector and occupancy rate distribution are compared in Fig. 5-31 and Fig. 5-32 respectively when ZirPro grinding media with size range +0.7-1.4 mm, +1.6-2.0 mm and +2.0-2.4 mm are used at V_t=6.54 m/s (1000 RPM).

The results indicate the grinding media size has no clear influence on the circulation of the charge. A similar flow path is observed when these 3 different sizes of the grinding media are used. The occupancy rate is greatly improved in the mill chamber when the grinding media size is increased (see Fig. 5-32).

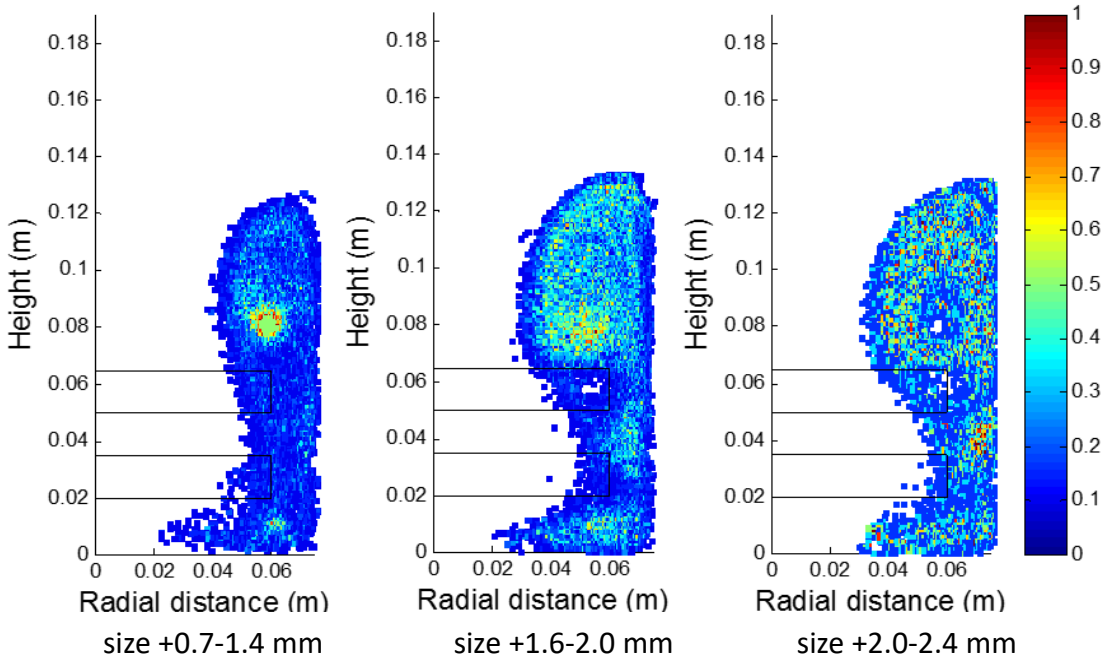

Fig. 5-32. The occupancy rate obtained using ZirPro grinding media size +0.7-1.4 mm, +1.6-2.0 mm and +2.0-2.4 mm at V_t=6.54 m/s (1000 RPM).

The transfer of the momentum in the impeller band is increased when a larger size of the grinding media is used under an identical rotational speed. As seen in Fig. 5-32, the occupancy rate is increased with increasing the grinding media size. This implies that a smaller grinding media may not move as rapidly as a larger grinding media. However, the smaller grinding media fills more space in the impeller band. The velocity of the grinding media and the filling rate in the impeller band affect grinding efficiency simultaneously. It is important to identify the influence caused by the different size of the grinding media.

5.3.4. Influence of stirrer configuration

It was reported that the configuration of the stirrer in a grinding chamber would affect the flow pattern of the charge (Altun et al., 2013). It is observed through PEPT that a large area in the upper band is not fully fluidised. To sufficiently utilise the area in the grinding chamber and improve the stress intensity of the grinding media, some new stirrer configurations are designed and applied in the laboratory scale mill. The flow behaviour is demonstrated by the velocity map obtained with PEPT.

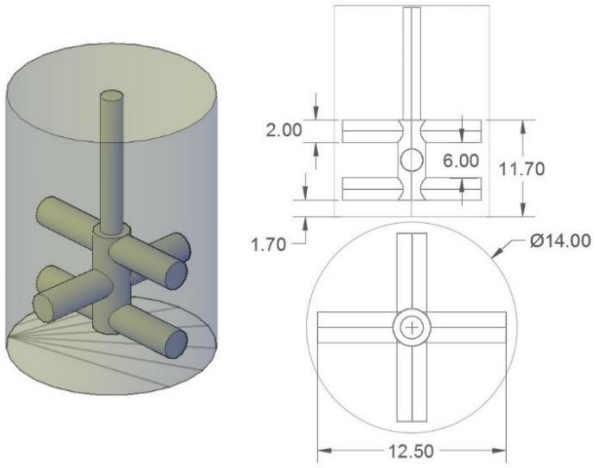

Fig. 5-33. Geometry for the grinding chamber with the 3 layers of the pin stirrer (Type a-1) (units in cm).

Fig. 5-33 exhibits the sketch of stirrer *Type a-1.* Its relative geometry position to the grinding chamber is shown in the figure. The configuration is based on the standard stirrer *Type a*, but this new type is mounted with an extra pair of stirrer arms. Compared to the standard stirrer *Type a* of which the geometry dimension is shown in Fig. 5-13, *Type a-1* increases the height of the impeller band (see Fig. 5-33) from 7 cm (for *Type a*) to 11.7 cm (*for Type a-1*). The impeller band is where the stirrer rotates and the collision between particles and grinding media happens frequently as the stirrer continually interacts with the charge. A

larger area in the chamber will be swept over by stirrer *Type a-1* as more stirrer arms are added.

To avoid the suspensions being stuck in a confined space or the gap between the adjacent stirrer arms, the solids concentration was dropped from 75 % (w/w) to 65 % (w/w) for this experiment. The total mass of the slurry (calcite and water) was kept the same (1 kg) as the previous experiments. ZirPro grinding media (size +0.7-1.4 mm) was used. The V_t was dropped to 4.58 m/s (700 RPM) to avoid spilling the slurry over the top of the grinding chamber. The detailed PEPT results of the 3D-velocity distribution, velocity vector and occupancy rate are shown in Fig. 5-34.

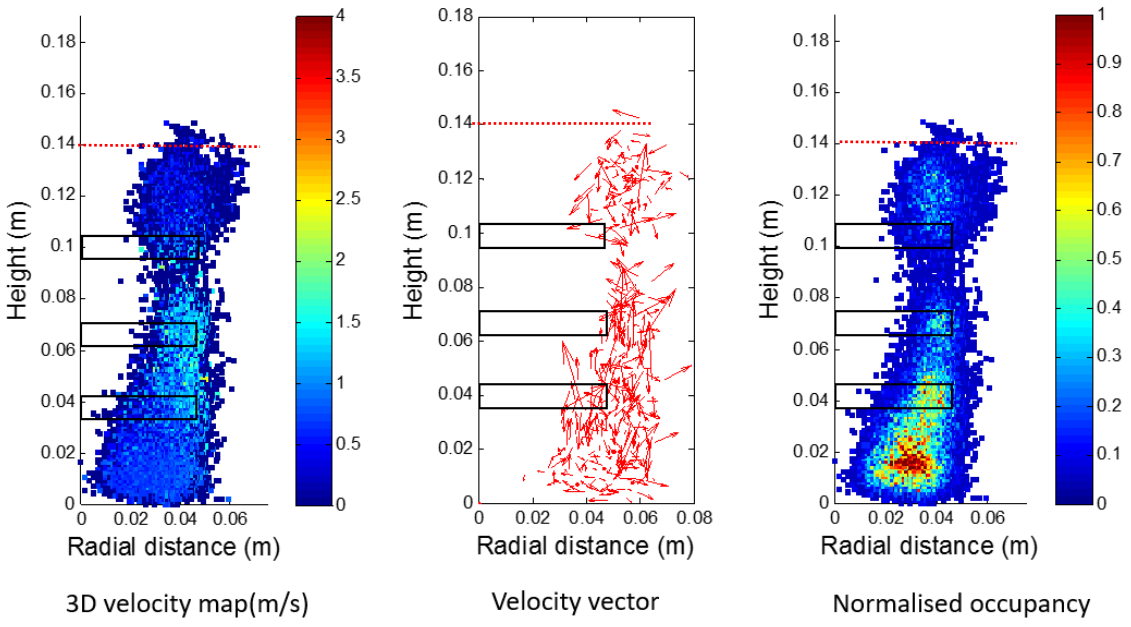

Fig. 5-34. The 3D-velocity map (left, units in m/s), vector (middle) and normalised occupancy rate (right) obtained using 3 layers of the pin stirrer (Type a-1) at V_t=4.58 m/s (700 RPM). The colour bar units in m/s.

As seen from the 3D-velocity map (see Fig. 5-34 left), the maximum velocity reaches approximately 2 m/s. The slurry level is slightly beyond 0.14 m indicated by the red line in the figures. The tip speed is reduced to 4.58 m/s in the experiment lower than the tip

speed used in the previous experiments with the standard stirrer *Type a*, however the level of the slurry is still increased to 0.14 m. The overall distribution of the 3D-velocity is not improved but the fluidisation of the charge is improved when using stirrer *Type a-1*. It is also shown that the impeller band is filled with more grinding media.

The velocity vector (see Fig. 5-34 middle) shows a disordered flow path of the tracer. The circulation path in the upper and lower band observed when using the standard stirrer *Type a* has disappeared. More disordered motion of the grinding media is observed when using *Type a-1*. This undoubtedly increases number of the collisions between mineral particle/mineral particle, mineral particle/wall and mineral particle/grinding media. The occupancy distribution (see Fig. 5-34 left) demonstrates that the tracer flows more around the impeller band and a more homogenous system is obtained.

To compress the slurry towards the impeller band and reduce the void area above the height 0.12 m in the grinding chamber, a thick top cover was applied with stirrer *Type a-1* at the same operating conditions.

The detailed geometry for the grinding chamber is shown in Fig. 5-35. The thickness of the top cover (new thick lid) is 5.3 cm which reduces the chamber height from 19.0 to 13.7 cm. By reducing the empty volume in the upper band, the thick lid forces the slurry to fill into the unoccupied area in the impeller band to improve the efficiency of the moment transfer.

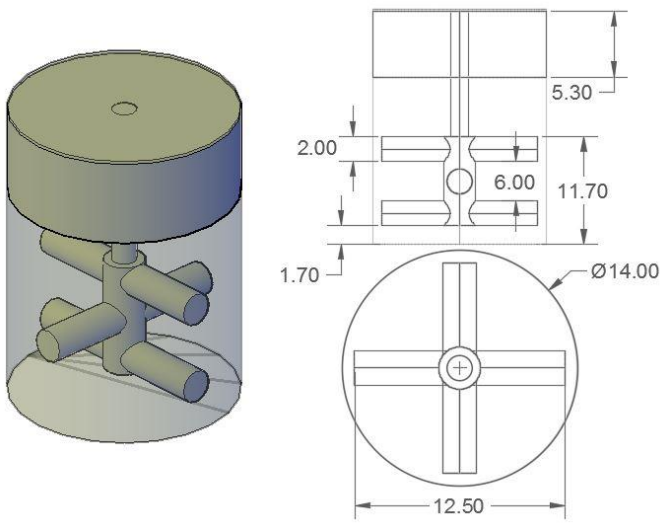

Fig. 5-35. Detailed geometry for the grinding chamber with the 3 layers of pin stirrer (Type a-1) and a thickness enhanced top cover (units in cm).

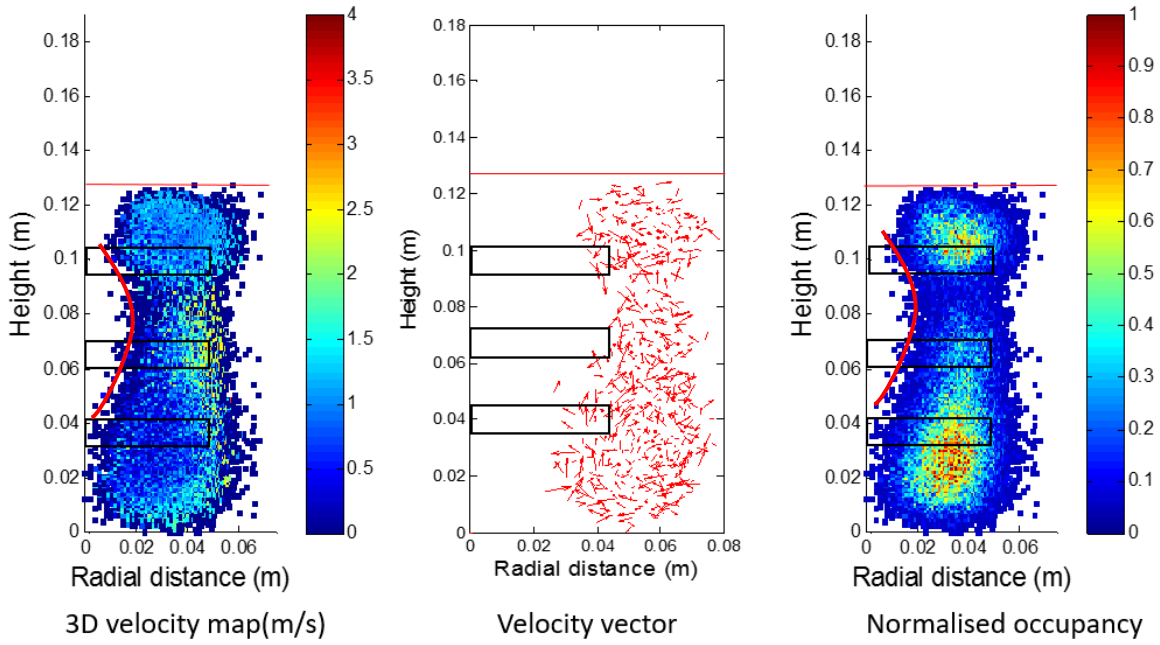

Fig. 5-36. The 3D-velocity map (left, units in m/s), velocity vector (middle) and normalised occupancy rate (right) obtained using 3 layers of the pin stirrer and the thick lid at V_t=4.58 m/s (700 RPM).

The detailed PEPT results are shown in Fig. 5-36. When the thick lid is used with stirrer *Type a-1*, the slurry level is at 0.12 m a drop from 0.14 m. The unoccupied field observed in area between the chamber height 0.02 m to 0.1 m is minimised indicated by the red curve in Fig.

5-36. Due to the constant tip speed, the overall magnitude of the velocity is not increased and the maximum velocity is approximately 2 m/s. An interesting phenomenon is that the two circulation loops disappear and the transition boundary between the impeller band and the upper band disappears. The distribution of the velocity is more uniform across the whole grinding chamber. A clear improvement in the motion of the grinding media in the upper band (>8 cm) is observed. The vector map also proves that the system is highly homogeneous. No stable flow path is indicated in Fig. 5-36 (middle).

The occupancy rate is shown in Fig. 5-36 (right). A high occupancy rate is observed in both the upper and lower bands. By using a thick top lid, filling of the grinding media in the stirrer band is increased. This also improves the uniformity in distribution of frequency over the whole grinding chamber. Particularly, it alters the flow behaviour above the stirrer. A more dynamic flow is observed.

As seen from Fig. 5-36, when the thick lid is applied, the effect of vortex is greatly reduced. Due to the centrifugal force, the charge is driven to the chamber wall and a vortex is observed around the stirrer shaft without the thick lid. This vortex reduces filling of the grinding media in the field and causes a waste of energy. The application of the thick lid reduces the empty space in the chamber. This effectively drops the level of the charge and drives them to flow back into the centre of the grinding chamber. As the volume of the grinding chamber is reduced with the thick lid, the heat generated from the grinding process is difficulty to dissipate. This causes a rise in the temperature. It is estimated that the temperature could be increased by 10$\sim$20 ℃ inside the chamber.

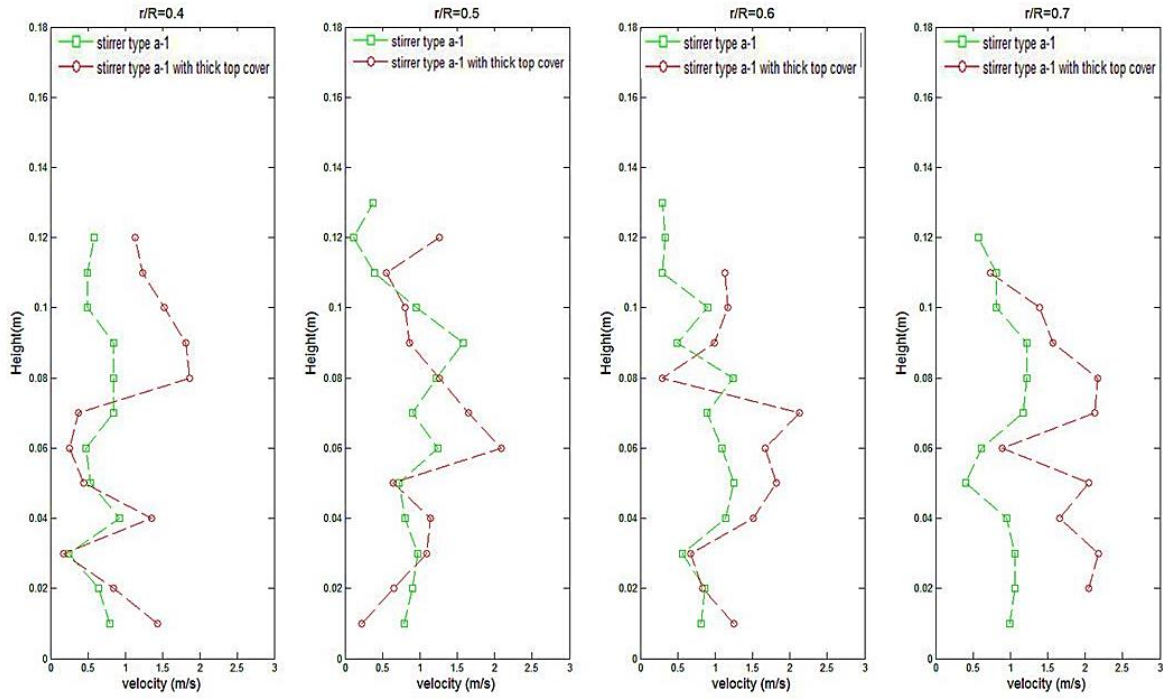

Fig. 5-37. The 3D-velocity profile obtained using stirrer Type a-1 with and without thick lid at V_t=4.58 m/s (700 RPM). The radial position r/R=0.4, 0.5, 0.6 and 0.7.

The comparison of 3D-velocity profiles obtained using the normal lid and the thick lid are shown in Fig. 5-37 (radial position r/R= 0.4, 0.5, 0.6 and 0.7). At the radial position r/R=0.4, there is no obvious difference in the magnitude of the 3D-velocity below the chamber height 0.08 m. However, above the height 0.08 m, the 3D-velocity obtained with the thick lid is faster. This proves that the thick lid is effective in improving the motion of the grinding media in the upper band.

At the position r/R=0.5, 0.6 and 0.7, an improvement is observed across the grinding chamber. The 3D-velocity magnitude obtained with the thick lid still illustrates faster movement of the grinding media than the result obtained using the normal lid. This simple approach of replacing the normal lid with a thicker lid greatly enhances the overall

distribution of the 3D-velocity. It efficiently alters the flow pattern and increases the movement of the slurry without extra energy input.

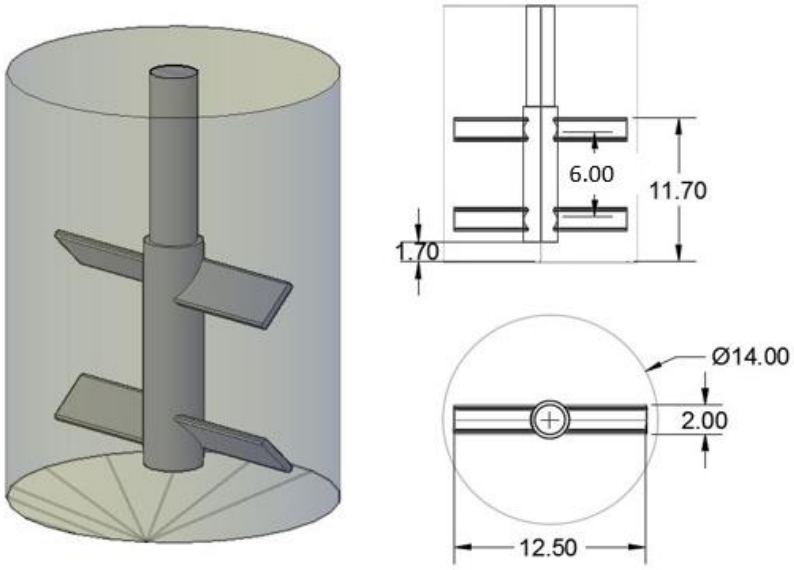

Fig. 5-38. Detailed geometry for stirrer Type a-2 (2 pairs of the pitched blades) and its relative position in the grinding chamber (units in cm).

Another design of the stirrer (*Type a-2)* is shown in Fig. 5-38. It replaces the pin stirrer by pitched flat blades. The pitched angle of the upper blade is designed to generate force pushing the charge downwards while the lower blade pushes the charge upwards. To provide enough space between the 2 pairs of blades, the gap between the adjacent stirrers is increased from 1.3 cm (standard stirrer *Type a*) to 6 cm. The design concept is to maximise the collision and contact within the region swept by the stirrer and draw the slurry flowing back into the region rather than centrifuging it away.

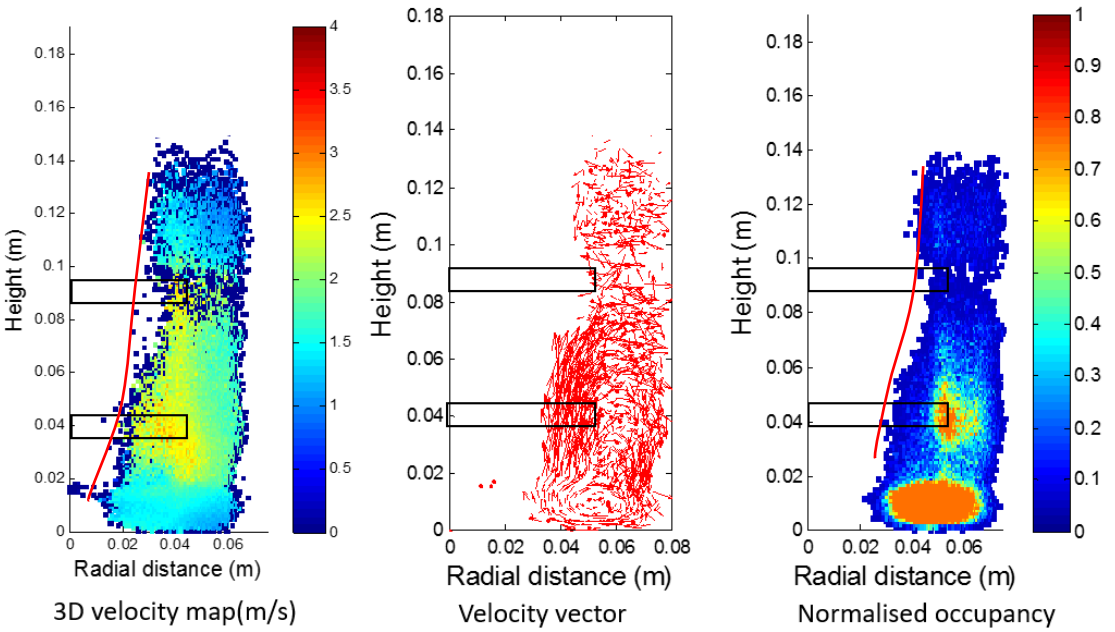

Fig. 5-39. The 3D-velocity map (left), velocity vector (middle) and normalised occupancy rate (right) obtained using stirrer Type a-2 at 5.23 m/s (800 RPM).

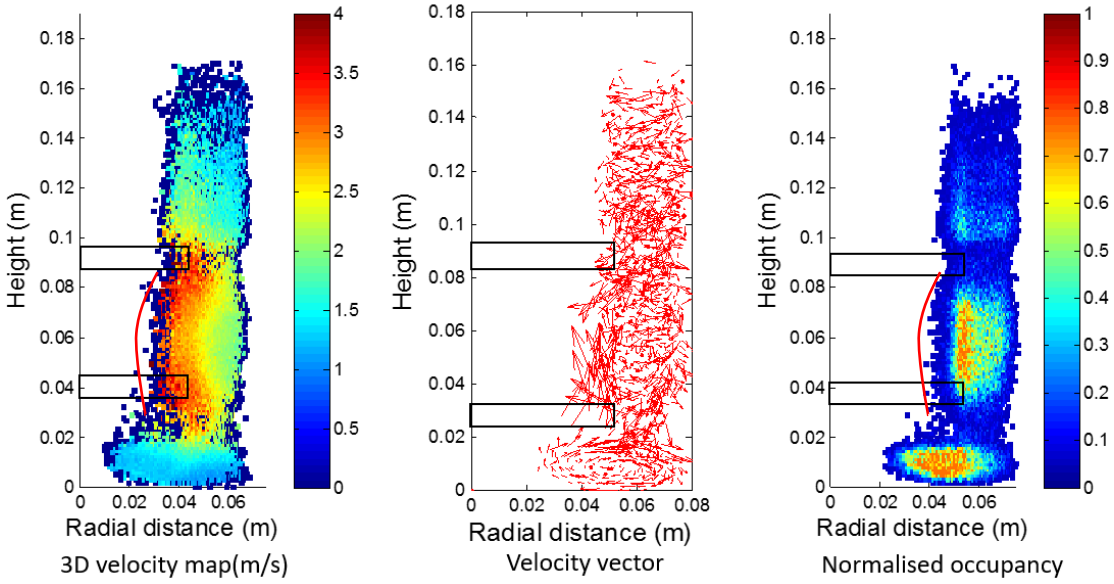

Fig. 5-40. The 3D-velocity map (left), velocity vector (middle) and normalised occupancy rate (right) using stirrer Type a-2 at V_t=7.85 m/s (1200 RPM).

The PEPT results obtained at V_t=5.23 m/s (800 RPM) and V_t=7.85 m/s (1200 RPM) are shown in Fig. 5-39 and Fig. 5-40. The comparison of the 3D-velocity profiles is shown in Fig. 5-41.

As seen from Fig. 5-39 (left), the magnitude of the 3D-velocity is in the range 0∼2.5 m/s at V_t=5.23 m/s. The high-speed region is mainly located in the gap between the blades. Particularly in the region adjacent to the tip of the blade, a circulation loop is formed within the gap. This new flow pattern is caused by the increased distance between the blades. Unlike the velocity map obtained using stirrer *Type a*, the occupied area in the impeller band is greatly improved. Due to the pump force caused by the pitched blade, the charge tends to move downwards the bottom. This also reduces the amount of the charge in the upper band.

The velocity vector obtained at V_t=5.23 m/s is shown in Fig. 5-39 (middle). The loop within the impeller band (chamber height 0.02∼0.08 m) is clearly illustrated. The slurry is pushed upwards from the bottom by the force generated from the lower stirrer blade. The slurry from the upper band is pushed down towards the impeller band. The direction of the circulation is also changed. The grinding media near the shaft is moving upward and near the wall is moving downward.

Fig. 5-39 (right) shows the distribution of the occupancy rate. When tip speed is reduced to 5.23 m/s (800 RPM), the charge is not fully fluidised using stirrer *Type a-2*. Mostly, the tracer is located at the bottom because the motion of the loop is clock-wise pushing to the bottom. The rotational speed is not fast enough and the grinding media is not pushed up near the centre of the chamber. Thus, a higher tip speed V_t=7.85 m/s (1200 RPM) is applied. PEPT results are shown in Fig. 5-40.

As seen from the 3D-velocity map in Fig. 5-40 (left), the magnitude of the 3D-velocity is expanded to 0~4 m/s when the V_t is increased to 7.85 m/s. The velocity vector (see Fig. 5-40, middle) clearly demonstrated a fully fluidised system. Due to the stress generated from the stirrer towards the wall. The slurry is moving along the chamber wall. The filling field is slightly reduced in the impeller band due to the stronger centrifugal force caused by a higher tip speed. However, the whole system is more homogeneous.

The normalised occupancy rate map (see Fig. 5-40, left) shows a higher occupancy rate in the impeller band (height 0.02~0.08 m) when a higher tip speed is applied. This also increases the motion of the grinding media towards the chamber wall. The level of the charge in the vessel is greatly increased, approaching 0.16 m.

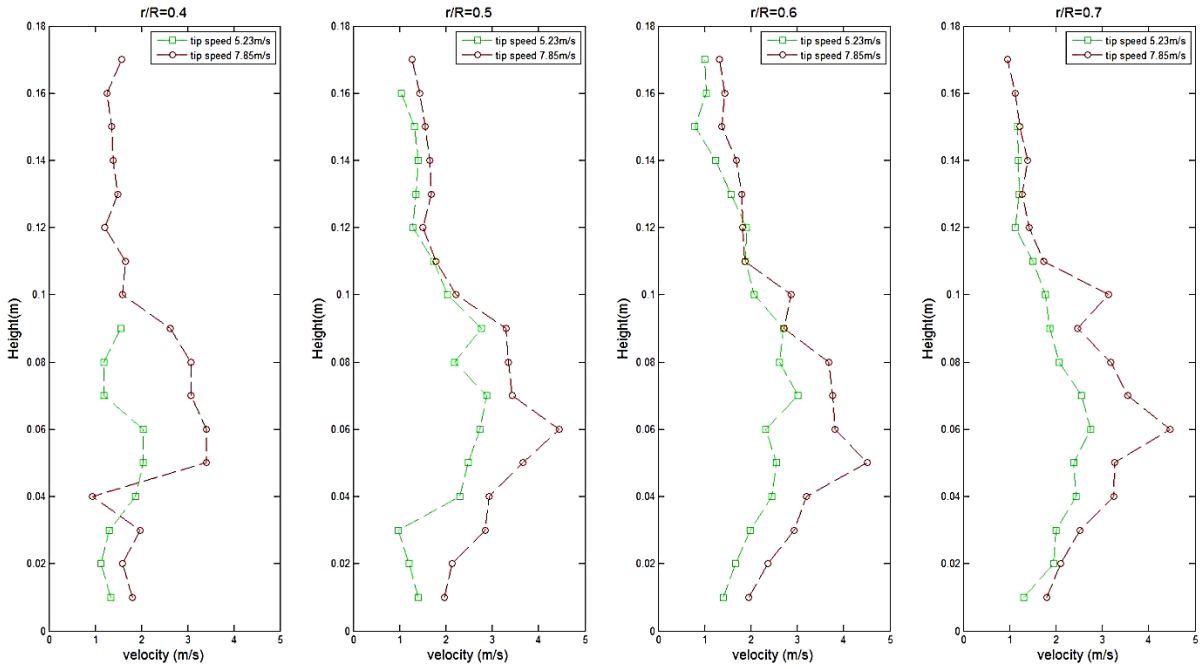

Fig. 5-41. The 3D*-velocity profile obtained using ZirPro and stirrer Type a-2 at V_t=5.23 m/s (800 RPM) and 7.85 m/s (1200 RPM) at radial position r/R=0.4, 0.5, 0.6 and 0.7.*

The comparison of the 3D-velocity profiles at V_t=5.23 m/s (800 RPM) and 7.85 m/s (1200 RPM) are shown in Fig. 5-41. Overall, a higher tip speed shows a faster velocity profile at

the radial position r/R=0.4, 0.5, 0.6 and 0.7. Due to the strong centrifugal forces generated by stirrer *Type a-2*, the level height is improved at both tip speeds. The velocity transition is smooth from the bottom to the top. Even at the height beyond 0.08 m (upper band), the velocity magnitude is within the range 1~2 m/s. This is a great improvement over the 3D-velocity magnitude compared to the other stirrer types used under the same tip speed.

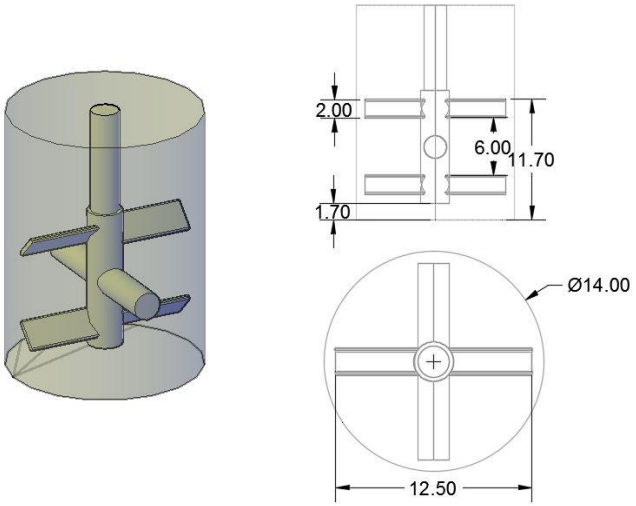

Fig. 5-42. Detailed geometry for stirrer Type a-3 consisted by 2 layers of pitched blades and a pair of pin stirrers (units in cm).

Fig. 5-42 displays the configuration of stirrer *Type a-3.* Note this stirrer type is different from the '*Type a-3*' shown in the Chapter 4. By adding a pin stirrer arm with offset 90° to *Type a-2*, the purpose of *Type a-3* is to improve the stress intensity in the impeller band. The pin stirrer is located between the 2 flat blades.

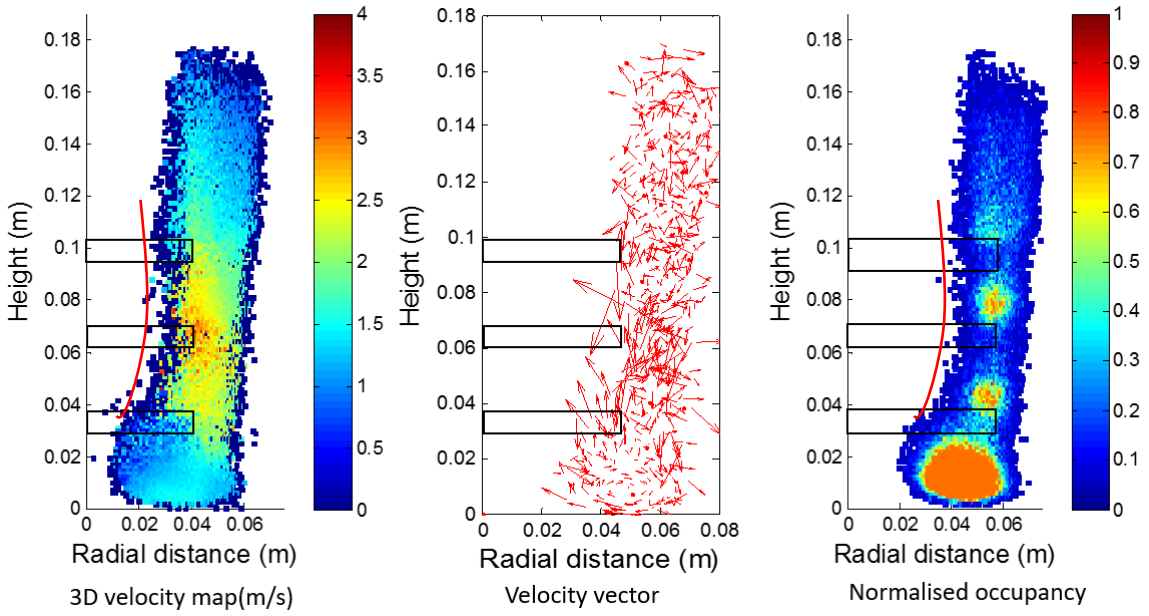

Fig. 5-43. The 3D-velocity map (left), velocity vector (middle) and normalised occupancy rate (right) using stirrer Type a-3 at V_t=5.23 m/s (800 RPM).

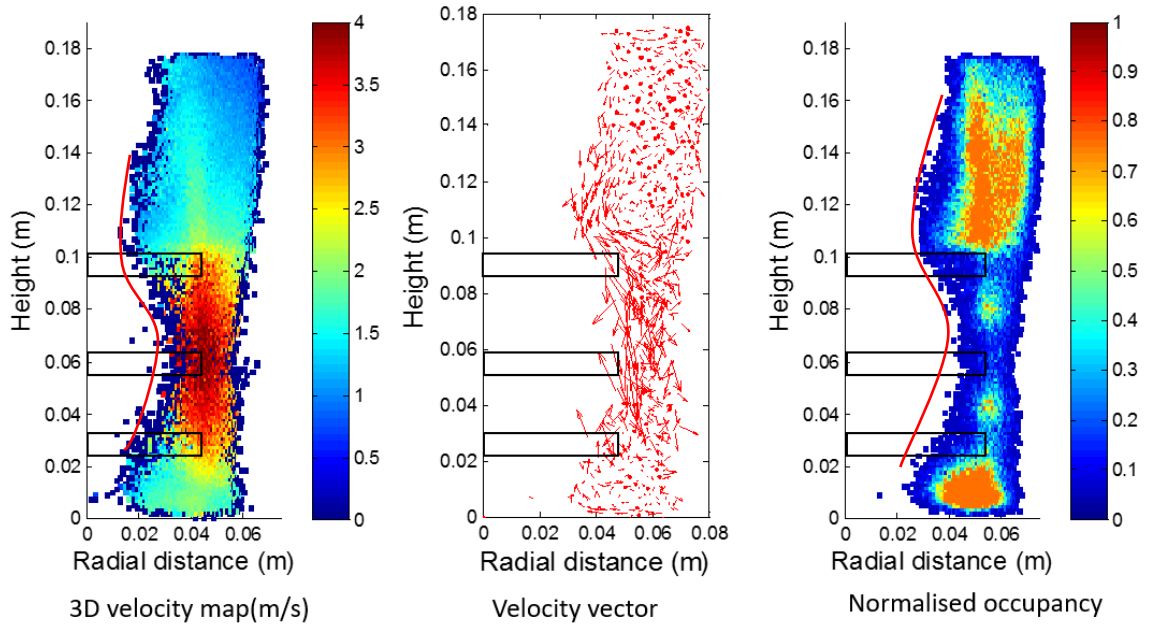

Fig. 5-44. The 3D-velocity map (left), velocity vector (middle) and normalised occupancy rate (right) using stirrer Type a-3 at V_t=7.85 m/s (1200 RPM).

The PEPT results obtained using stirrer *Type a-3* are also compared at V_t=5.23 m/s (800 RPM) and 7.85 m/s (1200 RPM) shown in Fig. 5-43 and Fig. 5-44 respectively. As seen from Fig. 5-43 (left), the 3D-velocity distribution is similar to the results obtained using *Type a-2* at V_t=5.23 m/s, an obvious difference is that the small loop observed within the gap between the blades has disappeared. The high-velocity field is more centralised around the tip of the pin stirrer. The charge is moving along the wall of the chamber. The pin stirrer arm will generate more strong collisions around the stirrer tip than the blade arm. The observed peak velocity is 2.5 m/s which is close to the value obtained using stirrer *Type a-2* at the same tip speed.

The filling area within the impeller band is decreased compared to the results obtained using *Type a-2* (indicated by the red curve in Fig. 5-39 and Fig. 5-40). Instead of drawing the charge into the impeller band, *Type a-3* pushes the charge towards the chamber wall. The observed location of the tracer is mostly alongside the wall and the level of the charge is increased to 0.17 m. Also, a higher occupancy rate is observed at the grinding chamber bottom indicating insufficient motion of the grinding media at V_t=5.23 m/s.

Fig. 5-44 displays the PEPT results obtained at V_t=7.85 m/s (1200 RPM) using stirrer *Type a-3*. As seen from the 3D-velocity map in Fig. 5-44 (left), the 3D-velocity magnitude at the height from 0.02 m to 0.08 m is significantly improved. The outline of the high-velocity field is like a rhomb (the colour 'red' area). The maximum 3D-velocity in the field approaches 4 m/s. This is contributed by the extra pin stirrer which strengthens the kinetic energy transfer from the stirrer to the grinding media in the height band 0.02 m to 0.1 m. The higher centrifugal force reduces the filling of the charge in the impeller band.

The occupancy rate obtained at V_t=7.85 m/s with stirrer *Type a-3* is shown in Fig. 5-44 (right). The system is fully fluidised. The level of the charge has reached the top cover. The high occupancy rate is observed at the upper band (height from 0.1 m to 0.17 m) and the lower band (height below 0.02 m). The velocity vector (see Fig. 5-44, middle) indicates complete disordered motion of the grinding media.

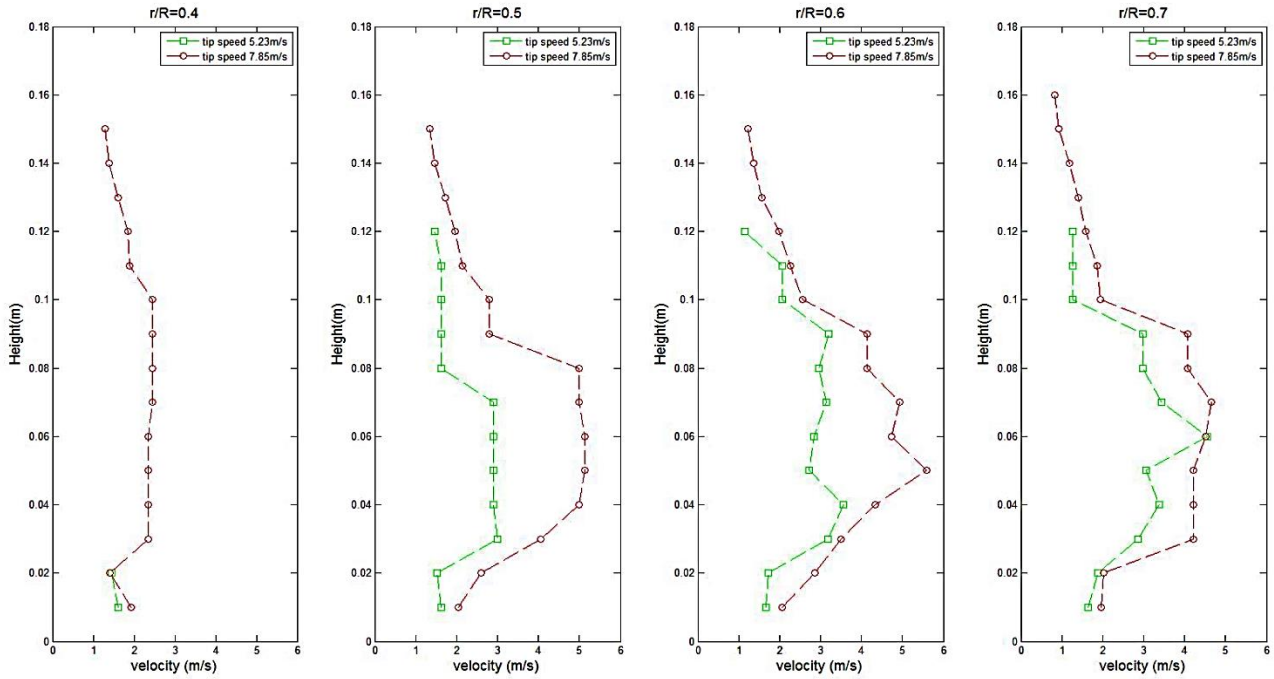

Fig. 5-45. The 3D-velocity profile obtained using ZirPro grinding media and stirrer Type a-3. V_t=5.23 m/s (800 RPM) and 7.85 m/s (1200 RPM) at radial position r/R=0.4, 0.5, 0.6 and 0.7.

The detailed 3D-velocity profiles obtained at both tip speeds (V_t=5.23 m/s and V_t=7.85 m/s) using *Type a-3* are compared at radial position r/R= 0.4, 0.5, 0.6 and 0.7 in Fig. 5-45. At r/R=0.5, 0.6 and 0.7, the 3D-velocity measured at V_t=7.85 m/s (1200 RPM) is in the range 0~5 m/s at the chamber height from 0.02 m to 0.08 m. This is much higher than the velocity magnitude obtained at V_t=5.23 m/s. In the upper band where the chamber height is above 0.1 m, the velocity drops to the range 0~3 m/s. A higher magnitude of 3D-velocity is still observed in the upper band at V_t=7.85 m/s compared to the results at V_t=5.23 m/s.

At radial position r/R=0.4, the tracer is not well tracked when the height is higher than 0.02 m at V_t=5.23 m/s. This indicates the filling of grinding media near the centre of the chamber is not sufficient. When V_t is increased to 7.85 m/s, the 3D-velocity is around 2 m/s at r/R=0.4. Overall, *Type a-3* demonstrates an improvement on the motion of the grinding media. However, the grinding media is lifted too high along the grinding chamber wall, the shear stress from the wall and friction may waste a lot of energy. The less filling area in the impeller band may drop the grinding efficiency.

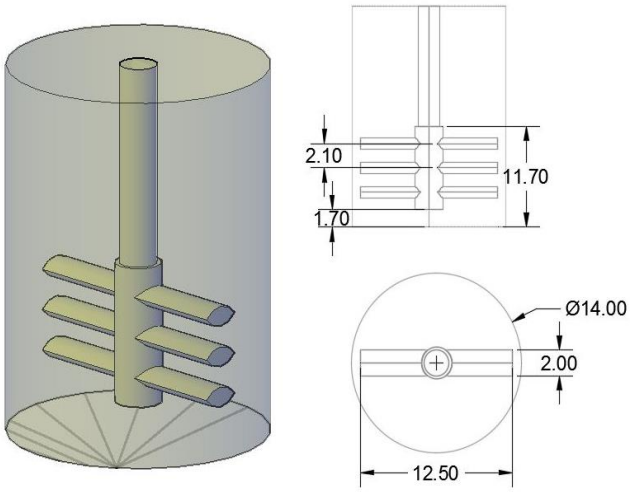

Fig. 5-46. Detailed geometry for stirrer Type a-4 consisted of 3 pairs of flat stirrers (units in cm).

Fig. 5-46 shows the configuration of stirrer *Type a-4*. It is configured with 3 parallel pin stirrer arms and the cross-section shape is oval. This design is unlike the flat blade and it will not push the charge in a specific direction. The tests were also conducted at V_t=5.23 m/s (800 RPM) and 7.85 m/s (1200 RPM). The distance between the adjacent stirrers is 2.1 cm. The diameter and clearance distances are the same as the other stirrer types.

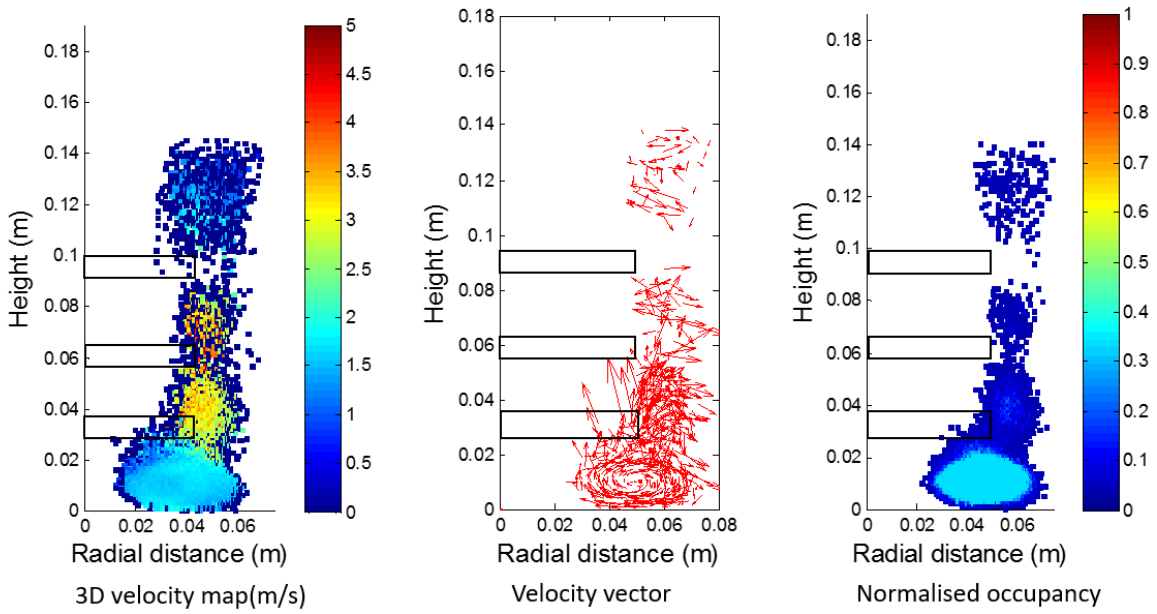

Fig. 5-47. The 3D-velocity map (left), velocity vector (middle) and normalised occupancy rate (right) obtained using stirrer Type a-4 at V_t=5.23 m/s (800 RPM).

The PEPT results obtained at V_t=5.23 m/s (800 RPM) are shown in Fig. 5-47 (left). The stirrer arms for *Type a-4* are mounted parallel at a relatively close distance (2.1 cm).

When the stirrer (*Type a-4)* rotates, the charge is pushed as a solid block. The distance between the adjacent stirrer arms does not provide sufficient space for the grinding media to flow through. Also, very low packing density is observed in the impeller band (height 0.02~0.1 m) at V_t=5.23 m/s. The charge is not sufficiently accelerated and most of the charge is settled at the bottom. As seen from the occupancy rate (see Fig. 5-47, right), the tracer is mostly tracked at the bottom. The effective area for the collision is limited to the narrow gap between the stirrer tip and the chamber wall.

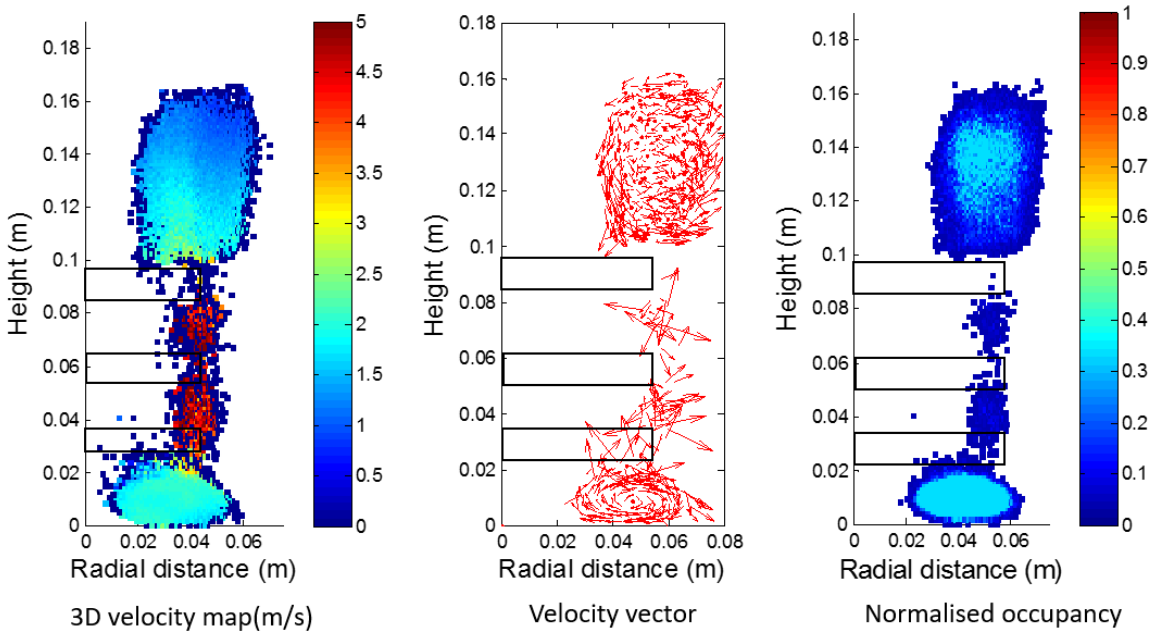

Fig. 5-48. The 3D-velocity map (left), velocity vector (middle) and normalised occupancy rate using stirrer Type a-4 at V_t=7.85 m/s (1200 RPM).

The PEPT results obtained at V_t=7.85 m/s are shown in Fig. 5-48. When the V_t is increased from 5.23 m/s (800 RPM) to 7.85 m/s (1200 RPM), the charge is squeezed by the stirrer and the level height is increased to from 0.14 m (V_t=5.23 m/s) to 0.16 m (V_t=7.85 m/s). A high occupancy rate is still observed at the bottom and upper band. The filling of the charge in the impeller band is very low. A narrow region of high velocity is observed in the band of height from 0.02 m to 0.1 m. The maximum 3D-velocity is approaching 5 m/s, but the velocity magnitude in the rest of the chamber is not very high. The effective grinding area is only within the high-speed field.

As seen in the map of velocity vector shown in Fig. 5-48 (middle), no stable path of the circulation is observed in the impeller band. A loop is observed at the bottom. This implies the slurry is accelerated, but it moves around at the bottom without effective contact with the stirrer.

The PEPT results obtained at V_t= 5.23 m/s and 7.85 m/s imply that the effective grinding area is not improved when using stirrer *Type a-4*. The void area in the impeller band (height 0.02~0.1 m) is increased. The PEPT results demonstrate that the layout of the parallel stirrer arms may not be suitable for fluidising the charge. An offset angle between the adjacent stirrer arms is necessary when several pairs of the stirrer are used for the grinding process with a highly viscous suspension.

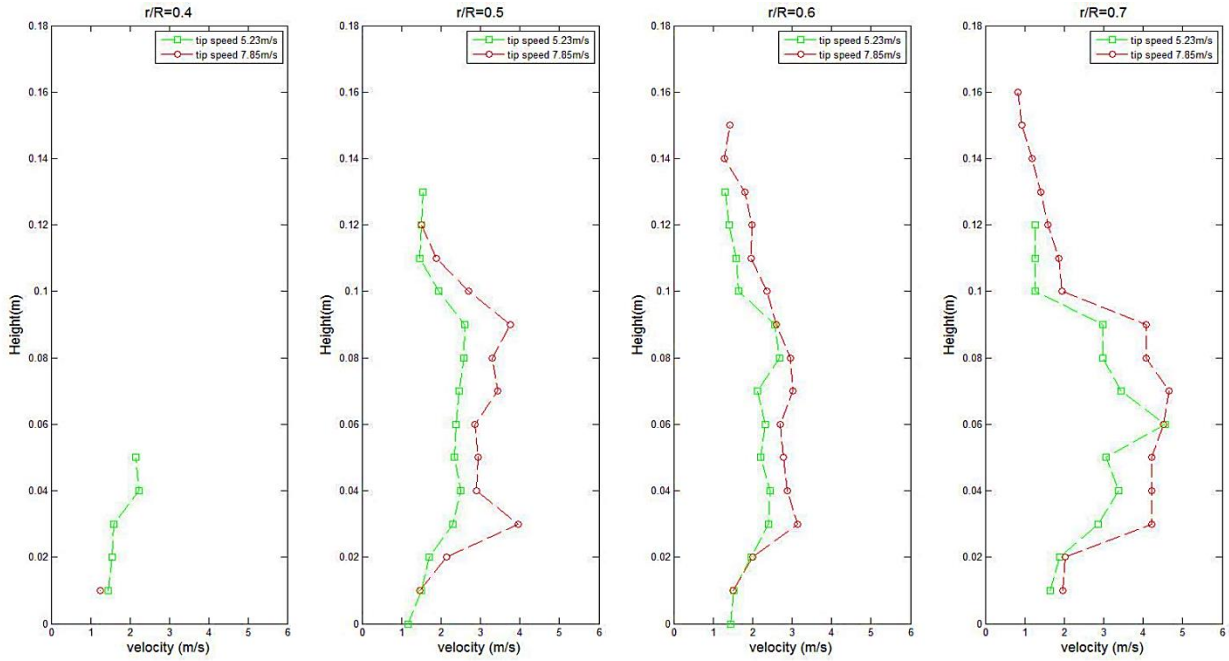

Fig. 5-49. The 3D-velocity profiles obtained using ZirPro grinding media with stirrer Type a-4 at V_t=5.23 m/s (800 RPM) and 7.85 m/s (1200 RPM). The radial position r/R=0.4, 0.5, 0.6 and 0.7.

The comparison of 3D-velocity profiles obtained at V_t=5.23 m/s and 7.85 m/s are shown in Fig. 5-49. At the radial position r/R=0.4, few locations of the tracer are observed at both tip speeds with stirrer *Type a-4*. No evident motion of the grinding media is tracked in the field near the shaft. When the radial position approaches to the wall of the grinding chamber (e.g. r/R=0.5, 0.6 and 0.7), the tracer is tracked again. The overall velocity magnitude is in the range 1~4 m/s at both tip speeds.

As radial position r/R is increased, the overall velocity is gradually increased. The distribution of the 3D-velocity in the vertical direction is not uniform. At r/R=0.7, the peak velocity is approaching 5 m/s in the chamber height between 0.02 m to 0.1 m for both tip speeds. In chamber height above 0.1 m, the maximum 3D-velocity is dropped to 2 m/s. When r/R is reduced to 0.5, the 3D-velocity is in the range 2~4 m/s. The distribution of the velocity is stable in the band with the height from 0.02 m to 0.1 m, but the magnitude of the 3D-velocity is lower than the values observed at r/R=0.7. This again indicates that the high velocity region is within the gap between the stirrer tip and the wall of the chamber. By using stirrer *Type a-4*, an inhomogeneous system is observed. The kinetic energy is not sufficiently transferred from the impeller band to the other fields.

5.4. Conclusions

In this chapter, the PEPT results under different operating conditions and stirrer configurations are demonstrated and analysed. The maps for azimuthally averaged 3D-velocity, velocity vector and occupancy rate distribution are plotted to show the visualised information for the motion of the grinding media. The 3D-velocity profiles at various radial positions in the grinding chamber are compared to show the magnitude of the velocity under the corresponding experimental conditions.

The tip speed (V_t) at 9.81 m/s (1500 RPM) is proved to be the most helpful in improving the motion of the grinding media in the laboratory scale mill. The grinding media ZirPro is proved to be more effective in kinetic energy transfer than Carbolite as it has a greater density. A larger size of the grinding media (ZirPro +2.0-2.4 mm) shows a higher magnitude of the 3D-velocity but a finer size (ZirPro +0.7-1.4 mm) shows better packing density in the impeller band.

The PEPT results demonstrate the influences from different stirrers. *Type a-1* demonstrates a better flow pattern by expanding the impeller band compared to the results obtained using the standard stirrer *Type a.* A thickness enhanced top cover shows improvement in the velocity of the grinding media. The performances of stirrer *Type a-2*, *Type a-3* and *Type a-4* are examined at V_t=5.23 m/s (800 RPM) and 7.85 m/s (1200 RPM). The influences of flat blade and different offset angles on the flow pattern are observed. The stirrer *Type a-2* is proved to be the most optimal configuration for improvement in fluidisation of the grinding media as it demonstrates a higher occupation in the impeller band by increasing the gap between the stirrer arms.

Chapter 6 Discrete Element Method (DEM) simulation

6.1. Introduction

In a stirred media mill, a large quantity of grinding media is mixed with the mineral slurry in a high shear environment. It is impossible to track the motion of each grinding media by PEPT. A more powerful tool is desired for the description of grinding media trajectories and collisions in detail. In the past decades, numerical simulation methods have been extensively used to model the flow of granular materials. These methods can be classified into two broad categories: the continuum method and the discrete method (Bertrand et al., 2005; Chu et al., 2009; Jayasundara et al., 2011; Kloss et al., 2012). The continuum method treats the bulk modelling particles as an artificial continuum phase because the behaviour of a large number of particles is similar to a fluid (Tamburini et al., 2013). The Computational Fluid Dynamic (CFD) technique (based on Navier–Stokes equations) is a typical continuum method applied in either fluid or particle modelling. The downside of CFD is that no accurate description of the behaviour of individual particles is considered.

DEM based on contact models (e.g. Hertz-Mindlin model) enables the dynamic information to be achieved on each modelling particle. The method can track the motion of millions of particles simultaneously. DEM also has capability to calculate the realistic contact force between the particles (Kloss et al., 2012). It was firstly applied to ball mills by Mishra and Rajamani (1990). Then, it has been expanded to rotating drums and grinding mills (Beinert et al., 2015; Chu et al., 2009; Cleary et al., 2006; da Cunha et al., 2013; Morrison et al., 2009; Sinnott et al., 2006; Yang et al., 2006). The application of this technology is becoming popular due to more advanced computing technology. This enables a greater number of the particles to be tracked with more complicated mathematical models.

In this study, DEM is employed to simulate the movement of the grinding media particles within both laboratory scale and pilot scale mills. The simulation results obtained in the laboratory scale mill is validated with the corresponding PEPT data. As the stirrer with the pitched blade shows an advantage in improving grinding efficiency, *Type a-5* is used for a further investigation with DEM. The simulation results obtained with *Type a-5* are compared with the results using standard stirrer *Type a* to demonstrate how the grinding efficiency is improved.

The simulation on the pilot scale mill is analysed by comparing the results obtained from the standard stirrer *Type b* and a new stirrer *Type b-1. Type b-1* is a scaled-up configuration from *Type a-5*. The performance of the pilot scale mill using these two stirrers is investigated via DEM. The results provide a comprehensive understanding of the performance of these two stirrers in the pilot scale mill.

6.2. Simulation set-up

The most important issue for modelling a stirred media mill is the motion of the grinding media. Each grinding media is mathematically represented by a spherical particle with constant diameter and density. To describe the movement for the spherical particle, it is required to define both translational and rotational accelerations for each particle based on the corresponding momentum balances (Kloss et al., 2012). Eq. [6.1] and Eq. [6.2] shown below are used to calculate the translation and rotational velocities respectively (Zhu et al., 2007).

$$m_i \frac{dV_i}{dt} = \sum_j (F_{ij}^{cn} + F_{ij}^{ct} + F_i^g) \quad [6.1]$$

and

$$I_i \frac{d\omega_i}{dt} = \sum_j (R_i \times F_{ij}^{ct} - \mu_r R_i \left| F_{ij}^{cn} \right| \widehat{\omega_i}) \quad [6.2]$$

m_i, V_i and ω_i are the mass, transitional and angular velocity respectively for a particle i. t is time. F_{ij}^{cn} and F_{ij}^{ct} represent the normal contact forces and tangential contact forces applied on particle i from particle j. F_i^g indicates the gravity applied on the particle i. The first term on the right side of Eq. [6.2] is tangential torque and the second term is rolling friction torque.

The diameter of a grinding media ($1 \sim 2 \times 10^{-3}\ m$) is much larger than the size of a molecule ($< 10^{-10}\ m$). Thus, the influence of the non-contact forces (van der Waals, electrostatic forces) is not considered because these forces have no evident impact on the motion of grinding media (Blais and Bertrand, 2017; Cleary et al., 2006; Sinnott et al., 2006; Yang et al., 2006). The major forces considered in a single collision are contact forces and gravity (Bertrand et al., 2005; Di Renzo and Di Maio, 2004).

6.2.1. Simulation system

The simulation is conducted in both laboratory scale and pilot scale mills shown in Fig. 6-1 and Fig.6-2 respectively. The laboratory scale mill employs the standard pin stirrer (*Type a*) which consists of a central shaft with the pin stirrers (90° offset to each other) shown in Fig. 6-1a. The experimental results in Chapter 4 and Chapter 5 indicate that the grinding efficiency can be improved by using some different stirrer configurations. *Type a-5* demonstrates a better performance over the other types considering the product fineness and the energy efficiency. Thus, it has been used for the study with DEM. *Type a-5* is a combination of pin and blade stirrers shown in Fig.6-1b. This configuration is designed to mix the grinding media while simultaneously push it down towards the bottom of the mill chamber. This design increases the circulation of the grinding media within the mill. It has

been applied on the pilot scale mill. The performance in the pilot scale mill is investigated via DEM simulation. Fig. 6-2 shows the standard pin stirrer *Type b* (see Fig.6-2a) and *Type b-1 (*see Fig. 6-2b) used in the pilot scale mill.

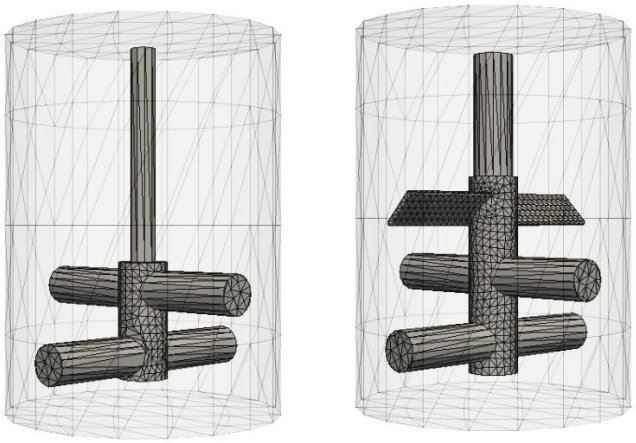

a **b**

Fig. 6-1. 3D CAD pictures of the laboratory mill with Type a (a) and Type a-5 (b). The chamber wall is transparent in order to show the stirrer configuration.

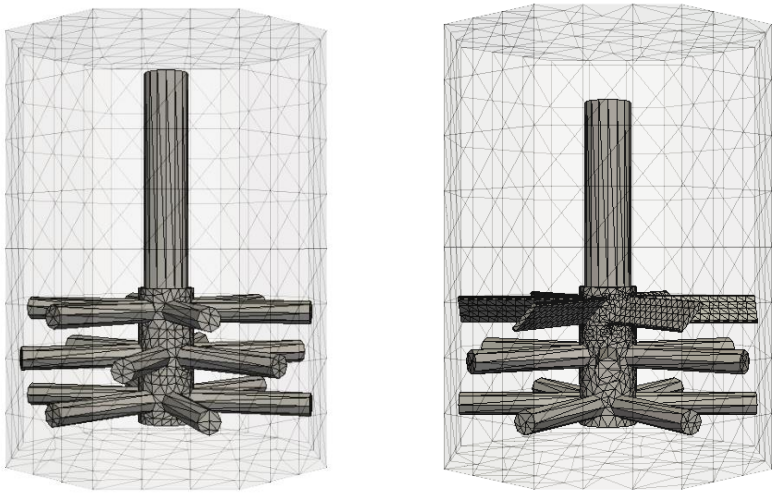

a **b**

Fig. 6-2. 3D CAD pictures of the pilot scale mill with Type b (left) and Type b-1 (right). The chamber wall is transparent in order to show the stirrer configuration.

In DEM simulation, the geometries for each grinding chamber and stirrer are used as boundary conditions. The grinding media is assumed not to break nor wear over all the simulation.

6.2.2. Simulation parameters

The Hertz-Mindlin contact model is used to calculate the contact forces between the grinding media. To begin a simulation, the grinding chamber is filled up with the uniform size of spherical particles. When all particles settle down at the bottom, the stirrer is set to rotate at a constant rotational speed. The V_t in both mills is fixed at 5.23 m/s equivalent to 800 RPM for the laboratory scale mill and 384 RPM for the pilot scale mill. The simulation time scale is 1.5 s with a time step Δt=1×10^{-5} s which is below 20 % of the Rayleigh-time (t_r) which describes the time that a shock wave needs to propagate through the particle body (Beinert et al., 2015). During this simulation time, the stirrer rotates 20 revolutions and 10 revolutions in the laboratory scale and pilot scale respectively. A stable equilibrium state is observed in both mills.

The physical properties of the grinding media used in the Hertz-Mindlin model are listed in Table 6-1. For the simulation in the laboratory scale mill, the total weight of grinding media is 1.758 kg based on the experimental condition. The grinding media is defined as a spherical particle of diameter 1.4 mm and density 3,200 kg/m^3. The total number of media injected into the chamber is 374,104.

Table 6-1. The detailed parameters used in DEM simulation for both laboratory scale and pilot scale mills for the grinding media (Beinert et al., 2015).

Parameters	Laboratory mill	Pilot mill
Number of media particles	374,104	350,140
Media density, ρ (kg/m^3)	3,200	3,200
Media diameter, R *(mm)*	1.4	3.0
Total media mass *(kg)*	1.758	15.837
Young's modulus, *Y (Pa)*	1.2×10^7	1.2×10^7
Poisson ratio, v	0.24	0.24
Coefficient of restitution, e	0.52	0.52
Coefficient of friction, μ_r	0.17	0.17
Duration of simulation ($second$)	1.5 (20 rev)	1.5 (10 rev)

In the pilot scale mill, the mass of the grinding media is scaled up to 15.837 kg which is identical to the total weight used in the experiment. To maintain the total number of grinding media on the same level as the laboratory scale mill, the diameter of the grinding media is increased to 3.0 mm and the total number of the grinding media is 350,140. The rest of the simulation parameters for the grinding media are identical in both scales.

6.3. Results and discussion

6.3.1. Laboratory scale mill

The DEM simulation begins with a packed media bed in the laboratory scale mill (see Fig. 6-3). The total number of particles simulated equals the actual mass of grinding media ($1.758\ kg$) used in the experiment. Then, the standard stirrer (*Type a*) rotates at V_t= $5.23\ m/s$ equivalent to 800 RPM. Newton's second Law is applied over time step 1×10^{-5} *s* to update the force and position of each grinding media. The simulation results are recorded at every 0.1 *s* (1×10^4 iterations). A dynamic equilibrium state of the system is observed after t=0.8 *s* (12 revolutions of the stirrer). To fully fluidise the particles, the modelling results are collected at t=1.5 *s* when 20 revolutions of the stirrer are achieved.

Fig. 6-3. Initially packed particle bed in the laboratory scale mill with standard stirrer Type a (t=0 s).

Compared to PEPT, an advantage of DEM is that all grinding media can be tracked and demonstrated simultaneously. As PEPT results are derived from the movement of one tracer, this may not completely describe the velocity field in some regions with extremely high velocity. Also, the 3D motion of the tracer obtained from PEPT is needed to transfer

into a 2D velocity map to show the velocity distribution. For the simulation with DEM, the position and velocity of grinding media can be directly shown in a 3D graph. This reflects the actual flow situation in the mill. Those grinding media being driven by the stirrer can be clearly observed in DEM results.

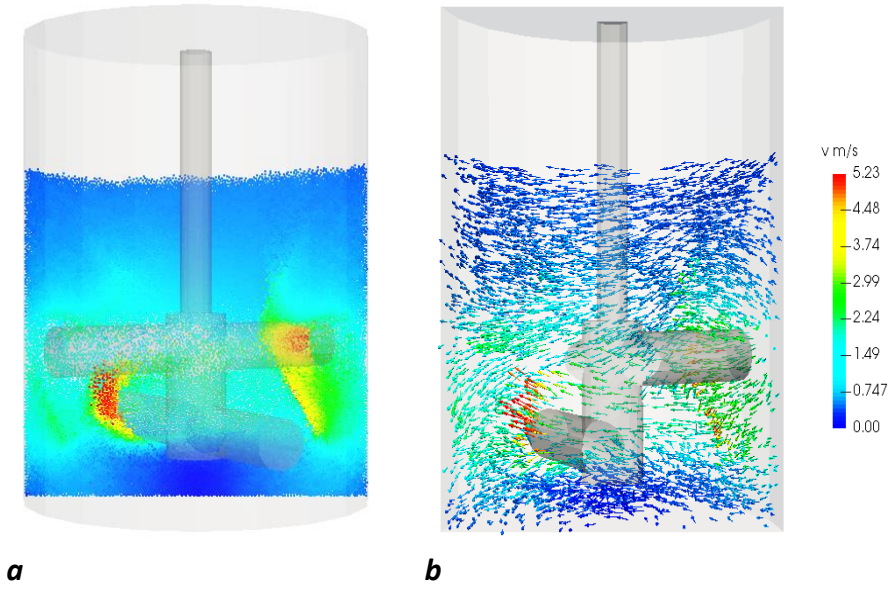

Fig. 6-4. The distribution of instantaneous velocity in a cliped section in the laboratory mill using the standard stirrer (Type a) at V_t=5.23 m/s. (a) instantaneous velocity distribution and (b) velocity vector at time 1.5s.

The DEM results (actual instantaneous velocity distribution) obtained in the laboratory scale mill using the standard stirrer (*Type a*) at V_t=5.23 m/s (800 RPM) are shown in Fig. 6-4a. A high velocity field is observed in the impeller band along the chamber wall and the edge of the pin stirrer. The maximum instantaneous velocity is observed at the tip of the pin stirrer where the grinding media absorbs the kinetic energy from the stirrer. The slip phenomenon between the grinding media and stirrer is clearly indicated in Fig. 6-4a (colour 'red' to 'green'). The low velocity distribution is observed in the upper band and the bottom (colour

'dark blue'). A clear velocity gradient is formed between the stirrer and the rest region along the wall. The magnitude of the velocity in the chamber is consistent with the results obtained with PEPT.

The velocity vector of the grinding media is shown in Fig. 6-4b. Due to the symmetry, the mill chamber is split by a plane in the middle and only half is demonstrated. It shows a swirling motion of the bulk particles (anti-clockwise seen from the top). At the tip of the stirrer, the grinding media is observed to flow around as a 'half-circle' shape instead of piling up in front of the surface of the stirrer. In the area above the stirrer, the velocity vector points down towards the bottom. The velocity vector from the bottom is pointing up. This indicates the circulation on the vertical direction. The flow pattern is the same as the results observed from PEPT.

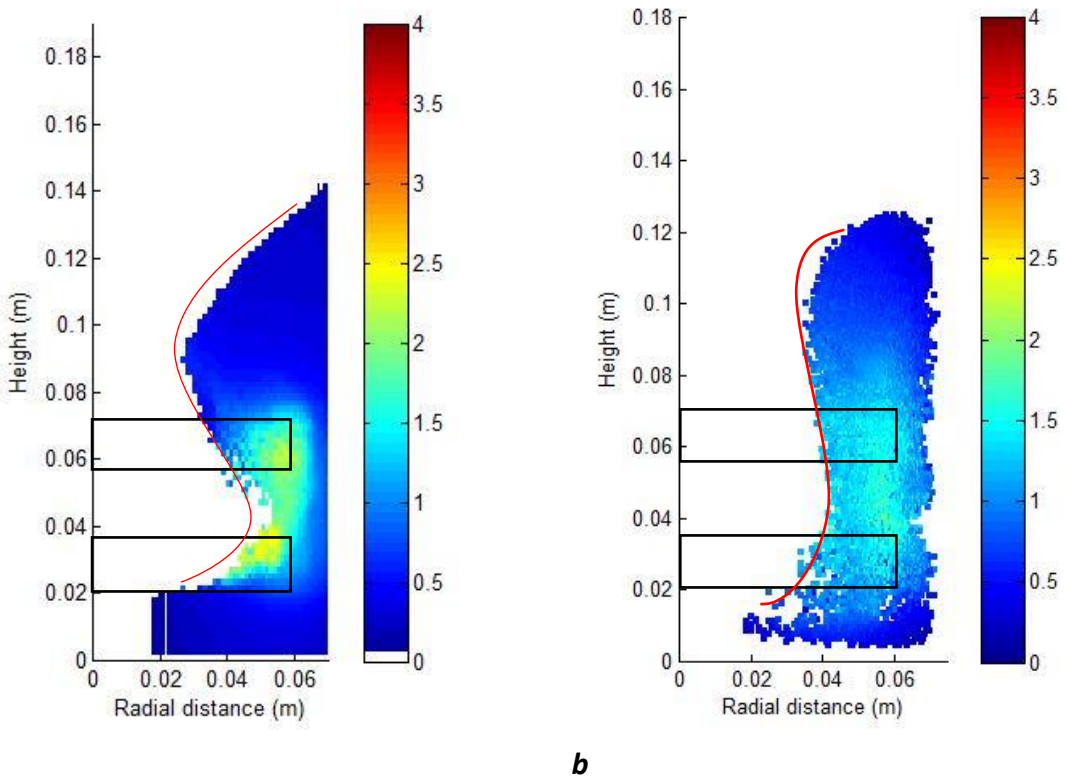

Fig. 6-5. Comparison of the azimuthally averaged velocity map obtained by DEM (left) and PEPT (right) at V_t= 5.23 m/s (standard stirrer).

To compare DEM simulations and PEPT measurements on the 3D-velocity of grinding media, Fig. 6-5 shows azimuthally averaged 3D-velocity maps obtained using DEM (see Fig. 6-5a) and PEPT (see Fig .6-5b) at V_t=5.23 m/s. The standard stirrer (*Type a*) is used. Both methods identify the high velocity region within the height band from 0.02 m to 0.08 m (impeller band). No obvious motion of grinding media is observed in the area outside the impeller band. The 3D-velocity map obtained from DEM shows higher resolution than PEPT because the instantaneous velocity is recorded instead of the average velocity calculated from the trajectories. The free surface (indicated by the red curve) predicted by DEM is more detailed than the results calculated from PEPT.

The magnitude of the azimuthally averaged 3D-velocity profiles at different radial positions (r/R=0.5∼0.9) are compared in Fig. 6-6. Overall, the 3D-velocity increases when the radial position (r/R) is increased from the shaft to the chamber wall. At r/R=0.5 and 0.6, the simulated 3D-velocity of the grinding media by DEM is slightly smaller than the results by PEPT because in the chamber at a height of 0.02∼0.06 m, a larger void field is observed from the results obtained using DEM. Fewer grinding media are tracked by DEM in the area around the stirrer. However, this phenomenon observed from DEM may be closer to the real flow behaviour as the instantaneous position is tracked by DEM. When the radial position r/R is increased to 0.7, 0.8 and 0.9, the magnitude of the 3D-velocity obtained from the two methods is consistent.

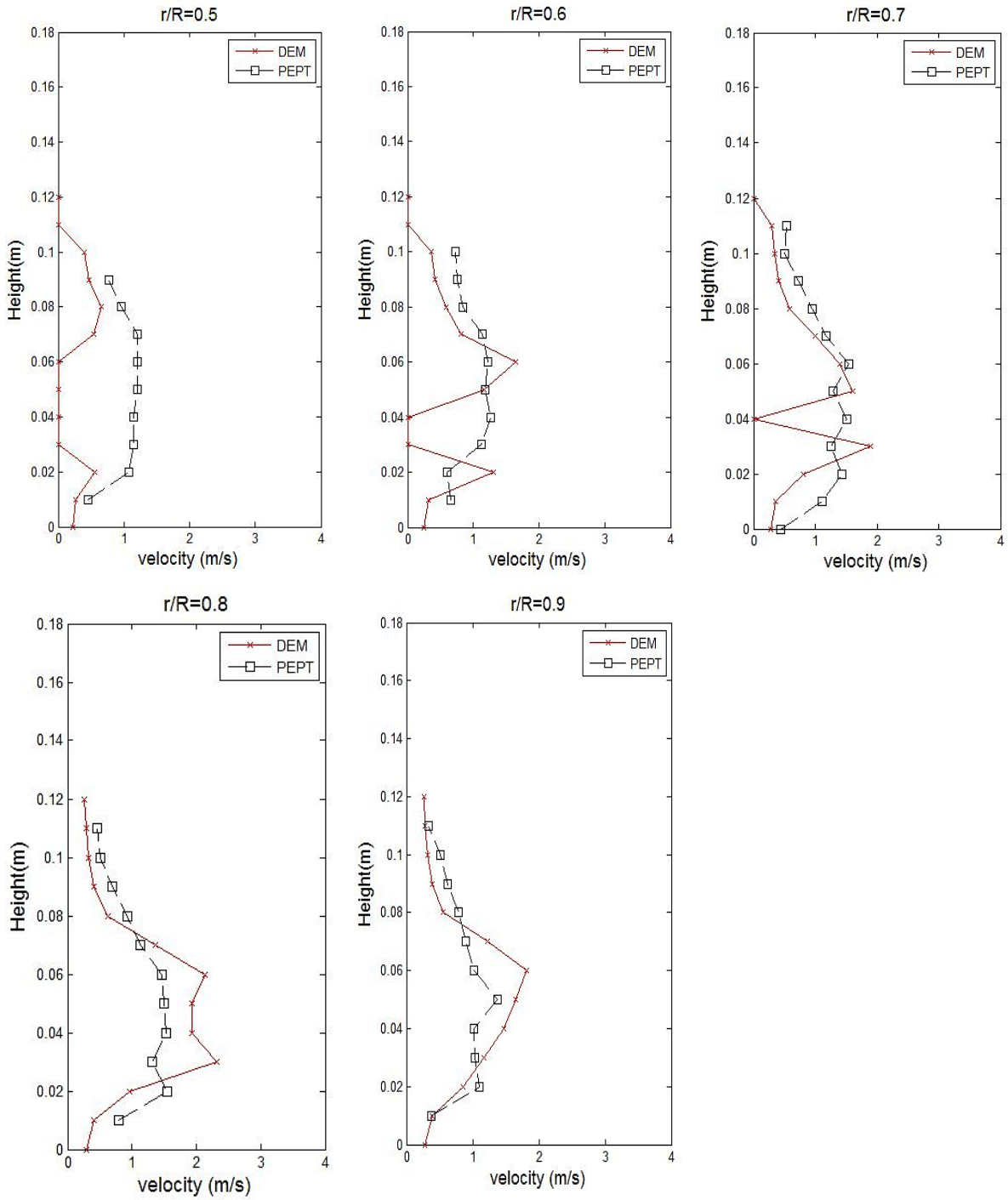

Fig. 6-6. Comparison of the azimuthally averaged 3D-velocity distribution obtained using DEM and PEPT at radial position r/R=0.5, 0.6, 0.7, 0.8 and 0.9.

DEM demonstrates a more detailed velocity distribution at the tip of the stirrer and the location near to the wall in the visualised velocity map (see Fig. 6-4). In a stirred media mill, a large amount of the grinding media fills up in the gap between the stirrer tip and wall due

to the centrifugal force. DEM clearly illustrates the gradient of the instantaneous velocity and flow direction in this area. The contact between the grinding media and stirrer surface is clearly indicated in the velocity map obtained by DEM. The discrepancies between the results are mainly observed at the chamber centre near the shaft because the particles in this region are still in a transitional state and no stable flow pattern is observed by DEM.

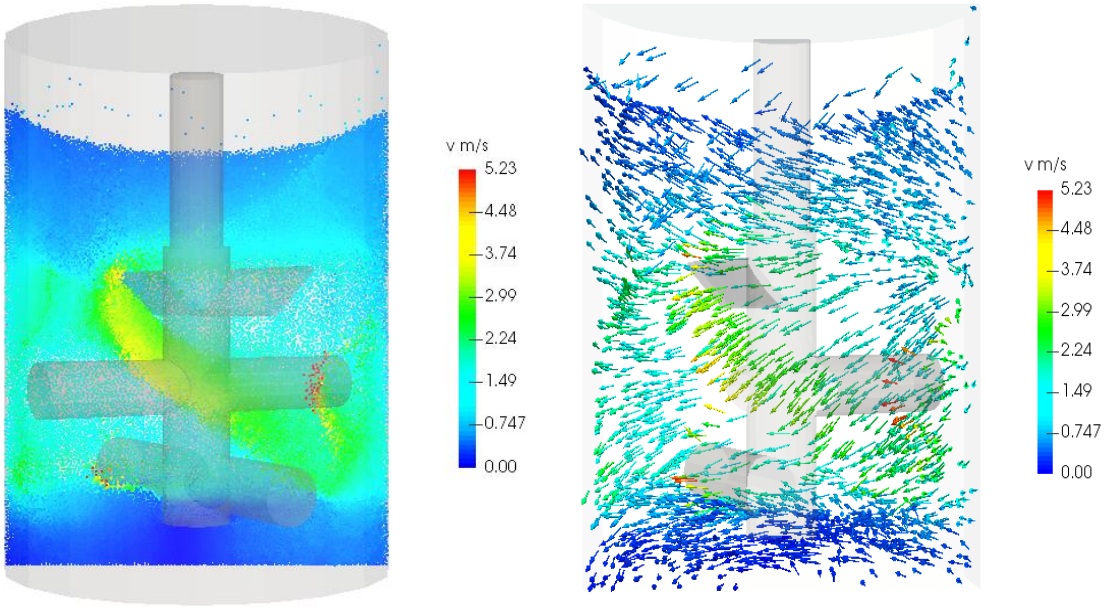

Fig. 6-7. The distribution of instantaneous velocity obtained using Type a-5 at V_t=5.23 m/s (800 RPM). (a) Velocity distribution and (b) velocity vector.

Fig.6-7 shows simulated velocity distributions using *Type a-5* at V_t=5.23 *m/s* (800 RPM) in the laboratory scale mill. Compared to *Type a*, stirrer *Type a-5* has a pitched flat blade to provide downwards pumping force. The impact on flow behaviour of the grinding media from the pitched flat blade is clearly demonstrated by DEM results. As seen in Fig. 6-7a, the magnitude of the velocity near the tip of the pitched blade is between 3~4 m/s. A high velocity tail is observed starting from the tip of the blade. The velocity vector (see Fig. 6-7b) shows that the grinding media in front of the pitched blade are pushed downwards.

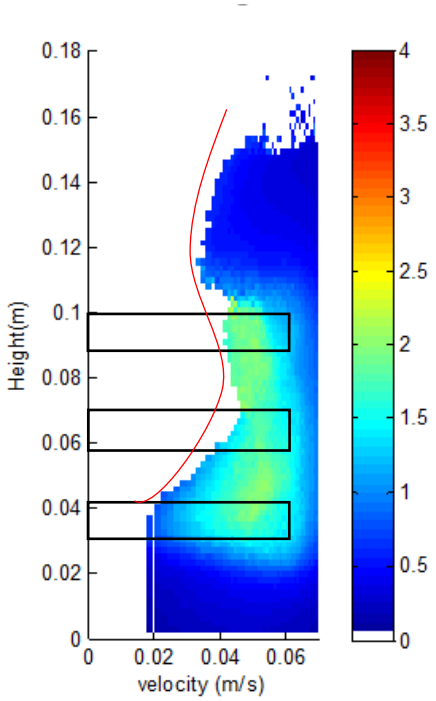

Fig. 6-8. The azimuthally averaged 3D-velocity map obtained using Type a-5.

The azimuthally averaged 3D-velocity map obtained using stirrer *Type a-5* is shown in Fig. 6-8. The high velocity field is indicated by the colour green and is greatly increased compared to the results obtained using the standard stirrer *Type a (see Fig. 6-5a)*. The height level of grinding media is also increased from 0.13 m *(Type a*) to 0.16 m (*Type a-5*). Although more grinding media particles are observed in the chamber bottom, the overall circulation in the vertical direction is accelerated. Particularly, the movement in the upper band (height > 0.08 m) is improved. This implies more kinetic energy can be absorbed by the grinding media and more intensive collisions may happen between the grinding media.

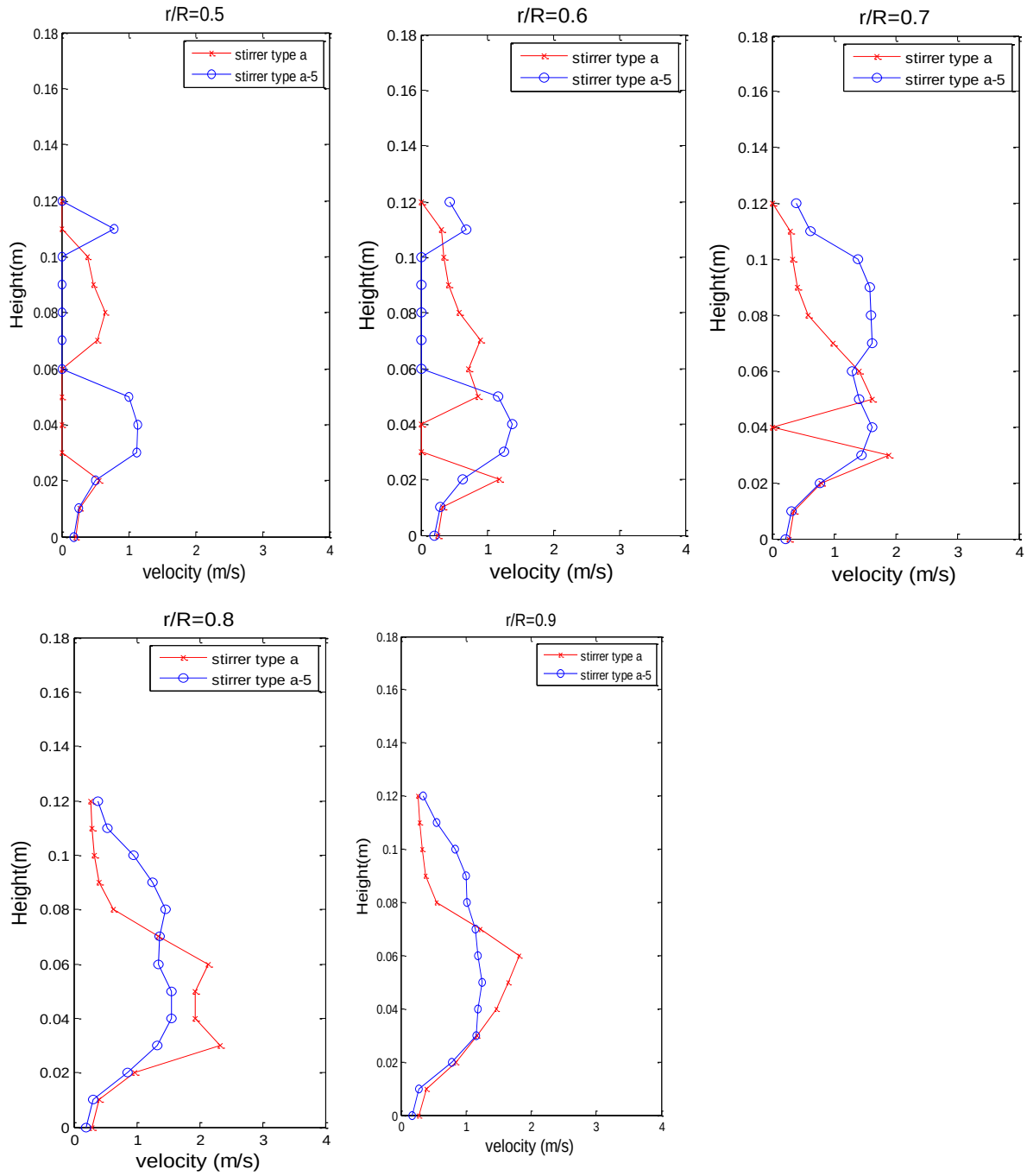

Fig. 6-9. Comparison of the azimuthally averaged 3D-velocity distribution obtained using the stirrer Type a and stirrer Type a-5 at the radial position r/R=0.5, 0.6, 0.7, 0.8 and 0.9.

The detailed 3D-velocity profiles at radial position r/R=0.5, 0.6, 0.7, 0.8 and 0.9 are shown in Fig. 6-9 to compare DEM results obtained using *Type a* and *Type a-5.* At the radial position r/R=0.5 and 0.6 where near the shaft, the 3D-velocity of grinding media obtained using stirrer *Type a* shows higher values over the results obtained using *Type a*-5 in the area

where the height is between 0.06~0.1 m. When the height is dropped below 0.06 m, the velocity of the grinding media generated using *Type a-5* becomes higher. This phenomenon is probably caused by the extra forces provided by the flat blade. The grinding media is pushed down into the impeller band and fewer grinding media are filling in the band with height 0.06 to 0.1 m when *Type a-5* is used.

When the r/R is increased to 0.7, 0.8 and 0.9 where is near the tip of the stirrer, the higher velocity is observed for *Type a-5* in the upper band (> 0.08 m). This implies that stirrer *Type a-5* effectively pushes the grinding media in the upper band back to the impeller band (0.02~0.08 m). Although the peak speed is observed with stirrer *Type a* in the impeller band (0.02~0.08 m), the overall distribution of the grinding media velocity obtained using stirrer *Type a-5* is smoother and higher. *Type a-5* shows a better performance than *Type a* in driving the movement of the grinding media across the whole grinding chamber.

6.3.2. Pilot scale mill

The DEM results obtained for the pilot scale mill with the standard pin stirrer (*Type b*) are shown in Fig. 6-10. The V_t is 5.23 m/s (384 RPM) for the pilot scale mill. The stirrer *Type b* for the pilot scale mill is an equivalent configuration to *Type a* used in the laboratory scale mill. Thus, a similar flow trend of the grinding media is observed in the pilot scale mill. A vortex is formed in the centre near the shaft and bulk grinding media particles are driven by the stirrer to move anti-clockwise (as seen from the top) as shown in the distribution of the velocity vector (see Fig. 6-10b). The grinding chamber volume is increased from 2.9 L (laboratory scale) to 22.8 L for the pilot scale mill by 7.8 times. The number of the pin stirrer arms is increased from 2 pairs to 9 pairs to ensure sufficient contact between the grinding

media and the stirrer. As seen from the instantaneous velocity distribution (Fig. 6-10a), more particles with a velocity larger than 2.6 m/s (50 % of tip speed) are observed. The grinding media with high velocity coloured by red and yellow are observed within the region near to the stirrer. No obvious movement of the grinding media is observed in the upper band or the bottom when using *Type b*.

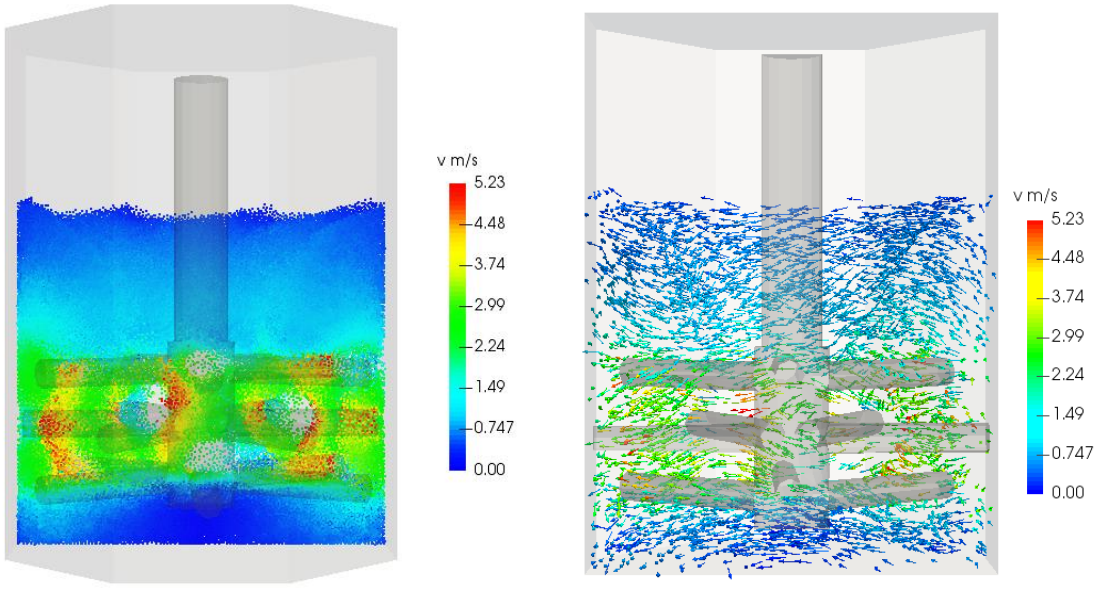

a ***b***

Fig. 6-10. The distribution of instantaneous velocity obtained in the pilot scale mill using standard stirrer (Type b) at V_t=5.23 m/s. (a) velocity distribution and (b) velocity vector.

In the laboratory scale mill, the performance of stirrer *Type a-5*, a combination of the pin stirrer and flat blade, demonstrates an evident improvement in the media velocity above the impeller band. Thus, the stirrer *Type b-1,* an equivalent design, is applied in the pilot scale mill to improve the velocity magnitude in the upper band (height > 0.15 m). Fig. 6-11 shows DEM results obtained using stirrer *Type b-1* in the pilot scale mill. It is clearly seen from the instantaneous velocity distribution (see Fig. 6-11a) that the media with high velocity are generated from the stirrer to a higher location indicated by the colour green. To

quantitatively compare the velocity distribution across the mill chamber, the azimuthally averaged 3D-velocity maps using these 2 types are shown in Fig. 6-12.

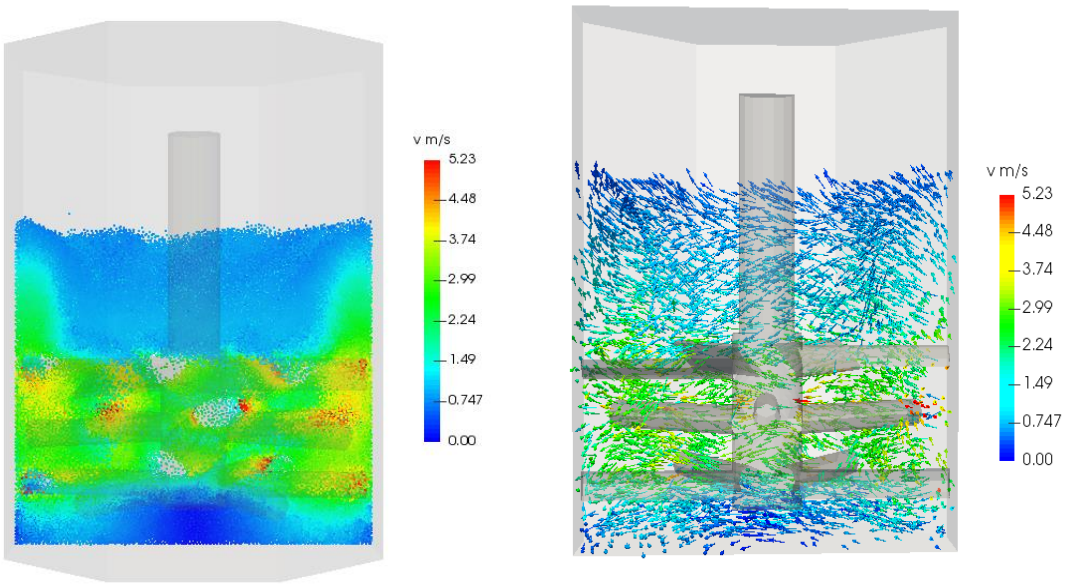

Fig. 6-11. The distribution of instantaneous velocity in the pilot scale mill using stirrer Type b-1 at V_t=5.23 m/s. (a) velocity distribution and (b) velocity vector.

The application of the pitched flat blade improves flow in the upper region within the laboratory scale mill. A similar influence on the pilot scale mill is also observed using stirrer *Type b-1*. In the impeller band (height 0.05~0.15 m), the peak velocity is approaching 4 m/s indicated by the colour yellow on the azimuthally averaged 3D-velocity maps (see Fig. 6-12).

In the area above the height of 0.15 m (upper band) and below the height of 0.05 m (lower band), there is an evident improvement in the magnitude of velocity when stirrer *Type b-1* is used. The outlines of the free surface indicated by the red curves in Fig. 6-12 indicate that more grinding media particles fills in the impeller band using *Type b-1*.

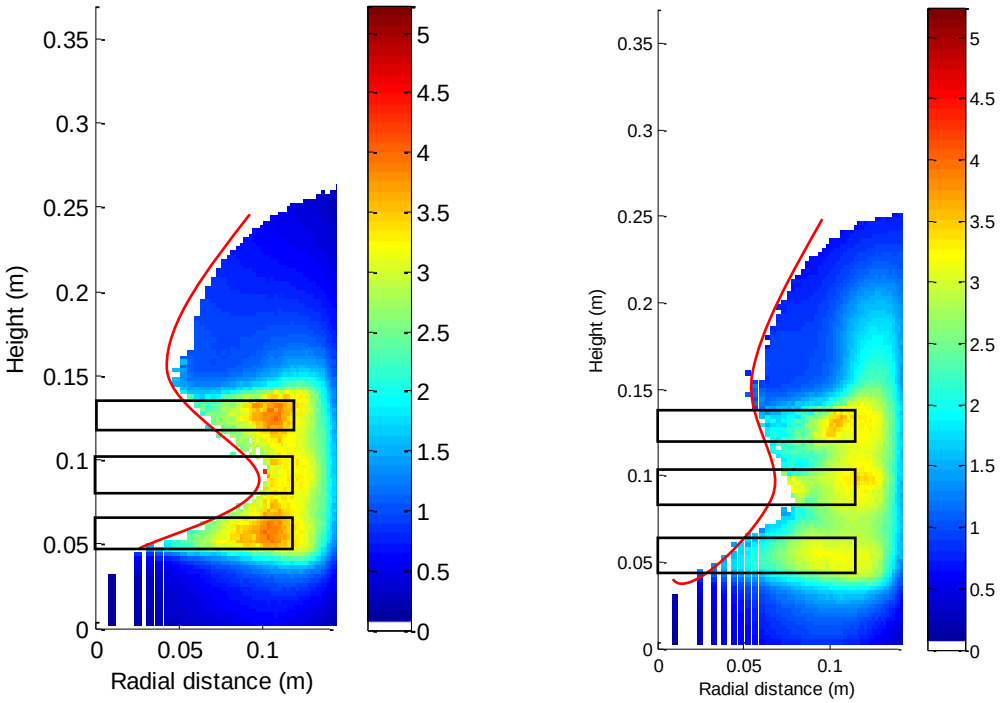

a ***b***

Fig. 6-12. Comparison of the azimuthally averaged 3D-velocity maps obtained in the pilot scale mill using Type b (a) and Type b-1 (b) at V_t=5.23 m/s (376 RPM).

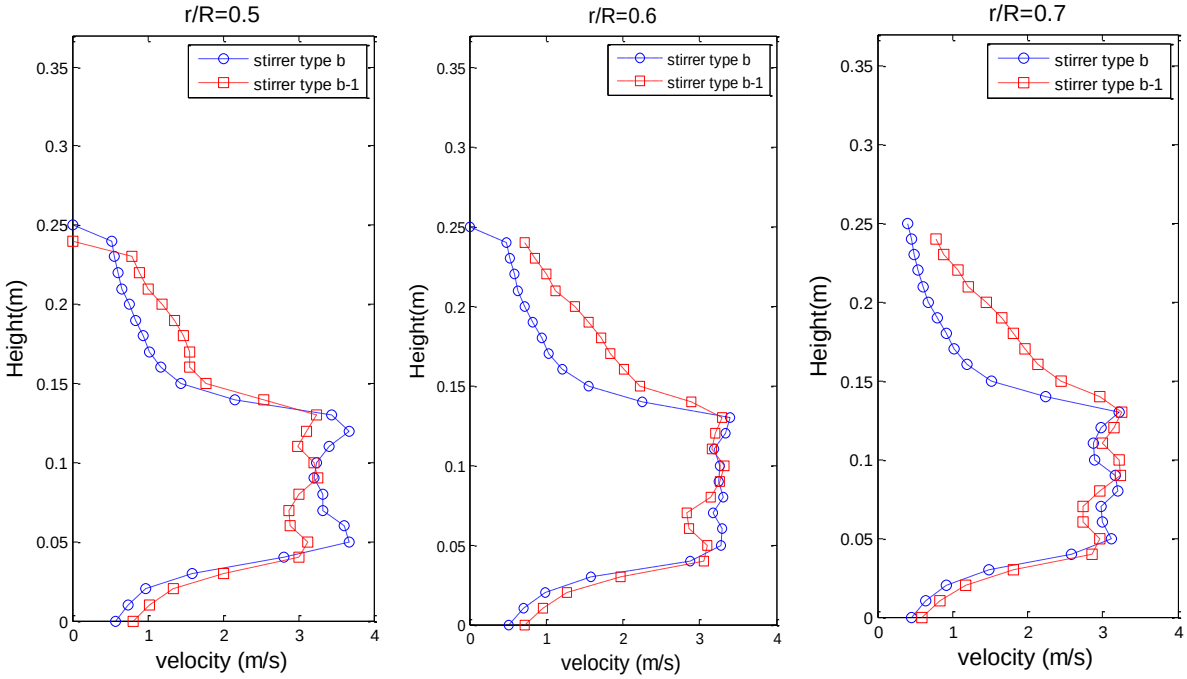

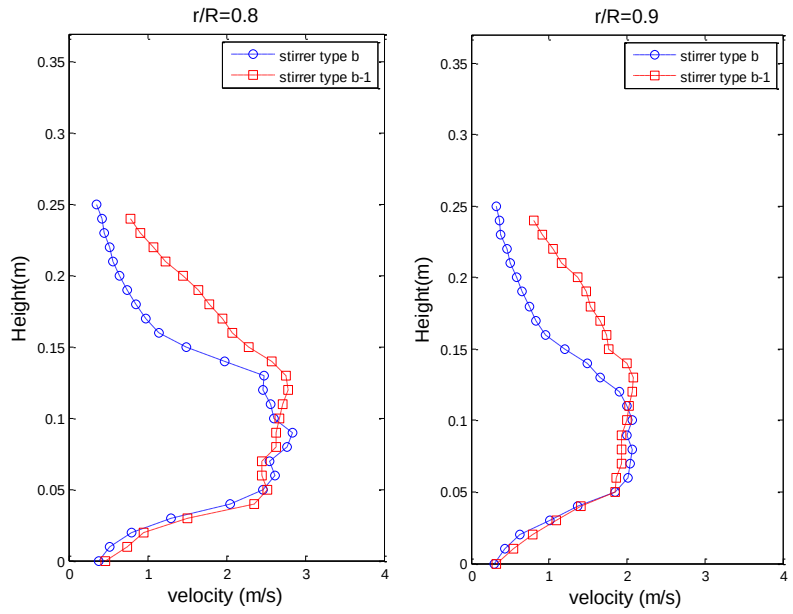

Fig. 6-13. Comparison of the azimuthally averaged 3D-velocity profiles obtained in the pilot scale mill using Type b (the standard stirrer) and stirrer Type b-1 at radial position r/R=0.5, 0.6, 0.7, 0.8 and 0.9.

Fig. 6-13 shows the 3D-velocity profiles along the vertical axis at different radial positions (r/R=0.5, 0.6, 0.7, 0.8, and 0.9). The velocity of the grinding media in the impeller band (0.05~0.15 m) is almost identical using these 2 stirrers. However, in the band height from 0.15 to 0.25 m, the 3D-velocity for stirrer *Type b-1* shows a significant increase over the results obtained using stirrer *Type b*. At the chamber bottom (height below 0.05 m) *Type b-1* also slightly improves the movement of the grinding media.

Combining the instantaneous velocity distribution obtained from both scales, a global circulation flow pattern within the grinding chamber can be deduced. Grinding media is transported upwards along the chamber wall then they flow towards the centre in the region above the stirrer. The attrition and drag force from the chamber wall are important factors for the generation of the velocity gradient which is a main source of the shear stress.

Then, grinding media beads begin to flow downwards when they approach the stirrer shaft. When grinding media beads flow down to the impeller band, they are centrifuged by the stirrer to move towards the chamber wall again. At the chamber bottom the grinding media beads flow towards to the centre then they move upwards to the impeller band to be centrifuged. With a large loop above the stirrer and a small loop beneath the stirrer, two loops complete the whole circulation of the grinding media within the vertically stirred mill.

The modified stirrer with the pitched blades clearly accelerates the circulation of the grinding media under the same operating conditions without increasing the rotational speed. The improvement is demonstrated by both PEPT and DEM results. The peak velocity observed using both stirrers *Type b* and *Type b-1* remains close. However, in the area above the impeller band where grinding media usually moves slowly, the improvement in the velocity is significant using stirrer *Type b-1*. Additionally, the velocity distribution in the chamber bottom is also slightly increased by using *Type b-1*.

The DEM simulation results obtained in the pilot scale mill are consistent with the simulation results obtained in the laboratory scale mill. The performances on both scales imply the scale up of stirrer design from laboratory is feasible in practice. The stirrer configuration and the chamber shape applied in the pilot scale mill are already identical to the plant scale. The simulated results in the pilot scale mill provide a reliable guidance for the application of the stirrer in the plant scale mill. The configuration of *Type b-1* has been accepted by Imerys as a new stirrer for the plant scale mill. A significant improvement in grinding efficiency (3∼5 %) is achieved.

6.4. Conclusions

In this study, a numerical model based on the Hertz-Mindlin contact theory is applied to study the movement of grinding media in both laboratory scale and pilot scale mills. The modelling results are obtained through DEM. The simulated velocity of the grinding media by DEM is compared with the results obtained with PEPT. Apart from a slight discrepancy observed around the centre of the grinding chamber (r/R < 0.6), DEM presents an accurate prediction in the velocity of grinding media especially the velocity distribution near the chamber wall ($r/R \geq 0.6$). The stirrer (*Type a-5*) with an addition pair of pitched flat blades shows a better performance than the normal pin stirrer (*Type a*). This is demonstrated by the results obtained from DEM on both scales. This further validates the reliability in improving the grinding efficiency via modifying the stirrer configuration.

Overall, the DEM simulation enables modelling of the grinding media flow in a stirred media mill. The low cost and ability to adapt with any mill geometries enable DEM to investigate the grinding process, particularly for analysing different scales of the mill.

Chapter 7 Conclusions and further work recommendations

Wet grinding in vertically stirred media mills is inherently a very complicated process. The work in this study tries to contribute the understanding of the grinding mechanism inside the mill chamber. The study is performed in a laboratory scale and a pilot scale mill via a large amount of the experimental data obtained under various conditions. The detailed flow behaviour is investigated by both PEPT and DEM. The results of DEM simulation are validated with PEPT. The results obtained from both PEPT and DEM show a consistent outcome with the experimental results.

7.1. Conclusions

The study investigates the grinding process in vertically stirred media mills under different operating conditions. First, the rheology of the feed slurry was analysed at 50 %, 65 % and 75 %(w/w) solids concentrations. A higher solids concentration produces a higher viscosity of the suspension. The trend of the shear rate against the shear stress indicates that the slurry shows a typical shear thinning behaviour (non-Newtonian behaviour). The morphology of calcite was studied through the Scanning Electron Microscopy (SEM). The product obtained under different specific energy input were compared and demonstrated. The morphology of calcite was also compared with wollastonite and perlite.

The operating parameters including specific energy input, rotational speed, solids concentration, grinding media type and dosage of dispersant were examined in the laboratory scale mill. The experimental results obtained at a wide range of tip speeds indicate that the reduction in product size was not evident when increasing rotational speed but a higher speed significantly reduces the grinding time. A linear relationship was observed between the power draw and the tip speed. The experiments over a range of

solids concentration indicate that a finer product was obtained when the solids concentration is reduced for a highly viscous slurry. The product size obtained using ZirPro grinding media size ranges: +0.7-1.4 mm, +1.6-2.0 mm and +2.0-2.4 mm indicate that a better grinding efficiency was achieved using a finer size of the grinding media. The analysis of the dispersant dosage shows that a lower level of dispersants was suitable for the wet grinding process with highly viscous slurry.

The investigation into novel stirrer configurations and different lid thickness is carried out by examining the product quality and related PEPT results. The results indicate that increasing the number of stirrer arms is helpful in improving the flow behaviour and gives a finer product. By replacing the pin stirrer with the blade stirrer, the flow direction of the grinding media is effectively controlled by the blade stirrer to generate the desired motion. The thick lid provided compression force over the slurry. The grinding efficiency is greatly improved by some modification.

To confirm the promising results obtained in the laboratory scale mill, the process has been scaled up to a pilot scale mill. Consistent grinding results have been reproduced in the pilot scale mill and they confirm the trends observed in the laboratory scale mill.

A numerical model based on the Hertz-Mindlin contact theory has simulated the grinding media movement in the vertically stirred media mill. The simulated results from DEM are consistent with the results from PEPT. The impact caused by the new design of the stirrer is illustrated by DEM in both laboratory and pilot scale mills. The stirrer (*Type a-5*) with an addition pair of the pitched flat blades shows better performance than the normal pin stirrer (*Type a*) at both scales. This further validates the new stirrer configuration in improving the grinding efficiency.

As the promising results are observed by using a combination of flat stirrer arm and pin stirrer arm (e.g. *Type a-5* in the laboratory scale mill and *Type b-1* in the pilot scale mill). This type of the stirrer is implemented at an industrial scale by Imerys for production of the calcium carbonate. The new type stirrer has increased the contact surface with the mineral slurry and the force used to break the mineral particle. The rate of wear on the liner of the stirrer and chamber wall is increased. This may lead to an extra cost on the material used for covering the surface of the stirrer and grinding chamber. However, the grinding efficiency is improved (less energy is required for achieving the same product fineness by using the new stirrer) and the total grinding time is reduced. Overall, the energy saving is obtained up to 3% comparing to the standard stirrer currently used in the grinding process.

7.2. Further work recommendations

In the future, this research can be extended in many ways to further optimise the grinding process. It is observed that the temperature inside the grinding chamber can be very high when the grinding time is long. This means some input energy is wasted as heat. This is a potential area to save more the energy. Also, there are many other types of dispersant being developed. Their influence over the grinding efficiency is still unknown. It is recommended to expand the study to other types of dispersant. The experimental data obtained in this study is based on a batch process. The grinding in a continuous model is suggested in the future study.

PEPT has been proven to be an effective tool for studying the motion of grinding media in a stirrer media mill. Some modification in the stirrer configurations are studied by PEPT. In the future, some other modification such as baffles, helical blades, shape of the chamber is recommended to be investigated through PEPT.

Also, it is recommended to transfer the PEPT data into a trigonometric function through Fourier analysis to simplify the data analysis. When different impeller speeds are applied, the general function of the tracer position against the grinding time shows variation in period and amplitude. This implies that Fourier analysis could be a possible to investigate the PEPT data.

The simulation of DEM is at an early stage for the grinding process. The contacting forces considered in the study are very limited. A more sophisticated model is recommended in the future study for a more realistic description of the grinding behaviour. The study in different stirrer configurations is also recommended.

References

Altun, O., Benzer, H., Enderle, U., 2013. Effects of operating parameters on the efficiency of dry stirred milling. Minerals Engineering 43-44, 58-66.

Altun, O., Benzer, H., Enderle, U., 2014. The effects of chamber diameter and stirrer design on dry horizontal stirred mill performance. Minerals Engineering 69, 24-28.

Austin, L.G., 1971a. Introduction to the mathematical description of grinding as a rate process. Powder Technology 5, 1-17.

Austin, L.G., 1971b. Methods for Determination of Breakage Distribution Parameters. Powder Technology 5, 215-222.

Austin, L.G., 1981. An Analysis of Fine Dry Grinding in Ball Mills. Powder Technology 28, 83-90.

Bakalis, S., Cox, P.W., Russell, A.B., Parker, D.J., Fryer, P.J., 2006. Development and use of positron emitting particle tracking (PEPT) for velocity measurements in viscous fluids in pilot scale equipment. Chemical Engineering Science 61, 1864-1877.

Bakalis, S., Karwe, M.V., 2002. Velocity distributions dnd volume flow rates in the nip and translational regions of a co-rotating,self-wiping, twin-screw extruder. Journal of Food Engineering 5, 273-282.

Balaz, P., 2008. Mechanochemistry in Nanoscience and Minerals Engineering, 1-102. Springer, Berlin.

Baláž, P., Godočíková, E., Kril'ová, L., Lobotka, P., Gock, E., 2004. Preparation of nanocrystalline materials by high-energy milling. Materials Science and Engineering: A 386, 442-446.

Barigou, M., 2004. Particle tracking in opaque mixing systems: an overview of the capabilities of PET and PEPT. Chemical Engineering Research and Design 82, 1258–1267.

Barley, R.W., Conway-Baker, J., Pascoe, R.D., Kostuch, J., McLoughlin, B., Parker, D.J., 2004. Measurement of the motion of grinding media in a vertically stirred mill using positron emission particle tracking (PEPT) Part II. Minerals Engineering 17, 1179-1187.

Becker, M., Kwade, A., Schwedes, J., 2001. Stress intensity in stirred media mills and its effect on specific energy requirement. Int. J. Miner. Process 61, 189–208.

Beinert, S., Fragnière, G., Schilde, C., Kwade, A., 2015. Analysis and modelling of bead contacts in wet-operating stirred media and planetary ball mills with CFD–DEM simulations. Chemical Engineering Science 134, 648-662.

Bernhardt, C., Reinsch, E., Husemann, K., 1999. The influence of suspension properties on ultra-fine grinding in stirred ball mills. Powder Technology 105, 357–361.

Bertrand, F., Leclaire, L.A., Levecque, G., 2005. DEM-based models for the mixing of granular materials. Chemical Engineering Science 60, 2517-2531.

Bilgili, E., Scarlett, B., 2005. Population balance modelling of non-linear effects in milling processes. Powder Technology 153, 59-71.

Blais, B., Bertrand, F., 2017. CFD-DEM investigation of viscous solid–liquid mixing: Impact of particle properties and mixer characteristics. Chemical Engineering Research and Design 118, 270-285.

Breitung-Faes, S., Kwade, A., 2013. Prediction of energy effective grinding conditions. Minerals Engineering 43-44, 36-43.

Chu, K.W., Wang, B., Yu, A.B., Vince, A., Barnett, G.D., Barnett, P.J., 2009. CFD–DEM study of the effect of particle density distribution on the multiphase flow and performance of dense medium cyclone. Minerals Engineering 22, 893-909.

Chiti, F., 2007. Lagrangian studies of turbulent mixing in a vessel agitated by a rushton turbine: Positron Emission Particle Tracking (Pept)and Computational Fluid Dynamics (CFD), School of Chemical Engineering. The University of Birmingham.

Cleary, P.W., Sinnott, M., Morrison, R., 2006. Analysis of stirred mill performance using DEM simulation: Part 2 – Coherent flow structures, liner stress and wear, mixing and transport. Minerals Engineering 19, 1551-1572.

Cleary, P.W., Sinnott, M., Morrison, R., 2006b. Prediction of slurry transport in SAG mills using SPH fluid flow in a dynamic DEM based porous media. Minerals Engineering 19, 1517-1527.

Conway-Baker, J., Barley, R.W., Williams, R.A., Jia, X., Kostuch, J., McLoughlin, B., Parker, D.J., 2002. Measurement of the motion of grinding media in a vertically stirred mill using positron emission particle tracking (PEPT). Minerals Engineering 15, 53–59.

da Cunha, E.R., de Carvalho, R.M., Tavares, L.M., 2013. Simulation of solids flow and energy transfer in a vertical shaft impact crusher using DEM. Minerals Engineering 43-44, 85-90.

Deryaguin, B. V. and Landau, L. D., 1941. A theory of the stability of strongly charged lyophobic sols and of the adhesion of strongly charged particles in solutions of electrolytes. Acta Physicochim. USSR 14, 633.

Derjaguin, B.V., Muller, v.M., Toporov, y.P., 1975. Effect of Contact Deformations on the Adhesion of Particles. Journal of Colloid Interface Science 53.

Di Renzo, A., Di Maio, F.P., 2004. Comparison of contact-force models for the simulation of collisions in DEM-based granular flow codes. Chemical Engineering Science 59, 525-541.

Drzymala, J., 2007. Mineral processing foundations of theory and practice of minerallurgy, Oficyna Wydawnicza PWr.

Engstrom, J., Wang, C., Lai, C., Sweeney, J., 2013. Introduction of a new scaling approach for particle size reduction in toothed rotor-stator wet mills. International journal of pharmaceutics 456, 261-268.

Fan, X., Parker, D.J., Smith, M.D., 2006. Labelling a single particle for positron emission particle tracking using direct activation and ion-exchange techniques. Nuclear Instruments and Methods in Physics Research Section A: Accelerators, Spectrometers, Detectors and Associated Equipment 562, 345-350.

Gaudin, A.M., Meloy, T.P., 1962. Model and comminution distribution equation for repeated fracture. Transactions of the AIME 223 43–50.

Giuseppina Montante, A.P., 2014. Hydrodynamics of a Model Stirred Anaerobic Digester. Chemical engineering transactions 38, 49-54.

Gock, E., Kurrer, K.-E., 1999. Eccentric vibratory mills — theory and practice. Powder Technology, 302–310.

Goniva, C., Kloss, C., Deen, N.G., Kuipers, J.A.M., Pirker, S., 2012. Influence of rolling friction on single spout fluidized bed simulation. Particuology 10, 582-591.

Greenwood, R., Rowson, N., Kingman, S., Brown, G., 2002. A New Method For Determining The Optimum Dispersant Concentration In Aqueous Grinding. Powder Technology 123, 199-207.

Gupta, C.K., 2003. Chemical Metallurgy:Principles and Practice. Wiley-VCH Verlag GmbH & Co., KGaA,Weinheim.

Guida, A., Nienow, A.W., Barigou, M., 2010. PEPT measurements of solid–liquid flow field and spatial phase distribution in concentrated monodisperse stirred suspensions. Chemical Engineering Science 65, 1905-1914.

Guida, A., Nienow, A.W., Barigou, M., 2011. Mixing of dense binary suspensions: Multi-component hydrodynamics and spatial phase distribution by PEPT. AIChE Journal 57, 2302-2315.

He, M., Wang, Y., Forssberg, E., 2004. Slurry rheology in wet ultrafine grinding of industrial minerals: a review. Powder Technology 147, 94-112.

Heath, A., Keikkala, V., Paz, A., Lehto, H., 2017. A power model for fine grinding HIGmills with castellated rotors. Minerals Engineering 103-104, 25-32.

Holdich, R.G., 2002. Fundamentals of Particle Technology. Midland Information Technology and Publishing.

Imerys, 2017, Company Profile, viewed 13 October 2017, available from: http://www.imerys.com/scopi/group/imeryscom/imeryscom.nsf/pagesref/SCOI-8S4DUX?Opendocument&lang=en

Jankovic, A., Valery, W., Rosa, D.L., 2003. Fine grinding in the australian mining industry, 3rd International Conference on Recent Advances in Materials,Minerals and Environment (RAMM 2003), Malaysia.

Jayasundara, C.T., Yang, R.Y., Guo, B.Y., Yu, A.B., Govender, I., Mainza, A., Westhuizen, A.v.d., Rubenstein, J., 2011. CFD–DEM modelling of particle flow in IsaMills – Comparison between simulations and PEPT measurements. Minerals Engineering 24, 181-187.

Jeong, S.W., Kim, J., Lee, D.H., 2015. Effect of operating variables on synthesis of multi-walled carbon nanotubes in fluidized beds. Chemical Engineering Science 134, 496-503.

Johnson, K.L., Kendall, K., Roberts, A.D., 1971. Surface Energy and the Contact of Elastic Solids. Mathematical and Physica Sciences 324 301-313.

Kanda, Y., Kotake, N., 2007. Chapter 12 Comminution Energy and Evaluation in Fine Grinding, in: Agba D. Salman, M.G., Michael J. Hounslow (Ed.), Handbook of Powder Technology, pp. 529-550.

Kelly, E.G., Spottiswood, D.J., 1989. Introduction to Mineral Processing. Mineral Engineering Services.

Kimura, M., Narumi, M., Kobayashi, T., 2007. Design Method of Ball Mill by Discrete Element Method. SUMITOMO KAGAKU 2007-2.

Kloss, C., Goniva, C., Hager, A., Amberger, S., Pirker, S., 2012. Models, algorithms and validation for opensource DEM and CFD-DEM. Progress in Computational Fluid Dynamics, An International Journal 12, 140.

Kwade, A., 2004. Mill selection and process optimization using a physical grinding model. International Journal of Mineral Processing 74, 93-101.

Kwade, A., Blecher, L., Schwedes, J., 1996. Motion and stress intensity of grinding beads in a stirred media mill.Part 2: Stress intensity and its effect on comminution. Powder Technology 86, 69-76.

Kwade, A., Schwedes, J., 2007. Chapter 6 Wet Grinding in Stirred Media Mills, in: Agba D. Salman, M.G., Michael J. Hounslow (Ed.), Handbook of Powder Technology, pp. 251-382.

Kumar, A., 2015. Grinding Mills InfoMine, TechnoMine Mining Technology.

Launder, B.E., Spalding, D.B., 1974. The numerical computation of turbulent flows. Computer methods in applied mechanics and engineering 3, 269-289.

Lian, G., Thornton, C., Adams, M.J., 1993. A Theoretical Study of the Liquid Bridge Forces between Two Rigid Spherical Bodies. Journal of Colloidand Interface Science 161, 138-147.

Liu, L., 2013. Computational fluid dynamics modelling of complex fluid flow in stirred vessels, School of Chemical Engineering. University of Birmingham.

Liu, L., Barigou, M., 2013. Numerical modelling of velocity field and phase distribution in dense monodisperse solid–liquid suspensions under different regimes of agitation: CFD and PEPT experiments. Chemical Engineering Science 101, 837-850.

Marigo, M., 2012. Discrete Element Method Modelling of Complex Granular Motion in Mixing Vessels: Evaluation and Validation, School of Chemical Engineering. The University of Birmingham.

Metso, 2017, Basics in minerals processing, viewed 30 October 2017, available from: http://www.metso.com/miningandconstruction/MaTobox7.nsf/DocsByID/EAE6CA3B8E216295C2257E4B003FBBA6/$File/Basics-in-minerals-processing.pdf

Mishra, B.K., Rajamani, R.K., 1990. Motion Analysis in Tumbling Mills by the Discrete Element Method. KONA Powder and Particle Journal 8, 92-98.

Montante, G., Paglianti, A., Magelli, F., 2012. Analysis of dilute solid–liquid suspensions in turbulent stirred tanks. Chemical Engineering Research and Design 90, 1448-1456.

Moore, P., 2012 Dust to dust-from primary crushing to ultrafine grinding, new comminution technology continues to give mines the edge in recovery and efficiency. International Mining 56.

Morrison, R.D., Cleary, P.W., Sinnott, M.D., 2009. Using DEM to compare the energy efficiency of pilot scale ball and tower mills. Minerals Engineering 22, 665-672.

Moys, M.H., 2015. Grinding to nano-sizes: Effect of media size and slurry viscosity. Minerals Engineering 74, 64-67.

Ohenoja, K., Illikainen, M., Niinimäki, J., 2013. Effect of operational parameters and stress energies on the particle size distribution of TiO2 pigment in stirred media milling. Powder Technology 234, 91-96.

Öksüzoğlu, B., Uçurum, M., 2016. An experimental study on the ultra-fine grinding of gypsum ore in a dry ball mill. Powder Technology 291, 186-192.

Orumwense, O.A., 1992. The Kinetics of Fine Grinding In An Annular Ball Mill. Powder Technology 73, 101-108.

Ouattara, S., Frances, C., 2014. Grinding of calcite suspensions in a stirred media mill: Effect of operational parameters on the product quality and the specific energy. Powder Technology 255, 89-97.

Padros, C.B., 2014. Discrete element simulations with LIGGGHTS, Zienkiewicz Centre for Computational Engineering (ZC2E) College of Engineering. Swansea University.

Parker, D.J., C.J.Broadbent, Fowles, P., Hawkesworth, M.R., McNeil, P., 1993. Positron emission particle tracking a technique for studying flow within engineering equipment. Nuclear Instruments and Methods in Physics Research 82, 1258-1267.

Radziszewski, P., 2013. Assessing the stirred mill design space. Minerals Engineering 41, 9-16.

Ramsay, J., Simmons, M.J.H., Ingram, A., Stitt, E.H., 2016. Mixing of Newtonian and viscoelastic fluids using “butterfly” impellers. Chemical Engineering Science 139, 125-141.

Ravina, L. and Moramarco, N., 1993. Everything you want to know about coagulation & flocculation. Zeta-Meter, Inc. Virginia, USA.

Sinnott, M., Cleary, P.W., Morrison, R., 2006. Analysis of stirred mill performance using DEM simulation: Part 1– Media motion, energy consumption and collisional environment. Minerals Engineering 19, 1537-1550.

Shi, F., Morrison, R., Cervellin, A., Burns, F., Musa, F., 2009. Comparison of energy efficiency between ball mills and stirred mills in coarse grinding. Minerals Engineering 22, 673-680.

Steffe, J.F., 1996. Rheological methods in food process engineering, 2nd ed. Freeman Press, USA.

Tamburini, A., Cipollina, A., Micale, G., Brucato, A., Ciofalo, M., 2013. CFD simulations of dense solid–liquid suspensions in baffled stirred tanks: Prediction of solid particle distribution. Chemical Engineering Journal 223, 875-890.

Tamblyn, R.J., 2009. Analysis of energy requirements in stirred media mills, School of Chemical Engineering. The University of Birmingham.

Theuerkauf;, J., Schwedes, J., 1999. Theoretical and experimental investigation on particle and fluid motion in stirred media mills. Powder Technology 105, 406-412.

Tromans, D., 2008. Mineral comminution: Energy efficiency considerations. Minerals Engineering 21, 613-620.

Varinot, C., Hiltgun, S., Pons, M.n., Dodds, J., 1997. Identification of the fragmentation mechanisms in wet-phase fine grinding in a stirred bead mill. Chemical engineering Science 52, 3605-3612.

Varinot, C., Berthiaux, H., Dodds, J., 1999. Prediction of the product size distribution in associations of stirred bead mills. Powder Technology 105, 228-236.

Van Lam Cheun U, Y., 2009. Solids motion in fluidised beds of fine particles, Department of Chemical Engineering. The University of Birmingham.

Verwey, E. J. W. and Overbeek, J. Th. G., 1948. Theory of the Stability of Lyophobic Colloids. Elsevier, Amsterdam.

Wang, Y., Forssberg, E., 2000. Product size distribution in stirred media mills. Minerals Engineering 13, 459-465.

Wang, Y., Forssberg, E., 2007. Enhancement of energy efficiency for mechanical production of fine and ultra-fine particles in comminution. China Particuology 5, 193-201.

Willett, C.D., Adams, M.J., Johnson, S.A., Seville, J.P.K., 2000. Capillary Bridges between Two Spherical Bodies. Langmuir 16, 9396-9405.

Wills, B.A., 2016. Mineral Processing Technology: An Introduction to the Practical Aspects of Ore Treatment and Mineral Recovery.Chapter 5 Comminution. Butterworth-Heinemann.

Wills, B.A., Finch, J.A., 2016. Mineral Processing Technology: An Introduction to the Practical Aspects of Ore Treatment and Mineral Recovery.Chapter 7 Grinding Mills. Butterworth-Heinemann.

Xiao, X., Zhang, G., Feng, Q., Xiao, S., Huang, L., Zhao, X., Li, Z., 2012. The liberation effect of magnetite fine ground by vertical stirred mill and ball mill. Minerals Engineering 34, 63-69.

Yang, R.Y., Jayasundara, C.T., Yu, A.B., Curry, D., 2006. DEM simulation of the flow of grinding media in IsaMill. Minerals Engineering 19, 984-994.

Yang, Y., Rowson, N.A., Tamblyn, R., Ingram, A., 2017. Effect of operating parameters on fine particle grinding in a vertically stirred media mill. Separation Science and Technology, 1143-1152.

Yekeler, M., Ozkan, A., Austin, L.G., 2001. Kinetics of fine wet grinding in a laboratory ball mill. Powder Technology 114, 224-228.

Zheng, J., Harris, C.C., Somasundaran, P., 1997. The effect of additives on stirred media milling of limestone. Powder Technology 91, 173-179.

Zhu, H.P., Yu, A.B., 2003. The effects of wall and rolling resistance on the couple stress of granular materials in vertical flow. Physica A: Statistical Mechanics and its Applications 325, 347-360.

Zhu, H.P., Zhou, Z.Y., Yang, R.Y., Yu, A.B., 2007. Discrete particle simulation of particulate systems: Theoretical developments. Chemical Engineering Science 62, 3378-3396.

Appendix I List of published paper and attended meetings

Yang, Y.; Rowson, N.A.; Tamblyn, R.; Ingram, A., 2017. Effect of operating parameters on fine particle grinding in a vertically stirred media mill. Separation Science and Technology. Vol. 52, Issue 6, 2017. http://dx.doi.org/10.1080/01496395.2016.1276931

2016 American Institute of Chemical Engineers (AIChE) Annual Meeting, San Francisco, USA. "Analysis about Effects of Operating Parameters on Fine Particle Grinding Process with Vertically Stirred Media Mills".

The 69th Annual Meeting of the American Physical Society (APS) –Division of Fluid Dynamics, Portland, USA. "Optimising Operating Conditions on Fine Particle Grinding Process with Vertically Stirred Media Mill".

The 23rd Joint Annual CSCST-SCI Conference, September 2016. The University of Nottingham, UK.

2016 PERCAT LES & EPS Research Conference. June 2016. The University of Birmingham, UK.

Appendix II The code developed in Matlab to analyse PEPT data.

The scripts below are used to transfer the PEPT original data into visualised 3D-velocity maps. The scripts are modified from the programs previously developed by Richard Tamblyn and Fabio Chiti (Chiti, 2007; Tamblyn, 2009).

Chiti, F., 2007. Lagrangian studies of turbulent mixing in a vessel agitated by a rushton turbine: Positron Emission Particle Tracking (Pept)and Computational Fluid Dynamics (CFD), School of Chemical Engineering. The University of Birmingham.

Tamblyn, R.J., 2009. Analysis of energy requirements in stirred media mills, School of Chemical Engineering. The University of Birmingham.

Script 1 for loading PEPT original data

```
%% Routine to load new files
clc
clear
clear java
close all

%% File Location Path
fileout=['D:\my data\2014-5-12 PEPT data\media size12052014\']; %file
folder output
filein=['D:\my data\2014-5-12 PEPT data\media size12052014\'];  %file
folder input
filename=input('insert only file name to transfer:');           %PEPT
filename

%% Open successive files
data1(1,1:4)=0;
[t,x,y,z,a,a,a,a]=textread([filein filename
'.txt'],'%f %f %f %f %f %f %f %f',-1,'headerlines',16);
data=[t,x,y,z];
data(:,1)=data(:,1)+data1(end,1);
data1=[data1; data];
data1(1,:)=[];

%% Showing portion of file to be cut
data=data1;
clear a* data1 dir_in i* n* t x y z
data(data(:,1)==0,:)=[];                                        %del
ete zero rows
clear i j gap n_int c_info a b intv id final_id dcm_obj fig

close
sav=input('insert only name of file to save in:');
save([fileout sav '.mat'])      %file name to save the final results
clc
clear all
```

Script 2 for routine used to generate azimuthally averaged 3D-velocity map

```
%%
clc
clear all
% % % % % % % % % % % % % % % % % % % % % % % % % % % % % % % % % % % % %
file_name=input('put a file name to load(.mat):\n \n');
load(file_name);
% % % % % % % % % % % % % % % % % % % % % % % % % % % % % % % % % % % % % %
d=125/1000;              % (m) diameter of impeller mm or 125mm for lab
batch pot or supermill 260mm
rev=input('put the rev:\n \n');                % (RPM) revolution of the
impeller
Vtip=pi*d*rev/60;        %(m/s)

disp('');
disp('');
disp('the calculation is on the way...')


% fdata=filtra(data,'off');            % Runs the filtrad (Chiti, 2007)
routine toremove noise.
% fdata=intrpselective(fdata,30,50);  % Runs intrpselective (Chiti,2008) to
account for high speed particle

ff(:,1)=data(:,1)/1000;    % time(s)
ff(:,2)=data(:,2)/1000;
ff(:,3)=data(:,4)/1000;    % sweep y and z data(m),
ff(:,4)=data(:,3)/1000;
% parameters
xasis=max(ff(:,2))-min(ff(:,2));
yasis=max(ff(:,3))-min(ff(:,3));
zasis=max(ff(:,4))-min(ff(:,4));
totaltime=ff(end,1)-ff(1,1);
% Normalises x and y about central axis
fdata(:,1)=ff(:,1)-ff(1,1);       % time (s) %Defines start time as zero(s)
fdata(:,2)=ff(:,2)-mean(ff(:,2)); % asis x (m)
fdata(:,3)=ff(:,3)-mean(ff(:,3)); % axis y (m)
fdata(:,4)=ff(:,4)-min(ff(:,4));  % axis z (m)
% xyz=fdata;

% calculate the velocity using cylindrical coordinates
[th,r,z]=cart2pol(fdata(:,2),fdata(:,3),fdata(:,4));

delta=0;
th1=zeros(length(th),1);                              % converted th is
range from -pi--+pi
th1(1)=th(1);
for i=2:length(th)                                    % Ensures all values
of theta are in correct range
     if(th(i)-th(i-1)<-pi)
       delta=delta+2*pi;
     elseif(th(i)-th(i-1)>pi)
       delta=delta-2*pi;
     end
     th1(i)=th(i)+delta;
end
th=th1;
```

```
clear delta i th1;
% % % % % % % % % % % % % % % % % % % % % % % % % % % % % % % % % % % % % %

rthz=[fdata(:,1) r th z];

cyl=sub1(rthz);

cyl(:,5)=cyl(:,5).*cyl(:,1);                         %rad/s-m/s change to
tangential velocity
cyl(:,7)=sqrt(cyl(:,4).^2+cyl(:,5).^2+cyl(:,6).^2);  %3-D velocity for
cylindrical coordinates
occ=sub2(cyl);
occ(:,6)=occ(:,6).*totaltime; %%residal time(s)
tofn=sum(occ(:,7));

for i=1:11;
vec(:,i)=occ(occ(:,7)>=2,i);  % get rid of all the 0 velocities
end

sav=input('insert name of file to save in:');
save(sav)

disp('')
disp('')
disp('the calculation is finished')
pause(1)
```

Script 3 for sub-function used for calculation of the tracer velocity

```
function [vel]=sub1(pos)
pnt=5;                 %number of points used to calculate the velocitiewss
step=1;

n_el=size(pos,1);      %calculate rows of f_data ,
                       %n_el=size(f_data,2) calculates the columns of data;

T=pos(:,1);            %t (s) time
X=pos(:,2);            %r (m) radial                 //x
Y=pos(:,3);            %theta (rad) no unite angular //y
Z=pos(:,4);            %z (m) height                 //z

                          %Creating the velocity matrix
j=0;
vel=zeros(n_el,8);        %creat zeros matrix
err=zeros(n_el,3);

for i=pnt:step:n_el,
    %if (diff(T((i-(pnt-1)):i))<mdt)                 % checks if all the
dt<mdt
        j=j+1;
        vel(j,1)=mean(X((i-(pnt-1)):i));             %r average distance
for 6 points(m)
        vel(j,2)=mean(Y((i-(pnt-1)):i));             %y direction (rad)
```

```
        vel(j,3)=mean(Z((i-(pnt-1)):i));             %distance in z
direction (m)

        [Vx,err(j,1)]= velfit(T((i-(pnt-1)):i),X((i-(pnt-
1)):i),pnt); %conse points method calculates the velocity (m/s)
        vel(j,4)=Vx;

        [Vy,err(j,2)]= velfit(T((i-(pnt-1)):i),Y((i-(pnt-
1)):i),pnt); %rad/s
        vel(j,5)=Vy;

        [Vz,err(j,3)]= velfit(T((i-(pnt-1)):i),Z((i-(pnt-1)):i),pnt); %m/s
        vel(j,6)=Vz;


vel(j,7)=sqrt(vel(j,4).^2+vel(j,5).^2+vel(j,6)^2);            %velocity for
cartersian coordinate 3-D velocity   m/s

        vel(j,8)=mean(T((i-(pnt-1)):i));                                %5
points time average(sec)
end
vel(j+1:end,:)=[];  % get rid of the last 4 zero points
```

Script 4 for sub-function used to calculate azimuthally averaged variables

```
function Occ=sub2(A)
%%routine to calculate the azimuthal average variables
%occupancy:

%A(r,theta,z,ur,ur theta,uz, T) to occupancy(r,theta,z,ur,utheta,uz,o)

n_el=size(A,1);            %A refers to speed matrix and how many rows
             %the R will be divided to get equal volume bins
n_r=100;      %radial  grid factor
n_rho=2;     %angular grid factor
n_phi=200;   %height  grid factor


%equal volume raius spacing
r_m=max(A(:,1));              %max diameter
phi_m=min(A(:,3));            %min height
H=max(A(:,3))-min(A(:,3));
Vcell=((r_m^2)*H.*pi)/(n_r*n_rho*n_phi);
drho=2*pi/n_rho;
dphi=(max(A(:,3))-min(A(:,3)))/n_phi;
R=zeros(n_r,1);
i=1;
while (R(i)<r_m)
    i=i+1;
    R(i)=(R(i-1)^2+Vcell*n_rho/(pi*dphi))^0.5;
end
H=zeros(n_r+1,n_phi+1,5);

pass=zeros(n_r+1,n_phi+1);
total_T=A(end,8);
xx=1;
zz=1;
```

```
%% first loop to calculate the time averaged velocity for each cell
for i=2:n_el-1;

    x=max(find(R<=A(i,1)));
    z=floor((A(i,3)-phi_m)/dphi)+1;
    dt=(A(i+1,8)-A(i-1,8))/2;

    H(x,z,1)=H(x,z,1)+A(i,4)*dt;     %u
    H(x,z,2)=H(x,z,2)+A(i,5)*dt;     %v
    H(x,z,3)=H(x,z,3)+A(i,6)*dt;     %w
    H(x,z,4)=H(x,z,4)+1;             %location

if (x~=xx||z~=zz)                    %im in the same cell
    pass(x,z)=pass(x,z)+1;
end
H(x,z,5)=H(x,z,5)+dt;      %time in the cell
j=1;
Occ=zeros(n_r*n_phi,11);             %number of elements on a plate
for i1=1:n_r,
    for i3=1:n_phi,
        Occ(j,1)=(R(i1)+R(i1+1))/2; %r positions
        Occ(j,2)=i3*dphi+phi_m;     %z positions

if (H(i1,i3,4)>=1)
Occ(j,3)=Occ(j,3)+(H(i1,i3,1)/H(i1,i3,5));   %radia
Occ(j,4)=Occ(j,4)+(H(i1,i3,2)/H(i1,i3,5));   %tangential
Occ(j,5)=Occ(j,5)+(H(i1,i3,3)/H(i1,i3,5));   %z

end

        Occ(j,6)=Occ(j,6)+H(i1,i3,5)/total_T; %frequency based on total
numbers of vitural particles
        Occ(j,7)=Occ(j,7)+H(i1,i3,4);         %total number of loc
       %Occ(j,7)=Occ(j,7)+pass(i1,i3);       %total number of pass
j=j+1;
    end
end

Occ(:,11)=sqrt(Occ(:,3).^2+Occ(:,4).^2+Occ(:,5).^2); %square velocity
Occ(:,1)=Occ(:,1);
Occ(:,2)=Occ(:,2);
```

Appendix III The code developed in LIGGGHTS for DEM

The below scripts are the homemade scripts used in open-source DEM software LIGGGHTS (LIGGGHTS stands for LAMMPS improved for general granular and granular heat transfer simulations).

The script A used in LIGGGHTS for laboratory scale mill.

```
#----------------------------------------------------------------------------------------------------------#
atom_style        sphere
atom_modify       map array
boundary          f f f
newton            off
hard_particles    yes
processors        4 3 1
communicate       single vel yes
units             si
region            reg block -0.07 0.07 -0.07 0.07 0 0.19 units box
create_box        1 reg
neighbor          0.002 bin
neigh_modify      delay 0
#----------------------------------------------------------------------------------------------------------#
#Material properties
fix  m1 all property/global youngsModulus          peratomtype           5.0e6  #1.2e7    #5.0e6
fix  m2 all property/global poissonsRatio          peratomtype           0.24   #0.44 #constant
fix  m3 all property/global coefficientRestitution  peratomtypepair    1   0.52    #(0.5)     #0.21
fix  m4 all property/global coefficientFriction     peratomtypepair    1    0.2    #0.17#(0.15)
#0.5 0.5 0.5
#----------------------------------------------------------------------------------------------------------#
#particle distributions
fix pts1 all particletemplate/sphere 15485863 atom_type 1 density constant 3200 radius
constant 0.001
```

```
fix pdd1 all particledistribution/discrete 32452843 1 pts1 1.0

#-----------------------------------------------------------------------------------------------------------------#

#import mesh from cad:

fix cad1        all mesh/surface/stress file meshes/s3.stl   type 1

fix cad2        all mesh/surface/stress file meshes/t1.stl   type 1

fix stirrer_wall all wall/gran model hertz tangential history mesh n_meshes 2 meshes cad1 cad2

#region of insertion t2 mesh

#region bc1 cylinder z  0.03  0.03 0.02 0.01 0.12 units box

#region bc2 cylinder z -0.03  0.03 0.02 0.01 0.12 units box

#region bc3 cylinder z  0.03 -0.03 0.02 0.01 0.12 units box

#region bc4 cylinder z -0.03 -0.03 0.02 0.01 0.12 units box

#-----------------------------------------------------------------------------------------------------------------#

#region of insertion t1 mesh

region bc1 cylinder z  0.03  0.03 0.02 0.01 0.19 units box

region bc2 cylinder z -0.03  0.03 0.02 0.01 0.19 units box

region bc3 cylinder z  0.03 -0.03 0.02 0.01 0.19 units box

region bc4 cylinder z -0.03 -0.03 0.02 0.01 0.19 units box


fix ins  all insert/rate/region seed 67867967 distributiontemplate pdd1 vel constant 0. 0. -10.0 insert_every 1000 overlapcheck yes all_in yes mass 0.43 massrate 5.0 region bc1

fix ins2 all insert/rate/region seed 15485867 distributiontemplate pdd1 vel constant 0. 0. -10.0 insert_every 1000 overlapcheck yes all_in yes mass 0.43 massrate 5.0 region bc2

fix ins3 all insert/rate/region seed 32452867 distributiontemplate pdd1 vel constant 0. 0. -10.0 insert_every 1000 overlapcheck yes all_in yes mass 0.43 massrate 5.0 region bc3

fix ins4 all insert/rate/region seed 49979693 distributiontemplate pdd1 vel constant 0. 0. -10.0 insert_every 1000 overlapcheck yes all_in yes mass 0.43 massrate 5.0 region bc4

#seed number 15485867, 32452843, 32452867, 49979687, 49979693, 67867967

#total mass is 1.785kg

#-----------------------------------------------------------------------------------------------------------------#

#pair style
```

```
#model = ‘hertz’ tangential = ‘history’ rolling_friction = ‘off’ cohesion = ‘off’ surface = ‘default’

pair_style   gran model hertz tangential history

pair_coeff   * *

#-------------------------------------------------------------------------------------------------------------------#

timestep   1.e-5

fix          1 all nve/sphere

fix          2 all gravity 9.81 vector 0.0 0.0 -1.0

fix          3 all buoyancy level 0.2 dim z density 1000

#fix       5 all check/timestep/gran 1 0.20 0.1

#fix       4 all viscous 5.130e-4

#gamma= 3pi*eta*d  #1.1304e-4

#-------------------------------------------------------------------------------------------------------------------#

#thermo settings

#rotational kinetic energy

compute       1 all erotate/sphere

thermo_style   custom step atoms ke c_1 vol

thermo                10000

thermo_modify  lost ignore norm no

#-------------------------------------------------------------------------------------------------------------------#

#period time per round => 800RPM 0.075  1000 RPM 0.06  1200 RPM 0.05 1500 RPM 0.04

run    60000

fix    movecad1 all move/mesh mesh cad1 rotate origin 0. 0. 0. axis 0. 0. 1. period 0.075  #

dump   dmp        all custom   10000 post/dump*.particle id type x y z ix iy iz vx vy vz fx fy fz omegax omegay omegaz radius

dump   dumpstl     all mesh/stl 10000 post/dump*.stl

run    160000

#unfix  movecad1

#dump   dmp        all custom   10000 post/dump*.particle id type x y z ix iy iz vx vy vz fx fy fz omegax omegay omegaz radius
```

```
#dump   dumpstl     all mesh/stl 10000 post/dump*.stl
#run    160000
```

The script B used in LIGGGHTS for pilot scale mill.

```
#----------------------------------------------------------------------------------------------------------#
atom_style       sphere
atom_modify    map array
boundary      f f f
newton          off
hard_particles yes
processors     4 3 1
communicate    single vel yes
units          si
region        reg block -0.14 0.14 -0.14 0.14 -0.01 0.38 units box
create_box     1 reg
neighbor       0.003 bin
neigh_modify   delay 0
#----------------------------------------------------------------------------------------------------------#
#Material properties
fix  m1 all property/global youngsModulus          peratomtype           5.0e7    #1.2e7  #5.0e6
fix  m2 all property/global poissonsRatio          peratomtype           0.24     #0.44 #constant
fix  m3 all property/global coefficientRestitution  peratomtypepair    1    0.52     #0.21
fix  m4 all property/global coefficientFriction     peratomtypepair    1    0.17     #0.17 0.5 0.5
0.5
#----------------------------------------------------------------------------------------------------------#
#particle distributions
fix pts1 all particletemplate/sphere 15485863 atom_type 1 density constant 3200 radius
constant 0.0015
fix pdd1 all particledistribution/discrete 32452843 1 pts1 1.0
#----------------------------------------------------------------------------------------------------------#
```

#import mesh from cad:

fix cad1 all mesh/surface/stress file meshes/s380d.stl type 1

fix cad2 all mesh/surface/stress file meshes/t380.stl type 1

fix stirrer_wall all wall/gran model hertz tangential history mesh n_meshes 2 meshes cad1 cad2

#region of insertion t2 mesh

#region bc1 cylinder z 0.03 0.03 0.02 0.01 0.12 units box

#region bc2 cylinder z -0.03 0.03 0.02 0.01 0.12 units box

#region bc3 cylinder z 0.03 -0.03 0.02 0.01 0.12 units box

#region bc4 cylinder z -0.03 -0.03 0.02 0.01 0.12 units box

#----------#

#region of insertion t1 mesh

region bc1 cylinder z 0.05 0.05 0.04 0.2 0.32 units box

region bc2 cylinder z -0.05 0.05 0.04 0.2 0.32 units box

region bc3 cylinder z 0.05 -0.05 0.04 0.2 0.32 units box

region bc4 cylinder z -0.05 -0.05 0.04 0.2 0.32 units box

fix ins all insert/rate/region seed 67867967 distributiontemplate pdd1 vel constant 0. 0. -10.0 insert_every 1000 overlapcheck yes all_in yes mass 3.96 massrate 10.0 region bc1

fix ins2 all insert/rate/region seed 15485867 distributiontemplate pdd1 vel constant 0. 0. -10.0 insert_every 1000 overlapcheck yes all_in yes mass 3.96 massrate 10.0 region bc2

fix ins3 all insert/rate/region seed 32452867 distributiontemplate pdd1 vel constant 0. 0. -10.0 insert_every 1000 overlapcheck yes all_in yes mass 3.96 massrate 10.0 region bc3

fix ins4 all insert/rate/region seed 49979693 distributiontemplate pdd1 vel constant 0. 0. -10.0 insert_every 1000 overlapcheck yes all_in yes mass 3.96 massrate 10.0 region bc4

#seed number 15485867, 32452843, 32452867, 49979687, 49979693, 67867967

#total mass is 1.785kg

#----------#

#pair style

#model = ‘hertz’ tangential = ‘history’ rolling_friction = ‘off’ cohesion = ‘off’ surface = ‘default’

```
pair_style   gran model hertz tangential history

pair_coeff   * *

#-------------------------------------------------------------------------------------------------------------------#

timestep   1.e-5

fix          1 all nve/sphere

fix          2 all gravity 9.81 vector 0.0 0.0 -1.0

fix         3 all buoyancy level 0.38 dim z density 1000

#fix       5 all check/timestep/gran 1 0.20 0.1

#fix       4 all viscous 5.130e-4

#gamma= 3pi*eta*d  #1.1304e-4

#-------------------------------------------------------------------------------------------------------------------#

#thermo settings

#rotational kinetic energy

compute       1 all erotate/sphere

thermo_style   custom step atoms ke c_1 vol

thermo                10000

thermo_modify  lost ignore norm no

#-------------------------------------------------------------------------------------------------------------------#

#period time per round => 800RPM=>384RPM 0.075 and 0.156  1000RPM 0.06
1200RPM=>576RPM 0.05 and 0.1042 1500RPM=> 0.04

run    60000

fix    movecad1 all move/mesh mesh cad1 rotate origin 0. 0. 0. axis 0. 0. 1. period 0.156

dump   dmp        all custom   10000 post/dump*.particle id type x y z ix iy iz vx vy vz fx fy fz
omegax omegay omegaz radius

dump   dumpstl     all mesh/stl 10000 post/dump*.stl

run       160000
```